HYDROGEL BIOINKS FOR EXTRUSION BIOPRINTING APPLICATIONS

SYNTHETIC DYNAMIC COVALENT HYDROGEL BIOINKS FOR EXTRUSION BIOPRINTING APPLICATIONS

By EVA MUELLER, B.Eng.Biosci., M.A.Sc.

A Thesis Submitted to the School of Graduate Studies in Partial Fulfillment of the Requirements for the Degree Doctor of Philosophy

McMaster University

DOCTOR OF PHILOSOPHY (2022) McMaster University

Department of Chemical Engineering Hamilton, Ontario

TITLE: Synthetic Dynamic Covalent Hydrogel Bioinks for Extrusion Bioprinting Applications

AUTHOR: Eva Mueller

B.Eng.Biosci., McMaster University

M.A.Sc., McMaster University

SUPERVISOR: Professor Todd R. Hoare

PAGES: xxiv, pp 245

LAY ABSTRACT

Three-dimensional (3D) printing is a layer-by-layer fabrication method that is just beginning to be explored for “soft” materials like gels. Current 3D-printed hydrogels need templates that need to be removed after printing, are mechanically weak, and require secondary processing steps that can be potentially harmful to living cells. These limitations are particularly problematic when hydrogels are used as an “ink” for 3D bioprinting, a form of 3D printing that prints a material “ink” and living cells together. 3D bioprinting allows for advanced drug screening and lays the foundation for growing replacement organs. This thesis is focused on developing new strategies for printing fast-gelling hydrogels and engineering the chemistry of these hydrogels to provide cells with the structural and biochemical cues required to better mimic native tissues. Such 3D-printed cell-loaded scaffolds can enable the printing of more “life-like” tissues with improved performance in tissue engineering and drug screening applications.

ABSTRACT

Soft hydrogels provide a favorable environment for cells to grow, proliferate and differentiate. However, in the context of 3D bioprinting, hydrogels are often limited by templates, weak mechanics, and/or a need to work at non-physiological temperature/pH to enable gelation. Recently, we have developed *in situ*-gelling poly(oligoethylene glycol methacrylate) (POEGMA) and zwitterionic hydrogels based on dynamic hydrazone chemistry that occurs without UV crosslinking, templating, or catalysts, providing an excellent platform for directly incorporating cells during printing. However, the mixing of any dynamic covalent hydrogels presents a challenge to ensure sufficient crosslinking during the 3D printing process. This research highlights the first demonstration of using dynamic covalent POEGMA and zwitterionic hydrogels as a synthetic bioink platform for extrusion bioprinting using a customized extrusion printer. Three mixing strategies were employed: (1) using a modified coaxial needle for diffusion-based mixing of low-viscosity functional polymers; (2) using an embedded strategy via the FRESH (freeform reversible embedding of suspended hydrogels) bioprinting method to 3D print hydrazone-crosslinked POEGMA hydrogels; and (3) using a pre-mixing approach to print pre-formed zwitterionic hydrogels to fabricate small-scale liver mimics, which showed excellent cell viability (>90%, human hepatoma cells) after two weeks and improved albumin secretion when co-printed with fibroblast cells. The tunable gelation kinetics (from instantaneous to several minutes) allowed for these mixing modalities to be evaluated and optimized in terms of print fidelity, homogeneity of the printed constructs, and overall cell viability/functionality. To overcome the immiscibility of zwitterionic-only polymers with common ionic polysaccharides, a copolymer system (comprised of DMAPS and OEGMA) was developed and evaluated in terms of swelling, protein uptake, and anti-coagulant properties. Dual-crosslinked hydrogels based on ionic crosslinking (from calcium-crosslinked sodium alginate) and covalent crosslinking (from the functional synthetic copolymers) have potential benefits in creating cell-based therapeutics that maintain high cell viability and avoid fibrotic responses.

ACKNOWLEDGEMENTS

This PhD would not have been possible without the many people I have had the privilege to work with over the years. I would like to start by saying thank you to my supervisor and mentor: Dr. Todd Hoare. Your guidance and support over the years has helped me grow into the researcher and person I am today, and I will forever be grateful for the opportunities you have given me. From the countless internal conferences, presenting at large international conferences, to trusting me with many extracurricular activities – this journey would not have been possible without your support, and I look forward to having your guidance as I continue my career.

To my committee members – Dr. Boyang Zhang and Dr. Ryan Wylie – thank you for guiding me through the research. This work would not have been possible without your continuous feedback, immense knowledge in the field, and help along the way. Thank you.

To the entire Department of Chemical Engineering – you have supported me in countless ways and allowed me to call this department my home for the past 10 years. Thank you.

I have had the privilege to work with the most talented and helpful students over the years. To Norma, Ridhdhi, Isabelle, Ron, Keith, Albert, Terrel, Gero, Melaina – thank you for all your hard work in progressing new and exciting research. I wish you nothing but the best in your future endeavours and know that I will always be here to support you.

To my colleagues and friends in the Hoare Lab, both past and present, you have made this journey one that I will never forget. I owe you all more than I can say here. To the 'old' Hoare Lab crew – Daryl, Emilia, Scott, Trevor, Fei, Rabia – thank you for showing me the wonders of research and that teamwork is at the centre of our work. To Madeline – thank you for being my science and conference partner in crime, today and always. To Kelli and Nicola – I will forever hear your contagious laughs through the halls of JHE. To all the current members in the Hoare Lab – Matt, Andrew, Doren, Nate, Nahieli, Norma, Ridhdhi, Gurpreet, Dru, Samaneh, Afshin, Laura, Chloe – you all inspire me every day. I will forever cherish the friendships and the many memories – from organizing internal conferences, planning ChEGSS events (even during a worldwide pandemic!), Intramural sports, Phoenix Cups, orchestra performances and more. These are all so special to me and have shaped me into the person I am today.

Lastly, I want to thank those closest to me.

To my parents, your endless and unwavering support means the world to me. Thank you for all that you have done and continue to do – I would not be where I am without you both. To Tim and Brittany, I have looked up to you since day one of this journey, and I appreciate your words of wisdom more than you know. And finally, to my best friend and partner in life, Kushal, thank you for always being so supportive, for being there with the biggest smile (or, a surprise waiting) and for being my biggest cheerleader throughout everything, I love you and I am looking forward to our next adventure together.

TABLE OF CONTENTS

LIST OF FIGURES

CHAPTER 1: Introduction and Objectives

CHAPTER 2: Click Chemistry Hydrogels for Extrusion Bioprinting: Progress, Challenges, and Opportunities

CHAPTER 3: Coaxial Extrusion Bioprinting of Hydrazone Crosslinked POEGMA Hydrogels: Effect of Needle Geometry On Print Quality

CHAPTER 6: Polysulfobetaine-Poly(Oligoethylene Glycol Methacrylate) Copolymers with Improved Anti-Fouling and Anti-Coagulant Properties

CHAPTER 7: 3D Printing of Interpenetrating Zwitterionic Dynamic Covalent Hydrogels and Calcium-Alginate Hydrogels for the Fabrication of Longer-Lasting Implants

LIST OF TABLES

CHAPTER 2: Click Chemistry Hydrogels for Extrusion Bioprinting: Progress, Challenges, and Opportunities

CHAPTER 3: Coaxial Extrusion Bioprinting of Hydrazone Crosslinked POEGMA Hydrogels: Effect Of Needle Geometry On Print Quality

CHAPTER 4: FRESH Bioprinting of Dynamic Hydrazone-Crosslinked Synthetic Hydrogels

CHAPTER 5: Free-Form Bioprinting using Pre-Mixed Ketone and Hydrazide Functionalized Zwitterionic Polymers

CHAPTER 6: Polysulfobetaine-Poly(Oligoethylene Glycol Methacrylate) Copolymers with Improved Anti-Fouling and Anti-Coagulant Properties

CHAPTER 7: 3D Printing of Interpenetrating Zwitterionic Dynamic Covalent Hydrogels and Calcium-Alginate Hydrogels for the Fabrication of Longer-Lasting Implants

LIST OF ABBREVIATIONS

AA	acrylic acid
ADH	adipic acid dihydrazide
AIBMe	2,2-azobisisobutryic acid dimethyl ester
APS	ammonium persulfate
BHT	butylated hydroxytoluene
BSA	bovine serum albumin
CLSM	confocal laser scanning microscopy
CFD	computational fluid dynamics
CFSE	carboxyfluorescein succinimidyl ester
DAPI	4′,6-diamidino-2-phenylindole
DIW	distilled deionized water
DMAPS	[2-(methacryloyloxy)ethyl]dimethyl-(3-sulfopropyl)ammonium hydroxide
DMEM	Dulbecco's modified Eagle's medium
DMEMAm	N-(2,2-dimethoxyethyl) methacrylamide
ECM	extracellular matrix
EDC	N'-ethyl-n-(3-dimethylaminopropyl)-carbodiimide
EDTA	ethylenediamine tetraacetic acid
FBS	fetal bovine serum
GFP	green fluorescent protein
GPC	gel permeation chromatography
FITC	fluorescein isothiocyanate
HCl	hydrochloric acid
HEPES	N-2-hydroxyethylpiperazine-n-2-ethane sulfonic acid
$M(EO)_2MA$	di(ethylene glycol) methyl ether methacrylate
$OEGMA_{500}$	oligo (ethylene glycol) methyl ether methacrylate
MEHQ	methyl ether hydroquinone
MWCO	molecular weight cut-off
NaOH	phosphate buffered saline
PBS	sodium hydroxide
PEG	poly (ethylene glycol)

PNP	pooled normal plasma
POEGMA	poly(oligoethylene glycol methacrylate)
PS	penicillin-streptomycin
TGA	thioglycolic acid
M_n	number-average molecular weight

LIST OF SYMBOLS

Pr	printability index
C	circularity
L	length
A	area
$\vec{u}$	velocity vector
ρ	density
p	pressure
I	identity tensor
μ	dynamic viscosity
F	force
ω_i	mass fraction of component i
D	diffusion coefficient
η	viscosity
K	flow consistency index
Υ	shear rate
n	power law constant
H_A	actual height
H_T	theoretical height
H_M	height maintenance
SR	swelling ratio
W_t	final (tested) weight
W_0	initial weight

DECLARATION OF ACADEMIC ACHIEVEMENT

Mueller, E.; Abrishamkar, A.; Galaev, R.; Kwan Kiu L.; Hoare, T., Coaxial Extrusion Bioprinting of Hydrazone Crosslinked POEGMA Hydrogels: Effect of Needle Geometry on Print Quality, *to be submitted.*

Mueller, E.; Preciado, N.; Xu, F.; Kalab, T.; Hoare, T., Free-form Bioprinting using Pre-mixed Ketone and Hydrazide Functionalized Zwitterionic Polymers, *to be submitted.*

Mueller. E.; Lopez, H.; Zhou Fu, Z.; Yin, R.; Fredenburgh, J.; Weitz J.; Hoare T., Polysulfobetaine-Poly(Oligoethylene Glycol Methacrylate) Copolymers with Improved Anti-Fouling and Anti-Coagulant Properties, *to be submitted.*

Mueller, E.; Xu, F.; Hoare, T., FRESH Bioprinting of Dynamic Hydrazone-Crosslinked Synthetic Hydrogels. *Biomacromolecules* **2022**, 23 (11), 4883-4896.

Xu, F.; Dawson, C.; Lamb, M.; **Mueller, E.**; Stefanek, E.; Akbari, M.; Hoare, T., Hydrogels for Tissue Engineering: Addressing Key Design Needs Toward Clinical Translation. *Front. Bioeng. Biotechn.* **2022**, 10, 849831.

Mueller, E.; Poulin, I.; Bodnaryk, W. J.; Hoare, T., Click Chemistry Hydrogels for Extrusion Bioprinting: Progress, Challenges, and Opportunities. *Biomacromolecules* **2022**, 23 (3), 619-640.

Mueller, E.; Himbert, S.; Simpson, M.S.; Bleuel, M.; Rheinstadter, M.; Hoare, T., Cationic, anionic, and amphoteric dual pH/temperature-responsive degradable microgels via self-assembly of functionalized oligomeric precursor polymers. *Macromolecules* **2020**, 54 (1), 351-363.

Aljabo, A.; **Mueller, E**.; Abdul-Azeez, D.; Hoare T.; Jain, A., Gravity steam reprocessing in healthcare facilities for the reuse of N95 respirators. *J. Hospital Infection* **2020**, 106(4), 698-708.

Sivakumaran, D.; Bakaic, E.; Campbell, S. B.; Xu, F.; **Mueller, E.**; Hoare, T., Fabricating Degradable Thermoresponsive Hydrogels on Multiple Length Scales via Reactive Extrusion, Microfluidics, Self-assembly, and *Electrospinning. J. Vis. Exp.* **2018**, (134), e54502.

Mueller, E.; Alsop, R. J.; Scotti, A.; Bleuel, M.; Rheinstadter, M. C.; Richtering, W.; Hoare, T., Dynamically Cross-Linked Self-Assembled Thermoresponsive Microgels with Homogeneous Internal Structures. *Langmuir* **2018,** *34* (4), 1601-1612.

Sivakumaran, D.*; **Mueller, E.*;** Hoare, T., Microfluidic production of degradable thermoresponsive poly (N-isopropylacrylamide)-based microgels. *Soft Matter* **2017,** *13* (47), 9060-9070.

Sivakumaran, D.; **Mueller, E.;** Hoare, T., Temperature-Induced Assembly of Monodisperse, Covalently Cross-Linked, and Degradable Poly(N-isopropylacrylamide) Microgels Based on Oligomeric Precursors. *Langmuir **2015***, 31, 5767-5778.

CHAPTER 1

Introduction and Objectives

1.1 Tissue Engineering

Tissue engineering combines biomaterial scaffolds with cells and biologically active molecules to create functional tissues. The main goal of tissue engineering is to replace, maintain, or improve damaged tissues within the human body[1, 2]. Engineering suitable replacement tissues is a challenging but exciting field of research that combines the expertise of an interdisciplinary group including biomaterial scientists, cell biologists, engineers and more[3].

Cells are the building blocks of tissues that have different functions within the human body. These cells produce and create their own support structures, known as the extracellular matrix (ECM), that act as both a support structure as well as also a relay station for signalling between groups of cells. The signals are important for cells to communicate with their surrounding environments and to organize themselves into functional tissues. In the context of tissue engineering, biomaterial scaffolds aim to replace all or some of the beneficial properties of the ECM to provide a temporary or even permanent support for the cells[4]. Growth factors and other bioactive molecules can also be introduced into the scaffold to mimic the native environment for the encapsulated cells. If the compositions of these components and culture conditions are carefully tuned, a functional tissue develops (**Figure 1.1**).

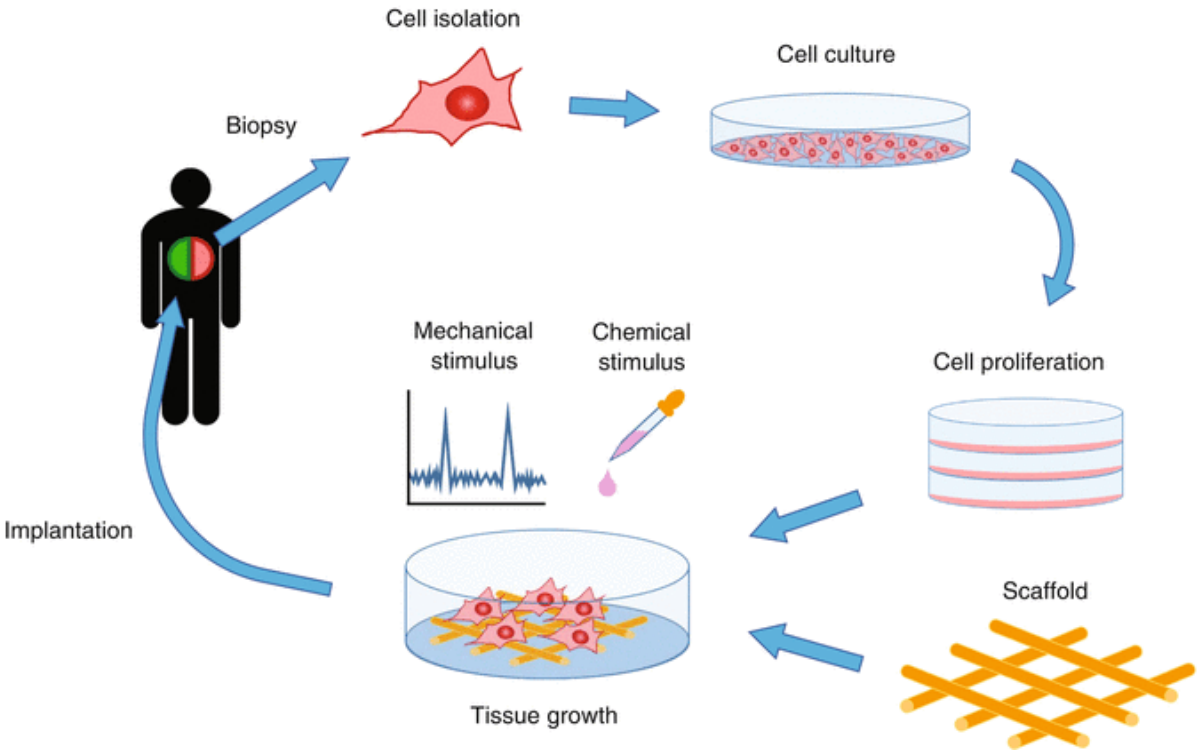

Figure 1.1: Typical tissue engineering pathway[4]. Adapted with permission from Noh et al, Copyright 2018, Springer Nature.

Functional engineered tissues have already played an important role in treating various conditions within patients. For example, small arteries[5, 6], skin grafts[7, 8], and cartilage[9] have all been successfully implanted in patients; however, these procedures still come at a high financial cost and remain largely experimental and not widely used. The field is rapidly evolving to build more complex tissues and organs, aiming to ultimately resolve the high number of organ transplant requests. In Canada alone, over 4000 patients are waitlisted for organs every year[10]. While the complexity of large-scale organs remains a challenge for the field, the shift from conventional two-dimensional (2D) cell culturing to three-dimensional (3D) tissue models has made a significant impact in designing improved *in vitro* drug screening tools[11]. More functional and representative tissue mimics can reduce the need for animal testing and accelerate the identification and translation of new drugs to the market. There is a significant need given that over 90% of drugs that have reached the clinical trial phase through pre-screening conventional *in vitro* tests and *in vivo* testing in animals have failed in humans[12]. Engineering tissues used in this context can reduce costs, address ethical concerns, and reduce (or even eliminate) potential side effects in human trials[13]. However, this approach still faces many obstacles to achieve these goals, such as the lack of vascularization typically achieved (as is critical for thicker tissues), how to enable effective scale-up of tissue manufacturing, and

how to create composite tissues containing multiple cell types and length scales of structural organization[14, 15].

1.2 Bioprinting

3D bioprinting is the process of printing cells, bioactive molecules, and biomaterials (often termed bioinks) in a pre-defined geometry, allowing for the fabrication of high-resolution 3D constructs[16-19]. Tissue-like architectures with multiple different cell types can be fabricated using computer-aided designs. Current 3D bioprinting technologies can be divided into indirect and direct fabrication methods. Indirect 3D bioprinting involves the creation of a sacrificial mold that contains the desired biomaterial and subsequently gets removed[20, 21]; in comparison, direct 3D bioprinting allows for layer-by-layer printing of the tissue mimic without any template[22]. Typically, 3D bioprinting involves three major steps associated with the fabrication of viable tissue constructs: (1) the development of a 3D computer-aided design of the desired construct, (2) the co-printing of cells and biomaterials of interest, and (3) the maturation of cells within fabricated tissue constructs[23]. The immense impact of bioprinting technologies can be seen in light of the rapidly growing market, with the global 3D bioprinting market valued at USD 1.7 billion in 2021 and expected to grow at a rapid compound annual growth rate of 16% from 2022 to 2030[24].

With the rise of tissue engineering applications and the use of 3D bioprinting as a platform to mimic native tissues more accurately *in vitro*, several commercial and customized printers have been designed and fabricated. These printers can be generally divided into one of three modalities: inkjet printing, extrusion-based printing, and laser-assisted printing (**Figure 1.2**)[22].

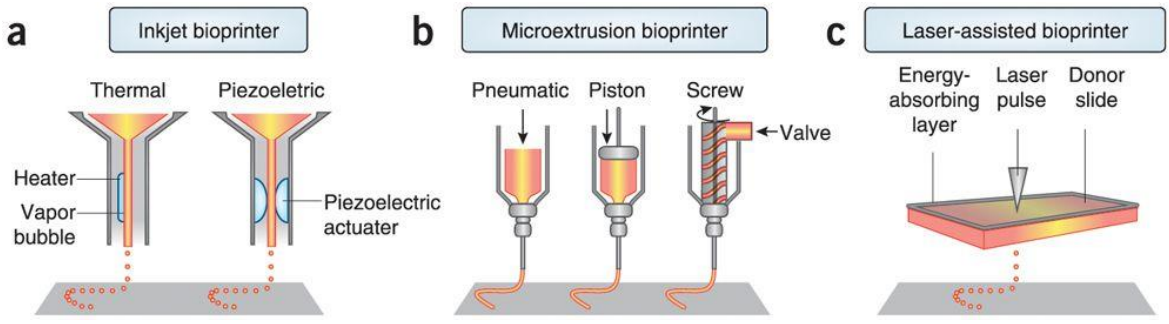

Figure 1.2: 3D bioprinting modalities[17]. Adapted with permission from Murphy et al., Copyright 2014, Springer Nature.

1.2.1 Inkjet Printing

Inkjet printing uses thermal or acoustic forces to print small volumes of liquid to predefined locations on a substrate. Thermal inkjet printers electrically heat the nozzle (from 200 to 300°C) to force droplet formation[22]. Though this localized heating is quite high, research has shown no substantial impact on molecular structures or the viability of mammalian cells, mostly due to the short duration of the heating. Inkjet printers can also use acoustic waves, either by applying a voltage to the piezoelectric material or by directly applying acoustic forces with an ultrasound, to break the liquid into droplets[22]. Although acoustic inkjet printers eliminate the need for extreme temperatures and pressures that exist in thermal inkjet printers, the high frequencies are a concern that may damage the cell membrane and cause cell lysis. Overall, inkjet printing is a high-speed, high resolution and low-cost printing method that is non-contact and ejects tiny droplets to form the final construct[25]. Some drawbacks include low cell densities and the low required material viscosity. Inkjet bioprinting has been demonstrated to enable the regeneration of skin[26] and cartilage[27] because it has the capacity to directly deposit cells and materials into the damaged tissues, in some cases via hand-held devices[28].

1.2.2 Extrusion Printing

Extrusion printing is a low-cost and versatile method that uses the extrusion of materials through a nozzle to create a printed structure[29]. Extrusion systems can either be operated pneumatically or mechanically (using a piston or screw). Though pneumatic control may be hindered by the delay of the compressed gas volume, it typically has simpler components as it only relies on air pressure to drive the flow. Mechanical systems provide more direct control but require more complex components and often operate at reduced maximum force. Extrusion bioprinting allows for effective printing of a wide range of bioinks with viscosities ranging from 30 mPa/s to over 6 x 10^7 mPa/s[22] (although more viscous materials typically result in better shape fidelity upon printing). Thermo-gelation is a common crosslinking technique used in extrusion bioprinting due to the ability to heat/cool the nozzle and/or the platform. Shear-thinning materials are also often used due to the decrease in viscosity of most polymer solutions upon exposure to high shear, as is experienced when a bioink is pushed through a nozzle. Extrusion printing allows for high cell densities compared to inkjet printing but is limited by lower cell viabilities due to the higher shear stresses at the nozzle[22]. Furthermore, increasing print resolution (<100 μm) and speed remain a challenge for several extrusion bioprinting applications. Even with these limitations however, constructs can be fabricated to form

clinically relevant tissue sizes. Recent efforts also have been placed on enabling simultaneous extrusion bioprinting using multiple materials[30], as may be relevant for the fabrication of more complex tissues/organs.

1.2.3 Laser-Assisted Printing

Laser-assisted bioprinting typically consists of a pulsed laser beam, a focusing system, a donor transport support, and a receiving substrate[22]. It functions by generating high-pressure bubbles from laser pulses that propel cell-containing materials toward the receiving substrate. This printing modality does not rely on a nozzle, avoiding the clogging issues that can arise in both inkjet and extrusion printing, and offers high resolution. However, the preparation of the whole system is time-consuming and costly, while the final construct may contain metallic residues[22].

1.3 Hydrogels as Bioinks

Hydrogels are water-swollen polymeric networks that have been used in a broad range of biomedical applications[31-33]. The high tunability of hydrogel chemical composition, the type/density of crosslinking, the degradability, the mechanics, and the cytocompatibility have led hydrogels to be successfully used in bioprinting applications[34, 35]. Hydrogel-based bioinks can be based on natural or synthetic polymers, or a combination thereof, depending on the final tissue engineering application. Natural polymers are typically the most common material choice due to their similar properties to the natural extracellular matrix and typically high cell compatibility[36]. Hydrogels based on natural polymers include alginate[37], cellulose[38], chitosan[39], hyaluronic acid[40], and collagen[41]. However, these naturally derived hydrogels often lack the mechanical strength and tunability that can be achieved using synthetic polymers. Compared to natural polymers, synthetic polymers typically enable more control over the chemical, physical and mechanical properties due to their ability to be synthetically modified and functionalized[34]. However, compatibility with cells and (in particular) the ability to provide adhesion sites for cells often remains a limitation, one that can at least in part be addressed by using composite hydrogels[42] or grafting adhesive moieties to the backbone of the synthetic polymers (i.e., the adhesive tripeptide Arg-Gly-Asp (RGD) or other peptide ligands)[43].

1.4 Bioink Requirements

The ideal hydrogel bioink for extrusion bioprinting applications must be printable, maintain cell viability, and induce (or prevent) a desired cellular response[44, 45]. Printability is strongly influenced by the rheological properties of the chosen bioink and how the print is stabilized after printing. Cell viability is directly impacted by the transport of biomolecules, nutrients, and waste in and out of the printed scaffold as well as the presence of adhesion sites within the scaffold to promote cell-biomaterial and cell-cell interactions. Cell behaviour can be directed through mechanobiological cues (i.e., matching the stiffness of the printed scaffold with the stiffness of the native tissue environment), biochemical cues (i.e., the inclusion of important biomolecules for the desired tissue formation), and the micro/macroporosity of the printed scaffold (i.e., allowing for local cell migration and remodelling). Moreover, the ideal hydrogel bioink must be degradable at a suitable rate for tissue regeneration. For delivering cells meant to integrate into host tissues to provide functional repair, degradation is typically targeted over the course of a few weeks depending on the regeneration rate of the cells being delivered[46, 47]; for cell therapeutics meant to continuously produce and release a biological bioactive, very slow degradability or even non-degradability is typically desirable[48, 49].

1.5 Assessment of Printability

Printability is a term used frequently in extrusion bioprinting and refers to the suitability of a hydrogel bioink to be successfully printed with good shape fidelity to the intended computer-aided design. While the concept of good or poor printability comes intuitively through qualitative observations, increased efforts have been placed on defining printability using more quantitative tools that take the rheological requirements, filament characterization and final shape fidelity into consideration (**Figure 1.3**)[50, 51].

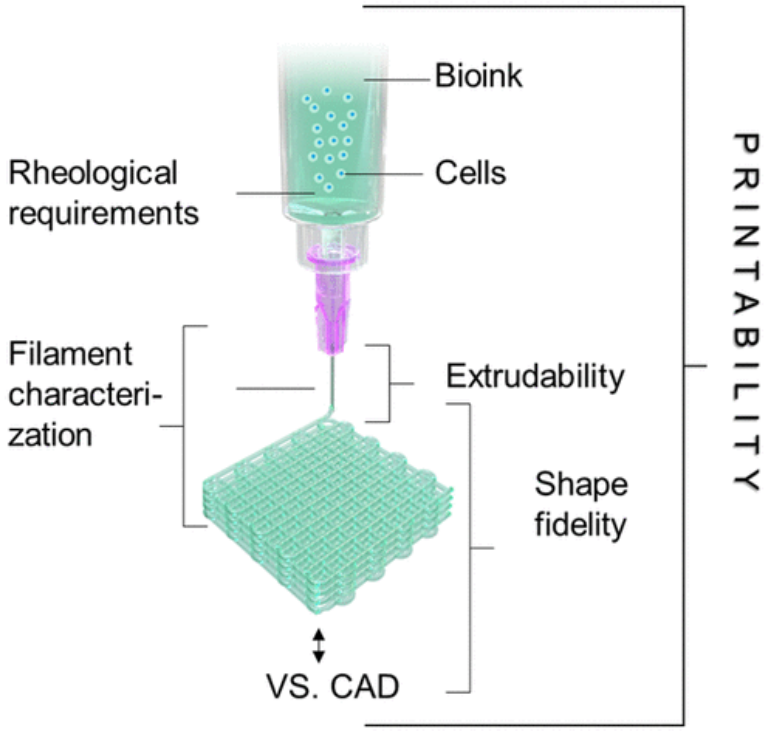

Figure 1.3: The concept of printability for hydrogel bioinks in extrusion bioprinting[50]. Adapted with permission from Schwab et al., Copyright 2020, American Chemical Society.

Rheological properties of the hydrogel bioinks arguably have the most important influence on printability. During the extrusion printing process, the hydrogel bioink undergoes a transition from a resting state (pre-printing) to a high shear rate (during printing) and finally back to the resting state (post-printing). Rheological properties such as the viscosity, viscoelasticity, elastic recovery, and shear stress of both the bioinks and the printed gels best describe these transition stages[50-52]. The printing of low-viscosity hydrogel bioinks has thus more recently been explored, especially in the context of embedded bioprinting in which a support bath is used to stabilize the 3D structure during printing. More viscous hydrogel bioinks are typically easier to print as they can hold their printed shape more easily. However, high viscosity also leads to increased shear stress that can directly affect the cells that are encapsulated, requiring that such bioinks exhibit shear-thinning properties in which the bioink viscosity decreases when high shear rates are applied. Viscoelasticity is the property that describes both viscous flow and elastic shape retention in a material upon the application of a stress, with the shear response of a fluid relevant to bioprinting applications typically measured by the storage (or elastic) modulus (G') and the loss (or viscous) modulus (G") using oscillatory rheology; the storage modulus refers to the amount of energy stored elastically during deformation while the loss modulus correlates with the amount of energy dissipated by the material. Elastic shape

retention can be related to the recovery of either the shear modulus or the viscosity over time upon removal of a stress. Good printability is typically achieved when rapid switches between low and high viscosity, or primarily elastic responses are observed upon small or large deformations[50-51].

After the rheological properties, filament formation and characterization are typically the next steps in defining overall printability. The ability for filaments to be formed uniformly is directly related to the interplay between the intrinsic rheological properties of the ink (shear thinning and rapid shear recovery) and the printing parameters used to deposit the ink (pressure, speed, nozzle offset). These printing parameters can vary widely between different bioinks and printers and need to be optimized for each formulation. Typically, printability is best assessed using planar structures composed of 1-2 layers and extending in the x and y planes, enabling the filament uniformity/size and the pore geometry to be measured[50]. The quality of the print can then be semi-quantitatively expressed using the printability index (Pr)[52], as defined by Equation 1.1, where C represents the circularity, L the length, and A the area of the printed square patterns.

$$\mathrm{Pr} = \frac{\pi}{4} * \frac{1}{C} = \frac{L^2}{16A} \tag{1.1}$$

Once the chosen bioink formulation shows good reproducibility in the planar structures, the shape fidelity across multiple layers is evaluated. The final printed constructs are directly compared to the pre-defined geometry of the computational design; that is, the theoretical and experimental heights are compared, and the structural integrity of the overall structure is visually inspected. Filament merging and the potential for collapse upon layering (as is sometimes observed with softer bioinks) are potential outcomes of multi-layered prints that are directly linked to the overall printability of the bioink.

1.6 Bioink Development

Bioprinting provides a flexible platform to fabricate hydrogel scaffolds for tissue engineering applications. The majority of current bioink formulations are based on the rapid calcium-induced crosslinking of sodium alginate[37, 55] or the light-triggered polymerization of gelatin methacrylate (GelMA)[56, 57], either alone or combined with other materials that can be entrapped

or co-gelled within the bioink. However, one of the major limitations in the field of bioprinting is the lack of materials that are designed specifically for use in bioprinting. Adapting hydrogel scaffolds produced in other ways to 3D bioprinting is not a trivial process due to the long and demanding list of properties required for a bioink. In particular, there is often a trade-off between good printability and optimal cell viability[53]. For example, bioinks that can be printed with high print fidelity and resolution due to their excellent shear-thinning properties are not always ideal for co-printing with cells because of the high shear stress imparted to the cells during the printing process that can lead to a higher number of cell deaths and/or the inability to print more shear-sensitive cell types[44]. For example, Nair et al. conducted a study to predict the cell viability (using rat adrenal medulla endothelial cells) as a function of the maximum shear stress induced during the printing[54]. The study showed that the pressure had a more significant effect on cell viability compared to the nozzle diameter, and the percentage of live cells was reduced by ~40% when constructs are printed at 40 psi compared to 5 psi[54].

The term of 'universal bioink' has been previously used in literature to describe a bioink capable of being printed with any commercial or non-commercial printer without requiring any external or post-printing crosslinking step but can provide co-printed cells with the optimal mechanical and biochemical properties for biological function[59]. Given the large range of mechanics between different potential target tissues (**Figure 1.4**), a key current focus in the bioink area lies in designing bioinks that are optimized for a targeted cell type/tissue. The mechanical properties can be tuned by either manipulating the chemical composition directly (i.e., through increased density of functional group that can be crosslinked and/or by mixing dynamic crosslinkers[60]) or by modulating secondary covalent crosslinking mechanisms or other chemical reactions[61].

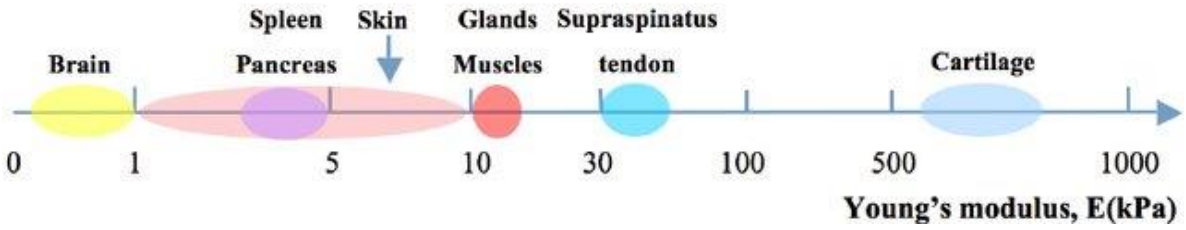

Figure 1.4: Young's modulus of natural soft tissues and organs[62]. Adapted with permission from Liu et al., Copyright 2015, Creative Commons License.

1.7 Dynamic Hydrogel Bioinks

Historically, the design of hydrogels has been based on materials crosslinked via static (permanent) crosslinks (i.e., carbon-carbon backbones in photocrosslinked bioinks[57]), highly labile physical interactions that can reverse in physiological conditions (i.e., ionic calcium-alginate interactions[37]), or thermoresponsive interactions that can be altered upon exposure to physiological salt concentrations[41]. While such hydrogels are useful for studying fundamental cell-material interactions, they cannot readily reproduce the complexity, temporal dynamics, and heterogeneous nature of native tissue development and repair[18, 63]. Designing more dynamic hydrogels can better reproduce the dynamic development of native tissues and thus lead to more realistic/biomimetic microenvironments to be fabricated to better direct tissue maturation. Novel chemistry approaches, in particular the application of orthogonal reactions in which crosslinking can only occur within the polymer precursors themselves and not between the polymers and any biological molecules, have allowed for alteration of the network structure and/or the specific patterning of peptides and proteins[64]. In particular, the use of bioink chemistries that are dynamically reversible in the aqueous microenvironment have the potential to better mimic the continual remodeling of native tissues and thus innovate the next generation of bioinks useful for extrusion bioprinting[65]. **Figure 1.5** demonstrates this evolution of bioink design towards more dynamic chemistries and structures that can better mimic the complexity of the native ECM. In a static matrix, the encapsulated cells cannot move as freely as they can in native ECM that can either naturally degrade over time and/or be dynamically remodeled by cells to enable cell spreading, organization, and signaling to promote the formation of organized tissues[65]. Creating hydrogels that are printable, can facilitate this dynamic reconformation, and can degrade at tunable rates thus offers significant potential to better facilitate functional tissue regeneration.

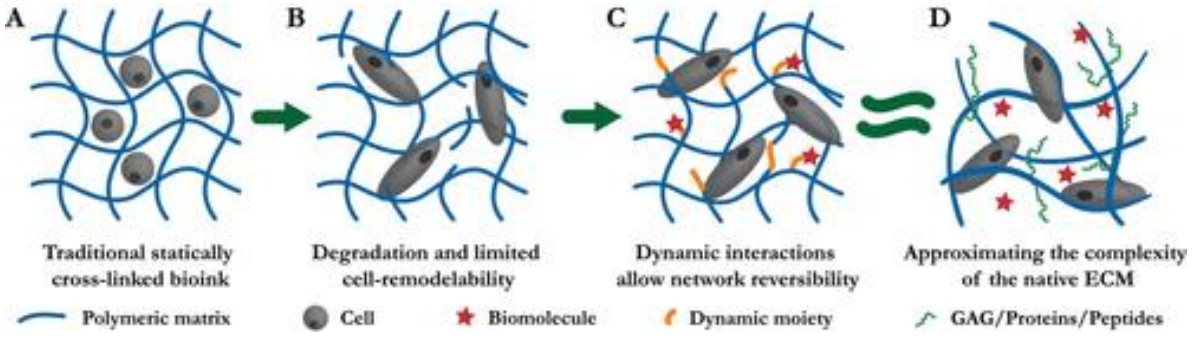

Figure 1.5: Evolution of bioink design to better mimic the biological extracellular matrix[65]. Adapted with permission from Morgan et al., Copyright 2020, Wiley Online Library.

1.8 Objectives

This thesis broadly aims to develop a synthetic bioink platform based on dynamic hydrazone chemistry for extrusion bioprinting applications. This overall goal will be pursued through four specific objectives:

1. To demonstrate the printability of dynamic covalent hydrogel bioinks into high-resolution 3D structures without the need for UV irradiation, non-physiological pH/temperature, or any other templating or post-processing strategies. To date, commercially available hydrogel-based bioinks are limited to ionic crosslinking, photocrosslinking, and thermoresponsive crosslinking, with dynamic covalent chemistry only now being explored in a research context. As such, there is significant opportunity to leverage the advantages of dynamic covalent chemistry as a crosslinking mechanism for bioinks, provided the printability challenges around such inks are resolved.

2. To fabricate hydrogel bioinks with improved mechanical strength to better match the strength and elasticity of the extracellular matrix of target biological tissues (i.e., the liver). Matching the mechanics of the target tissue typically increases both cell viability and functionality. A trade-off often exists between stability over time and suitable mechanics – a challenge that can be solved using synthetic hydrogel bioinks.

3. To evaluate different mixing modalities that allow for effective mixing of two or more functional, low-viscosity precursor polymers that crosslink into stable covalently crosslinked hydrogel structures during the printing process. Given the increased shear experienced by cells when delivered in more viscous bioinks, there is typically a trade-off between printability and cell viability; however, the *in situ* crosslinking potential of dynamic covalent hydrogels offers potential for cell delivery in a low viscosity medium that can rapidly gel upon printing, provided that the mixing required for rapid gelation can be successfully integrated in the printing process.

4. To engineer the chemistry of dynamic covalent hydrogel matrices to provide cells with both the structural and biochemical cues needed to form functional 3D tissues. For example, synthetic polymer chemistry enables the tunability of the hydrogel matrix to ensure limited non-specific protein adsorption that is critical for cell therapeutics; however, the incorporation

of natural ECM components and/or other bioactive molecules may also be advantageous for promoting long-term cell viability and/or spreading. Designing bioinks that can meet both these target objectives may thus open new possibilities for using bioinks to fabricate implants or cell-based therapeutics.

1.9 Outline

This thesis is composed of eight chapters in total, including this introduction, a comprehensive literature review on the development of dynamic covalent bioinks, five research chapters, and concluding remarks.

Chapter 2 – *Background and Literature Review*
This chapter aims to review existing crosslinking modalities employed in hydrogel bioinks for extrusion bioprinting applications, characterize the advantages and disadvantages of different click chemistries reported, highlight current examples of click chemistry hydrogel bioinks, and discuss the design of mixing strategies to enable effective 3D extrusion bioprinting of dynamic covalent hydrogels. This chapter is based on a review that has been published in *Biomacromolecules*.

Chapter 3 – *Coaxial Extrusion Bioprinting of Hydrazone Crosslinked POEGMA Hydrogels: Effect of Needle Geometry on Print Quality*
Coaxial bioprinting of dynamic covalent hydrogel bioinks was achieved through a modified coaxial needle that incorporated a mixing zone to enable the functional precursor polymers to more homogeneously crosslink prior to deposition on the print support. Both computational fluid dynamics modelling and experimental validation studies were employed to optimize the printing process, leading to a demonstration of free-form printing of 2.5D structures using a home-built extrusion bioprinter.

Chapter 4 – *FRESH Bioprinting of Dynamic Hydrazone-Crosslinked Synthetic Hydrogels*
Embedded printing using the FRESH (freeform reversible embedding of suspended hydrogels) method was demonstrated to enable the printing of hydrazide-functionalized POEGMA polymer (combined with collagen type I to promote cell adhesion) into a support bath containing aldehyde-functionalized POEGMA. FRESH bioprinting of POEGMA hydrogels showcased the dynamic nature of hydrazone chemistry, as the higher concentration (10 wt%) prints re-arranged from a core-shell crosslink distribution to a more uniform structure over a three-day period. This work has been published in *Biomacromolecules.*

Chapter 5 – *Free-Form Bioprinting using Pre-Mixed Ketone and Hydrazide Functionalized Zwitterionic Polymers*

Free-form printing of pre-mixed hydrazide and ketone functionalized zwitterionic polymers (which can form a hydrazone-crosslinked hydrogel upon mixing) was optimized for the printing of small-scale liver mimics. The prints maintained excellent cell viability (>90% using human hepatoma cells, HepG2) after two weeks; co-printing with fibroblast cells resulted in improved cell retention and significantly enhanced albumin secretion consistent with native liver tissue function.

Chapter 6 – *Polysulfobetaine-Poly(Oligoethylene Glycol Methacrylate) Copolymers with Improved Anti-Fouling and Anti-Coagulant Properties*

To mitigate the poor miscibility of common ionic polysaccharides with poly(sulfobetaines), copolymers of sulfobetaine and OEGMA monomers were developed and crosslinked via hydrazone chemistry. The resulting hydrogels showed tunable differences in terms of swelling, single-protein adsorption/absorption and anticoagulation properties, and (arguably most importantly for a bioink) improved miscibility of various ionic carbohydrates (i.e., sodium alginate and others) compared to the zwitterionic-only polymers, enabling printing of a broader range of natural/synthetic hybrid bioinks that can address multi-faceted challenges in tissue engineering and cell therapeutics.

Chapter 7 – *3D Printing of Interpenetrating Zwitterionic Dynamic Covalent Hydrogels and Calcium-Alginate Hydrogels for the Fabrication of Longer-Lasting Implants*

Dual-crosslinked interpenetrating network hydrogels based on both ionic crosslinking (from calcium-crosslinked sodium alginate) and covalent crosslinking (from the functional synthetic copolymers based on hydrazone chemistry) were printed using the FRESH bioprinting method. The printed hydrogel structures showed improved stability and suitable compressive modulus values (~7 kPa for liver tissue applications), offering potential benefits in the context of creating cell-based therapeutics in which both maintaining high cell viability as well as avoiding fibrotic responses are critical.

Chapter 8 – *Concluding Remarks*

This chapter summarizes the main contributions of this thesis and discusses future work towards developing a platform of clinically relevant synthetic hydrogel bioinks based on dynamic covalent chemistry for extrusion bioprinting applications.

1.10 References

1. Langer, R.; Vacanti, J. P., Tissue Engineering. *Science* **1993,** *260* (5110), 920-926.
2. Vacanti, J. P.; Langer, R., Tissue engineering: the design and fabrication of living replacement devices for surgical reconstruction and transplantation. *Lancet* **1999,** *354*, S32-S34.
3. Khademhosseini, A.; Langer, R., A decade of progress in tissue engineering. *Nat. Protoc.* **2016,** *11* (10), 1775-1781.
4. Noh, S.; Myung, N.; Park, M.; Kim, S.; Zhang, S.-U.; Kang, H.-W., 3D bioprinting for tissue engineering. *Clinical Regen. Med. Urology*, **2018**, 105-123.
5. Pashneh-Tala, S.; MacNeil, S.; Claeyssens, F., The tissue-engineered vascular graft—past, present, and future. *Tiss. Eng. Part B* **2016,** *22* (1), 68-100.
6. Song, H.-H. G.; Rumma, R. T.; Ozaki, C. K.; Edelman, E. R.; Chen, C. S., Vascular tissue engineering: progress, challenges, and clinical promise. *Cell Stem Cell* **2018,** *22* (3), 340-354.
7. Metcalfe, A. D.; Ferguson, M. W., Tissue engineering of replacement skin: the crossroads of biomaterials, wound healing, embryonic development, stem cells and regeneration. *J. Roy. Soc. Interf.* **2007,** *4* (14), 413-437.
8. Sierra-Sánchez, Á.; Kim, K. H.; Blasco-Morente, G.; Arias-Santiago, S., Cellular human tissue-engineered skin substitutes investigated for deep and difficult to heal injuries. *NPJ Regen. Med.* **2021,** *6* (35).
9. Chung, C.; Burdick, J. A., Engineering cartilage tissue. *Adv. Drug Delivery Rev.* **2008,** *60* (2), 243-262.
10. Canadian Institute for Health Information. Summary Statistics on Organ Transplants, Wait-lists and Donors, **2022**.
11. Marei, I.; Samaan, T. A.; Al-Quradaghi, M. A.; Farah, A. A.; Mahmud, S. H.; Ding, H.; Triggle, C. R., 3D Tissue-Engineered Vascular Drug Screening Platforms: Promise and Considerations. *Front. Cardiovasc. Med.* **2022,** *9*, 847554.
12. The Conversation., 90% of drugs fail clinical trials - here's one way researchers can select better drug candidates, **2022**.
13. Khalil, A. S.; Jaenisch, R.; Mooney, D. J., Engineered tissues and strategies to overcome challenges in drug development. *Adv. Drug Deliv. Rev.* **2020,** *158*, 116-139.
14. Nerem, RM.; Seliktar, D., Vascular tissue engineering. *Ann. Rev. Biomed. Eng.* **2001,** *3*, 225-43.
15. Derby, B., Printing and prototyping of tissues and scaffolds. *Science* **2012,** *338* (6109), 921-926.
16. Thayer, P.; Martinez, H.; Gatenholm, E., History and trends of 3D bioprinting. *3D Bioprinting* **2020**, 2140, 3-18.
17. Murphy, S. V.; Atala, A., 3D bioprinting of tissues and organs. *Nat. Biotech.* **2014,** *32* (8), 773-785.
18. Burdick, J. A.; Murphy, W. L., Moving from static to dynamic complexity in hydrogel design. *Nat. Comm.* **2012,** *3*, 1269.
19. Murphy, S. V.; De Coppi, P.; Atala, A., Opportunities and challenges of translational 3D bioprinting. *Nat. Biomed. Eng.* **2020,** *4* (4), 370-380.
20. Miller, J. S.; Stevens, K. R.; Yang, M. T.; Baker, B. M.; Nguyen, D.-H. T.; Cohen, D. M.; Toro, E.; Chen, A. A.; Galie, P. A.; Yu, X., Rapid casting of patterned vascular networks for perfusable engineered three-dimensional tissues. *Nat. Mater.* **2012,** *11* (9), 768.
21. Bertassoni, L. E.; Cecconi, M.; Manoharan, V.; Nikkhah, M.; Hjortnaes, J.; Cristino, A. L.; Barabaschi, G.; Demarchi, D.; Dokmeci, M. R.; Yang, Y., Hydrogel bioprinted

microchannel networks for vascularization of tissue engineering constructs. *Lab Chip* **2014,** *14* (13), 2202-2211.
22. Murphy, S. V.; Atala, A., 3D bioprinting of tissues and organs. *Nat. Biotech.* **2014,** *32* (8), 773.
23. Zhang, Y. S.; Yue, K.; Aleman, J.; Mollazadeh-Moghaddam, K.; Bakht, S. M.; Yang, J.; Jia, W.; Dell'Erba, V.; Assawes, P.; Shin, S. R., 3D bioprinting for tissue and organ fabrication. *Ann. Biomed. Eng.* **2017,** *45* (1), 148-163.
24. Grand Research. 3D Bioprinting Market Size, Share & Trends Analysis Report By Technology (Magnetic Levitation, Inkjet-based), By Application (Medical, Dental, Biosensors, Bioinks), By Region, And Segment Forecasts, 2022 – 2030.
25. Gao, G.; Yonezawa, T.; Hubbell, K.; Dai, G.; Cui, X., Inkjet-bioprinted acrylated peptides and PEG hydrogel with human mesenchymal stem cells promote robust bone and cartilage formation with minimal printhead clogging. *Biotechnology* **2015,** *10* (10), 1568.
26. Skardal, A.; Mack, D.; Kapetanovic, E.; Atala, A.; Jackson, J. D.; Yoo, J.; Soker, S., Bioprinted amniotic fluid-derived stem cells accelerate healing of large skin wounds. *Stem Cells Transl. Med.* **2012,** *1* (11), 792-802.
27. Cui, X.; Breitenkamp, K.; Finn, M.; Lotz, M.; D'Lima, D. D., Direct human cartilage repair using three-dimensional bioprinting technology. *Tiss. Eng. Part A* **2012,** *18* (11-12), 1304-1312.
28. Han, Y. L.; Hu, J.; Genin, G. M.; Lu, T. J.; Xu, F., BioPen: direct writing of functional materials at the point of care. *Sci. Rep.* **2014,** *4*, 4872.
29. Chimene, D.; Lennox, K. K.; Kaunas, R. R.; Gaharwar, A. K., Advanced bioinks for 3D printing: a materials science perspective. *Ann. Biomed. Eng.* **2016,** *44* (6), 2090-2102.
30. Liu, W.; Zhang, Y. S.; Heinrich, M. A.; De Ferrari, F.; Jang, H. L.; Bakht, S. M.; Alvarez, M. M.; Yang, J.; Li, Y. C.; Trujillo-de Santiago, G., Rapid continuous multimaterial extrusion bioprinting. *Adv. Mater.* **2017,** *29* (3), 1604630.
31. Caló, E.; Khutoryanskiy, V. V., Biomedical applications of hydrogels: A review of patents and commercial products. *Euro. Polym. J.* **2015,** *65*, 252-267.
32. Hoffman, A. S., Hydrogels for biomedical applications. *Adv. Drug Deliv. Rev.* **2012,** *64*, 18-23.
33. Chai, Q.; Jiao, Y.; Yu, X., Hydrogels for biomedical applications: their characteristics and the mechanisms behind them. *Gels* **2017,** *3* (1), 6.
34. Mancha Sánchez, E.; Gómez-Blanco, J. C.; López Nieto, E.; Casado, J. G.; Macías-García, A.; Díaz Díez, M. A.; Carrasco-Amador, J. P.; Torrejón Martín, D.; Sánchez-Margallo, F. M.; Pagador, J. B., Hydrogels for bioprinting: a systematic review of hydrogels synthesis, bioprinting parameters, and bioprinted structures behavior. *Front. Bioeng. Biotech.* **2020,** *8*, 776.
35. Murphy, S. V.; Skardal, A.; Atala, A., Evaluation of hydrogels for bio-printing applications. *J. Biomed. Mater. Res. Part A* **2013,** *101* (1), 272-284.
36. Fatimi, A.; Okoro, O. V.; Podstawczyk, D.; Siminska-Stanny, J.; Shavandi, A., Natural Hydrogel-Based Bio-Inks for 3D Bioprinting in Tissue Engineering: A Review. *Gels* **2022,** *8* (3), 179.
37. Jia, J.; Richards, D. J.; Pollard, S.; Tan, Y.; Rodriguez, J.; Visconti, R. P.; Trusk, T. C.; Yost, M. J.; Yao, H.; Markwald, R. R., Engineering alginate as bioink for bioprinting. *Acta Biomater.* **2014,** *10* (10), 4323-4331.
38. Mohamed, A. L.; Soliman, A. A.; Ali, E. A.; Abou-Zeid, N. Y.; Nada, A. A., Hydrogel bioink based on clickable cellulose derivatives: Synthesis, characterization and in vitro assessment. *Inter. J. Biolog. Macromol.* **2020,** *163*, 888-897.

39. Rajabi, M.; McConnell, M.; Cabral, J.; Ali, M. A., Chitosan hydrogels in 3D printing for biomedical applications. *Carbohyd. Polym.* **2021,** *260*, 117768.
40. Ding, Y.-W.; Zhang, X.-W.; Mi, C.-H.; Qi, X.-Y.; Zhou, J.; Wei, D.-X., Recent advances in hyaluronic acid-based hydrogels for 3D bioprinting in tissue engineering applications. *Smart Mater. Med.* **2022**, 4, 59-68.
41. Osidak, E. O.; Kozhukhov, V. I.; Osidak, M. S.; Domogatsky, S. P., Collagen as bioink for bioprinting: A comprehensive review. *Inter. J. Bioprinting* **2020,** *6* (3), 270.
42. Khoeini, R.; Nosrati, H.; Akbarzadeh, A.; Eftekhari, A.; Kavetskyy, T.; Khalilov, R.; Ahmadian, E.; Nasibova, A.; Datta, P.; Roshangar, L., Natural and synthetic bioinks for 3D bioprinting. *Adv. Nano Biomed. Res.* **2021,** *1* (8), 2000097.
43. Guvendiren, M.; Burdick, J. A., Engineering synthetic hydrogel microenvironments to instruct stem cells. *Curr. Opinion Biotech.* **2013,** *24* (5), 841-846.
44. Hölzl, K.; Lin, S.; Tytgat, L.; Van Vlierberghe, S.; Gu, L.; Ovsianikov, A., Bioink properties before, during and after 3D bioprinting. *Biofabrication* **2016,** *8* (3), 032002.
45. Skardal, A.; Devarasetty, M.; Kang, H.-W.; Mead, I.; Bishop, C.; Shupe, T.; Lee, S. J.; Jackson, J.; Yoo, J.; Soker, S., A hydrogel bioink toolkit for mimicking native tissue biochemical and mechanical properties in bioprinted tissue constructs. *Acta Biomater.* **2015,** *25*, 24-34.
46. Dhandayuthapani, B.; Yoshida, Y.; Maekawa, T.; Kumar, D. S., Polymeric scaffolds in tissue engineering application: a review. *Inter. J. Polym. Sci.* **2011,** *2011*, 290602.
47. Echeverria Molina, M. I.; Malollari, K. G.; Komvopoulos, K., Design challenges in polymeric scaffolds for tissue engineering. *Front. Bioeng. Biotech.* **2021**, 9, 2296-4185.
48. Li, J.; Mooney, D. J., Designing hydrogels for controlled drug delivery. *Nat. Rev. Mater.* **2016,** 1, 16071.
49. Zhu, J.; Marchant, R. E., Design properties of hydrogel tissue-engineering scaffolds. *Exp. Rev. Med. Devices* **2011,** *8* (5), 607-626.
50. Schwab, A.; Levato, R.; D'Este, M.; Piluso, S.; Eglin, D.; Malda, J., Printability and shape fidelity of bioinks in 3D bioprinting. *Chem. Rev.* **2020,** *120* (19), 11028-11055.
51. Gillispie, G.; Prim, P.; Copus, J.; Fisher, J.; Mikos, A. G.; Yoo, J. J.; Atala, A.; Lee, S. J., Assessment methodologies for extrusion-based bioink printability. *Biofabrication* **2020,** *12* (2), 022003.
52. Ouyang, L.; Yao, R.; Zhao, Y.; Sun, W., Effect of bioink properties on printability and cell viability for 3D bioplotting of embryonic stem cells. *Biofabrication* **2016,** *8* (3), 035020.
53. Malda, J.; Visser, J.; Melchels, F. P.; Jüngst, T.; Hennink, W. E.; Dhert, W. J.; Groll, J.; Hutmacher, D. W., 25th anniversary article: engineering hydrogels for biofabrication. *Adv. Mater.* **2013,** *25* (36), 5011-5028.
54. Nair, K.; Gandhi, M.; Khalil, S.; Yan, K. C.; Marcolongo, M.; Barbee, K.; Sun, W., Characterization of cell viability during bioprinting processes. *Biotech. J. Healthcare Nutr. Techn.* **2009,** *4* (8), 1168-1177.
55. Rastogi, P.; Kandasubramanian, B., Review of alginate-based hydrogel bioprinting for application in tissue engineering. *Biofabrication* **2019,** 11 (4), 042001.
56. Ying, G.; Jiang, N.; Yu, C.; Zhang, Y. S., Three-dimensional bioprinting of gelatin methacryloyl (GelMA). *Bio. Design Manufact.* **2018,** 1 (4), 215-224.
57. Pereira, R. F.; Bártolo, P. J., 3D bioprinting of photocrosslinkable hydrogel constructs. *J. App. Polym. Sci.* **2015,** *132* (48).
58. Bian, L., Functional hydrogel bioink, a key challenge of 3D cellular bioprinting. *AIP Publishing LLC*, **2020,** 4, 030401.
59. Skardal, A., Universal" bioink technology for advancing extrusion bioprinting-based biomanufacturing. *Elsevier* **2018**, e00026.

60. Morgan, F. L.; Fernández-Pérez, J.; Moroni, L.; Baker, M. B., Tuning Hydrogels by Mixing Dynamic Cross-Linkers: Enabling Cell-Instructive Hydrogels and Advanced Bioinks. *Adv. Healthc. Mater.* **2022,** *11* (1), 2101576.
61. Wang, L. L.; Highley, C. B.; Yeh, Y. C.; Galarraga, J. H.; Uman, S.; Burdick, J. A., Three-dimensional extrusion bioprinting of single- and double-network hydrogels containing dynamic covalent crosslinks. *J. Biomed. Mater. Res. A* **2018,** *106* (4), 865-875.
62. Liu, J.; Zheng, H.; Poh, P. S.; Machens, H.-G.; Schilling, A. F., Hydrogels for engineering of perfusable vascular networks. *Inter. J. Mol. Sci.* **2015,** *16* (7), 15997-16016.
63. Brown, T. E.; Anseth, K. S., Spatiotemporal hydrogel biomaterials for regenerative medicine. *Chem. Soc. Rev.* **2017,** *46* (21), 6532-6552.
64. Wylie, R. G.; Ahsan, S.; Aizawa, Y.; Maxwell, K. L.; Morshead, C. M.; Shoichet, M. S., Spatially controlled simultaneous patterning of multiple growth factors in three-dimensional hydrogels. *Nat. Mater.* **2011,** *10* (10), 799-806.
65. Morgan, F. L.; Moroni, L.; Baker, M. B., Dynamic bioinks to advance bioprinting. *Adv. Healthc. Mater.* **2020,** *9* (15), 1901798.

CHAPTER 2

Click Chemistry Hydrogels for Extrusion Bioprinting: Progress, Challenges, and Opportunities

Eva Mueller, Isabelle Poulin, William James Bodnaryk, and Todd Hoare

Declaration of Academic Achievement:

This chapter is based on a published review paper, with all text and figures/tables reproduced with permission from American Chemical Society (Copyright 2022). Isabelle Poulin helped with surveying the literature, compiling the existing reports from the literature into tables, and developing the preliminary drafts of the composite figures. Dr. William James Bodnaryk provided valuable chemistry knowledge and expertise to the 'click chemistry hydrogel' sections during the writing and review stages of this work. All writing and manuscript preparation were done by Eva Mueller and edited with the help of Dr. Todd Hoare.

Mueller, E.; Poulin, I.; Bodnaryk, W. J.; Hoare, T., Click Chemistry Hydrogels for Extrusion Bioprinting: Progress, Challenges, and Opportunities. *Biomacromolecules* **2022**, 23 (3), 619-640.

Click Chemistry Hydrogels for Extrusion Bioprinting: Progress, Challenges, and Opportunities

Eva Mueller, Isabelle Poulin, William James Bodnaryk, and Todd Hoare

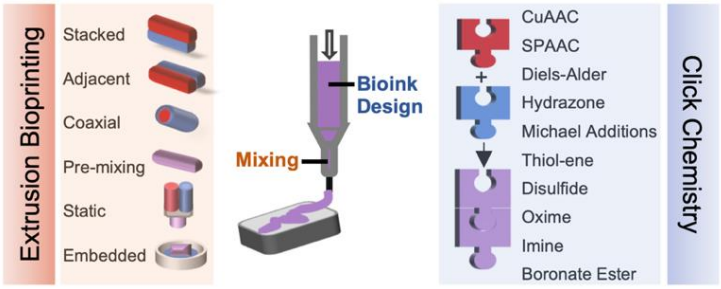

The emergence of 3D bioprinting has allowed a variety of hydrogel-based "bioinks" to be printed in the presence of cells to create precisely defined cell-loaded 3D scaffolds in a single step for advancing tissue engineering and/or regenerative medicine. While existing bioinks based primarily on ionic crosslinking, photocrosslinking, or thermogelation have significantly advanced the field, they offer technical limitations in terms of the mechanics, degradation rates, and the cell viabilities achievable with the printed scaffolds, particularly in terms of aiming to match the wide range of mechanics and cellular microenvironments. Click chemistry offers an appealing solution to this challenge given that proper selection of the chemistry can enable precise tuning of both the gelation rate and the degradation rate, both key to successful tissue regeneration; simultaneously, the often bio-orthogonal nature of click chemistry is beneficial to maintain high cell viabilities within the scaffolds. However, to-date, relatively few examples of 3D-printed click chemistry hydrogels have been reported, mostly due to the technical challenges of controlling mixing during the printing process to generate high-fidelity prints without clogging the printer. This review aims to showcase existing crosslinking modalities, characterize the advantages and disadvantages of different click chemistries reported, highlight current examples of click chemistry hydrogel bioinks, and discuss the design of mixing strategies to enable effective 3D extrusion bioprinting of click hydrogels.

Key words: 3D bioprinting, hydrogels, click chemistry, biomaterials, tissue engineering

2.1 Introduction

Tissue engineering and regenerative medicine require biomaterials that can mimic the three-dimensional structures found natively within the human body. Such biomaterials must be biocompatible, biodegradable, and reproducible to prepare while being capable of presenting cells with the appropriate mechanical and chemical cues to enable tissue regeneration[1-3]. The emergence of 3D bioprinting has allowed many such biomaterials (typically called "bioinks" in this context) to be printed in the presence of cells to create precisely defined cell-loaded scaffolds in a single step[4]. Hydrogels are particularly attractive for bioprinting due to their ability to match soft tissue-like mechanics, control diffusion according to the hydrogel pore size, and provide a hydrated environment for cells to survive, proliferate, and differentiate[1, 5, 6]. 3D printing of hydrogel scaffolds with well-defined shapes and dimensions thus offers the potential to create scaffolds with mechanical strength, unique chemical characteristics, and micro/nanostructures that better mimic the native extracellular matrix (ECM).

The cell-laden biomaterial or mixture of biomaterials used to fabricate a three-dimensional tissue construct via bioprinting is typically termed the "bioink"[1]. Several commercial and customized printers have been designed that can print hydrogel-based bioinks, typically using one of five modalities: inkjet printing, laser-assisted printing, stereolithography, microfluidic-based or extrusion printing[7]. Among those modalities, extrusion-based printing (also known as pressure-assisted bioprinting) in which bioink materials are extruded into 3D constructs through a nozzle has become the most popular given that it can allow for numerous bioinks (including pre-formed hydrogels, not possible using other methods) to be printed at cell-friendly conditions, albeit typically at lower resolution and print fidelity relative to other techniques[7, 8].

The creation of targeted structures by extrusion bioprinting may be achieved either by templating or in free form. Templated hydrogel bioinks require the use of a pre-printed sacrificial template to print the desired structure without compromising on print fidelity; for example, microchannel networks have been templated inside a photocrosslinkable hydrogel matrix to improve both mass transport and cell viability/differentiation[5]. While templates are useful for printability, they typically require several (often cell-unfriendly) processing steps such as the use of organic solvents, higher temperatures, and/or lower pH (either during printing[9] or for template removal[5]) that can limit their potential to enable co-printing of viable

cells. Hydrogel bioinks that can be free-form printed directly into a 3D gel structure in a single processing step avoid such issues. Free-form bioprinted hydrogels are typically fabricated using one of four methods depending on the chosen hydrogel bioink: (1) extrusion of a pre-formed hydrogel bioink with the potential for shear thinning (i.e., hydrazone crosslinked hyaluronic acid[10], alginate/gelatin[10]); (2) *in situ* photocrosslinking of methacrylated or acrylated pre-polymer solutions (i.e., GelMA[11], PEGDA[12]); (3) printing a polyelectrolyte into a counterion solution to facilitate ionic crosslinking (i.e., sodium alginate/calcium chloride[3]); or (4) extrusion of a thermoresponsive gelling pair onto a cooled or heated support that induces thermogelation upon contact (i.e., collagen[13], gelatin[14], Pluronic F127[15]). However, each of these approaches can limit the utility of the resulting scaffolds in tissue engineering applications[16, 17]. Hydrogels based on natural polymers like hyaluronic acid (among the most widely used shear-thinning bioinks[18]) can inherently activate certain cell signaling pathways that may be undesirable for the regeneration of specific tissues[19]. Several crosslinking approaches require the use of conditions that are not favorable for cell viability, such as UV irradiation (photocrosslinking) and the use of non-physiological temperatures (thermoresponsive polymer gelation). Finally, the use of physical rather than chemical crosslinking in the case of calcium/alginate ionogels and thermoresponsive hydrogels can limit both the overall mechanical strength as well as the tunability of the degradation times for mimicking different types of tissues, particularly within the compositional limits in which printability is preserved. As such, alternative gelation strategies that can facilitate rapid gelation (as required for 3D printing) but avoid the need for external energy/irradiation while enabling the direct fabrication of hydrogels with tunable mechanics and degradation rates would be of significant benefit.

Click chemistry offers an attractive solution to this challenge. While there is not uniform agreement in the literature as to what types of chemistries can and cannot be considered as "click", for the purpose of this review the term "click chemistry" is taken to encompass a class of reactions that according to Sharpless' original definition in 2001 are "high yielding, wide in scope, create only by-products that can be removed without chromatography, are stereospecific, simple to perform, and can be conducted in easily removable or benign solvents"[20]; in the case of hydrogels, the by-products are either nothing or water and the solvent is water[21]. Given that stereospecificity is not particularly relevant to the challenge of *in situ* hydrogel crosslinking, in this review we consider not only true click reactions but also "click-like" reactions that are not necessarily stereospecific but still satisfy all other criteria of the

definition. In addition to these core requirements, in many (but not all) cases click chemistry is also bio-orthogonal in that the chemistry can proceed without any cross-reactivity from native functional groups in the body. While bio-orthogonality is by no means a prerequisite for cytocompatibility, avoiding the potential for covalent bond formation and (especially) irreversible covalent bond formation with proteins, cells, and other ECM components can be beneficial for promoting improved cytocompatibility[22] and avoiding undesirable inflammatory responses[6]. In the specific context of hydrogel bioinks, click-chemistry based hydrogels are formed spontaneously upon mixing two or more reactive precursors without the need for any type of template, external energy source, or linking agent(s), making the chemistry ideal to integrate into bioprinting processes. Furthermore, depending on the choice of the click chemistry pair used, click chemistry offers the potential for improved flexibility and multi-functionality in bioinks due to the tunable gelation times, mechanics, and degradation times achievable[23-26]. However, despite these clear advantages in the context of 3D bioprinting, there are still relatively few reports of using click chemistry-based bioinks due to the inherent mismatch between existing bioprinting technologies (including extrusion-based bioprinting) and click chemistry, which requires intimate mixing of the two (or more) reactive precursor polymers on the rapid timescale of 3D bioprinting. In addition, while the gelation time directly influences the mechanics, stability, and crosslink density of the printed constructs, it must be tightly controlled in the context of 3D printing to also ensure adequate preservation of the shape fidelity of the printed structure. As such, while click chemistry offers the potential for improved chemical, mechanical, and degradation flexibility to better mimic a wider range of tissues, its implementation with 3D extrusion printers remains somewhat challenging.

While the use of click chemistry in injectable hydrogel and bioink development has been considered in previous reviews[6], herein we review the design and practical implementation of click chemistry-based bioinks from a chemistry-focused perspective in which different compositional approaches (both in terms of polymer backbone selection and crosslinking modality) are clearly benchmarked, in our view essential to enabling the rational design of 3D printing bioinks. Specifically, this review is focused on: (1) a brief review of existing extrusion-based bioprinting crosslinking modalities outside of click chemistry (ionic, thermal, and UV crosslinking) and the associated challenges with these current bioinks; (2) a thorough analysis of the diverse range of click chemistry methods that have been reported for bulk (or *in-situ*) hydrogel tissue engineering applications; (3) a discussion of the methods by which click chemistry precursor polymers can be mixed in the context of 3D bioprinting, a key

consideration for achieving the desired homogeneous gelation on the rapid timescale of the printing process and in our view the key barrier toward wider-spread use of click chemistry-based bioinks; and (4) progress, challenges, and opportunities in using click chemistry for extrusion bioprinting.

2.2 Conventional Crosslinking Strategies for Hydrogel Bioinks

To convert a bioink into a 3D printed construct, it must undergo a crosslinking reaction before, during, or after printing that converts the flowable bioink to a stable and shape-defined hydrogel network forming the desired printed structure. Various chemical and physical crosslinking strategies can be used to induce this transition, with the vast majority of current hydrogel-based bioinks using one of ionic crosslinking, photocrosslinking, and thermoresponsive phase transitions to enable gelation (**Figure 2.1**).

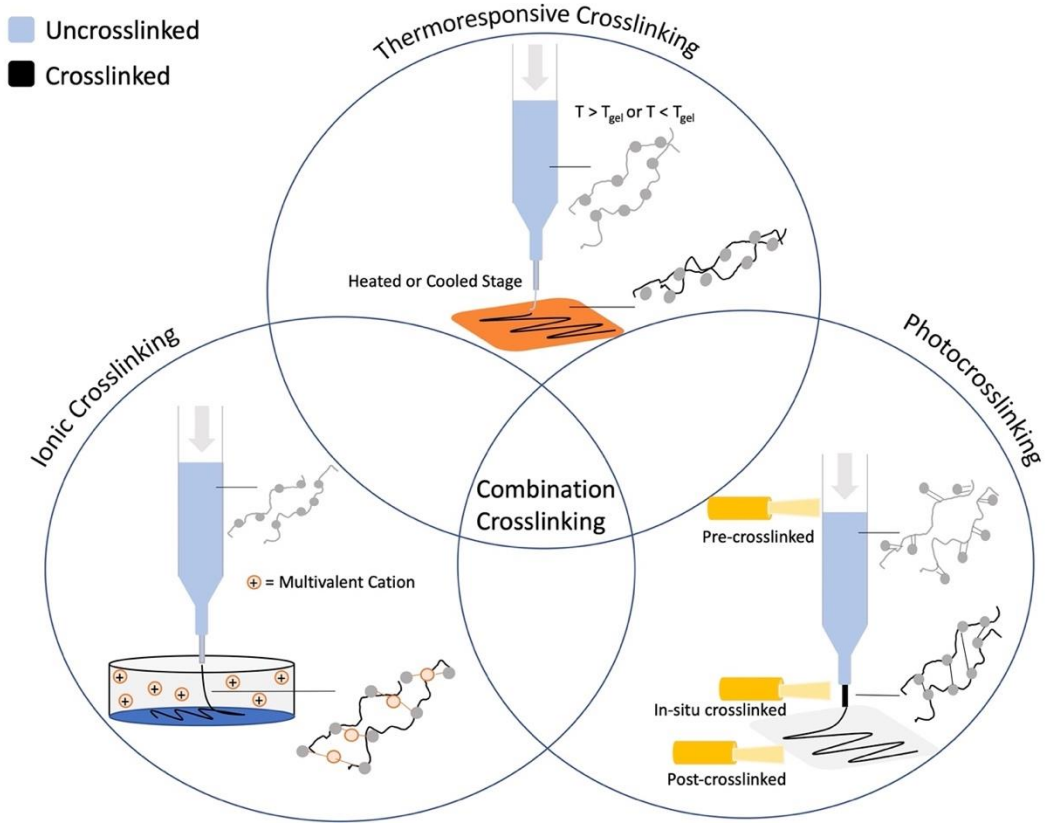

Figure 2.1: Conventional crosslinking strategies for hydrogel bioinks used in extrusion bioprinting

In ionic crosslinking, a multivalent cation is introduced to a precursor solution containing a charged polymer, with the multivalence of the crosslinking cation enabling multiple electrostatic interactions with adjacent polymer chains to trigger gelation (**Figure 2.1**). Although calcium is by far the most prominent ionic crosslinker in the literature (most commonly paired with alginate, which forms a tight "egg crate" electrostatic assembly with calcium)[10, 27-29], gallium, strontium, barium, and zinc have also been demonstrated to be effective multivalent cation crosslinkers for bioinks[30]. The choice of different cations can determine both the stability of the ionic crosslink[31] as well as allow for the fabrication of multi-functional hydrogels. Ionic crosslinking is beneficial for bioink design since it can allow for very rapid gelation, with times ranging from milliseconds to a few minutes[32, 33] as is typically required for 3D printing applications. However, this extremely fast gelation can also lead to inhomogeneous crosslinking, resulting in structural inconsistencies throughout the crosslinked network and therefore the formation of relatively mechanically weak hydrogels[34], although homogeneity and thus mechanics can be improved using techniques that slow the gelation through carefully controlled crosslinking strategies[35]. Furthermore, even if gelation is sufficiently fast to enable shape fidelity, the use of potentially cytotoxic (e.g. gallium or strontium) or biologically important metal ions (e.g. calcium, a key regulator of cell transport) may limit the use of some of these crosslinkers in some bioprinting applications[3, 36]; in particular, the release of calcium ions (by far the most commonly used cation used in 3D bioprinting) may promote localized blood clotting responses[37]. Ionic interactions are also often unstable in the presence of other competing ions in the body that can undergo cation exchange with the crosslinking ion, resulting in difficult-to-control degradation rates that can significantly limit the timescale over which the printed scaffolds can persist once implanted[38].

In photocrosslinking, hydrogels are rapidly formed in the presence of light at an appropriate wavelength by the activation of optically active functional groups or photocatalysts[3]. In the most common manifestation of this method, precursor polymers are mixed with a photoinitiator that can be cleaved at a specific light intensity/wavelength, typically in the ultraviolet or low visible wavelength range. This cleavage event generates free radicals that can then initiate crosslinking between moieties in the precursor polymers, most often vinyl, methacrylate, or acrylate groups, to create a crosslinked network between polymer chains (**Figure 2.1**); precursor polymers without such functionalities can in some cases also photocrosslink via hydrogen abstraction reactions that may proceed particularly upon exposure to higher intensity irradiation[39]. The light intensity, duration of exposure, and area under light can be fine-tuned

to control the crosslinking and physicochemical properties of resulting hydrogels[39]. Furthermore, controlling the chain morphology of the precursor polymers (i.e. using a hyperbranched polymer rather than a linear polymer[40] or a pre-formed microgel[41]) can tune the homogeneity, mechanics, and porosity of the photopolymerized hydrogel, consistent with gelation using other crosslinking strategies. Photocrosslinking can also occur at different times during the printing process, with pre-crosslinking[42, 43] (printing already formed hydrogels via shear thinning), post-crosslinking[44, 45] (irradiation of the fully printed structure with light), and *in-situ*-crosslinking[46-48] (irradiation during the printing process to fix structures simultaneous to printing) all possible (**Figure 2.1**). Photocrosslinking is widely used for 3D bioprinting due to its cost effectiveness, its ability to be carried out at room or physiological temperature, and its comparative flexibility of precursor polymer types in that any material that can be functionalized with a free radical polymerizable group can be used[3]. However, photocrosslinking typically requires the use of cytotoxic photoinitiators or the introduction of cytotoxic photopolymerizable functional groups[49] into bioinks as well as the use of low wavelength light that can impact cell viability at certain wavelengths and intensities[28]; any of the free radicals produced by photoinitiators, the photoinitiator fragments, and/or the UV light may have harmful effects on cells by damaging cell membranes, nucleic acids, and proteins[50], as indicated both by changes in cell viability as well as cell gene expression. Only few studies exist that systematically document these concerns, and the practical impact of any kind of photo-induced toxicity is found to be insignificant in many publications[51]; however, concerns still do persist over the use of photocrosslinking particularly for the bioprinting of more sensitive cell types or using higher intensity/lower wavelength lights.

In thermoresponsive crosslinking, the potential of certain polymers to undergo a liquid-to-gel phase transition at some critical temperature is exploited to induce spontaneous gelation following printing. As shown in **Figure 2.1**, this gelation temperature (labelled T_{gel} in the figure) may be an upper critical solution temperature (i.e., gelation occurs upon cooling) or a lower critical solution temperature (i.e., gelation occurs upon heating), depending on the specific system considered. Combined with their easy extrusion, high print fidelity, and good print quality[52], the rapid temperature-induced gelation of thermoresponsive polymers has been leveraged in multiple 3D bioprinting applications, both as direct printing bioinks as well as their use as templates for printing other materials that can temporarily support weak printed structures but can be removed (via temperature switching) following secondary crosslinking of the printed structure[53]. Both natural and synthetic materials can be used as thermoresponsive

hydrogel precursors. Commonly used natural thermoresponsive bioink materials include gelatin[54], chitosan[55], methylcellulose (MC)[56], collagen[57], and agarose derivatives[58], although many hydrogels derived from such materials are often mechanically weak given the weak physical crosslinks that link the chains together[59]. Synthetic materials such as Pluronics[60], polyisocyanide (PIC)[61], and poly(N-isopropylacrylamide) (PNIPAM) and its derivatives[62]. have more tunable properties and typically higher mechanical strength relative to natural thermoresponsive polymers[59] but can introduce concerns over both the toxicity of the materials themselves (Pluronics)[63, 64] and/or potentially hard-to-remove residual monomers (PNIPAM) as well as the often poor clearance of such materials following gel dissolution, both of which create challenges with practical *in vivo* use.

One method to overcome the limitations of different conventional crosslinking methods is to use dual crosslinking strategies to exploit the benefits of both crosslinking strategies in terms of tuning hydrogel porosities, mechanical properties, and/or cell responses. For example, ionic crosslinking has been previously combined with photocrosslinking[65], physical crosslinking[66], or covalent crosslinking[67] to overcome the relatively weak mechanical strength of many ionically-crosslinked hydrogels while still exploiting their fast gelation kinetics relevant for 3D bioprinting. In some cases, a pre-formed (weak) gel formed with one type of crosslinking can subsequently be reinforced with a secondary crosslink after printing[68]. As one such example, Jeon *et al.* reported the formulation of a bioink based on oxidized and methacrylated alginate (OMA) microgels. OMA droplets were ionically crosslinked with calcium cations to first form the microgels; after printing the microgels into a gelatin support bath using the freeform reversible embedding of suspended hydrogels (FRESH) printing technique, the constructs were photocrosslinked into a hydrogel through exposure to low-level UV light to form hydrogels with storage moduli of ~100 kPa and tunable porosity based on the size and packing geometry of the initial microgel building blocks[65]. In another study, a dual-crosslinked hydrogel made from methacrylated alginate and silk fibroin was pre-crosslinked with calcium (gelation time <120 seconds) and then exposed to UV light for photocrosslinking to enhance the mechanics. The presence of the physically entrapped silk fibroin improved cell compatibility from 95% in pure alginate hydrogels to ~100% in the hybrid constructs, while the secondary photocrosslinking helped to compensate for the significant decrease in mechanical strength observed upon introducing silk fibroin (from 849 Pa to 72 Pa)[69]; however, it should be noted that the mechanics are still extremely weak even when the secondary reinforcement of photocrosslinking is introduced. Mechanically reinforced hydrogel bioinks can also be

fabricated by combining biological affinity-based crosslinking with ionic crosslinking. For example, by mixing alginate functionalized with complementary peptide binding domains that form a weak shear-thinning hydrogel network with calcium ions during the printing process, a maximum storage modulus of 4 kPa could be achieved (two orders of magnitude higher than hydrogels formed through the physical peptide-based crosslinks alone) while high cell viability was maintained (>96% due to the presence of the peptides)[66]. Temporal physical crosslinking can also be employed for short-term stabilization followed by a spontaneous covalent gelation process post-printing. For example, gallol-modified hyaluronic acid (HA) and gelatin bioinks were demonstrated to be printable based on shear-thinning of the physical interactions between HA and gelatin but could be reinforced after printing by a spontaneous oxidation process between the gallol functional groups, enabling better maintenance of the printed structure[70]. However, while dual crosslinking approaches can improve bioink properties, combinations of conventional crosslinking chemistries cannot always address the printability, degradability, and cell viability requirements of 3D bioinks, particularly in terms of facilitating a more diverse library of printable bioinks to better customize cell responses in the printed scaffold

Table 2.1: Conventional crosslinking strategies for extrusion hydrogel bioinks. Entries marked as "N/A" do not characterize the property listed explicitly in the manuscript cited.

Conventional Bioink Type	Polymer(s)	Mechanical Property	Gelation Time	Cell Viability	Reference
Ionic crosslinking	Alginate, gellan gum, calcium chloride	Compressive modulus (G): 1 – 85,000 Pa	N/A	N/A	[35]
	Alginate	Storage modulus (G'_{max}): ~100 Pa	N/A	Yes (no quantitative value)	[65]
	Alginate/Silk Fibroin (SF)	G'_{max}: 72 Pa Young's modulus (E): 25-35 Pa	<120s	~100%	[69]
	Methylcellulose/ Alginate	G: ~6000 – 37,000 Pa G'_{max}: 95-1052 Pa	N/A	95%	[71]
Photocrosslinking	Gelatin methacrylate (GelMA)/ Polyethylene oxide	E: 900 – 9800 Pa	<1s	>95%	[48]
	Norbornene-modified Hyaluronic Acid	G'_{max}: ~5000 Pa	<1s	>80%	[47]
	Gelatin, collagen, mesoporous bioactive glass	Shear strength: 45,000-90,000 Pa	30s	>70%	[46]
	GelMA/SF	G'_{max}: 1-2 Pa	<1s	>70 to >85%	[45]
	Polyethylene glycol methacrylate (PEGMA), Polyethylene glycol diacrylate (PEGDA)	G'_{max}: 100 – ~60,000 Pa	N/A	>80%	[43]
	Maleilated chitosan (MCS)/ methacrylated silk fibroin (MSF)	G: 320,000 Pa	340-560s	>80%	[41]

Thermoresponsive	Gelatin methacrylate	N/A	N/A	>95%	[54]
	Gelatin/Chitosan	G: 10,000-60,000 Pa	60-120s	>70%	[72]
	Methylcellulose	G'_{max}: ~2000 Pa[73] G'_{max}: 10^6 Pa[56]	N/A	Yes[73] >90%[56]	[56, 73]
	Chitosan	G'_{max}: 50 – 100,000 Pa	N/A	Yes (no quantitative value)	[74]
	Pluronic F127	G'_{max}: 1200 Pa	N/A	N/A	[75]
	Polyisocyanide	G'_{max}: 1100 Pa	<1s	N/A	[61]
	Poly(N-isopropylacrylamide-co-acrylic acid) (PNIPAM-AA), fibrin	N/A	<1s	100% for 3T3-J2 and HUVEC cells 80% for HaCaT cells	[62]
	PMeOx-b-PnPrOzi block copolymer, Laponite XLG nanoclay	G'_{max}: 5000 Pa Yield Stress: 240 Pa	<1s	N/A	[76]

2.3 Click Chemistry Hydrogels for Tissue Engineering

Relative to the leading ionic, photocrosslinking, and thermogelling approaches most broadly applied for 3D bioprinting and reviewed in the previous section, click chemistry offers several functional benefits while also introducing other complicating factors into the printing process. In this section, common click chemistry techniques will be discussed by highlighting their key features, recent applications, and their advantages and shortcomings in the context of tissue engineering more generally and 3D bioprinting more specifically. In particular, the significantly different gelation times, degradability, and cytocompatibilities of various click crosslinks enable the production of a diverse range of scaffolds that may be more or less suitable to 3D bioprinting versus other types of fabrication techniques depending on the type of 3D bioprinting approach used and the requirements of any specific printed structure. In addition, in contrast to most of the conventional bioprinting approaches described in the previous section, click chemistry-based bioinks may be comprised of multiple polymers functionalized with the same click functional group(s) to enable simultaneous printing and crosslinking of multiple materials together to form a cohesive structure. This flexibility avoids the need to apply sequential post-processing/curing steps to integrate multiple types of components while maintaining suitable mechanical strength and (in contrast to photocrosslinking) facilitating the potential to directly print scaffolds with tunable degradation times, as is typically desired for tissue engineering. As such, while specific polymer examples are discussed for each type of click chemistry reviewed below, the same chemical approach could be used to fabricate a fully crosslinked hydrogel of essentially any composition provided the appropriate functional groups to enable gelation can be successfully functionalized to, or are natively present on, the targeted polymers.

2.3.1 Copper-catalyzed azide-alkyne cycloaddition (CuAAC)

CuAAC occurs when a terminal alkyne is mixed with an aliphatic azide in the presence of a copper catalyst, yielding a 1,4-disubstituted 1,2,3-triazole[77]. Although cycloaddition reactions are exothermic, a high activation barrier exists between the reagent compounds, resulting in low reaction rates even at high temperatures. By introducing copper (I) to catalyze the reaction, gelation can occur at physiological temperature[78], with gelation times varying from seconds to hours depending on the catalyst/monomer concentration, and electronic/structural characteristics of the polymer components[79-82]. CuAAC crosslinks are functionally stable under normal physiological conditions; although they can degrade in low pH conditions (pH < 2 depending on the pK_a of the nitrogen[83]), such conditions are not typically accessible *in vivo*[77].

As such, the degradation of CuAAC-crosslinked scaffolds depends not on the crosslink stability but rather the inherent degradability of the constituent polymers. For example, functionalizing gelatin with alkyne groups and mixing the precursor polymers with a small molecule PEG-diazide in the presence of copper resulted in the formation of hydrogels that were hydrolytically stable in PBS buffer at 37°C for seven weeks[84], while PEG hydrogels synthesized through CuAAC remained fully intact after two weeks *in vivo*[82]*;* alternately, when PEG-based hydrogels were synthesized to include an enzymatically-cleavable peptide sequence, the hydrogels degraded completely after 40-80 hours in trypsin[85].

CuAAC reactions are regiospecific and can occur under a broad range of temperatures, pH values, and solvents; the reaction also proceeds bio-orthogonally to native functional groups in tissues. However, copper ions can be toxic to cells when present above micromolar concentrations, problematic in cases such as 3D bioprinting in which rapid gelation (which is typically promoted by increasing the copper concentration) is required[86]. Thus, while CuAAC offers advantages in terms of its stability, tunability, bio-orthogonality, and relatively rapid reaction rate, the cytotoxicity of copper creates clear challenges in using CuAAC chemistry in practical 3D bioprinting applications. In addition, the utility of CuAAC for 3D bioprinting is inherently limited for synthetic polymers unless chemical modifications are made to the polymer backbones, given that the scaffolds would otherwise not clear from the body[77].

2.3.2 Strain-promoted azide-alkyne cycloaddition (SPAAC)

SPAAC click chemistry eliminates the need for copper in the click chemical reaction, allowing for effective crosslinking without the use of metals or other crosslinking agents. The SPAAC reaction takes advantage of a highly strained cyclooctyne precursor to lower the activation energy of the alkyne-azide reaction, enabling the formation of a triazole crosslink without the need for the copper catalyst required for CuAAC chemistry[87]. However, replacing the copper catalyst with ring strain does not reduce the activation energy to the same degree; while the rate constant for CuAAC is 10-200 $M^{-1}s^{-1}$, the SPAAC rate constant is only 10^{-2}-1 $M^{-1}s^{-1}$ [88]. As such, while gelation times are typically slower with SPAAC relative to CuAAC, proper selection of functional group densities and polymer precursor chemistry can still enable the rapid gelation typically required for 3D bioprinting applications. For example, Han *et al.* reported a SPAAC-crosslinked hyaluronic acid-based hydrogel for cartilage tissue engineering that was able to gel within 10-14 minutes while showing good biocompatibility *in vivo* and

effective cartilage regeneration[89], while Fan *et al.* reported chitosan/hyaluronan SPAAC hydrogels that could gel between 21-58 minutes depending on the ratios of the precursor polymers used[90]. Furthermore, by utilizing different functional groups with varying degrees of strain and differing electronics and/or different precursor polymer structures, even more relevant gelation rates can be achieved. For example, Hodgson *et al.* reported that SPAAC-crosslinked PEG hydrogels could gel in time frames as short as 10 seconds if PEG-based dendrons and aza-dibenzocyclooctyne (DIBAC) modified PEG were instead used as the building blocks, taking advantage of the "pre-crosslinking" of the PEG chains and the multivalent functionalization in the dendron to significantly accelerate gelation rates[91].

The slower gelation typically observed with SPAAC can also be addressed by combining SPAAC with faster physical or chemical gelation strategies. For example, Zhan *et al.* demonstrated that dual-crosslinked PEG hydrogels crosslinked with both SPAAC click chemistry and ionic calcium-phosphonate bonds could enable gelation times of <1 minute coupled with enhanced mechanical strength and retained biocompatibility[92], while Brown *et al.* combined SPAAC click chemistry with on-demand photocrosslinking to simulate muscle stiffening with age or disease[93]. However, the drawbacks of both ionic crosslinking and photocrosslinking are both re-introduced (at least in part) through such approaches.

The bio-orthogonality of SPAAC is highly beneficial for maintaining high cytocompatibility. For example, Xu *et al.* found that cells encapsulated in SPAAC-crosslinked poly(ethylene-glycol)-co-polycarbonate hydrogels maintained significantly higher viability than cells encapsulated in photocrosslinked PEG hydrogels[94], while cells encapsulated in PEG hydrogels formed through SPAAC maintained >95% viability with hMSC cells[95]. However, similar to CuAAC, the triazole bond via SPAAC is not degradable under typical physiological conditions but rather only reversible in non-physiological pH conditions[95]. As such, either degradable polymers or synthetic polymers with engineered degradation points are required to fabricate a degradable scaffold. The synthesis of cyclooctynes used in the SPAAC reaction is also complex, requiring rigorous reaction conditions and typically resulting in low yields[96]. Finally, given the higher activation energy and thus slower gelation rates achievable with SPAAC, pre-mixing of the bioink components before printing may be required to enable shape fixity, with potential impacts on cell viability as cells would need to be kept at non-physiological conditions over relatively long periods.

2.3.3 Diels-Alder

A Diels-Alder (DA) reaction occurs between a substituted alkene and a conjugated diene to form a substituted cyclohexene compound. This selective cycloaddition is thermally reversible, does not require a catalyst, and has a high reaction efficiency[97]. Applying such chemistry to 3D bioprinting can however be challenging given that elevated reaction temperature and/or acidic pH is typically required to facilitate the reaction under time frames relevant to bioprinting; even under such conditions, gelation using DA chemistry can be slower than other click chemistry methods. For example, Guaresti *et al.* showed that gelation of chitosan hydrogels crosslinked via DA chemistry still required 60 minutes at 85°C and 40-120 minutes at 65°C in the presence of acetic acid[98]. Rational choice of the DA gelling pair can however accelerate the reaction to be more relevant to a 3D bioprinting context. For example, hyaluronan-methylfuran hydrogels exploit the higher reactivity of methylfurans to allow for gelation at physiological temperature and pH, although the subsequent degradation times were also observed to be faster than conventional hyaluronan-furan hydrogels[99].

Although retro-DA chemistry can occur to degrade the formed crosslinks, shifting the equilibrium back to the products typically requires higher temperatures and/or lower pH conditions than achieved physiologically. However, some DA-crosslinked hydrogels can still undergo very slow degradation under physiological conditions[100]. For example, while uncrosslinked chitosan was 82% degraded in the presence of lysozymes and 47% degraded in PBS after 14 days, DA-crosslinked chitosan-based hydrogels were <25% degraded under both of these conditions[98], indicating slow reversibility of the DA adduct consistent with findings of previous studies. In another study on PEG-based hydrogels, degradation was found to occur over the range of a few days to several weeks through the hydrolysis of the maleimide residues exposed slowly over time due to the retro-DA reaction that exists in equilibrium with the forward DA reaction, creating unreactive maleamic acid derivatives that can no longer participate in DA crosslink formation and resulting in the slow dissolution of the gel[101].

Given that the DA reactions are also bio-orthogonal, hydrogels formed through DA-click chemistry generally maintain good cytocompatibility. HA-PEG hydrogels maintained >98% cell survival after 21 days *in vitro*[102], while >95% cell viability was achieved in DA-crosslinked Pluronic F127/Gelatin/PEG hydrogels[103]. However, given the slow rate of the DA reaction, the ability to encapsulate viable cells during printing may be compromised if the polymer

concentration or the degree of bio-orthogonal functional group substitution is significantly increased to accelerate the gelation times to be amenable to bioprinting[99].

While the electron-poor dieneophile is combined with an electron-rich diene in a conventional DA reaction, the inverse of this reaction (commonly termed inverse electron-demand Diels-Alder (IEDDA) chemistry) represents an attractive strategy for hydrogel synthesis due to its faster reaction rate under physiological pH and temperature[22, 104, 105]. IEDDA crosslinking most commonly typically involves reactions between phenyltetrazine derivatives and strained cycloalkenes (i.e., norbornene[106, 107]). While IEDDA-crosslinked hydrogels have been shown to be cytocompatible and useful for peptide immobilization, the hydrogels formulated using the phenyltetrazine functionality and the dienophile are considerably more thermodynamically stable due to the irreversibility of the IEDDA crosslink resulting from the generation of nitrogen during the synthesis[108-110]. The degradability can be specifically engineered into the backbone polymers (i.e., via the inclusion of disulfide bonds[111]).

2.3.4 Imine

Imine or Schiff base click chemistry occurs when an amine reacts with an aldehyde under acidic conditions. Hydrogels crosslinked via imine chemistry typically gel rapidly. For example, mixing chitosan with dialdehyde-functionalized PEG results in gelation within <1 minute[112], and mixing an aldehyde-functionalized chondroitin sulfate derivative with N-succinyl-chitosan (SC) results in gelation within 34-41 seconds[113]. However, imines are also highly pH labile, particularly in aqueous acidic conditions, due to the higher electrophilicity present in the original carbon-nitrogen double bond of imines relative to oximes and hydrazones[114]. As such, imine crosslinking can create highly degradable scaffolds and/or (given the noted shear thinning potential of imines[115]) extrudable 3D bioinks with transient crosslinking capacity.

The hydrolytic degradation rate of the imine bond can be tuned depending on hydrophobicity of the polymer and/or the functional groups adjacent to the reactive functional groups. Chitosan/oxidized hyaluronic acid imine-crosslinked hydrogels degraded completely in 10 days in a lysozyme solution, but only achieved 80% degradation after 10 days in PBS; however, degradation occurred much more rapidly *in vivo* in mice, with significant degradation noted after 2 days[116], while N-succinyl-chitosan/oxidized chondroitin sulfate hydrogels took 5 weeks to achieve 50% degradation *in vivo*[113]; in the latter case, degradation was slowed due to the

~48% substitution degree of succinyl groups on chitosan that created the potential for a secondary ionic-bonded network with the remaining amine groups in the native chitosan after the imine-crosslinked gel was formed. Although imine crosslinking is not bio-orthogonal, the very fast gelation rates achieved can still enable relatively good maintenance of cell viability, particularly at lower functional group contents that (given the fast nature of imine crosslinking) can still facilitate gelation on a relevant timescale for 3D bioprinting. For example, chitosan/hyaluronic acid-based hydrogels crosslinked through an imine bond were found to support 70% to 98% cell viability, with higher cytocompatibility maintained when the concentration of the hydrogel was decreased[116]. This result is consistent with the findings of a previous study using the same materials, wherein cell viabilities were maintained at >85% for various cell types at several hydrogel concentrations[117].[118], it is difficult to drive the reaction sufficiently quickly to make 3D bioprinting practical without using molding or templating strategies in conjunction with printing.

2.3.5 Oxime

An oxime bond is generated by the reaction of a hydroxylamine with an aldehyde or ketone. This reaction is ideal for the formation of hydrogels since it is fast, bio-orthogonal, does not require any catalysis or UV irradiation, and only forms water as a by-product[119]. While gelation can occur at physiological or near-physiological pH, slightly acidic conditions significantly accelerate gel formation. For example, PEG hydrogels synthesized through oxime bond formation gelled after 6 minutes at pH 6 but required 30 minutes to gel at pH 7.2[120], while hydrogels formed by mixing alkoxy-amine and aldehyde-functionalized alginate precursor polymers showed accelerated gelation when the temperature increased from 4 to 50℃ [121].

Oxime bonds are significantly more resistant to hydrolysis than many other hydrolysable click crosslinks[122]. For example, oxime-crosslinked hyaluronan hydrogels designed as a vitreous substitute were shown to remain stable *in vivo* over 28 days before enzymatic degradation of the HA finally induced slow subsequent degradation[120]. A similar study using alginate precursors found that gelation occurred after 30 minutes at physiological pH and noted that the degradation of the oxime bond was over two orders of magnitude slower than that observed with a hydrazone bond[123]. As such, oximes may be particularly relevant in cases in which slow degradation is desirable.

One disadvantage of oxime click chemistry is that the reaction contains similar functionalities that are present in biomolecules and cells, such that it is not bio-orthogonal. However, due to the faster gelation time and greater stability relative to disulfide bonds and thioether groups respectively, the oxime reaction is widely used for modifying different biomacromolecules like peptides, proteins, and DNA[124]. Oxime-crosslinked poly(ethylene glycol), hyaluronic acid and collagen all demonstrated excellent cell viability and supported the adhesion of human mesenchymal stem cells in tunable soft scaffolds[125], while hydrogels formed by crosslinking eight-armed aminooxy poly(ethylene glycol) with glutaraldehyde maintained high cell viability and allowed the encapsulated mesenchymal stem cells to stay metabolically active for at least seven days[119].

2.3.6 Hydrazone

Hydrazone crosslinking is a coupling reaction between an aldehyde or ketone and a hydrazide group[126]. This click chemistry is attractive since it can occur rapidly, enabling gelation over time frames from seconds to minutes (depending on the density of the functional groups) as is ideal for 3D bioprinting applications[127]. Furthermore, depending on the functional groups appended to the carbonyl and hydrazide components to change the electronic and steric environment of the crosslinked material, the hydrolytic degradability of hydrazone-crosslinked hydrogels can be tuned from weeks to months at neutral pH[128], enabling control of the clearance rate of the printed scaffolds. This dynamic equilibrium between the reactants and the formed hydrazone bond is beneficial in tissue engineering applications to mimic the dynamic interactions that are natively present in the extracellular matrix. Our group has extensively explored the use of hydrazone chemistry to fabricate poly(oligo(ethylene glycol) methyl ether methacrylate) (POEGMA) and poly(N-isopropylacrylamide) (PNIPAM)-based hydrogels with high cytocompatibility, achieving gelation times from <1 second to 30 minutes at physiological temperature/pH conditions that are tunable based on the compositions of the monomers used in hydrogel synthesis, the polymer concentration, and the morphology of the resulting hydrogel building blocks[129, 130]. Successful delivery of retinal epithelial cells[131] and myoblasts[132] has been achieved with these hydrogels. Other groups have also shown the benefits of hydrazone chemistry for rapid gelation. Hyaluronan/alginate hydrogels fabricated using hydrazone chemistry displayed a gelation time ranging from 30 seconds to 5 minutes depending on the precursor composition, full degradation after ~24 hours in hyaluronidase enzyme solution, and demonstrated potential for acting as supportive matrices for human

pluripotent stem cell-derived neuronal cells[133], while a gelatin/hyaluronic acid hydrazone-crosslinked hydrogel could be tuned to degrade over periods ranging from 1 day to 3 weeks in PBS at 37°C depending on the ratio of gelatin to HA and the amount of hydrazide/aldehyde functionalization on the precursor polymers[127]. Secondary crosslinking can also prolong the degradation of the hydrazone-crosslinked networks; for example, hydrazide-modified elastin-like protein and aldehyde-modified hyaluronic acid can be mechanically reinforced with secondary thermoresponsive crosslinking of the engineered proteins that results in a ten-fold slower erosion rate compared to the control hydrogel without secondary thermal crosslinking[134].

A key drawback of aldehyde/hydrazide hydrazone chemistry in tissue engineering applications is that aldehyde group can from imine bonds with amine groups on native proteins, with the resulting non-bio-orthogonality offering the potential to induce local toxicity if aldehydes are present at high concentrations and/or in a stoichiometric excess during the gelation process[128]. The use of aldehydes can however be entirely avoided if ketones are instead used as the electrophile[128], although the lower reactivity of ketones relative to aldehydes (due to their higher steric hinderance around the carbonyl) typically results in slower gelation times. To achieve similar a gelation time and mechanical strength to that achieved with aldehyde-functionalized precursor polymers alone, the mole fraction of ketone functional groups can be increased[128] or a mixture of ratios of both ketone and aldehyde-functionalized precursor polymers can be used that lowers the risk of residual aldehyde groups being present while still maintaining faster gelation times.

2.3.7 Thiol-Michael Addition

A Michael addition is characterized by the reaction of a nucleophile with an α,β-unsaturated carbonyl to form a thioether bond[135]. Thiol-Michael additions use a thiol group as the nucleophile to react with the electrophilic double bond of a maleimide, acrylate, or vinyl sulfone to produce a thioester crosslink[136]. This click chemistry can exhibit a rapid reaction rate that can be tuned depending on which of maleimides, vinyl sulfones, or acrylate groups (or other unsaturated electrophiles) are used[137]. For the thiol-maleimide reaction, PEG-based hydrogels have been reported to gel as quickly as 2-4 seconds under physiological conditions[138, 139]; reactions between thiols and vinyl sulfones or acrylates occur slightly more slowly but still can facilitate gelation in less than one minute. For example, poly(*N*-

isopropylacrylamide) (PNIPAAm)-based hydrogels crosslinked through thiol-vinyl sulfone chemistry could gel in 25-37 seconds[140], thiol-acrylate crosslinked poly(ferrocenylsilane)-PEG hydrogel could gel within 1 minute[141], and thiol-acrylate dextran-PEG hydrogels were reported to gel in 22-50 seconds[69]. In all cases, the gelation is typically rapid relative to other click chemistry methods. In addition, the pK_a of the Michael-type donor can regulate the speed of the thiol-maleimide reaction, with the gelation rate increasing at a high pH (up to 10, which can be characteristic of some wounds) while slowing under acidic pH (5.8 or lower)[139].

Thiol-Michael crosslinks are generally resistant to degradation, although retro-Michael chemistry has been reported with the thiol-maleimide reaction pair[142] due to the slow hydrolysis of the small fraction of exposed maleimide groups even when the equilibrium lies strongly on the side of the coupling reaction (similar to the retro-DA reaction outlined earlier). Degradation of thiol-maleimide bonds can also occur slowly via hydrolysis in the presence of reducing agents like glutathione provided that an aromatic thiol is used as the nucleophile[139] or in the presence of reducing agents like glutathione provided that an aromatic thiol is used as the nucleophile[142]; the latter facilitates slow degradation on the order of 10-100 times lower than a comparable disulfide bond. In comparison, thiol-vinyl sulfone hydrogels were found to undergo no significant degradation after one week in metalloproteinase solutions[143], while thiol-acrylate hydrogels showed no degradation over several days in the same protease solution[144]. Given the slow to negligible degradation rates observed, similar strategies to those outlined in the CuAAC/SPAAC section have thus been implemented with thiol-Michael chemistry to engineer degradability into the hydrogels. For example, thiol-modified chitosan hydrogels covalently crosslinked with a water-soluble bismaleimide could be enzymatically degraded after 24 hours in a lysozyme-containing solution[145], while collagen hydrogels prepared using the same approach showed complete degradation after only 6 hours in a collagenase enzyme solution[146]. In a separate study, the degradation of three thiol-maleimide click reactions between multi-arm poly(ethylene glycol) macromers (functionalized with either a thiol, a photodegradable maleimide or an aryl thiol) could be tuned from seconds to days using externally applied light, reducing conditions, and hydrolysis, achieving degradation rate constants ranging from 10^{-1} min^{-1} to ~10^{-4} min^{-1} [147].

The cytocompatibility of thiol-Michael click hydrogels is generally high but can vary to some degree depending on the type and concentration of particularly the electrophile used to form the adduct. Thiol-acrylate hydrogels based on PEG could maintain a cell viability of 94% after

a 24-hour incubation period[148], while another thiol-acrylate crosslinked hydrogel based on dextran-PEG maintained cell viabilities of >95% at all time points for various formulations[149]. Thiol-maleimide crosslinked PEG hydrogels have also been reported to show nearly 100% viability at the 2-hour time point[139]. While the potential negative impact of residual vinyl sulfone groups on cell viability has been raised in some studies[150, 151], Hubbell *et al.* and Stewart *et al.* both reported excellent cell viabilities >93% in hydrogels crosslinked using vinyl sulfones[152, 153]; as such, high cytocompatibility can be maintained provided the correct stoichiometry is used to minimize the presence of any residual vinyl sulfone groups.

2.3.8 Amine-Michael Addition

In an amine-Michael (also known as aza-Michael) addition reaction, the Michael donor is a nucleophilic amine group and the Michael acceptor is an electron-deficient alkene[154]. Relative to thiol-Michael additions, amine-Michael addition is significantly slower in water to the point that organic solvents (dichloroethane, acetonitrile, etc.) and/or high temperatures (up to 80°C) are often used to drive the reaction forward. However, slower gelation is still possible under physiological conditions, with a polyamidoamine (PAMAM)/polyethylene glycol diacrylate (PEGDA) hydrogels reported to gel after 49 minutes[155] and PEG-based hydrogels prepared at varying polymer concentrations reported to gel over timescales ranging from 1 hour to >1 day[156]. As such, while amine-Michael addition is not suitable for continuous 3D bioprinting, it may be suitable for templated 3D bioprinting processes in which slower gelation times are acceptable.

While evidence exists that amine-Michael click chemistry hydrogels can degrade slowly under some conditions via the oxidation of the secondary or tertiary amine crosslinks[157], designing predictably degrading bioinks typically requires combining this chemistry with other degradation methods. For example, amine-Michael crosslinked hydrogels prepared based on mixing poly(amidoamine) (PAMAM) and PEGDA diacrylate synthesized with either pH-cleavable acetal or reducible disulfide linkages were found to degrade via slow hydrolysis at physiological pH (27% degradation after 22 days)[155].

Although the amine-Michael reaction is not bio-orthogonal, relatively high cytocompatibilities of encapsulated cells have been reported. PAMAM dendrimer-based hydrogels crosslinked via amine-Michael reactions achieved >80% cell viabilities over a range of different polymer

concentrations[158], while polydopamine amine-Michael hydrogels maintained cell viabilities of >85% across several different polymer compositions[159]. Thus, provided the slow gelation rate is not problematic for the particular modality of 3D bioprinting chosen, suitable cell scaffolds can be fabricated using amine-Michael chemistry[159].

2.3.9 Thiol-ene

The thiol-ene click reaction occurs when a thiol group reacts with an alkene to form an alkyl sulfide in the presence of free radicals, typically generated via photoirradiation with or without the presence of a photoinitiator. While we fully acknowledge that thiol-ene click chemistry does not fall under the conventional definition of click chemistry in that it requires an external energy component in the form of UV light, it is a broadly used modality in tissue engineering due to its high yield, stereoselectivity (unlike most of the other click or click-like reactions summarized above), and high thermodynamic driving force; indeed, thiol-ene is a leading *in situ*-gelation technique used to-date in in 3D bioink development, motivating us to include it in the review despite it not being a true click or click-like chemistry. Although the reaction mechanism of a thiol-ene reaction is very similar to a thiol-Michael addition reaction, Michael addition reaction rates increase with the electron-deficiency of the acceptor while electron-rich alkenes are typically preferred in a thiol-ene reaction[160]. Due to its ability to be carried out in aqueous solutions at physiological conditions with relatively fast kinetics under photopolymerization conditions, thiol-ene click chemistry is attractive for 3D bioprinting[161]. For example, using PEG precursor polymers, the gelation time for thiol-ene crosslinked hydrogels was found to be tunable from 18 seconds to 2 minutes depending on the pH and precursor polymer concentrations[162], while gelation times of ~3 minutes were reported in another study using a PEG-DA and silk fibroin-based hydrogel[163]. Using PEG precursor polymers, the gelation time for thiol-ene crosslinked hydrogels could be tuned between 18 seconds to 2 minutes depending on the pH, precursor concentrations, and other factors[162]; similar fast gelation times of <3 minutes were reported in another study using a PEG-DA and silk fibroin-based hydrogel[163].

Thioether bonds formed from the thiol-ene click reaction are relatively stable under typical physiological conditions, although some degree of degradation may occur through redox reactions (similar to the amine-Michael reactions mentioned above)[164]. Consequently, thiol-ene chemistry is more commonly used in conjunction with either inherently degradable

polymers or polymers engineered to degrade under physiologically-relevant conditions. For example, Li *et al.* fabricated a starch hydrogel through thiol-ene click chemistry in which the enzymatic cleavage of starch allowed for complete degradation in 2-8 hours in an amylase solution[165].

One potential drawback of this chemistry is the requirement for UV irradiation and thus the generation of free radicals in the crosslinking process, which can induce cytotoxicity[166]. In a study by Mohammed et al., thiol-ene click chemistry-based polyanhydrides (PAH) demonstrated promising cell viabilities (>85%), with statistically relevant toxicity reported at 4000 mg/L PAH toward HDFa fibroblast cells (~57%) that requires further exploration and can be attributed to the free radical generation in the crosslinking process[167]. However, a recent report of a dual pH- and thermo-responsive chitosan/PNIPAM-based hydrogel system that relies on UV-initiated thiol-ene crosslinking between the thiol groups in PNIPAM and the allyl groups in chitosan did maintain very high cytocompatibility with human mesenchymal stem cells after 24 hours (>95%)[168].

2.3.10 Disulfide Formation

Disulfide bonds are formed through the oxidation of two thiol groups, a reaction accelerated by the presence of oxidizing agents and/or neutral pH values[169]. The gelation kinetics even under accelerated conditions for disulfide crosslinking are very slow compared to the other click chemistry methods presented, although can be accelerated in the presence of oxidizing agents[170]. For example, Gyarmati *et al.* showed that hydrogels synthesized through disulfide crosslinking transitioned from liquid to gel in the range of 6 and 24 hours in solutions of varying pH values and in the range of 10 and 1000 seconds in the presence of chemical oxidizing agents (cystamine and 3,3'-dithiodipropionic acid, respectively), with the resulting hydrogels showing no sign of degradation for up to 1 week in PBS buffer and no obvious signs of degradation after 1 week *in vivo*[171]. Acceleration of the gelation rate can also be achieved by adding activated disulfides (i.e., pyridyl disulfide) to form hydrogels via disulfide exchange reactions instead of thiol oxidation[172], although this approach leaves behind small molecule by-products that may be undesirable in tissue engineering applications.

The key advantage of this crosslinking approach is that the disulfide bonds are responsive to exposure to reductive environments, including increased local reducing agent concentrations

(i.e., of glutathione or dithiothreitol) and/or slightly lower local pH values that are indicative of many types of disease sites or infection sites[173]; in this context, enhanced degradation can occur to target the delivery of drugs or cells to a targeted site. In particular, the use of disulfide bonds is suitable for developing smart hydrogels responsive to glutathione and other reducing agents, which allows for redox-responsive degradation[174].

Thiol-containing polymers can react with naturally occurring thiols, disulfides, and electrophiles[175], making disulfide crosslinking not bio-orthogonal; however, accelerating the reaction using the techniques outlined earlier reduces the likelihood of thiol cross-reactivity with native functional groups to the degree that an element of "kinetic bio-orthogonality" may be achievable in practice[172]. Direct encapsulation of cells in hydrogels crosslinked with disulfide bonds has also been shown to be effective. Disulfide crosslinked hyaluronan hydrogels maintained high viability and supported proliferation of L-929 murine fibroblasts over three days of culture *in vitro*[176], while several different cell types including fibroblasts, endothelial cells, and mesenchymal stem cells, remained viable after 7 days (using a live-dead assay) in injectable hyaluronic acid hydrogels crosslinked via disulfide bonds[177]. As such, while disulfide crosslinking may be appropriate as a secondary crosslinking strategy for *in situ* gelling hydrogels for tissue engineering applications. However, the very slow degradability under physiological conditions of both the oxime bond and multi-arm PEG prevents cell spreading after 7 days since cells cannot effectively remodel the scaffold on this timescale. As such, incorporating degradability into the polymer backbone may be important with oxime crosslinks if they are to be used for tissue regeneration applications.

2.3.11 Boronate Ester

Boronate ester click chemistry involves the reaction of a boronic acid with a diol to form a boronate ester bond. This reaction is both spontaneously and rapid, resulting in fast gelation rates at slightly basic pH values (pH 8-9) that can also be achieved at physiological temperature and pH with proper selection of the boronic acid[178, 179]. For example, Amaral et al. demonstrated that mixing phenylboronic acid-functionalized beta-glucan laminarin with poly(vinyl alcohol) resulted in the formation of a boronate ester-crosslinked hydrogel within seconds under physiological conditions[180].

The degradability of boronate esters can vary significantly depending on both the pH (accelerated under acidic conditions) as well as the surrounding environment of the hydrogel. In particular, the potential exchange of the diol for naturally-derived carbohydrates containing *cis*-diol groups with higher binding affinities to the boronic acid group can enable degradation of the gel in response to biological signals, making boronate-ester click chemistry a promising candidate for responsive scaffolding applications[181]. Although certain boronate ester derivatives were found to withstand degradation for up to 3 months in pure water, degradation can in other cases occur within minutes under some physiologically-relevant conditions[181, 182]. Dual-crosslinked hydrogels are thus often pursued to take advantage of the fast gelation rate of boronate esters coupled with a more hydrolytically stable gelation chemistry. For example, Wu *et al.* constructed a dual-crosslinked hydrogel that combined conventional boronate ester crosslinking with a nopoldiol-based benzoxaborolate (a cyclic hemiboronic acid with a lower pK_a than conventional arylboronic acids) by using complementary diol and benzoxaborole-based monomers to facilitate the dual crosslinking network. While the conventional boronate ester bonds between the arylboronic acid and a diol degraded in 120 minutes in a polyol solution, the dual-crosslinked hydrogel remained intact for 10 to 20 days even in acidic pH[182]. Liu *et al.* similarly fabricated dual-crosslinked hydrogels by combining boronate ester and hydrazone bonding; while single-crosslinked boronate ester gels reached their gelation point faster (after ~2 hours, although this could be accelerated by using higher degrees of functionalization and/or polymer concentrations), the dual-crosslinked structures displayed significantly higher mechanical strength and persistence under physiological conditions[183]. As such, boronate esters particularly well suited to forming weak/fast-degrading scaffolds and/or supporting double crosslinking processes.

Boronate esters have been reported to be cytocompatible for cell encapsulation. For example, a hydrogel formed by mixing hyaluronic acid modified with a boronic acid derivative and 1-amino-1-deoxy-D-fructose maintained >80% viability of encapsulated fibroblast cells after 7 days of cell culture[27], while hydrogels formed by mixing phenylboronic acid-functionalized beta-glucan laminarin and poly(vinyl alcohol) enabled full maintenance of preosteoblast viability over 48 hours[180]. Of note, due to the dynamic nature of the boronate ester bond, hydrogels crosslinked with boronate esters have also been demonstrated to exhibit tunable viscoelastic properties enabling investigation of the timescale-dependent mechanotransduction of cells as the material responds to an imposed stress or strain by reversible crosslinking/decrosslinking[184].

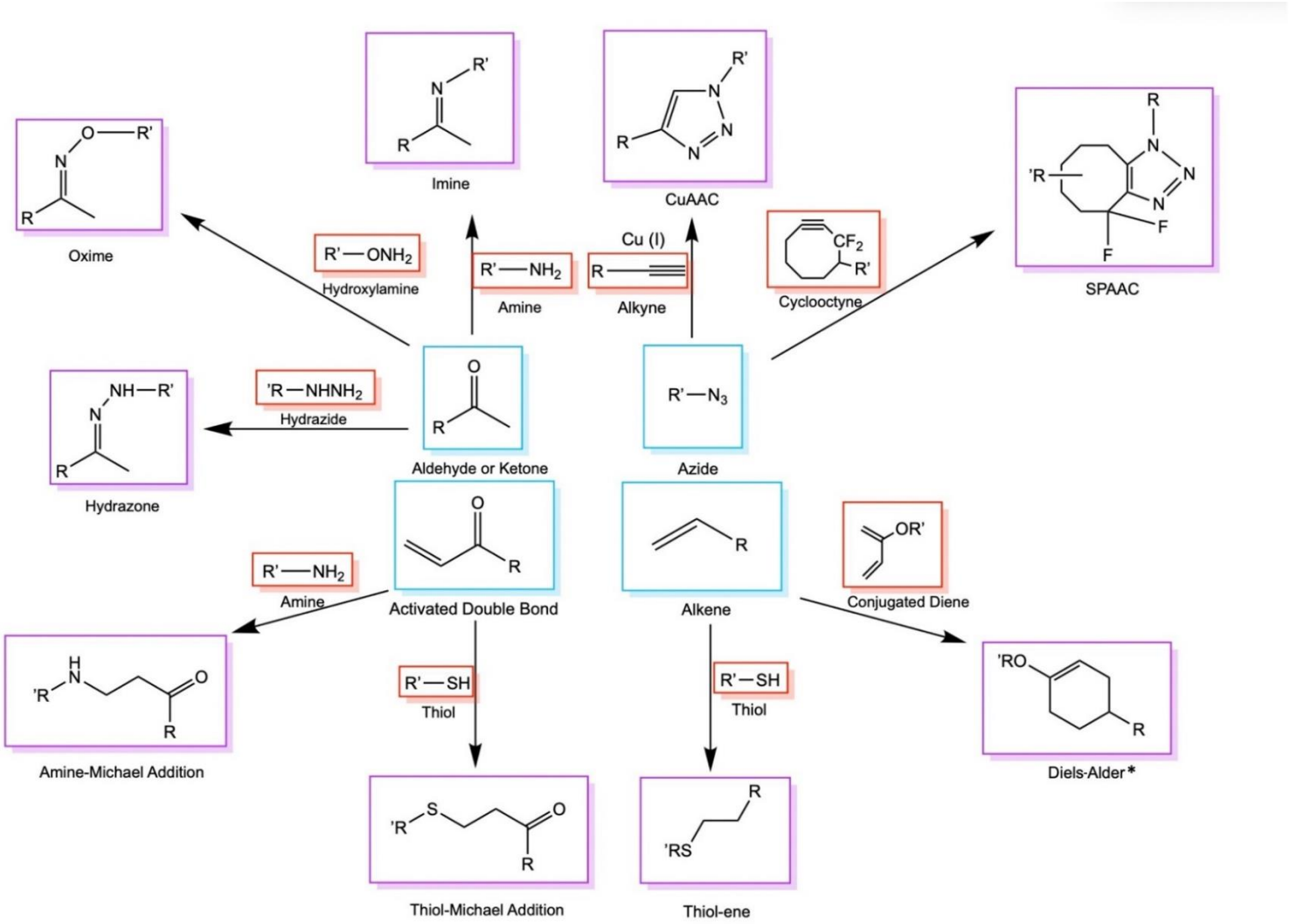

Figure 2.2: Available click chemistry methods for tissue engineering applications. *Diels-Alder is represented as R = electron-withdrawing group and R' = electron-donating group; if these groups are switched, the same scheme represents an inverse Diels-Alder reaction.

Table 2.2: Comparison of click chemistry methods for tissue engineering applications and their relative gelation and degradation rates under physiological conditions

Click Chemistry	Relative Gelation Rate	Rate Constant ($M^{-1}s^{-1}$)	Relative Degradation Rate	Advantages	Disadvantages	Ref
CuAAC	++++	$10 – 10^2$	-	• Can occur over a wide range of temperature and pH conditions • Bio-orthogonal	• Copper catalyst can be cytotoxic • Only reversible at sub-physiological pH	77-82, 84-86, 93, 158, 185, 186
SPAAC	+++	$10^{-2} – 10$	-	• Does not require catalysts or cofactors • Provides sufficient mechanical strength to resist high strain • Bio-orthogonal	• Difficult to synthesize reagent cyclooctanes • Gelation time is longer than CuAAC • Only reversible at sub-physiological pH	87-92, 94-96
Diels-Alder	+	$10^{-6} – 10^{-3}$	+	• Does not require catalysts or cofactors • Reaction accelerates in aqueous media • Bio-orthogonal • High stability	• Requires high temperatures to react or degrade at an appreciable rate • Slow reversibility	97-103, 187, 188
Hydrazone (aldehyde-hydrazide)	+++	$10^{-2} – 10^2$	+++	• Does not require catalysts or cofactors • Tunable reversibility (dynamic)	• Not bio-orthogonal • Aldehyde groups can induce local toxicity in high concentrations	126, 127, 129-133, 189
Hydrazone (hydrazide-ketone)	++	$10^{-4} – 10^{-3}$	+++	• Does not require catalysts or cofactors • Substantially bio-orthogonal • Ketones do not induce local toxicity • Tunable reversibility (dynamic)	• Ketones are less reactive to hydrazide, leading to slower gelation times	128
Thiol-Michael	++++	$10 – 10^3$	+	• High tolerance toward different functional groups • Rapid gelation	• Not bio-orthogonal • Typically requires basic pH or added catalysts	135-141, 143, 145, 146, 148,

					• Only cleavable via slow redox reactions	149, 152, 153, 190
Amine-Michael	+	N/A	+	• Does not require catalysts or cofactors	• Not bio-orthogonal • Only cleavable via slow redox reactions	154-156, 159, 191-196
Thiol-ene	++++	10^3 –10^5	Ox	• High reaction efficiency at mild conditions	• Radicals produced in initiation step may be cytotoxic • May require potentially cytotoxic small molecules to accelerate reaction • Only cleavable via slow redox reactions	112, 161-168, 197
Disulfide	+	N/A	+++	• Can be readily degraded in a reductive environment • Does not require catalysts or cofactors	• Not bio-orthogonal • Hard to create stiff hydrogels • Low selectivity	169-175
Oxime	++	10^{-3} – 10^1	+	• Precursor functional groups are more stable compared to thiols and imines • Minimal protonation at physiological pH	• Not bio-orthogonal • Substantial degradation does not occur at non-cytotoxic pH values	119-121, 123-125, 198, 199
Imine	+++	10^{-1} – 10^3	++++	• pH responsive and shear-responsive • Does not require catalysts or cofactors	• Limited hydrolytic stability • Not bio-orthogonal	113, 114, 116, 117, 169, 200-203
Boronate Ester	++	N/A	+++	• Unique glucose, pH, and oxidative responsiveness • Does not require catalysts or cofactors • Tunable reversibility (dynamic)	• Not bio-orthogonal due to non-specific binding of boronic acids with polyols • High pH sensitivity	27, 178-184

Note: Rates are referenced to physiological conditions, assuming the same polymer backbone but with the different click chemistry methods. ++++ very fast; +++ fast; ++ slow; + very slow; - (only degradable in non-physiological acidic conditions); ox (degradation only due to oxidation

2.4 Click Chemistry Bioinks

The outcome of a bioprinting process based on click chemistry bioinks is not only influenced by the chemistry chosen and the type of material used as a precursor polymer but also the mixing modality through which precursor polymers are combined. Indeed, the appropriateness of different click chemistry methods for 3D bioprinting can vary significantly depending on what type of mixing approach is used. While it should be emphasized that it is difficult to create a list of fully generalized criteria for 3D bioink design (particularly depending on whether a free-form or a templated strategy is used for extrusion printing), the ideal click chemistry bioink is 1) compatible with the chosen cell type(s), 2) mechanically robust to not only provide sufficient print fidelity during the printing but also provide the appropriate mechanical environment for long-term cell culture, 3) adaptable to different mixing modalities dependent on the final construct design (i.e., gelation time), and 4) degradable into cell-friendly components. If co-extrusion and gelation are sought to be conducted at the same time, more rapidly gelling linkages (i.e., hydrazones, oximes, imines, CuAAC/SPAAC, Michael additions, thiol-ene) are typically required. However, depending on the efficiency of mixing, rapid gelation can lead to highly heterogeneous crosslinking since polymerization occurs faster than the timescale of mixing, impacting the mechanics and functionality of the hydrogels produced[139]. For example, Darling *et al.* found that heterogeneous crosslinking through thiol-Michael additions led to significant differences in cell responses between the high and low crosslinked regions, which may inhibit the hydrogels from integrating into biological systems as desired[139]. Alternately, if the precursor polymers are mixed prior to printing, slower gelling crosslinking pairs (i.e., Diels-Alder, hydrazide-ketone, disulfide, boronate ester) can be used. However, in such cases, the residence time in the printer must be precisely controlled such that shape fixity can be achieved upon extrusion, leading to potentially high printing impacts of very subtle batch-to-batch variability in the starting materials or the need for secondary processing (i.e., UV irradiation for thiol-ene reactions) to preserve the fidelity of the printed structures. As such, consideration of the combination of gelation kinetics and mixing strategy is critical to the success of using click chemistry for bioink design.

2.5 Mechanisms of Mixing

Figure 2.3 demonstrates various mixing strategies available to continuously mix the reactive click chemistry precursor polymer(s) in the context of the 3D bioprinting. Mixing can occur by depositing complementary precursors sequentially in contact with one another to facilitate

crosslinking through stacked (**Figure 2.3A**) or adjacent (**Figure 2.3B**) mixing, a coaxial extrusion system wherein complementary precursors are in contact circumferentially (**Figure 2.3C**), pre-mixing of slow-gelling precursors (**Figure 2.3D**), using a static mixer to actively mix the precursors during extrusion (**Figure 2.3E**), or printing one precursor into a support bath containing the complementary precursor (**Figure 2.3F**). For the latter case, the most common embedded mixing approach is FRESH bioprinting, which uses a dense suspension of gelatin-based microspheres that can shear thin to facilitate printing but then fix the printed liquids in place once the shear of the needle is removed; subsequent heating to physiological temperature melts the gelatin to enable it to be removed following gelation of the printed feature[26, 204, 205]. Other viscous support baths including agarose and Pluronic derivatives (both removed by temperature changes[206]) and ceramic materials (removed through heating and sonication[207]) can also be used.

Each mixing strategy offers both advantages and disadvantages, as summarized schematically in **Figure 2.3**. Using a stacked or adjacent mixing approach (**Figure 2.3A** and **B**) is mechanistically simple in terms of extrusion and nozzle design but almost inevitably results in inhomogeneous crosslinking since only a single linear interface is formed between precursors; as such, it may be useful in cases where very thin layers of polymer are used or when homogeneous mixing is not of vital importance to the performance of the printed scaffold. A coaxial extrusion system (**Figure 2.3C**) also facilitates single-step extrusion printing, allows for a larger contact area between precursors by creating a cylindrical interface, and is ideal for bioprinting hollow or vascular-mimicking structures but is still unlikely to produce a homogeneously crosslinked network[208]. On the other hand, both pre-mixing (**Figure 2.3D**) and static mixing (**Figure 2.3E**) are much more likely to facilitate the printing of a homogeneous network but come with other drawbacks. Pre-mixing is a simple method by which a hydrogel can be printed with any extrusion-based bioprinter; however, it requires precise tuning of the gelation time such that precursors are extruded as liquids to avoid high shear forces that may damage cells but gel quickly enough after deposition to hold the desired shape. The consequence of this balance is that only a very narrow range of printing times exist over which a pre-mixed bioink can be printed, significantly limiting the size and complexity of the printed scaffold[23]. The static mixing approach faces a very similar balance between the gelation time and the residence time over which the precursor polymers are in intimate contact within the static mixer to avoid clogging (overly rapid rate of gelation rate) while maintaining good shape fidelity as well as high cell viability in the printed construct[209]. The embedded mixing approach

(**Figure 2.3F**) is much more flexible in terms of gelation time, requires only a simple single-channel nozzle, and enables the printing of significantly more complex prints compared to stacked or adjacent mixing. However, this method can also lead to inhomogeneous crosslinking given that gelation typically is driven by simple diffusion of one precursor polymer pre-loaded in the bath into the printed precursor polymer; it also requires extra support bath materials and preparation steps that incur higher costs and requires post-processing after printing to recover the final printed structure. Thus, depending on the prioritization of the homogeneity of the gel network versus the operational simplicity of the printing process, a different printing strategy may be selected.

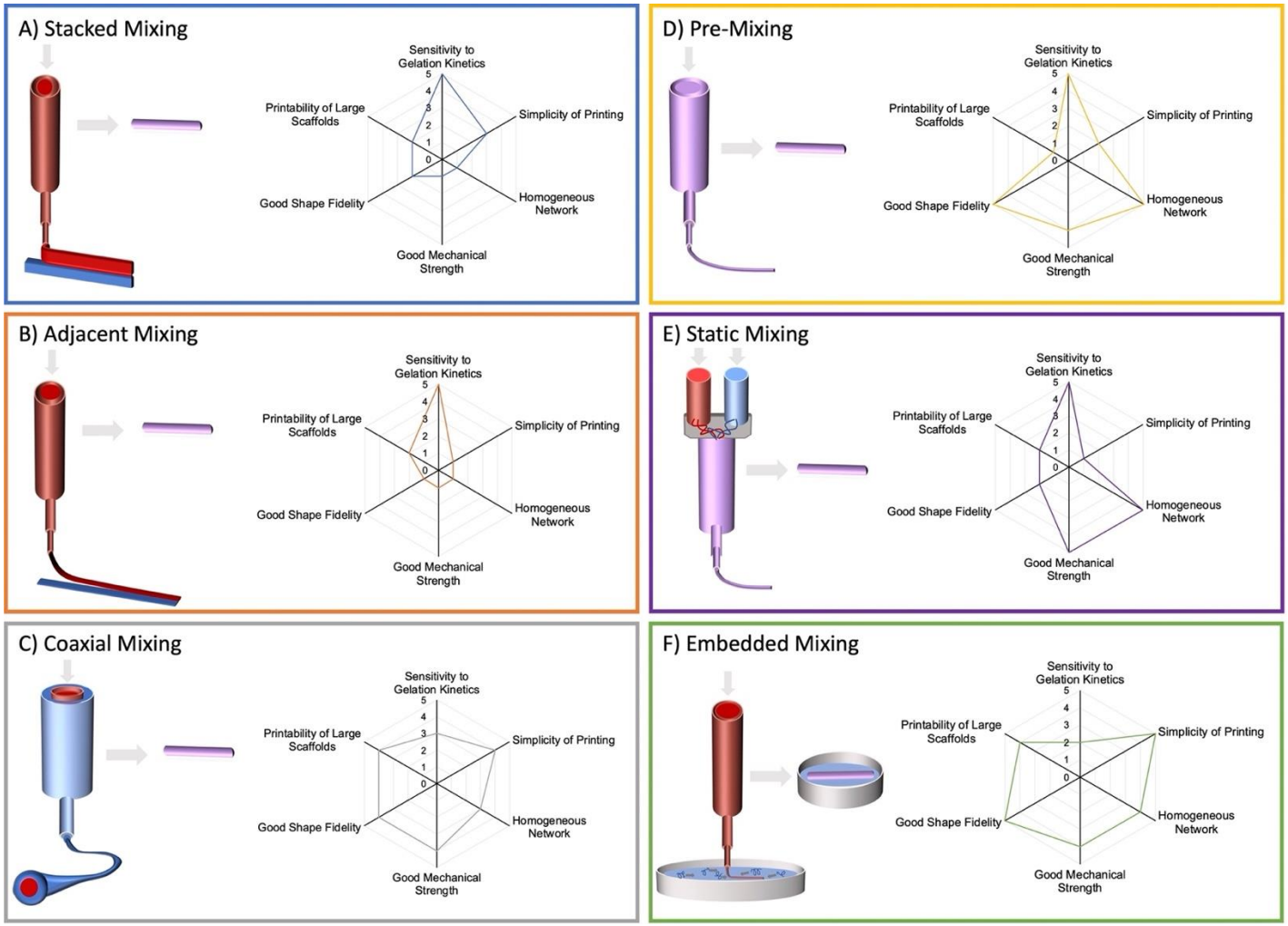

Figure 2.3: Mixing modalities available for 3D printing of click chemistry bioinks for (A) stacked mixing, (B) adjacent mixing, (C) coaxial mixing, (D) pre-mixing, (E) static mixing and (F) embedded mixing, and a comparison of the advantages and disadvantages relative to key considerations for successful 3D bioprinting. 1 = lowest, 2 = lower, 3 = average, 4 = higher, 5 = highest.

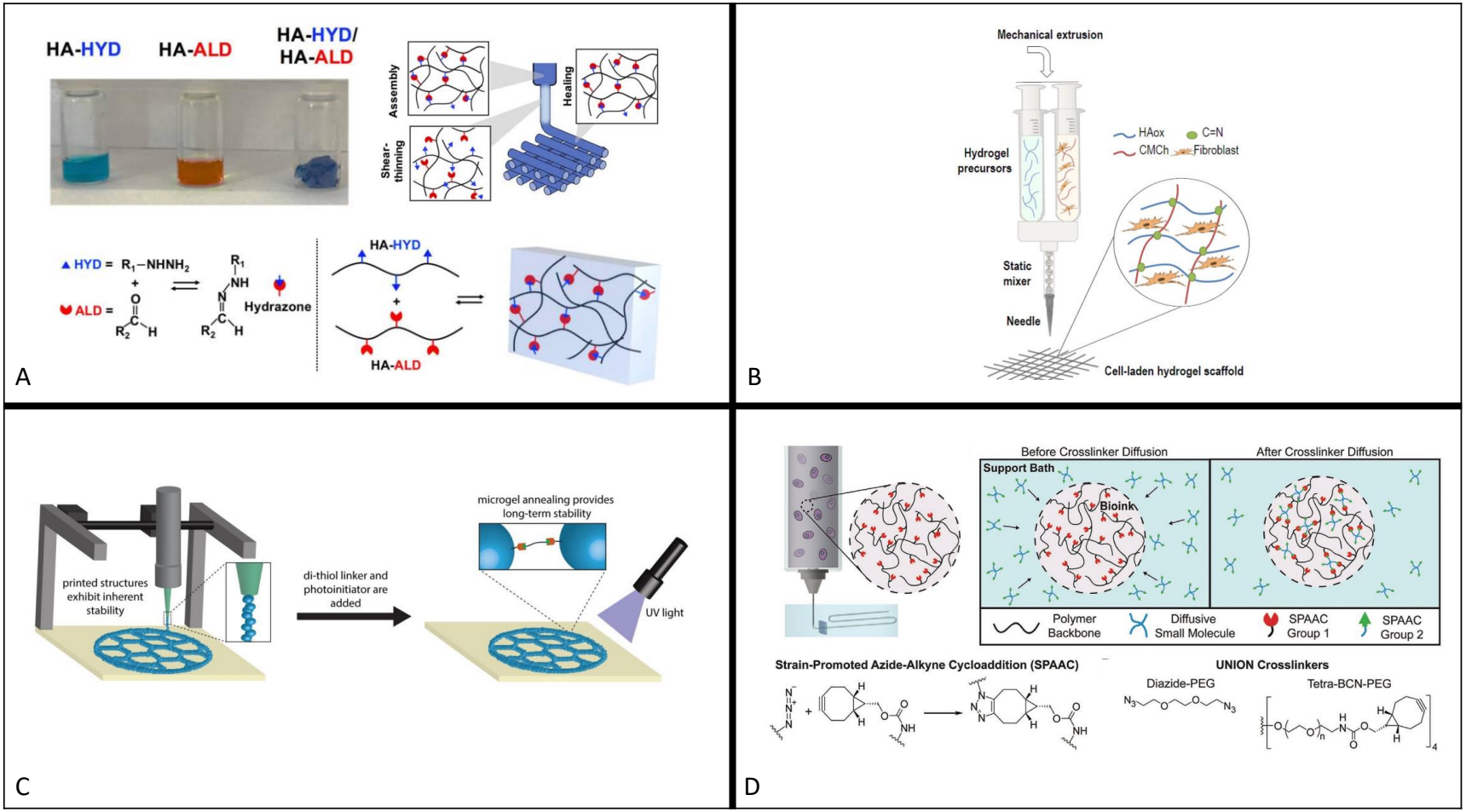

Figure 2.4*:* Reported click chemistry bioinks. (A) Hyaluronic acid hydrogel bioink formed via hydrazone click chemistry (reprinted with permission from Wang *et al.* [23] Copyright 2018 John Wiley and Sons); (B) Carboxymethyl chitosan/partially oxidized hyaluronic acid hydrogel bioink formed via imine click chemistry (‘*3D Printing of a Reactive Hydrogel Bio-Ink Using a Static Mixing Tool* ‘ by Puertas-Bartolomé *et al.* is licensed under CC-BY 4.0 [209]*)*; (C) Clickable PEG microspheres as building blocks for 3D bioprinting (reprinted with permission from Xin *et al.* [25], Copyright 2019 Royal Society of Chemistry*)*; and (D) Universal orthogonal (UNION) hydrogel bioink formed via SPAAC click chemistry (reprinted with permission from Hull *et al.* [26], Copyright 2021 John Wiley and Sons.

2.6 Examples of 3D Printed Click Bioinks

While there are still only a limited number of examples of successful extrusion-based printing of click chemistry bioinks, in the examples below we outline how these various mixing strategies have been implemented in conjunction with the use of hydrazone, thiol-ene, CuAAC, imine, and SPAAC click chemistry to achieve successful extrusion-based bioprinting.

2.6.1 Hydrazone

One of the first reports of 3D bioprinting using click hydrogels was Wang *et al.*'s 2018 report of fabricating a hydrazone-crosslinked shear-thinning and self-healing hyaluronic acid hydrogel using a pre-mixing strategy (**Figure 2.4A**)[23]. The researchers functionalized hyaluronic acid with hydrazide and aldehyde functional groups and manually mixed them in a single syringe barrel at various weight percentages, with pre-gelation observed to occur rapidly in the syringe. However, in order to preserve extrudability, the mechanics of the hydrogel were inherently limited, with the storage modulus of the printed hydrogel variable between 500 Pa to a maximum of 6000 Pa as the polymer weight percentage was increased[23]. The high shear thinning capacity of hyaluronic acid facilitated extrusion using practically achievable forces through a 25-gauge needle, enabling the production of various structures including well-defined lattices[23]. Such printability would not be achievable for bioinks that are not as shear-thinning, which must instead use precursor polymer combinations with longer gelation times that can cause downstream challenges with shape fixity. In a different study, oxidized alginate (containing aldehyde groups) was mixed with different small molecule crosslinkers (i.e., adipic acid dihydrazide, hexamethylene disemicarbazide, and aminooxy propyl hydroxyl amine dihydrochloride) to compare the printability of bioinks formed via hydrazone, semicarbazone, and oxime click chemistry respectively, using a pre-mixing approach while exploiting the dynamic shear thinning of the hydrogels during printing[210]. The semicarbazone and hydrazone-crosslinked hydrogels were printable without the need for additional ionic crosslinking and could promote the adhesion of fibroblast cells, while oxime crosslinked hydrogels were found to be elastic and non-reversible (at least on the time scale of the experiment) and could not be printed due to the formation of a non-continuous gel slurry upon extrusion. Alternately, the dynamic crosslinking in dual hydrazone and oxime crosslinked hydrogels by mixing oxidized alginate with dihydrazide and bishydroxlamine crosslinkers increases the mechanical stiffness and stress relaxation across an order of magnitude (with a shear storage modulus of ~2500 Pa for hydrazone compared to ~250 Pa for oxime), while the reversibility of hydrogels with high

hydrazone content enables printability using the pre-mixing approach[211]. Human dermal fibroblast cells were successfully bioprinted using the dual hydrazone-oxime crosslinked hydrogels (>85% viability), suggesting that the shear-thinning behaviour of the hydrogels protects the fibroblasts from the shear stress during the extrusion process. However, to our knowledge, there has yet to be a demonstration of hydrazone-based gelation via dynamic mixing of the precursor polymers despite the achievable fast gelation times associated with hydrazone chemistry.

2.6.2 Imine

The highly dynamic nature of an imine bond offers multiple potential printing pathways, with any of the approaches proposed in **Figure 2.3** feasible. However, few examples exist of successful 3D bioprinting of imine-crosslinked hydrogels due to the fast hydrolysis of imines in aqueous conditions. Using a static mixing strategy, partially oxidized hyaluronic acid and carboxymethyl chitosan were loaded into separate syringes and extruded at a controlled rate through a static mixer (**Figure 2.4B**), facilitating homogeneous mixing between the precursors to rapidly (1-5 minutes gelation time) form imine crosslinks while exploiting the shear-thinning enabled by the reversible imine bond to ensure continuous printability[209]. Even in the context of the reversibility of imine bonds, the use of a static mixer to allow for good print quality without inducing crosslinking to a degree that could clog the nozzle limited the ultimate storage moduli of the printed hydrogels to 50-100 Pa; subsequent physical crosslinking by the formation of coordination complexes between hyaluronic acid and Fe (III) led to improved structural integrity and longer-term stability but required an additional processing step that reduces the net benefit of using the static mixer to generate a homogeneously crosslinked network in the first place[209].

In a recent study, the fast crosslinking of aldehyde hyaluronic acid and N-carboxymethyl chitosan (to form imide bonds) was combined with the slower crosslinking of gelatin and 4-arm poly(ethylene glycol) succinimidyl glutarate (PEG-SG) (to form amide bonds) to fabricate a dual-crosslinked hydrogel bioink using a pre-mixing strategy enabled by the slower amide formation rate and the high shear thinning of the dynamic imine crosslinks[24]. Using an EdU DNA incorporation assay, the percentage of EdU+ cells in the dual-crosslinked hydrogel construct was 44% on the ninth day (with a cell viability of 94%) compared to only 16% in calcium-crosslinked gelatin-alginate constructs. The relatively weak mechanical strength

(G'~100 Pa) allowed for good spreading of NIH/3T3 cells, and cells in tissue-like constructs demonstrated considerable cell-cell interconnections. However, even with the additional amide crosslinks (4% PEG-SG), the printed constructs fully degraded in less than two weeks.

2.6.3 Thiol-ene

Given the rapid nature of the thiol-ene reaction under UV irradiation, thiol-ene chemistry has been widely explored as the primary crosslinking mechanism for 3D bioprinting. For example, Xin *et al.* used thiol-ene click chemistry to crosslink PEG-norbornene and PEG-dithiol precursor polymers that were pre-mixed in a non-stoichiometric ratio to introduce excess norbornene groups (**Figure 2.4C**)[25]. Prior to exposure of the precursors to UV light, no gelation occurs, enabling facile pre-mixing of the reactive precursor polymers. The mixture was then electrosprayed in the presence of UV irradiation to form microgels that could subsequently be extruded at high concentrations to form "jammed" microgel structures with some degree of shape fixity. The PEG microgels contained unreacted norbornene groups that, upon addition of bis-thiol crosslinker and a photoinitiator, were further annealed using thiol-ene crosslinking to provide long-term stability. This strategy of pipetting additional crosslinker onto a partially-gelled hydrogel may allow pre-mixed bioinks to be printed without clogging the printer nozzle but is only viable in cases in which the partially-gelled structures have low viscosity and the crosslinker added can sufficiently penetrate the printed hydrogel structure; otherwise, highly heterogeneous networks would be formed. Such an approach also requires keeping printed cells out of media for a longer period of time, a potential challenge for maintaining high cytocompatibility. A second exposure of UV irradiation is subsequently used to increase the storage modulus from 1000 Pa to 1600 Pa while significantly improving the stability of the printed bioink against degradation/dissolution by improving the cohesion between the printed microgels[25]. Human mesenchymal stem cells (hMSC) were mixed with microgels 30 minutes prior to extrusion printing and maintained high viability (>90%) over 10 days following printing, suggesting that the microporosity of the microgel printed structures outweighs the potential negative effects of the higher shear forces to which cells are exposed during extrusion. Alginate functionalized with norbornene was similarly 3D printed to form bulk hydrogels using thiol-ene click chemistry. The bioink was pre-mixed and exposed to UV irradiation simultaneous to extrusion. Full gelation was observed within minutes, and storage moduli ranging from 500 Pa to 10000 Pa were achievable as the crosslinker density was increased[29]. Careful selection of the type of alkene used for the gelation can also improve 3D printing

outcomes. For example, mixing norbornene-functionalized carboxymethyl cellulose (NorCMC) and carbic(norbornene)-functionalized carboxymethyl cellulose (cCMC) enabled gelation within 5-120 seconds under UV exposure, with the NorCMC precursors (minimum gelation time ~5 seconds) gelling faster than the cCMC precursor (minimum gelation time ~18 seconds). Both CMC derivatives facilitated successful encapsulation of cells in the printed scaffolds, with cell viabilities >80% achieved for all formulations at all tested time points[212].

The combination of allyl-functionalized gelatin (GelAGE) with dithiothreitol[213] or 8-arm thiol-functionalized poly(ethylene glycol)[214] was also reported as a thiol-ene clickable bioink that offers a wider fabrication window than the conventional photocrosslinking of methacrylated gelatin. The commonly used UV photoinitiator I2959 was compared to an alternative system based on visible-light (Ru/SPS), with the visible light-based crosslinking approach demonstrating improved viability of co-printed human articular chondrocytes due to its decreased potential for DNA damage; indeed, while the extrusion-based 3D bioprinting was performed for the GelAGE at a sub-physiological temperature of 4-10℃, the chondrocyte-laden constructs could still promote long-term viability for up to three weeks. Bioink performance can be further enhanced using a sequential dual-step crosslinking approach, with a primary (light-free) crosslinking step driven by slow thiol-allyl interactions first conducted at 10℃ for 90 minutes (yielding a maximum complex viscosity of ~3%), a four-layered grid pattern printed, and then a secondary photocrosslinking process performed to stabilize the final construct[214]. Using this approach, both human articular chondrocytes and mesenchymal stem cells could be bioprinted with >80% viability maintained after 7 days.

Given the triggerable nature of thiol-ene crosslinking via UV exposure, thiol-ene chemistry has also been used to extrude pre-mixed hydrogels made using another chemistry method to subsequently stiffen the hydrogel through a second crosslinking step. Such an approach was demonstrated in the Wang *et al.* pre-mixed hydrazone bioink study previously discussed[23], where hyaluronic acid was also functionalized with norbornene that could be post-crosslinked using dithiol crosslinkers under UV light via a thiol-ene reaction. The double crosslinked networks showed a 300% increase in the hydrogel storage modulus, indicating that photo-stiffening serves as a potential means of enhancing scaffold mechanics.

2.6.4 Boronate Ester

Limited examples of the use of boronate ester bioinks have been reported to-date. The first report of the use of boronate esters for 3D hydrogel bioprinting was by Biswas et al., who described thixotropic, dynamic and self-healable G-quadruplex hydrogels based on guanosine and boronic acid[215]. Due to the non-physiological gelation temperature of this bioink (80℃, as required to solubilize the guanosine in a basic solution), hydrogels were fabricated using a pre-mixing approach prior to co-printing with adult human dermal fibroblast cells, with >90% cell viability maintained after 24 hours. To address the physiological relevant conditions during printing while still leveraging the dynamic nature of boronate esters, Amaral et al. recently reported a dynamic extrusion bioink comprising boronic-acid functionalized laminarin and alginate in which a combination of dynamic covalent boronate bonds with fast ionic post-printing gelation using calcium cations was demonstrated to provide suitable rheological properties for printing while maintaining high viabilities (>90%) of pre-osteoblastic cells, fibroblasts, and adenocarcinoma cells over a 14-day period[216]. The elastic moduli of these hydrogels over time were linked directly to the printed cell densities, with modulus drops of 1160 to 355 Pa and 92 to 21 Pa observed for high and low cell densities respectively over 7 days; this result is likely attributable to the exchange/screening of ionic crosslinks in the hydrogel under cell culture conditions over time. However, while the printed structures achieved are very weak, the highly dynamic nature of these bioinks does offer the potential to engineer adaptable biomechanical properties and biodegradability into the bioink while still maintaining sufficient structural support for the encapsulated cells.

2.6.5 CuAAC

Since CuAAC cannot proceed in the absence of the copper catalyst (at least not at a rate amenable to gelation) but proceeds quickly in the presence of a catalyst, the use of an embedded mixing strategy in which copper is only available in the support bath offers potential to enable 3D bioprinting. For example, Mohamed *et al.* functionalized carboxymethyl cellulose precursors with azide and alkyne groups, pre-mixed them homogeneously in a vortex, then extruded the mixture into a coagulant solution containing copper iodide and DMSO to facilitate gelation[217]. Due to the diffusion limitations of using a gelling bath approach to deliver the crosslinker or crosslinking catalyst (copper) into the bulk of the printed hydrogel, only weaker hydrogels (Young's moduli <10 kPa) were achieved[217]. However, relatively minimal cytotoxicity testing was performed in this work, with good results shown (<2% cytotoxicity)

but only at one tested concentration and without clearly identifying the copper concentration used for the cytotoxicity testing; as such concerns may still be present around the cell compatibility of this printing process. However, using a similar embedded mixing modality with other click chemistry pairs (i.e., at least one precursor in the printing syringe with the complementary precursor polymer and/or the catalyst for gelation present in the bath) may be a viable option for bioprinting non-thixotropic bioinks without requiring precise tuning of external devices or equipment.

2.6.6 SPAAC

The most advanced examples of 3D printing using click chemistry hydrogels exploit SPAAC as the primary crosslinking approach and leveraging an embedded mixing strategy to avoid the extrusion force challenges of pre-gelation, the *in-situ* clogging issues associated with the static mixer approach, and the inhomogeneous mixing associated with the other approaches. Hull *et al.* reported the fabrication of universal orthogonal network (UNION) bioinks by which bicyclononyne and azide functionalized polymers including hyaluronic acid, PEG, gelatin, and/or recombinant elastin-like protein (ELP) were printed using the FRESH bioprinting strategy[26]. One precursor was loaded into the syringe while the other precursor functionalized with the complementary group was added to the support bath (**Figure 2.4D**). When the bioink was extruded into the bath, the complementary precursors diffused into the printed structure, leading to crosslinking and gelation. The support bath was then melted away to leave behind the isolated, stiffened 3D construct. Using this crosslinking mechanism, hydrogels were fabricated with storage moduli ranging from 200 Pa to 10000 Pa, enabling the production of a scaffold with a broader range of mechanics than achievable with many other reported click bioinks but still with a limited upper window of mechanics relative to what is required to mimic the broadest possible range of biological tissues[26]. A major drawback of this method is that it requires long gelation times of up to one hour before the mechanics become sufficient such that the printed scaffold can self-support without the need for the gelation bath. This may be non-ideal for cell encapsulation since cells must be kept in non-physiological conditions for extended periods of time. In addition, the stability of the triazole bond formed via SPAAC limits the applications of such bioinks to permanent scaffolds that contain biodegradable polymer backbones, at least if non-degradable polymers are used[26]. However, the UNION printing approach does demonstrate the broad diversity of materials that can be printed using click chemistry approaches and, provided that the limitations presented in terms of gelation

times, mechanics, and degradation times can be resolved, represents an attractive strategy for overcoming the challenges of printing click chemistry-based bioinks.

Table 2.3: Reported click chemistry-based hydrogel bioinks for extrusion bioprinting applications

Click Chemistry	Polymer(s)	Mixing strategy	Embedded printing?	Gelation time	Mechanical Property	Ref
Hydrazone	Aldehyde + hydrazide hyaluronic acid	Pre-mixing	No	Immediate	G'_{max}: 500 – 6000 Pa Up to 3× enhancement after thiol-ene photostiffening	23
Hydrazone	Oxidized alginate (+ adipic acid dihydrazide)	Pre-mixing	No	~45 minutes	G'~ 200 Pa	210
Hydrazone/oxime	Oxidized alginate (+ dihydrazide + bishydroxlamine)	Pre-mixing	No	~6 min (oxime) ~ 20 min (hydrazone)	G' ~ 2500 Pa (hydrazone) G' ~250 Pa (oxime)	211
Thiol-ene	Norbornene + dithiol poly(ethylene glycol)	Pre-mixing, then pipetting crosslinker onto printed structures	No	Immediate upon exposure to UV light	G'_{max}: 1000 Pa (before photostiffening) 1600 Pa (after photostiffening)	25
Thiol-ene	Norbornene- alginate + dithiol poly(ethylene glycol)	Pre-mixing	No	1 – 4 min	G'_{max}: 50 – 10000Pa	29
Thiol-ene	Norbornene + thiol carboxymethyl cellulose	Pre-mixing	No	Within 3 hours in the absence of UV light 5 – 120s in the presence of UV light	G'_{max}: 3200-9300 Pa (cCMC) G'_{max}: 4600 – 8700 Pa (NorCMC)	212
Thiol-ene	Allylated gelatin (+ dithiothreitol or 8-arm thiol-functionalized poly(ethylene glycol))	Pre-mixing	No	N/A	Young's modulus ~ 50,000-100,000 Pa	213, 214
CuAAC	Azido-hydroxyethyl cellulose + propargyl carboxymethyl cellulose + copper (I) catalyst	Pre-mixing	Yes	N/A	E: ~0.001 kg/mm^2	217
Imine	Carboxymethyl chitosan + Hyaluronic acid	Static mixer	No	0.9 – 4.7 min	G'_{max}: <1 – 10 Pa Requires post-print stabilization with Fe (III)	209

SPAAC	Several polymers (gelatin, hyaluronic acid, ELP, and PEG all demonstrated)	Passive diffusion of crosslinkers post-printing	Yes	5-10 min	G'_{max}: 200 – 10000 Pa	[26]
Boronate ester	Boronic acid/guanosine self-assembled into a G-quadruplex	Pre-mixing	No	5 min	G' ~ 100-850 Pa	[215]
Boronate ester	Boronic acid functionalized laminarin + alginate	Pre-mixing	No	N/A	G' ~ 12,000 Pa	[216]

2.7 Conclusions and Future Perspectives

Click chemistry hydrogel bioinks offer several key advantages over conventional hydrogel bioinks strategies, including access to a wider range of mechanics, the avoidance of cytotoxic crosslinking agents (i.e., facilitating gelation at room or physiological temperature typically without the need for externally irradiation or templates), the capacity to tune the scaffold degradation rate based on the environment-specific degradation of the crosslink, and the potential of many click chemistry methods to dynamically rearrange to mimic the dynamic nature of native tissues.

While this review has illustrated these advantages and the diverse uses of click chemistry hydrogels in tissue engineering applications, there remains a significant gap to exploit these advantages in practical extrusion bioprinting to afford commercialization of the bioink platform. Commercial printers have been primarily designed to support the more conventional crosslinking strategies, in particular direct extrusion/shear thinning or photo-crosslinking (the latter by integrating a UV light source within the printer). As such, outside of perhaps thiol-ene chemistry, these printers have limited flexibility to print click chemistry bioinks that require direct contact between two (or more) precursor bioinks and/or mixing to occur for fabricating a homogeneously crosslinked construct. To overcome this limitation, customized printers are becoming increasingly popular to accommodate this mixing requirement. However, the effects of mixing on the mechanical properties, crosslink density, polymer distribution, stability, and resolution of the printed hydrogel bioink have not been extensively studied despite the critical importance of such factors in regulating the shape fixity/stability of the scaffold and the responses of cells to the scaffold. As such, the development of both improved mixing strategies as well as a better understanding of the mixing dynamics and fluid mechanics associated with different printer geometries are essential to better exploit the use of rapid-gelling click chemistry-based bioinks that to-date have largely resulted in heterogeneous prints or nozzle clogging challenges over time. In addition, there is significant future potential to exploit the “mix-and-match” nature of click chemistry that enables facile integration of very different materials functionalized with the same click functional groups into a single crosslinked hydrogel that better mimic the complex composition of the extracellular matrix; such mixed bioinks can be challenging to make using physically-crosslinked bioinks given that additives typically interfere with the chosen mechanism of physical crosslinking and thus the presence of additives significantly reduces the mechanical strength achievable with the printed

constructs. Furthermore, by controlling the mixing of the precursor components to introduce multi-dimensional structuring and/or localized chemical versatility tunability for specific applications (i.e., incorporating covalently linked ligands, cell-adhesive components, fluorophores, and/or nanoparticle components), bioinks of different mechanics, chemical moieties, and cellular components can be systematically designed to meet the requirements of mimicking a vast range of tissues for drug testing and future tissue replacement strategies.

2.8 Acknowledgements

We gratefully acknowledge the NSERC Discovery Grant (RGPIN-2017-06455) for the funding.

2.9 References

1. Chimene, D.; Kaunas, R.; Gaharwar, A. K., Hydrogel Bioink Reinforcement for Additive Manufacturing: A Focused Review of Emerging Strategies. *Adv. Mater.* **2020,** *32* (1), e1902026.
2. Decante, G.; Costa, J. B.; Silva-Correia, J.; Collins, M. N.; Reis, R. L.; Oliveira, J. M., Engineering bioinks for 3D bioprinting. *Biofabrication* **2021,** *13* (3), 032001.
3. GhavamiNejad, A.; Ashammakhi, N.; Wu, X. Y.; Khademhosseini, A., Crosslinking Strategies for 3D Bioprinting of Polymeric Hydrogels. *Small* **2020,** *16* (35), e2002931.
4. Gungor-Ozkerim, P. S.; Inci, I.; Zhang, Y. S.; Khademhosseini, A.; Dokmeci, M. R., Bioinks for 3D bioprinting: an overview. *Biomater. Sci.* **2018,** *6* (5), 915-946.
5. Bertassoni, L. E.; Cecconi, M.; Manoharan, V.; Nikkhah, M.; Hjortnaes, J.; Cristino, A. L.; Barabaschi, G.; Demarchi, D.; Dokmeci, M. R.; Yang, Y.; Khademhosseini, A., Hydrogel bioprinted microchannel networks for vascularization of tissue engineering constructs. *Lab Chip* **2014,** *14* (13), 2202-11.
6. Gopinathan, J.; Noh, I., Click Chemistry-Based Injectable Hydrogels and Bioprinting Inks for Tissue Engineering Applications. *Tissue Eng. Regen. Med.* **2018,** *15* (5), 531-546.
7. Li, J.; Chen, M.; Fan, X.; Zhou, H., Recent advances in bioprinting techniques: approaches, applications and future prospects. *J. Transl. Med.* **2016,** *14*, 271.
8. Morgan, F. L. C.; Moroni, L.; Baker, M. B., Dynamic Bioinks to Advance Bioprinting. *Adv. Healthc. Mater.* **2020,** *9* (15), e1901798.
9. Skardal, A.; Atala, A., Biomaterials for integration with 3-D bioprinting. *Ann. Biomed. Eng.* **2015,** *43* (3), 730-46.
10. Ozbolat, I. T.; Hospodiuk, M., Current advances and future perspectives in extrusion-based bioprinting. *Biomaterials* **2016,** *76*, 321-43.
11. Ying, G.; Jiang, N.; Yu, C.; Zhang, Y. S., Three-dimensional bioprinting of gelatin methacryloyl (GelMA). *Bio. Des. Manuf.* **2018,** *1* (4), 215-224.
12. Frost, B. A.; Sutliff, B. P.; Thayer, P.; Bortner, M. J.; Foster, E. J., Gradient Poly(ethylene glycol) Diacrylate and Cellulose Nanocrystals Tissue Engineering Composite Scaffolds via Extrusion Bioprinting. *Front. Bioeng. Biotechnol.* **2019,** *7*, 280.
13. Osidak, E. O.; Kozhukhov, V. I.; Osidak, M. S.; Domogatsky, S. P., Collagen as Bioink for Bioprinting: A Comprehensive Review. *Int. J. Bioprint.* **2020,** *6* (3), 270-270.
14. Ouyang, L.; Armstrong, J. P. K.; Lin, Y.; Wojciechowski, J. P.; Lee-Reeves, C.; Hachim, D.; Zhou, K.; Burdick, J. A.; Stevens, M. M., Expanding and optimizing 3D bioprinting capabilities using complementary network bioinks. *Sci. Adv.* **2020,** *6* (38), eabc5529.
15. Müller, M.; Becher, J.; Schnabelrauch, M.; Zenobi-Wong, M., Nanostructured Pluronic hydrogels as bioinks for 3D bioprinting. *Biofabrication* **2015,** *7* (3), 035006.
16. Murphy, S. V.; Atala, A., 3D bioprinting of tissues and organs. *Nat. Biotechnol.* **2014,** *32* (8), 773-85.
17. Zhang, Y. S.; Yue, K.; Aleman, J.; Moghaddam, K. M.; Bakht, S. M.; Yang, J.; Jia, W.; Dell'Erba, V.; Assawes, P.; Shin, S. R.; Dokmeci, M. R.; Oklu, R.; Khademhosseini, A., 3D Bioprinting for Tissue and Organ Fabrication. *Ann. Biomed. Eng.* **2017,** *45* (1), 148-163.

18. Noh, I.; Kim, N.; Tran, H. N.; Lee, J.; Lee, C., 3D printable hyaluronic acid-based hydrogel for its potential application as a bioink in tissue engineering. *Biomater. Res.* **2019,** *23* (1), 3.
19. Burdick, J. A.; Prestwich, G. D., Hyaluronic acid hydrogels for biomedical applications. *Adv. Mater.* **2011,** *23* (12), H41-56.
20. Kolb, H. C.; Finn, M.; Sharpless, K. B., Click chemistry: diverse chemical function from a few good reactions. *Angew. Chem. Int. Ed.* **2001,** *40* (11), 2004-2021.
21. Zou, Y.; Zhang, L.; Yang, L.; Zhu, F.; Ding, M.; Lin, F.; Wang, Z.; Li, Y., "Click" chemistry in polymeric scaffolds: Bioactive materials for tissue engineering. *J. Control. Release.* **2018,** *273*, 160-179.
22. Madl, C. M.; Heilshorn, S. C., Bioorthogonal strategies for engineering extracellular matrices. *Adv. Funct. Mater.* **2018,** *28* (11), 1706046.
23. Wang, L. L.; Highley, C. B.; Yeh, Y. C.; Galarraga, J. H.; Uman, S.; Burdick, J. A., Three-dimensional extrusion bioprinting of single- and double-network hydrogels containing dynamic covalent crosslinks. *J. Biomed. Mater. Res. A* **2018,** *106* (4), 865-875.
24. Chen, H.; Fei, F.; Li, X.; Nie, Z.; Zhou, D.; Liu, L.; Zhang, J.; Zhang, H.; Fei, Z.; Xu, T., A structure-supporting, self-healing, and high permeating hydrogel bioink for establishment of diverse homogeneous tissue-like constructs. *Bioact. Mater.* **2021,** *6* (10), 3580-3595.
25. Xin, S.; Chimene, D.; Garza, J. E.; Gaharwar, A. K.; Alge, D. L., Clickable PEG hydrogel microspheres as building blocks for 3D bioprinting. *Biomater. Sci.* **2019,** *7* (3), 1179-1187.
26. Hull, S. M.; Lindsay, C. D.; Brunel, L. G.; Shiwarski, D. J.; Tashman, J. W.; Roth, J. G.; Myung, D.; Feinberg, A. W.; Heilshorn, S. C., 3D Bioprinting using UNIversal Orthogonal Network (UNION) Bioinks. *Adv. Funct. Mater.* **2021,** *31* (7), 2007983.
27. Figueiredo, T.; Jing, J.; Jeacomine, I.; Olsson, J.; Gerfaud, T.; Boiteau, J.-G.; Rome, C.; Harris, C.; Auzély-Velty, R., Injectable Self-Healing Hydrogels Based on Boronate Ester Formation between Hyaluronic Acid Partners Modified with Benzoxaborin Derivatives and Saccharides. *Biomacromol.* **2020,** *21* (1), 230-239.
28. Knowlton, S.; Yenilmez, B.; Anand, S.; Tasoglu, S., Photocrosslinking-based bioprinting: Examining crosslinking schemes. *Bioprinting* **2017,** *5*, 10-18.
29. Ooi, H. W.; Mota, C.; ten Cate, A. T.; Calore, A.; Moroni, L.; Baker, M. B., Thiol–Ene Alginate Hydrogels as Versatile Bioinks for Bioprinting. *Biomacromol.* **2018,** *19* (8), 3390-3400.
30. Zhou, Q.; Kang, H.; Bielec, M.; Wu, X.; Cheng, Q.; Wei, W.; Dai, H., Influence of different divalent ions cross-linking sodium alginate-polyacrylamide hydrogels on antibacterial properties and wound healing. *Carbohydr. Polym.* **2018,** *197*, 292-304.
31. Brus, J.; Urbanova, M.; Czernek, J.; Pavelkova, M.; Kubova, K.; Vyslouzil, J.; Abbrent, S.; Konefal, R.; Horsky, J.; Vetchy, D.; Vyslouzil, J.; Kulich, P., Structure and Dynamics of Alginate Gels Cross-Linked by Polyvalent Ions Probed via Solid State NMR Spectroscopy. *Biomacromol.* **2017,** *18* (8), 2478-2488.
32. Gwon, S. H.; Yoon, J.; Seok, H. K.; Oh, K. H.; Sun, J.-Y., Gelation dynamics of ionically crosslinked alginate gel with various cations. *Macromol. Res.* **2015,** *23* (12), 1112-1116.
33. Magami, S. M.; Williams, R. L., Gelation via cationic chelation/crosslinking of acrylic-acid-based polymers. *Polym. Inter.* **2019,** *68* (12), 1980-1991.
34. Kuo, C. K.; Ma, P. X., Ionically crosslinked alginate hydrogels as scaffolds for tissue engineering: Part 1. Structure, gelation rate and mechanical properties. *Biomaterials* **2001,** *22* (6), 511-521.

35. Dodero, A.; Pianella, L.; Vicini, S.; Alloisio, M.; Ottonelli, M.; Castellano, M., Alginate-based hydrogels prepared via ionic gelation: An experimental design approach to predict the crosslinking degree. *Eur. Polym. J.* **2019,** *118*, 586-594.
36. Chimene, D.; Lennox, K. K.; Kaunas, R. R.; Gaharwar, A. K., Advanced Bioinks for 3D Printing: A Materials Science Perspective. *Ann. Biomed. Eng.* **2016,** *44* (6), 2090-102.
37. Suzuki, Y.; Nishimura, Y.; Tanihara, M.; Suzuki, K.; Nakamura, T.; Shimizu, Y.; Yamawaki, Y.; Kakimaru, Y., Evaluation of a novel alginate gel dressing: cytotoxicity to fibroblasts in vitro and foreign-body reaction in pig skin in vivo. *J. Biomed. Mater. Res.* **1998,** *39* (2), 317-22.
38. Lee, K. Y.; Mooney, D. J., Alginate: properties and biomedical applications. *Prog. Polym. Sci.* **2012,** *37* (1), 106-126.
39. Pereira, R. F.; Bártolo, P. J., 3D bioprinting of photocrosslinkable hydrogel constructs. *J. App. Polym. Sci.* **2015,** *132* (48), 42458.
40. Hong, J.; Shin, Y.; Kim, S.; Lee, J.; Cha, C., Complex Tuning of Physical Properties of Hyperbranched Polyglycerol-Based Bioink for Microfabrication of Cell-Laden Hydrogels. *Adv. Funct. Mater.* **2019,** *29* (13), 1808750.
41. Zhou, Y.; Liang, K.; Zhao, S.; Zhang, C.; Li, J.; Yang, H.; Liu, X.; Yin, X.; Chen, D.; Xu, W.; Xiao, P., Photopolymerized maleilated chitosan/methacrylated silk fibroin micro/nanocomposite hydrogels as potential scaffolds for cartilage tissue engineering. *Int. J. Biol. Macromol.* **2018,** *108*, 383-390.
42. Ouyang, L.; Highley, C. B.; Sun, W.; Burdick, J. A., A Generalizable Strategy for the 3D Bioprinting of Hydrogels from Nonviscous Photo-crosslinkable Inks. *Adv. Mater.* **2017,** *29* (8), 1604983.
43. Rutz, A. L.; Hyland, K. E.; Jakus, A. E.; Burghardt, W. R.; Shah, R. N., A multimaterial bioink method for 3D printing tunable, cell-compatible hydrogels. *Adv. Mater.* **2015,** *27* (9), 1607-14.
44. Ouyang, L.; Highley, C. B.; Rodell, C. B.; Sun, W.; Burdick, J. A., 3D Printing of Shear-Thinning Hyaluronic Acid Hydrogels with Secondary Cross-Linking. *Biomater. Sci. Eng.* **2016,** *2* (10), 1743-1751.
45. Chen, N.; Zhu, K.; Zhang, Y. S.; Yan, S.; Pan, T.; Abudupataer, M.; Yu, G.; Alam, M. F.; Wang, L.; Sun, X.; Yu, Y.; Wang, C.; Zhang, W., Hydrogel Bioink with Multilayered Interfaces Improves Dispersibility of Encapsulated Cells in Extrusion Bioprinting. *Appl. Mater. Interfaces* **2019,** *11* (34), 30585-30595.
46. Wei, S. M.; Pei, M. Y.; Pan, W. L.; Thissen, H.; Tsai, S. W., Gelatin Hydrogels Reinforced by Absorbable Nanoparticles and Fibrils Cured In Situ by Visible Light for Tissue Adhesive Applications. *Polym.* **2020,** *12* (5), 1113.
47. Galarraga, J. H.; Kwon, M. Y.; Burdick, J. A., 3D bioprinting via an in situ crosslinking technique towards engineering cartilage tissue. *Sci. Rep.* **2019,** *9* (1), 19987.
48. Ying, G. L.; Jiang, N.; Maharjan, S.; Yin, Y. X.; Chai, R. R.; Cao, X.; Yang, J. Z.; Miri, A. K.; Hassan, S.; Zhang, Y. S., Aqueous Two-Phase Emulsion Bioink-Enabled 3D Bioprinting of Porous Hydrogels. *Adv. Mater.* **2018,** *30* (50), e1805460.
49. Choi, G.; Cha, H. J., Recent advances in the development of nature-derived photocrosslinkable biomaterials for 3D printing in tissue engineering. *Biomater. Res.* **2019,** *23*(1), 1-7.
50. Zhao, D.; Tie, C.; Cheng, B.; Yang, S.; Wang, X.; Sun, Z.; Yin, M.; Zhu, H.; Yin, M., Effect of altering photocrosslinking conditions on the physical properties of alginate gels and the survival of photoencapsulated cells. *Polym. Degrad. Stab.* **2020,** *179*, 109297.

51. Ruskowitz, E. R.; DeForest, C. A., Proteome-wide analysis of cellular response to ultraviolet light for biomaterial synthesis and modification. *Biomater. Sci. Eng.* **2019,** *5* (5), 2111-2116.
52. Suntornnond, R.; An, J.; Chua, C. K., Bioprinting of Thermoresponsive Hydrogels for Next Generation Tissue Engineering: A Review. *Macromol. Mater. Eng.* **2017,** *302* (1), 1600266.
53. Fitzsimmons, R. E. B.; Aquilino, M. S.; Quigley, J.; Chebotarev, O.; Tarlan, F.; Simmons, C. A., Generating vascular channels within hydrogel constructs using an economical open-source 3D bioprinter and thermoreversible gels. *Bioprinting* **2018,** *9*, 7-18.
54. Yin, J.; Yan, M.; Wang, Y.; Fu, J.; Suo, H., 3D Bioprinting of Low-Concentration Cell-Laden Gelatin Methacrylate (GelMA) Bioinks with a Two-Step Cross-linking Strategy. *Appl. Mater. Interf.* **2018,** *10* (8), 6849-6857.
55. Murugan, S. S.; Anil, S.; Sivakumar, P.; Shim, M. S.; Venkatesan, J., 3D-Printed Chitosan Composites for Biomedical Applications. *Adv. Polym. Sci.* **2021**, 288, 87-116.
56. Contessi Negrini, N.; Bonetti, L.; Contili, L.; Farè, S., 3D printing of methylcellulose-based hydrogels. *Bioprinting* **2018,** *10*, e00024.
57. Drzewiecki, K. E.; Malavade, J. N.; Ahmed, I.; Lowe, C. J.; Shreiber, D. I., A thermoreversible, photocrosslinkable collagen bio-ink for free-form fabrication of scaffolds for regenerative medicine. *Technology* **2017,** *5* (4), 185-195.
58. Hsieh, C. T.; Hsu, S. H., Double-Network Polyurethane-Gelatin Hydrogel with Tunable Modulus for High-Resolution 3D Bioprinting. *Appl. Mater. Interfac.* **2019,** *11* (36), 32746-32757.
59. Donderwinkel, I.; van Hest, J. C. M.; Cameron, N. R., Bio-inks for 3D bioprinting: recent advances and future prospects. *Polym. Chem.* **2017,** *8* (31), 4451-4471.
60. Kang, H. W.; Lee, S. J.; Ko, I. K.; Kengla, C.; Yoo, J. J.; Atala, A., A 3D bioprinting system to produce human-scale tissue constructs with structural integrity. *Nat. Biotech.* **2016,** *34* (3), 312-9.
61. Celikkin, N.; Simó Padial, J.; Costantini, M.; Hendrikse, H.; Cohn, R.; Wilson, C. J.; Rowan, A. E.; Święszkowski, W., 3D Printing of Thermoresponsive Polyisocyanide (PIC) Hydrogels as Bioink and Fugitive Material for Tissue Engineering. *Polymers* **2018,** *10* (5), 555.
62. Zhang, J.; Yun, S.; Karami, A.; Jing, B.; Zannettino, A.; Du, Y.; Zhang, H., 3D printing of a thermosensitive hydrogel for skin tissue engineering: A proof of concept study. *Bioprinting* **2020,** *19*, e00089.
63. Shamma, R. N.; Sayed, R. H.; Madry, H.; El Sayed, N. S.; Cucchiarini, M., Triblock Copolymer Bioinks in Hydrogel Three-Dimensional Printing for Regenerative Medicine: A Focus on Pluronic F127. *Tiss. Eng. Part B Rev.* **2021**, *28 (2),* 451-463.
64. Pluronic F127 as a Cell Encapsulation Material: Utilization of Membrane-Stabilizing Agents. *Tiss. Eng.* **2005,** *11* (5-6), 974-983.
65. Jeon, O.; Bin Lee, Y.; Hinton, T. J.; Feinberg, A. W.; Alsberg, E., Cryopreserved cell-laden alginate microgel bioink for 3D bioprinting of living tissues. *Mater. Today Chem.* **2019,** *12*, 61-70.
66. Dubbin, K.; Hori, Y.; Lewis, K. K.; Heilshorn, S. C., Dual-Stage Crosslinking of a Gel-Phase Bioink Improves Cell Viability and Homogeneity for 3D Bioprinting. *Adv. Healthc. Mater.* **2016,** *5* (19), 2488-2492.
67. Chimene, D.; Peak, C. W.; Gentry, J. L.; Carrow, J. K.; Cross, L. M.; Mondragon, E.; Cardoso, G. B.; Kaunas, R.; Gaharwar, A. K., Nanoengineered Ionic-Covalent Entanglement (NICE) Bioinks for 3D Bioprinting. *Appl. Mater. Interfac.* **2018,** *10* (12), 9957-9968.

68. Hull, S. M.; Brunel, L. G.; Heilshorn, S. C., 3D Bioprinting of Cell-Laden Hydrogels for Improved Biological Functionality. *Adv. Mater.* **2021**, 2103691.
69. Kim, E.; Seok, J. M.; Bae, S. B.; Park, S. A.; Park, W. H., Silk Fibroin Enhances Cytocompatibilty and Dimensional Stability of Alginate Hydrogels for Light-Based Three-Dimensional Bioprinting. *Biomacromol.* **2021,** *22* (5), 1921-1931.
70. Shin, M.; Galarraga, J. H.; Kwon, M. Y.; Lee, H.; Burdick, J. A., Gallol-derived ECM-mimetic adhesive bioinks exhibiting temporal shear-thinning and stabilization behavior. *Acta Biomater.* **2019,** *95*, 165-175.
71. Rastin, H.; Ramezanpour, M.; Hassan, K.; Mazinani, A.; Tung, T. T.; Vreugde, S.; Losic, D., 3D bioprinting of a cell-laden antibacterial polysaccharide hydrogel composite. *Carbohydr. Polym.* **2021,** *264*, 117989.
72. Roehm, K. D.; Madihally, S. V., Bioprinted chitosan-gelatin thermosensitive hydrogels using an inexpensive 3D printer. *Biofabrication* **2017,** *10* (1), 015002.
73. Cochis, A.; Bonetti, L.; Sorrentino, R.; Contessi Negrini, N.; Grassi, F.; Leigheb, M.; Rimondini, L.; Fare, S., 3D Printing of Thermo-Responsive Methylcellulose Hydrogels for Cell-Sheet Engineering. *Materials* **2018,** *11* (4), 579.
74. Ku, J.; Seonwoo, H.; Park, S.; Jang, K.-J.; Lee, J.; Lee, M.; Lim, J. W.; Kim, J.; Chung, J. H., Cell-Laden Thermosensitive Chitosan Hydrogel Bioinks for 3D Bioprinting Applications. *Appl. Sc.* **2020,** *10* (7), 2455.
75. Kondiah, P. J.; Kondiah, P. P. D.; Choonara, Y. E.; Marimuthu, T.; Pillay, V., A 3D Bioprinted Pseudo-Bone Drug Delivery Scaffold for Bone Tissue Engineering. *Pharmaceutics* **2020,** *12* (2), 166.
76. Hu, C.; Hahn, L.; Yang, M.; Altmann, A.; Stahlhut, P.; Groll, J.; Luxenhofer, R., Improving printability of a thermoresponsive hydrogel biomaterial ink by nanoclay addition. *J. Mater. Sci.* **2021,** *56* (1), 691-705.
77. Castro, V.; Rodriguez, H.; Albericio, F., CuAAC: An Efficient Click Chemistry Reaction on Solid Phase. *Comb. Sci.* **2016,** *18* (1), 1-14.
78. Hein, J. E.; Fokin, V. V., Copper-catalyzed azide-alkyne cycloaddition (CuAAC) and beyond: new reactivity of copper(I) acetylides. *Chem. Soc. Rev.* **2010,** *39* (4), 1302-15.
79. Ying, G.; Jiang, N.; Parra-Cantu, C.; Tang, G.; Zhang, J.; Wang, H.; Chen, S.; Huang, N.-P.; Xie, J.; Zhang, Y. S., Bioprinted Injectable Hierarchically Porous Gelatin Methacryloyl Hydrogel Constructs with Shape-Memory Properties. *Adv. Funct. Mater.* **2020,** *30* (46), 2003740.
80. Chen, R. T.; Marchesan, S.; Evans, R. A.; Styan, K. E.; Such, G. K.; Postma, A.; McLean, K. M.; Muir, B. W.; Caruso, F., Photoinitiated alkyne-azide click and radical cross-linking reactions for the patterning of PEG hydrogels. *Biomacromol.* **2012,** *13* (3), 889-95.
81. Koschella, A.; Hartlieb, M.; Heinze, T., A "click-chemistry" approach to cellulose-based hydrogels. *Carbohyd. Polym.* **2011,** *86* (1), 154-161.
82. Sun, Z.; Liu, S.; Li, K.; Tan, L.; Cen, L.; Fu, G., Well-defined and biocompatible hydrogels with toughening and reversible photoresponsive properties. *Soft Mat.* **2016,** *12* (7), 2192-9.
83. Zhai, W.; Chapin, B. M.; Yoshizawa, A.; Wang, H.-C.; Hodge, S. A.; James, T. D.; Anslyn, E. V.; Fossey, J. S., "Click-fluors": triazole-linked saccharide sensors. *Org. Chem. Front.* **2016,** *3* (8), 918-928.
84. Piluso, S.; Vukićević, R.; Nöchel, U.; Braune, S.; Lendlein, A.; Neffe, A. T., Sequential alkyne-azide cycloadditions for functionalized gelatin hydrogel formation. *Eur. Polym. J.* **2018,** *100*, 77-85.

85. Yigit, S.; Sanyal, R.; Sanyal, A., Fabrication and Functionalization of Hydrogels through "Click" Chemistry. *Chem. Asian J.* **2011,** *6* (10), 2648-2659.
86. Pickens, C. J.; Johnson, S. N.; Pressnall, M. M.; Leon, M. A.; Berkland, C. J., Practical Considerations, Challenges, and Limitations of Bioconjugation via Azide-Alkyne Cycloaddition. *Bioconjug. Chem.* **2018,** *29* (3), 686-701.
87. Agard, N. J.; Prescher, J. A.; Bertozzi, C. R., A strain-promoted [3 + 2] azide-alkyne cycloaddition for covalent modification of biomolecules in living systems. *J. Am. Chem. Soc.* **2004,** *126* (46), 15046-7.
88. Lang, K.; Chin, J. W., Bioorthogonal Reactions for Labeling Proteins. *Chem. Bio.* **2014,** *9* (1), 16-20.
89. Han, S.-S.; Yoon, H. Y.; Yhee, J. Y.; Cho, M. O.; Shim, H.-E.; Jeong, J.-E.; Lee, D.-E.; Kim, K.; Guim, H.; Lee, J. H.; Huh, K. M.; Kang, S.-W., In situ cross-linkable hyaluronic acid hydrogels using copper free click chemistry for cartilage tissue engineering. *Polym. Chem.* **2018,** *9* (1), 20-27.
90. Fan, M.; Ma, Y.; Mao, J.; Zhang, Z.; Tan, H., Cytocompatible in situ forming chitosan/hyaluronan hydrogels via a metal-free click chemistry for soft tissue engineering. *Acta Biomater.* **2015,** *20*, 60-68.
91. Hodgson, S. M.; McNelles, S. A.; Abdullahu, L.; Marozas, I. A.; Anseth, K. S.; Adronov, A., Reproducible Dendronized PEG Hydrogels via SPAAC Cross-Linking. *Biomacromol.* **2017,** *18* (12), 4054-4059.
92. Zhan, H.; Jiang, S.; Jonker, A. M.; Pijpers, I. A. B.; Lowik, D., Self-recovering dual cross-linked hydrogels based on bioorthogonal click chemistry and ionic interactions. *J. Mater. Chem. B* **2020,** *8* (27), 5912-5920.
93. Brown, T. E.; Silver, J. S.; Worrell, B. T.; Marozas, I. A.; Yavitt, F. M.; Gunay, K. A.; Bowman, C. N.; Anseth, K. S., Secondary Photocrosslinking of Click Hydrogels To Probe Myoblast Mechanotransduction in Three Dimensions. *J. Am. Chem. Soc.* **2018,** *140* (37), 11585-11588.
94. Xu, J.; Filion, T. M.; Prifti, F.; Song, J., Cytocompatible poly(ethylene glycol)-co-polycarbonate hydrogels cross-linked by copper-free, strain-promoted click chemistry. *Chem. Asian J.* **2011,** *6* (10), 2730-2737.
95. DeForest, C. A.; Anseth, K. S., Cytocompatible click-based hydrogels with dynamically tunable properties through orthogonal photoconjugation and photocleavage reactions. *Nat. Chem.* **2011,** *3* (12), 925-931.
96. Fu, S.; Dong, H.; Deng, X.; Zhuo, R.; Zhong, Z., Injectable hyaluronic acid/poly(ethylene glycol) hydrogels crosslinked via strain-promoted azide-alkyne cycloaddition click reaction. *Carbohydr. Polym.* **2017,** *169*, 332-340.
97. Wang, G.; Zhu, J.; Chen, X.; Dong, H.; Li, Q.; Zeng, L.; Cao, X., Alginate based antimicrobial hydrogels formed by integrating Diels–Alder "click chemistry" and the thiol–ene reaction. *RSC Adv.* **2018,** *8* (20), 11036-11042.
98. Guaresti, O.; García–Astrain, C.; Aguirresarobe, R. H.; Eceiza, A.; Gabilondo, N., Synthesis of stimuli–responsive chitosan–based hydrogels by Diels–Alder cross–linking `click´ reaction as potential carriers for drug administration. *Carbohyd. Polym.* **2018,** *183*, 278-286.
99. Smith, L. J.; Taimoory, S. M.; Tam, R. Y.; Baker, A. E. G.; Binth Mohammad, N.; Trant, J. F.; Shoichet, M. S., Diels-Alder Click-Cross-Linked Hydrogels with Increased Reactivity Enable 3D Cell Encapsulation. *Biomacromol.* **2018,** *19* (3), 926-935.
100. Liu, Y.; Zhou, C.; Sun, Y., A biomimetic strategy for controllable degradation of chitosan scaffolds. *J. Mater. Res.* **2012,** *27* (14), 1859-1868.

101. Kirchhof, S.; Brandl, F. P.; Hammer, N.; Goepferich, A. M., Investigation of the Diels–Alder reaction as a cross-linking mechanism for degradable poly(ethylene glycol) based hydrogels. *J. Mater. Chem. B* **2013,** *1* (37), 4855-4864.
102. Nimmo, C. M.; Owen, S. C.; Shoichet, M. S., Diels-Alder Click cross-linked hyaluronic acid hydrogels for tissue engineering. *Biomacromol.* **2011,** *12* (3), 824-30.
103. Abandansari, H. S.; Ghanian, M. H.; Varzideh, F.; Mahmoudi, E.; Rajabi, S.; Taheri, P.; Nabid, M. R.; Baharvand, H., In situ formation of interpenetrating polymer network using sequential thermal and click crosslinking for enhanced retention of transplanted cells. *Biomaterials* **2018,** *170*, 12-25.
104. Oliveira, B.; Guo, Z.; Bernardes, G., Inverse electron demand Diels–Alder reactions in chemical biology. *Chem. Soc. Rev.* **2017,** *46* (16), 4895-4950.
105. Blackman, M. L.; Royzen, M.; Fox, J. M., Tetrazine ligation: fast bioconjugation based on inverse-electron-demand Diels− Alder reactivity. *J. Amer. Chem. Soc.* **2008,** *130* (41), 13518-13519.
106. Alge, D. L.; Azagarsamy, M. A.; Donohue, D. F.; Anseth, K. S., Synthetically tractable click hydrogels for three-dimensional cell culture formed using tetrazine–norbornene chemistry. *Biomacromol.* **2013,** *14* (4), 949-953.
107. Desai, R. M.; Koshy, S. T.; Hilderbrand, S. A.; Mooney, D. J.; Joshi, N. S., Versatile click alginate hydrogels crosslinked via tetrazine–norbornene chemistry. *Biomaterials* **2015,** *50*, 30-37.
108. Haiber, L. M.; Kufleitner, M.; Wittmann, V., Application of the Inverse-Electron-Demand Diels-Alder Reaction for Metabolic Glycoengineering. *Front. Chem.* **2021,** *9*.
109. Pagel, M., Inverse electron demand Diels–Alder (IEDDA) reactions in peptide chemistry. *J. Pept. Sci.* **2019,** *25* (1), e3141.
110. Handula, M.; Chen, K.-T.; Seimbille, Y., IEDDA: An Attractive Bioorthogonal Reaction for Biomedical Applications. *Molecules* **2021,** *26* (15), 4640.
111. Delplace, V.; Pickering, A. J.; Hettiaratchi, M. H.; Zhao, S.; Kivijärvi, T.; Shoichet, M. S., Inverse electron-demand diels–alder methylcellulose hydrogels enable the Co-delivery of chondroitinase ABC and neural progenitor cells. *Biomacromol.* **2020,** *21* (6), 2421-2431.
112. Xu, Z.; Bratlie, K. M., Click Chemistry and Material Selection for in Situ Fabrication of Hydrogels in Tissue Engineering Applications. *Biomater. Sci. Eng.* **2018,** *4* (7), 2276-2291.
113. Lu, S.; Gao, C.; Xu, X.; Bai, X.; Duan, H.; Gao, N.; Feng, C.; Xiong, Y.; Liu, M., Injectable and Self-Healing Carbohydrate-Based Hydrogel for Cell Encapsulation. *Appl. Mater. Interfaces* **2015,** *7* (23), 13029-37.
114. Xu, J.; Liu, Y.; Hsu, S. H., Hydrogels Based on Schiff Base Linkages for Biomedical Applications. *Molecules* **2019,** *24* (16), 3005.
115. Uman, S.; Dhand, A.; Burdick, J. A., Recent advances in shear-thinning and self-healing hydrogels for biomedical applications. *J. Appl. Polym. Sci.* **2020,** *137* (25), 48668.
116. Li, L.; Wang, N.; Jin, X.; Deng, R.; Nie, S.; Sun, L.; Wu, Q.; Wei, Y.; Gong, C., Biodegradable and injectable in situ cross-linking chitosan-hyaluronic acid based hydrogels for postoperative adhesion prevention. *Biomaterials* **2014,** *35* (12), 3903-17.
117. Nguyen, N. T.; Nguyen, L. V.; Tran, N. M.; Nguyen, D. T.; Nguyen, T. N.; Tran, H. A.; Dang, N. N.; Vo, T. V.; Nguyen, T. H., The effect of oxidation degree and volume ratio of components on properties and applications of in situ cross-linking hydrogels based on chitosan and hyaluronic acid. *Mater. Sci. Eng.* **2019,** *103*, 109670.

118. Summonte, S.; Racaniello, G.; Lopedota, A.; Denora, N.; Bernkop-Schnürch, A., Thiolated polymeric hydrogels for biomedical application: Cross-linking mechanisms. *J. Contr. Rel.* **2020**, 330, 470-482.
119. Grover, G. N.; Lam, J.; Nguyen, T. H.; Segura, T.; Maynard, H. D., Biocompatible hydrogels by oxime Click chemistry. *Biomacromol.* **2012,** *13* (10), 3013-7.
120. Baker, A. E. G.; Cui, H.; Ballios, B. G.; Ing, S.; Yan, P.; Wolfer, J.; Wright, T.; Dang, M.; Gan, N. Y.; Cooke, M. J.; Ortín-Martínez, A.; Wallace, V. A.; van der Kooy, D.; Devenyi, R.; Shoichet, M. S., Stable oxime-crosslinked hyaluronan-based hydrogel as a biomimetic vitreous substitute. *Biomaterials* **2021,** *271*, 120750.
121. Sanchez-Moran, H.; Ahmadi, A.; Vogler, B.; Roh, K. H., Oxime Cross-Linked Alginate Hydrogels with Tunable Stress Relaxation. *Biomacromol.* **2019,** *20* (12), 4419-4429.
122. Kalia, J.; Raines, R. T., Hydrolytic stability of hydrazones and oximes. *Angew. Chem. Int. Ed.* **2008,** *47* (39), 7523-7526.
123. Hafeez, S.; Ooi, H. W.; Morgan, F. L. C.; Mota, C.; Dettin, M.; Van Blitterswijk, C.; Moroni, L.; Baker, M. B., Viscoelastic Oxidized Alginates with Reversible Imine Type Crosslinks: Self-Healing, Injectable, and Bioprintable Hydrogels. *Gels* **2018,** *4* (4).
124. Christman, K. L.; Broyer, R. M.; Schopf, E.; Kolodziej, C. M.; Chen, Y.; Maynard, H. D., Protein Nanopatterns by Oxime Bond Formation. *Langmuir* **2011,** *27* (4), 1415-1418.
125. Hardy, J. G.; Lin, P.; Schmidt, C. E., Biodegradable hydrogels composed of oxime crosslinked poly(ethylene glycol), hyaluronic acid and collagen: a tunable platform for soft tissue engineering. *J. Biomater. Sci. Polym. Ed.* **2015,** *26* (3), 143-61.
126. Larsen, D.; Kietrys, A. M.; Clark, S. A.; Park, H. S.; Ekebergh, A.; Kool, E. T., Exceptionally rapid oxime and hydrazone formation promoted by catalytic amine buffers with low toxicity. *Chem. Sci.* **2018,** *9* (23), 5252-5259.
127. Hozumi, T.; Kageyama, T.; Ohta, S.; Fukuda, J.; Ito, T., Injectable Hydrogel with Slow Degradability Composed of Gelatin and Hyaluronic Acid Cross-Linked by Schiff's Base Formation. *Biomacromol.* **2018,** *19* (2), 288-297.
128. Patenaude, M.; Campbell, S.; Kinio, D.; Hoare, T., Tuning Gelation Time and Morphology of Injectable Hydrogels Using Ketone–Hydrazide Cross-Linking. *Biomacromol.* **2014,** *15* (3), 781-790.
129. Xu, F.; Corbett, B.; Bell, S.; Zhang, C.; Budi Hartono, M.; Farsangi, Z. J.; MacGregor, J.; Hoare, T., High-Throughput Synthesis, Analysis, and Optimization of Injectable Hydrogels for Protein Delivery. *Biomacromol.* **2020,** *21* (1), 214-229.
130. Urosev, I.; Dorrington, H.; Muzzin, N.; Alsop, R.; Bakaic, E.; Gilbert, T.; Rheinstädter, M.; Hoare, T., Injectable Poly(oligoethylene glycol methacrylate)-Based Hydrogels Fabricated from Highly Branched Precursor Polymers: Controlling Gel Properties by Precursor Polymer Morphology. *Appl. Polym. Mater.* **2019,** *1* (3), 369-380.
131. Bakaic, E.; Smeets, N. M. B.; Badv, M.; Dodd, M.; Barrigar, O.; Siebers, E.; Lawlor, M.; Sheardown, H.; Hoare, T., Injectable and Degradable Poly(Oligoethylene glycol methacrylate) Hydrogels with Tunable Charge Densities as Adhesive Peptide-Free Cell Scaffolds. *Biomater. Sci. Eng.* **2018,** *4* (11), 3713-3725.
132. De France, K. J.; Yager, K. G.; Chan, K. J. W.; Corbett, B.; Cranston, E. D.; Hoare, T., Injectable Anisotropic Nanocomposite Hydrogels Direct in Situ Growth and Alignment of Myotubes. *Nano Lett.* **2017,** *17* (10), 6487-6495.
133. Karvinen, J.; Joki, T.; Ylä-Outinen, L.; Koivisto, J. T.; Narkilahti, S.; Kellomäki, M., Soft hydrazone crosslinked hyaluronan- and alginate-based hydrogels as 3D supportive

matrices for human pluripotent stem cell-derived neuronal cells. *React. Funct. Polym.* **2018,** *124*, 29-39.
134. Wang, H.; Zhu, D.; Paul, A.; Cai, L.; Enejder, A.; Yang, F.; Heilshorn, S. C., Covalently adaptable elastin-like protein–hyaluronic acid (ELP–HA) hybrid hydrogels with secondary thermoresponsive crosslinking for injectable stem cell delivery. *Adv. Funct. Mater.* **2017,** *27* (28), 1605609.
135. Nair, D. P.; Podgórski, M.; Chatani, S.; Gong, T.; Xi, W.; Fenoli, C. R.; Bowman, C. N., The Thiol-Michael Addition Click Reaction: A Powerful and Widely Used Tool in Materials Chemistry. *Chem. Mater.* **2014,** *26* (1), 724-744.
136. Mather, B. D.; Viswanathan, K.; Miller, K. M.; Long, T. E., Michael addition reactions in macromolecular design for emerging technologies. *Progr. Polym. Sci.* **2006,** *31* (5), 487-531.
137. Paez, J. I.; de Miguel-Jimenez, A.; Valbuena-Mendoza, R.; Rathore, A.; Jin, M.; Glaser, A.; Pearson, S.; Del Campo, A., Thiol-Methylsulfone-Based Hydrogels for Cell Encapsulation: Reactivity Optimization of Aryl-Methylsulfone Substrate for Fine-Tunable Gelation Rate and Improved Stability. *Biomacromol.* **2021,** *22* (7), 2874-2886.
138. Darling, N. J.; Hung, Y. S.; Sharma, S.; Segura, T., Controlling the kinetics of thiol-maleimide Michael-type addition gelation kinetics for the generation of homogenous poly(ethylene glycol) hydrogels. *Biomaterials* **2016,** *101*, 199-206.
139. Jansen, L. E.; Negron-Pineiro, L. J.; Galarza, S.; Peyton, S. R., Control of thiol-maleimide reaction kinetics in PEG hydrogel networks. *Acta Biomater.* **2018,** *70*, 120-128.
140. Wang, Z. C.; Xu, X. D.; Chen, C. S.; Yun, L.; Song, J. C.; Zhang, X. Z.; Zhuo, R. X., In situ formation of thermosensitive PNIPAAm-based hydrogels by Michael-type addition reaction. *Appl. Mater. Interfaces* **2010,** *2* (4), 1009-18.
141. Sui, X.; van Ingen, L.; Hempenius, M. A.; Vancso, G. J., Preparation of a Rapidly Forming Poly(ferrocenylsilane)-Poly(ethylene glycol)-based Hydrogel by a Thiol-Michael Addition Click Reaction. *Macromol. Rapid Commun.* **2010,** *31* (23), 2059-63.
142. Baldwin, A. D.; Kiick, K. L., Reversible maleimide–thiol adducts yield glutathione-sensitive poly (ethylene glycol)–heparin hydrogels. *Polym. Chem.* **2013,** *4* (1), 133-143.
143. Rizzi, S. C.; Ehrbar, M.; Halstenberg, S.; Raeber, G. P.; Schmoekel, H. G.; Hagenmüller, H.; Müller, R.; Weber, F. E.; Hubbell, J. A., Recombinant Protein-co-PEG Networks as Cell-Adhesive and Proteolytically Degradable Hydrogel Matrixes. Part II: Biofunctional Characteristics. *Biomacromol.* **2006,** *7* (11), 3019-3029.
144. Rizzi, S. C.; Hubbell, J. A., Recombinant Protein-co-PEG Networks as Cell-Adhesive and Proteolytically Degradable Hydrogel Matrixes. Part I: Development and Physicochemical Characteristics. *Biomacromol.* **2005,** *6* (3), 1226-1238.
145. Guaresti, O.; Basasoro, S.; González, K.; Eceiza, A.; Gabilondo, N., In situ cross–linked chitosan hydrogels via Michael addition reaction based on water–soluble thiol–maleimide precursors. *Eur. Polym. J.* **2019,** *119*, 376-384.
146. Pupkaite, J.; Rosenquist, J.; Hilborn, J.; Samanta, A., Injectable Shape-Holding Collagen Hydrogel for Cell Encapsulation and Delivery Cross-linked Using Thiol-Michael Addition Click Reaction. *Biomacromol.* **2019,** *20* (9), 3475-3484.
147. Kharkar, P. M.; Kiick, K. L.; Kloxin, A. M., Design of thiol-and light-sensitive degradable hydrogels using Michael-type addition reactions. *Polym. Chem.* **2015,** *6* (31), 5565-5574.
148. Moon, N. G.; Pekkanen, A. M.; Long, T. E.; Showalter, T. N.; Libby, B., Thiol-Michael 'click' hydrogels as an imageable packing material for cancer therapy. *Polymer* **2017,** *125*, 66-75.

149. Jukes, J. M.; van der Aa, L. J.; Hiemstra, C.; van Veen, T.; Dijkstra, P. J.; Zhong, Z.; Feijen, J.; van Blitterswijk, C. A.; de Boer, J., A newly developed chemically crosslinked dextran-poly(ethylene glycol) hydrogel for cartilage tissue engineering. *Tissue Eng. Part A* **2010,** *16* (2), 565-73.
150. Hsu, X. L.; Wu, L. C.; Hsieh, J. Y.; Huang, Y. Y., Nanoparticle-Hydrogel Composite Drug Delivery System for Potential Ocular Applications. *Polymers* **2021,** *13* (4), 642.
151. Murph, M. M.; Jiang, G. W.; Altman, M. K.; Jia, W.; Nguyen, D. T.; Fambrough, J. M.; Hardman, W. J.; Nguyen, H. T.; Tran, S. K.; Alshamrani, A. A.; Madan, D.; Zhang, J.; Prestwich, G. D., Vinyl sulfone analogs of lysophosphatidylcholine irreversibly inhibit autotaxin and prevent angiogenesis in melanoma. *Bioorg. Med. Chem.* **2015,** *23* (17), 5999-6013.
152. Patterson, J.; Hubbell, J. A., Enhanced proteolytic degradation of molecularly engineered PEG hydrogels in response to MMP-1 and MMP-2. *Biomaterials* **2010,** *31* (30), 7836-45.
153. Stewart, S. A.; Coulson, M. B.; Zhou, C.; Burke, N. A. D.; Stover, H. D. H., Synthetic hydrogels formed by thiol-ene crosslinking of vinyl sulfone-functional poly(methyl vinyl ether-alt-maleic acid) with alpha,omega-dithio-polyethyleneglycol. *Soft Matter* **2018,** *14* (41), 8317-8324.
154. Noordzij, G. J.; Wilsens, C., Cascade aza-Michael Addition-Cyclizations; Toward Renewable and Multifunctional Carboxylic Acids for Melt-Polycondensation. *Front. Chem.* **2019,** *7*, 729.
155. Patil, S. S.; Shinde, V. S.; Misra, R. D. K., pH and reduction dual-stimuli-responsive PEGDA/PAMAM injectable network hydrogels via aza-michael addition for anticancer drug delivery. *J. Polym. Sci. Part A: Polym. Chem.* **2018,** *56* (18), 2080-2095.
156. Gu, Y.; Zhou, S.; Yang, J., Aza-Michael Addition Chemistry for Tuning the Phase Separation of PDMS/PEG Blend Coatings and Their Anti-Fouling Potentials. *Macromol. Chem. Phys.* **2020,** *221* (6), 1900477.
157. Min, K.; Choi, W.; Kim, C.; Choi, M., Oxidation-stable amine-containing adsorbents for carbon dioxide capture. *Nat. Comm.* **2018,** *9* (1), 1-7.
158. Seitchik, J. L.; Peeler, J. C.; Taylor, M. T.; Blackman, M. L.; Rhoads, T. W.; Cooley, R. B.; Refakis, C.; Fox, J. M.; Mehl, R. A., Genetically encoded tetrazine amino acid directs rapid site-specific in vivo bioorthogonal ligation with trans-cyclooctenes. *J. Am. Chem. Soc.* **2012,** *134* (6), 2898-901.
159. Liu, C. Y.; Huang, C. J., Functionalization of Polydopamine via the Aza-Michael Reaction for Antimicrobial Interfaces. *Langmuir* **2016,** *32* (19), 5019-28.
160. Fairbanks, B. D.; Love, D. M.; Bowman, C. N., Efficient Polymer-Polymer Conjugation via Thiol-ene Click Reaction. *Macromol. Chem. Phys.* **2017,** *218* (18), 1700073.
161. Zhang, Y.; Liu, S.; Li, T.; Zhang, L.; Azhar, U.; Ma, J.; Zhai, C.; Zong, C.; Zhang, S., Cytocompatible and non-fouling zwitterionic hyaluronic acid-based hydrogels using thiol-ene "click" chemistry for cell encapsulation. *Carbohyd. Polym.* **2020,** *236*, 116021.
162. Du, H.; Zha, G.; Gao, L.; Wang, H.; Li, X.; Shen, Z.; Zhu, W., Fully biodegradable antibacterial hydrogels via thiol–ene "click" chemistry. *Polym. Chem.* **2014,** *5* (13), 4002-4008.
163. Liang, J.; Zhang, X.; Chen, Z.; Li, S.; Yan, C., Thiol-Ene Click Reaction Initiated Rapid Gelation of PEGDA/Silk Fibroin Hydrogels. *Polymers* **2019,** *11* (12), 2102.

164. Hoelscher, F.; Machado, T. O.; de Oliveira, D.; Hermes de Araújo, P. H.; Sayer, C., Enzymatically catalyzed degradation of poly (thioether-ester) nanoparticles. *Polym. Degrad. Stab.* **2018,** *156*, 211-217.
165. Li, Y.; Tan, Y.; Xu, K.; Lu, C.; Wang, P., A biodegradable starch hydrogel synthesized via thiol-ene click chemistry. *Polym. Degrad. Stab.* **2017,** *137*, 75-82.
166. Behravesh, E.; Jo, S.; Zygourakis, K.; Mikos, A. G., Synthesis of in Situ Cross-Linkable Macroporous Biodegradable Poly(propylene fumarate-co-ethylene glycol) Hydrogels. *Biomacromol.* **2002,** *3* (2), 374-381.
167. Mohammed, H. S.; Snyder, B. L.; Samways, D. S. K.; Shipp, D. A., Quantitative and qualitative toxicological evaluation of thiol-ene "click" chemistry-based polyanhydrides and their degradation products. *J. Biomed. Mater. Res. Part A* **2016,** *104* (8), 1936-1945.
168. Ding, H.; Li, B.; Liu, Z.; Liu, G.; Pu, S.; Feng, Y.; Jia, D.; Zhou, Y., Decoupled pH- and Thermo-Responsive Injectable Chitosan/PNIPAM Hydrogel via Thiol-Ene Click Chemistry for Potential Applications in Tissue Engineering. *Adv. Healthc. Mater.* **2020,** *9* (14), e2000454.
169. Bakaic, E.; Smeets, N. M. B.; Hoare, T., Injectable hydrogels based on poly(ethylene glycol) and derivatives as functional biomaterials. *Adv.* **2015,** *5* (45), 35469-35486.
170. Hu, B. H.; Su, J.; Messersmith, P. B., Hydrogels cross-linked by native chemical ligation. *Biomacromol.* **2009,** *10* (8), 2194-200.
171. Gyarmati, B.; Némethy, Á.; Szilágyi, A., Reversible disulphide formation in polymer networks: A versatile functional group from synthesis to applications. *Eur. Polym. J.* **2013,** *49* (6), 1268-1286.
172. Beaupre, D. M.; Weiss, R. G., Thiol- and Disulfide-Based Stimulus-Responsive Soft Materials and Self-Assembling Systems. *Molecules* **2021,** *26* (11), 3332.
173. Zhang, B.-y.; He, W.-D.; Li, L.-y.; Sun, X.-l.; Li, W.-t.; Zhang, K.-r., Reducibly degradable hydrogels of PNIPAM and PDMAEMA: Synthesis, stimulus-response and drug release. *J. Polym. Sci. Part A* **2010,** *48* (16), 3604-3612.
174. Meng, F.; Hennink, W. E.; Zhong, Z., Reduction-sensitive polymers and bioconjugates for biomedical applications. *Biomaterials* **2009,** *30* (12), 2180-98.
175. Hammer, N.; Brandl, F. P.; Kirchhof, S.; Messmann, V.; Goepferich, A. M., Protein Compatibility of Selected Cross-linking Reactions for Hydrogels. *Macromol. Biosci.* **2015,** *15* (3), 405-413.
176. Shu, X. Z.; Liu, Y.; Luo, Y.; Roberts, M. C.; Prestwich, G. D., Disulfide cross-linked hyaluronan hydrogels. *Biomacromol.* **2002,** *3* (6), 1304-1311.
177. Choh, S.-Y.; Cross, D.; Wang, C., Facile synthesis and characterization of disulfide-cross-linked hyaluronic acid hydrogels for protein delivery and cell encapsulation. *Biomacromol.* **2011,** *12* (4), 1126-1136.
178. Huang, Z.; Delparastan, P.; Burch, P.; Cheng, J.; Cao, Y.; Messersmith, P. B., Injectable dynamic covalent hydrogels of boronic acid polymers cross-linked by bioactive plant-derived polyphenols. *Biomater. Sci.* **2018,** *6* (9), 2487-2495.
179. Marco-Dufort, B.; Tibbitt, M. W., Design of moldable hydrogels for biomedical applications using dynamic covalent boronic esters. *Mater. Today Chem.* **2019,** *12*, 16-33.
180. Amaral, A. J. R.; Gaspar, V. M.; Mano, J. F., Responsive laminarin-boronic acid self-healing hydrogels for biomedical applications. *Polym. J.* **2020,** *52* (8), 997-1006.
181. Cho, S.; Hwang, S. Y.; Oh, D. X.; Park, J., Recent progress in self-healing polymers and hydrogels based on reversible dynamic B–O bonds: boronic/boronate esters, borax, and benzoxaborole. *J. Mater. Chem. A* **2021**, 9, 14630-14655.

182. Wu, D.; Wang, W.; Diaz-Dussan, D.; Peng, Y.-Y.; Chen, Y.; Narain, R.; Hall, D. G., In Situ Forming, Dual-Crosslink Network, Self-Healing Hydrogel Enabled by a Bioorthogonal Nopoldiol–Benzoxaborolate Click Reaction with a Wide pH Range. *Chem. Mater.* **2019,** *31* (11), 4092-4102.
183. Liu, Y.; Liu, Y.; Wang, Q.; Han, Y.; Chen, H.; Tan, Y., Doubly Dynamic Hydrogel Formed by Combining Boronate Ester and Acylhydrazone Bonds. *Polymers* **2020,** *12* (2), 487.
184. Marozas, I. A.; Anseth, K. S.; Cooper-White, J. J., Adaptable boronate ester hydrogels with tunable viscoelastic spectra to probe timescale dependent mechanotransduction. *Biomaterials* **2019,** *223*, 119430.
185. Li, L.; Zhang, Z., Development and Applications of the Copper-Catalyzed Azide-Alkyne Cycloaddition (CuAAC) as a Bioorthogonal Reaction. *Molecules* **2016,** *21* (10), 1393.
186. van Dijk, M.; van Nostrum, C. F.; Hennink, W. E.; Rijkers, D. T.; Liskamp, R. M., Synthesis and characterization of enzymatically biodegradable PEG and peptide-based hydrogels prepared by click chemistry. *Biomacromol.* **2010,** *11* (6), 1608-14.
187. Gonzalez, K.; Garcia-Astrain, C.; Santamaria-Echart, A.; Ugarte, L.; Averous, L.; Eceiza, A.; Gabilondo, N., Starch/graphene hydrogels via click chemistry with relevant electrical and antibacterial properties. *Carbohydr. Polym.* **2018,** *202*, 372-381.
188. Tang, S. Y.; Shi, J.; Guo, Q. X., Accurate prediction of rate constants of Diels-Alder reactions and application to design of Diels-Alder ligation. *Org. Biomol. Chem.* **2012,** *10* (13), 2673-82.
189. King, M.; Wagner, A., Developments in the field of bioorthogonal bond forming reactions-past and present trends. *Bioconjug. Chem.* **2014,** *25* (5), 825-39.
190. Derda, R.; Jafari, M. R., Synthetic cross-linking of peptides: molecular linchpins for peptide cyclization. *Prot. Pept. Lett.* **2018,** *25* (12), 1051-1075.
191. Kodolitsch, K.; Gobec, F.; Slugovc, C., Solvent- and Catalyst-Free Aza-Michael Addition of Imidazoles and Related Heterocycles. *Eur. J. Org. Chem.* **2020,** *2020* (19), 2973-2978.
192. Martello, F.; Tocchio, A.; Tamplenizza, M.; Gerges, I.; Pistis, V.; Recenti, R.; Bortolin, M.; Del Fabbro, M.; Argentiere, S.; Milani, P.; Lenardi, C., Poly(amido-amine)-based hydrogels with tailored mechanical properties and degradation rates for tissue engineering. *Acta Biomater.* **2014,** *10* (3), 1206-15.
193. Ranu, B.; Dey, S.; Hajra, A., Solvent-free, catalyst-free Michael-type addition of amines to electron-deficient alkenes. *Arkivoc* **2002,** *2002*, 76-81.
194. Southan, A.; Mateescu, M.; Hagel, V.; Bach, M.; Schuh, C.; Kleinhans, C.; Kluger, P. J.; Tussetschläger, S.; Nuss, I.; Haraszti, T.; Wegner, S. V.; Spatz, J. P.; Boehm, H.; Laschat, S.; Tovar, G. E. M., Toward Controlling the Formation, Degradation Behavior, and Properties of Hydrogels Synthesized by Aza-Michael Reactions. *Macromol. Chem. Phys.* **2013,** *214* (16), 1865-1873.
195. Wang, J.; He, H.; Cooper, R. C.; Yang, H., In Situ-Forming Polyamidoamine Dendrimer Hydrogels with Tunable Properties Prepared via Aza-Michael Addition Reaction. *ACS Appl. Mater. Interf.* **2017,** *9* (12), 10494-10503.
196. Wang, J.; Yang, H., Superelastic and pH-Responsive Degradable Dendrimer Cryogels Prepared by Cryo-aza-Michael Addition Reaction. *Sci. Rep.* **2018,** *8* (1), 7155.
197. Munar, I.; Findik, V.; Degirmenci, I.; Aviyente, V., Solvent Effects on Thiol-Ene Kinetics and Reactivity of Carbon and Sulfur Radicals. *J. Phys. Chem. A* **2020,** *124* (13), 2580-2590.

198. Kolmel, D. K.; Kool, E. T., Oximes and Hydrazones in Bioconjugation: Mechanism and Catalysis. *Chem. Rev.* **2017,** *117* (15), 10358-10376.
199. Kool, E. T.; Crisalli, P.; Chan, K. M., Fast alpha nucleophiles: structures that undergo rapid hydrazone/oxime formation at neutral pH. *Org. Lett.* **2014,** *16* (5), 1454-1457.
200. Li, Y.; Zhang, Y.; Shi, F.; Tao, L.; Wei, Y.; Wang, X., Modulus-regulated 3D-cell proliferation in an injectable self-healing hydrogel. *Coll. Surf. B Biointerf.* **2017,** *149*, 168-173.
201. Liu, S.; Kang, M.; Li, K.; Yao, F.; Oderinde, O.; Fu, G.; Xu, L., Polysaccharide-templated preparation of mechanically-tough, conductive and self-healing hydrogels. *Chem. Eng. J.* **2018,** *334*, 2222-2230.
202. Mohd Rasdi, F. R.; Phan, A. N.; Harvey, A. P., Rapid determination of reaction order and rate constants of an imine synthesis reaction using a mesoscale oscillatory baffled reactor. *Chem. Eng. J.* **2013,** *222*, 282-291.
203. Saito, H.; Hoffman, A. S.; Ogawa, H. I., Delivery of Doxorubicin from Biodegradable PEG Hydrogels Having Schiff Base Linkages†. *J. Bioact. Compat. Polym.* **2007,** *22* (6), 589-601.
204. Hinton, T. J.; Jallerat, Q.; Palchesko, R. N.; Park, J. H.; Grodzicki, M. S.; Shue, H.-J.; Ramadan, M. H.; Hudson, A. R.; Feinberg, A. W., Three-dimensional printing of complex biological structures by freeform reversible embedding of suspended hydrogels. *Sci. Adv.* **2015,** *1* (9), e1500758.
205. Shiwarski, D. J.; Hudson, A. R.; Tashman, J. W.; Feinberg, A. W., Emergence of FRESH 3D printing as a platform for advanced tissue biofabrication. *APL Bioeng.* **2021,** *5* (1), 010904.
206. Suntornnond, R.; An, J.; Chua, C. K., Roles of support materials in 3D bioprinting - Present and future. *Int. J. Bioprint.* **2017,** *3* (1), 006.
207. Nowicki, M.; Zhu, W.; Sarkar, K.; Rao, R.; Zhang, L. G., 3D printing multiphasic osteochondral tissue constructs with nano to micro features via PCL based bioink. *Bioprinting* **2020,** *17*, e00066.
208. Jeong, H. J.; Nam, H.; Jang, J.; Lee, S. J., 3D Bioprinting Strategies for the Regeneration of Functional Tubular Tissues and Organs. *Bioeng.* **2020,** *7* (2), 32.
209. Puertas-Bartolomé, M.; Włodarczyk-Biegun, M. K.; del Campo, A.; Vázquez-Lasa, B.; San Román, J., 3D Printing of a Reactive Hydrogel Bio-Ink Using a Static Mixing Tool. *Polymers* **2020,** *12* (9), 1986.
210. Hafeez, S.; Ooi, H. W.; Morgan, F. L.; Mota, C.; Dettin, M.; Van Blitterswijk, C.; Moroni, L.; Baker, M. B., Viscoelastic oxidized alginates with reversible imine type crosslinks: self-healing, injectable, and bioprintable hydrogels. *Gels* **2018,** *4* (4), 85.
211. Morgan, F. L.; Fernández-Pérez, J.; Moroni, L.; Baker, M. B., Tuning hydrogels by mixing dynamic cross-linkers: enabling cell-instructive hydrogels and advanced bioinks. *Adv. Healthc. Mater.* **2021**, 2101576.
212. Ji, S.; Abaci, A.; Morrison, T.; Gramlich, W. M.; Guvendiren, M., Novel bioinks from UV-responsive norbornene-functionalized carboxymethyl cellulose macromers. *Bioprinting* **2020,** *18*, e00083.
213. Bertlein, S.; Brown, G.; Lim, K. S.; Jungst, T.; Boeck, T.; Blunk, T.; Tessmar, J.; Hooper, G. J.; Woodfield, T. B.; Groll, J., Thiol–ene clickable gelatin: a platform bioink for multiple 3D biofabrication technologies. *Adv. Mater.* **2017,** *29* (44), 1703404.
214. Soliman, B. G.; Lindberg, G. C.; Jungst, T.; Hooper, G. J.; Groll, J.; Woodfield, T. B.; Lim, K. S., Stepwise control of crosslinking in a one-pot system for bioprinting of low-density bioinks. *Adv. Healthc. Mater.* **2020,** *9* (15), 1901544.

215. Biswas, A.; Malferrari, S.; Kalaskar, D. M.; Das, A. K., Arylboronate esters mediated self-healable and biocompatible dynamic G-quadruplex hydrogels as promising 3D-bioinks. *Chem. Comm.* **2018,** *54* (14), 1778-1781.
216. Amaral, A. J.; Gaspar, V. M.; Lavrador, P.; Mano, J. F., Double network laminarin-boronic/alginate dynamic bioink for 3D bioprinting cell-laden constructs. *Biofabrication* **2021,** *13* (3), 035045.
217. Mohamed, A. L.; Soliman, A. A. F.; Ali, E. A.; Abou-Zeid, N. Y.; Nada, A. A., Hydrogel bioink based on clickable cellulose derivatives: Synthesis, characterization and in vitro assessment. *Int. J. Biol. Macromol.* **2020,** *163*, 888-897.

CHAPTER 3

Coaxial Extrusion Bioprinting of Hydrazone Crosslinked POEGMA Hydrogels: Effect of Needle Geometry on Print Quality

Eva Mueller, Afshin Abrishamkar, Ron Galaev, Lau Kwan Kiu, Todd Hoare

Declaration of Academic Achievement:

Dr. Afshin Abrishamkar developed the computational model and ran the majority of the computational models/analysis and is thus the first co-author on this research work. Ron Galaev performed the printability studies with the functional precursors (using food colouring), and Lau Kwan Kiu helped with the preliminary computational modelling. The experimental design, analysis and writing of this manuscript were done by Eva Mueller, with the help of Dr. Todd Hoare. This manuscript will be submitted to *Bioprinting* by the end of November 2022.

Coaxial Extrusion Bioprinting of Hydrazone Crosslinked POEGMA Hydrogels: Effect of Needle Geometry on Print Quality

Eva Mueller, Afshin Abrishamkar, Ron Galaev, Lau Kwan Kiu, Todd Hoare

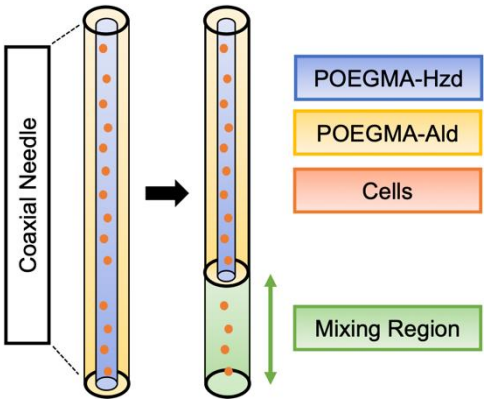

Facilitating effective mixing of two or more functional polymers remains a challenge when translating *in situ*-crosslinking click chemistry hydrogels to extrusion bioprinting applications. In this work, the conventional flush coaxial needle was modified to introduce a mixing region to promote the mixing of hydrazide and aldehyde-functionalized poly(oligoethylene glycol methacrylate) (POEGMA) polymers that form dynamic hydrazone bonds upon crosslinking. The inclusion of the mixing region significantly reduced the spreading of the printed fibers and improved the homogeneity of both the printed hydrogel and the encapsulated cells. Computational modelling based on non-Newtonian fluid behaviour in the mixing zone confirmed that increasing the length of the mixing zone improved the mixing efficiency, a finding supported by experimental printing results. As such, particularly with less viscous bioinks like the oligomeric hydrazide/aldehyde-functionalized POEGMA polymers used herein, the inclusion of this mixing region provides an effective means of printing functional precursor polymers that can chemically crosslink upon mixing.

Keywords: 3D bioprinting, dynamic covalent chemistry, coaxial bioprinting, poly(oligoethylene glycol methacrylate), hydrazone chemistry, computational modeling

3.1 Introduction

Extrusion bioprinting is the most widely used bioprinting technique due to its ability to create scaffolds with precise geometries and controllable pore interconnectivity and architecture at a comparatively low cost[1-3]. The main advantages of extrusion bioprinting over other techniques are the low cost, flexibility in the type of bioink to be printed, and the ability to print viscous bioinks with very high cell densities (or even cell spheroids) into three-dimensional (3D) scaffolds[4, 5]. While extrusion bioprinting allows for the application of a wide range of printable hydrogel bioinks, there remain several key challenges that limit its broad implementation to solve biofabrication challenges: (1) lower cell viability can be observed due to the higher shear stresses imparted on cells when co-printed with particularly high viscosity hydrogel bioinks through the small nozzles required for achieving higher print resolution[5]; (2) non-homogeneous constructs are often printed due to the inability to directly control the mixing profiles of the uncrosslinked precursors, leading to potentially poor print resolution and mechanics[6]; and (3) post-crosslinking is often required in the form of UV irradiation or via secondary ionic crosslinking to improve the final mechanics of the printed construct to ensure high print fidelity[7].

One nozzle design that has been extensively studied in the context of extrusion bioprinting to help address these challenges is the coaxial needle. Coaxial bioprinting is an extrusion technique that simultaneously deposits two or more flow streams in concentric rings to enable the fabrication of more complex tissue constructs compared to a single nozzle[8, 9]. Coaxial extrusion printing dates back over 120 years to the beginnings of electrospinning, which used a coaxial nozzle design in its first patent[10]. While the first extrusion-based coaxial systems were developed in the 1930s, the first biologically relevant application of a coaxial nozzle for cell encapsulation used a triaxial configuration with the cells in the core, a polymer sheath, and an outer airflow sheath[11]. The first coaxial bioprinting was reported four years after the first report on extrusion-based bioprinting in 2002[12], using only the differences in the viscosities of two materials extruded through a conventional syringe to spatially separate by the velocity profile and achieve a coaxial-like flow. The first true coaxial bioprinting setup was reported in 2011[13] by Kim et al., who reported printing of an alginate core with a collagen sheath to exploit both the mechanical benefits of alginate and the cell compatibility of collagen[13]. The intrinsic benefits of coaxial bioprinting include: (1) improved control of concentric multi-material deposition; (2) facilitation of a wider range of printable bioinks; (3) enablement of the

deposition of sacrificial materials; and (4) improved print resolution by better controlling the contact between bioink(s) and thus their crosslinking to form printable hydrogels[6]. In the latter case, the use of coaxial geometries to stream a crosslinking phase (i.e., calcium ion solutions) concentric to a bioink phase (typically alginate) has enabled the formation of continuously printable hydrogel fibers, taking advantage of the fast calcium-alginate ionic interactions to create prints with high print fidelity and good retention of the pre-programmed heterogeneity within the printed fibers[8,13]. However, the high lability of the calcium-alginate crosslink (via ion exchange) *in vivo* can limit the practical utility of such prints in implantable devices.

Dynamic covalent chemistry has been recently investigated as an attractive crosslinking strategy for extrusion bioprinting applications due to its potential to use non-viscous functional precursor polymers to rapidly form a crosslinked hydrogel network without any catalysts, non-physiological temperature and pH, or any other post-processing steps[14, 15]. In addition, relative to ionic crosslinking strategies such as calcium-alginate, the type of dynamic covalent bond formed and/or the chemistry surrounding that bond can be used to tune the degradation of the scaffold or render the scaffold non-degradable under normal physiological conditions, the latter of which may be preferred for long-term cell therapeutics; in this context, dynamic covalent chemistry can provide a platform in which the gelation kinetics[16], cell interactions[17], and mechanics can be precisely tuned based on the targeted tissue engineering application[18]. Of particular interest among different dynamic covalent chemistries, hydrazone chemistry is a hydrolytically-labile dynamic click chemistry reaction between *in situ*-gelling hydrazide with aldehyde/ketone functional groups. Prior to this thesis work, only pre-crosslinked hydrazone bioinks have been successfully printed via free-form extrusion bioprinting; even then, those prints needed to be mechanically reinforced through post-printing photocrosslinking to provide sufficient mechanical strength in the final print[19]. The limited printability of dynamic covalent chemistry-based bioinks is attributable to the challenging balance that must be struck between the residence time of any pre-mixed hydrazide/aldehyde polymer combination in the nozzle (necessary to avoid clogging) and the gelation kinetics of the precursor polymers (with rapid post-mixing gelation typically required to avoid the loss of print fidelity upon deposition on the printing support. Achieving this balance requires a precise understanding of how the precursor polymers mix and the impact of that mixing on the viscosity build-up as gelation proceeds.

To aid in the design of suitable hydrogel bioinks in the context of such challenges, recent efforts have been focused on leveraging computational modelling to minimize the number of variables that must be iterated in the experiments and ensure that the fluid dynamics of the system are well-understood prior to incorporating cells[20]. Various printing parameters can be determined computationally, including the pressures and velocity required to fully simulate the extrusion process[21] and the polymer concentrations at the point where crosslinking starts[22]. However, the shear stress within the nozzle has been demonstrated to be the key parameter that influences both printability and (more crucially) cell viability. Shear stress can be modelled using different Newtonian or non-Newtonian flow models[23, 24]. For example, Billiet et al. studied the effects of conical and cylindrical needle shapes on the cell viability of a hepatocarcinoma cell line using gelatin methacrylamide as the photocrosslinkable bioink, showing that conical needles imparted higher shear stress on cells[25]; in other studies, shear stress distributions using different nozzle geometries and/or flow rates were assessed for printing ionically-crosslinked hydrogel bioinks based on alginate sulfate and nanocellulose[26] and hyaluronic acid-based electrospun fibers in a gelatin methacrylate bioink[27]. Computational modelling approaches have also been applied directly to understand the shear dynamics in coaxial bioprinting approaches. For example, Silva et al. developed a computationally-aided design model of the three flow channels required for the triaxial extrusion of sodium alginate to determine the outlet velocity and pressure[28] while Mirani et al. used the model to optimize the printing of gelatin methacrylate through a microfluidic printhead to understand the diffusive and fluid dynamic behaviour of the coaxial flow[22]. However, to our knowledge, no previous studies have investigated the use of computational modeling to assess the printability of dynamic covalent chemistry-based hydrogel bioinks and thus inform the design of appropriate coaxial needles to facilitate improved print fidelity and stability.

In this work, a coaxial extrusion 3D printing setup was used to control the mixing of hydrazide and aldehyde-functionalized poly(oligoethylene glycol methacrylate) (POEGMA) precursor polymers that form dynamic hydrazone bonds upon crosslinking. To effectively mix the two functional precursors, a mixing region (hereafter referred to as “mixing zone”) was incorporated within the coaxial needle design. The effects of the inner needle gauge and the length of the mixing zone were assessed by leveraging both computational fluid dynamic modeling and practical extrusion printing experiments in which the print resolution, mixing efficiency, and reproducibility or the prints were assessed with and without cells. We demonstrate that the use of uneven length (i.e., centre-cut) coaxial needles can significantly

improve the mixing of the precursor polymers without inducing nozzle clogging, enabling free-form bioprinting of dynamic covalent hydrogel-based bioinks.

3.2 Experimental Section

3.2.1 Materials

Oligo(ethylene glycol) methyl ether methacrylate ($OEGMA_{500}$, M_n = 500 g/mol, Sigma-Aldrich, 95%) and di(ethylene glycol) methyl ether methacrylate ($M(EO)_2MA$, Sigma-Aldrich, 95%) were purified using a basic aluminum-oxide-packed column (Sigma-Aldrich, type CG-20) to remove the methyl ether hydro- quinone (MEHQ) and butylated hydroxytoluene (BHT) inhibitors before use. Acrylic acid (AA, Sigma-Aldrich, 99%), 2,2-azo-bis-isobutryic acid dimethyl ester (AIBMe, Wako Chemicals, 98.5%), dioxane (Caledon Laboratories, 99%), adipic acid dihydrazide (ADH, Alfa Aesar, 98%), N′-ethyl-N-(3-(dimethylamino)propyl)-carbodiimide (EDC, Carbosynth, Compton CA, commercial grade), sodium cyanoborohydride (Sigma-Aldrich), and thioglycolic acid (TGA, Sigma-Aldrich, 98%) were all used as received. N-(2,2-Dimethoxyethyl) methacrylamide (DMEMAm) was synthesized as previously reported[29]. Milli-Q grade distilled deionized water (DIW) was used for all experiments. The fluorescent probes, fluorescein isothiocyanate (FITC) and rhodamine-123 were purchased from Sigma Aldrich and used as received. For the cell experiments, NIH/3T3 and Psi2 12S6 epithelial cells were purchased from ATCC. Dulbecco's Modified Eagle's Medium (DMEM), fetal bovine serum (FBS), penicillin−streptomycin, trypsin−EDTA solution and phosphate buffered saline were all purchased from ThermoFisher. The live/dead assay and the cell tracker dyes (CFSA and Far-Red) were also purchased from ThermoFisher.

3.2.2 Precursor Polymer Synthesis and Characterization

The functional POEGMA polymers were synthesized as previously described[29]. Hydrazide functionalized POEGMA polymers were prepared by adding AIBMe (37 mg), $M(EO)_2MA$ (3.10 g), $OEGMA_{500}$ (0.9 g), acrylic acid (0.55 g), and thioglycolic acid (7.5 μL) to a 100 mL flask. 20 mL of dioxane was added, and the solution was purged with nitrogen for at least 30 min. The flask was then sealed and submerged in an oil bath maintained at 75°C for 4 hours under magnetic stirring. After removing the solvent, these carboxylic acid groups of the polymerized POEGMA-co-acrylic acid were subsequently converted to hydrazide groups via a carbodiimide-mediated conjugation using a five-fold molar excess of adipic acid dihydrazide. After adding EDC to the reaction mixture in DIW, the pH was maintained at 4.7 using 0.1 M

HCl over 4 hours. The solution was then dialysed (using 3.5 kDa MWCO dialysis tubing) against DIW for a minimum of six (6+ hours) cycles and lyophilized. The aldehyde functionalized POEGMA polymers were prepared similarly to the hydrazide functionalized polymers, but the acrylic acid was replaced with N-(2,2-dimethoxyethyl) methacrylamide (DMEMAm). After the reaction, the acetal groups were converted to aldehydes by dissolving the polymer in an excess of 1 M HCl. The solution was left to stir for 24 hours, dialyzed over 6 cycles (using 3.5 kDa MWCO dialysis tubing), and lyophilized.

The functional polymers were characterized in terms of their molecular weight and degree of functionalization using aqueous gel permeation chromatography (GPC) and ^{1}H NMR (600 MHz, Bruker), respectively. The GPC used an Agilent 1260 infinity II GPC system with an Agilent 1260 infinity refractive index detector and a Superpose 6 increase 10/300 GL (GE healthcare) column maintained at 30°C. The continuous phase was 1× PBS with 0.05% sodium azide pumped at a flow rate of 0.5 mL/min, and the system was calibrated with narrow PEG standards (molecular weights 3-60 kDa). The degree of hydrazide functionalization was determined using ^{1}H NMR (600 MHz, Bruker) by comparing the intensities of the $-CH_2$ group on ADH (0.89−1.06 ppm), the $-OCH_3$ signal on POEGMA (3.45 ppm), and the $-CH_3$ signal on the backbone of POEGMA (0.81 ppm) to obtain the hydrazide content. The degree of aldehyde functionalization was determined by ^{1}H NMR (600 MHz, Bruker) using d6-DMSO by comparing the ratio of aldehyde proton signal at 9.52 ppm to the methyl POEGMA proton signal at 0.81 ppm. The gelation kinetics were tested using a vial inversion test by pipetting 0.25 mL of each precursor polymer into a 2 mL Eppendorf tube and tracking the time required for no flow to be observed.

3.2.3 Synthesis of Fluorescently Labelled Precursor Polymers

FITC-labeled POEGMA-Hzd was prepared by reacting FITC (5 mg) with POEGMA-Hzd solution (1 g, 15 w/w% in DIW) under magnetic stirring for 12 hours at room temperature. A total of 2 mol% of the available hydrazide groups were targeted for labeling with FITC. The resulting polymer was then dialyzed (6+ hours for 6 cycles), lyophilized, redissolved in a 15 w/w% solution in DIW, and stored at 4°C. Rhodamine 123-labeled POEGMA-Ald was prepared by reacting rhodamine 123 (5 mg) with POEGMA-Ald solution (1 g, 15 w/w% in DIW) under magnetic 3 stirring for 24 hours. Sodium cyanoborohydride (8.25 mg, 10 mol eq. to rhodamine 123) was then added to the solution to generate a stable conjugate via reductive

amination, after which the solution was stirred for another 48 hours. The resulting polymer solution was dialyzed (6+ hours for 6 cycles) and lyophilized to dryness. The rhodamine 123-labeled POEGMA-Ald was stored at 15 w/w% in DIW at 4°C. In both cases, all reaction vessels and storage containers were covered by aluminum foil to prevent photobleaching.

3.2.4 Rheology

The rheological properties of the polymer precursors and the crosslinked hydrogels were measured using a Discovery hybrid rheometer (TA Instruments). The viscosity sweeps were performed over a shear rate range of 0.1 to 100 1/s at 25°C using a 1° aluminum cone-plate geometry (cone diameter 20 mm) and a volume of ~150 μL. The precursor polymer solutions (at 20 wt% for both POEGMA-Hzd and POEGMA-Ald) were individually pipetted directly onto the rheometer stage for testing. For the hydrazone-crosslinked POEGMA hydrogels, each precursor was sequentially pipetted on the rheometer stage (~75 μL of each precursor), mixed rapidly with a pipette, and allowed to fully gel (minimum 15 minutes) prior to testing.

3.2.5 Computational Modeling

Finite element simulations were conducted to model the diffusive and fluid dynamic behaviour inside the coaxial needle system. The computational model was developed in 3D using COMSOL Multiphysics 5.6 to predict the mixing under a laminar flow regime in a continuously flowing coaxial needle system. Computational fluid dynamics (CFD) and chemical reaction engineering modules were utilized for modeling by coupling the "laminar flow" and "transport of concentrated species" interfaces to simulate the flow patterns and intra-flows diffusion behavior inside the coaxial needle system. Steady state, incompressible Navier-Stokes, and convection-diffusion equations were solved simultaneously in the model, as shown in Equations 3.1-3.3:

$$\rho(\vec{u}\cdot\nabla)\vec{u} = \nabla\cdot[-pI + \mu(\nabla\vec{u} + (\nabla\vec{u})^T)] + F \tag{3.1}$$

$$\rho\nabla\cdot\vec{u} = 0 \tag{3.2}$$

$$\rho(\vec{u}\cdot\nabla)\omega_i = \nabla\cdot\left[\rho D\left(\nabla\omega_i + \omega_i\frac{\nabla M_n}{M_n}\right) - \rho\omega_i\sum_k\frac{M_i}{M_n}D_k\nabla \mathrm{x}_k + D^T\frac{\nabla \mathrm{T}}{T}\right] \tag{3.3}$$

where $\vec{u}$ is the velocity with components u_x, u_y, and u_z respectively in the x, y, and z directions, ρ is the density, p is the pressure, I is the identity tensor, μ is the dynamic viscosity, F is the

body force, ω_i is the mass fraction of component i, D is the diffusion coefficient, Mi is the molar mass, and M_n is calculated as per Equation 3.4:

$$Mn = (\sum_i \frac{\omega_i}{M_i})^{-1} \tag{3.4}$$

A 3D geometry was designed matching the coaxial needle dimensions and configurations, including the sheath needle, core needle, and mixing zone. To simulate the gelation process in models with Newtonian fluid behaviour (i.e., Newtonian models), the mixing zone was split into multiple identical domains with the same dimensions in even intervals, each having a different viscosity value correlated to the progression of the *in situ* gelation reaction. Both initial and final viscosities were obtained empirically, with the initial viscosity calculated as the average viscosity of the two prepolymers, the final viscosity being assigned to be the viscosity of the crosslinked hydrogel, and the values for the intermediate domains exponentially interpolated. In models with non-Newtonian fluid behaviour (i.e., non-Newtonian models), the power law model was used in which the viscosity is defined as a function of shear rate (Equation 3.5):

$$\eta = K \cdot \gamma^{n-1} \tag{3.5}$$

Here, η is the viscosity, K is the flow consistency index, Υ is the shear rate, and n is the power law constant. The power law constant depends on the fluid behavior and is greater than, equal to, or smaller than 1 for shear-thickening, Newtonian, and shear-thinning fluids, respectively. Based on the rheology measurements (**Figure 3.2B**), the power law constant for the shear-thinning polymers in this work was found to be n=0.15, which was applied to the fluids in the mixing zone; Newtonian fluid properties (n=1) were used to model the flow properties of the precursor solutions in the core and sheath needles, also consistent with the measured rheological properties of those precursor solutions (**Figure 3.2A**). The model was then meshed using a tetrahedral grid using boundary conditions of zero pressure at the outlet, input flow rates at the inlets, and no slip at the walls. Different parameters were varied as part of the computational modeling including the diameter of the sheath and core needles and length of core needle relative to the sheath needle, the latter of which determines the length of the mixing zone within the concentric needle. A schematic illustration of the geometry used for the COMSOL modelling can be seen in **Figure 3.1**.

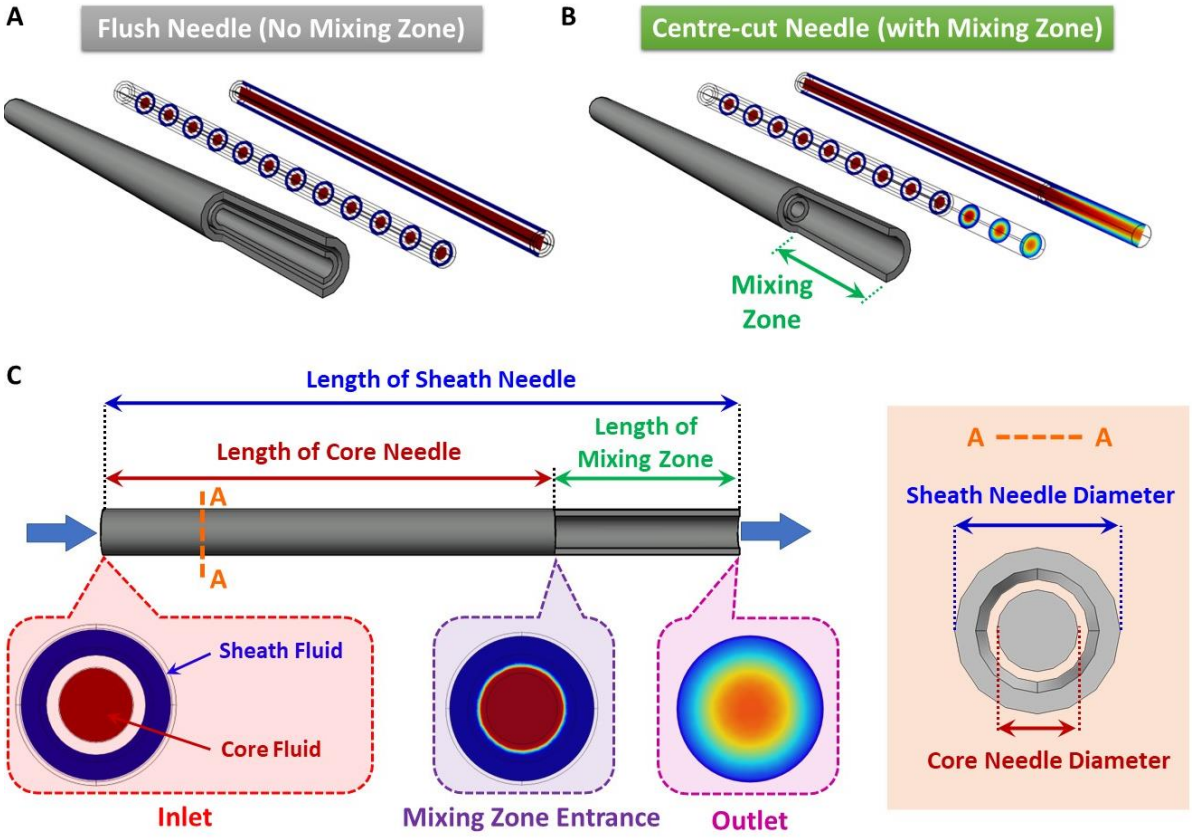

Figure 3.1: Computational modeling of the coaxial needle: (A,B) 3D geometry (left), cross-sectional planes of mass fraction (middle), and mass fraction plot along the flow direction (right) of a 3 mm long (A) flush needle design (i.e., no mixing zone) and (B) improved needle design (i.e., with a mixing zone); (C) 2D geometry of the improved needle illustrating the corresponding mass fraction plots at the inlet, mixing zone entrance, and outlet.

The mixing efficiency of each model was evaluated both quantitatively and qualitatively. Qualitatively, results were examined through visual outputs of the velocity profile and the mass fraction distribution of the two precursor polymer components. The velocity profile visually demonstrates the profile of the velocity vectors in the flow streams (indicative of the fluid flow pattern in the mixing zone confirming the laminar flow regime), while the mass fraction profile shows the fraction of each prepolymer as a function of the total needle diameter (indicative of the degree of radial mixing between the two streams in the mixing zone). Within the mass fraction profile, the core and sheath streams were respectively depicted as red and blue while the mixed fluid was depicted as green. Quantitively, the mixing efficiency was evaluated by estimating the mixing efficiency index, calculated by transforming the colored two-dimensional contour plot of the mass fraction at the outlet into grayscale and translating individual pixel-by-pixel data (at a pre-defined resolution) into numerical values. The standard

deviation for the pixel intensity was calculated across all pixels evaluated (>40,000 data points per cross-section) and was reported as the mixing efficiency value; lower standard deviation values correspond to more efficient mixing as less variability of polymer mass fraction is observed across the needle cross-section.

3.2.6 Customized 3D Bioprinter

The customized coaxial extrusion printer used for the printing experiments was controlled by a computer running G-codes and operated in four independently controlled axes using step motors. Two 1 mL syringes containing hydrazide and aldehyde functional polymer precursor solutions respectively were directly attached to either a flush (conventional) coaxial needle or a modified coaxial needle in which the core needle was shortened (i.e. centre-cut) to introduce a mixing zone prior to the needle tip. The volumetric flow rate was kept constant at 200 µL/min throughout all printing experiments.

3.2.7 Printing Experiments

Prior to beginning printing experiments, different patterns were coded using G-code (**Figure S3.1**). The effects of changing printing parameters were assessed by printing a series of identical single layer or multilayer patterns by systematically manipulating the parameter of interest, keeping all other parameters constant. The printability of each bioink/printing process tested was quantified based on the consistency of the diameters of the printed fibers across the entire print and the printability index (Pr), defined as in Equation 3.7[30]:

$$\mathrm{Pr} = \frac{\pi}{4} * \frac{1}{C} = \frac{L^2}{16A} \tag{3.7}$$

3.2.8 Cell Culture and Viability

NIH 3T3 mouse fibroblast cells and epithelial Psi2 12S6 mouse cells were cultured in DMEM medium with 10% FBS and 1% penicillin−streptomycin, with both cells cultured to ~80% confluency at 37°C and 5% CO_2 before subsequent use. Cell viability was assessed using LIVE/DEAD staining (ThermoFisher) following the manufacturer's instructions. Briefly, the printed constructs were washed with warm PBS over 3×5-minute intervals before adding the mixture of live (CFDA) and dead (propidium iodide) stains and incubating for 30 minutes at room temperature. Following staining, the printed constructs were washed three times with PBS and imaged using confocal microscopy (CLSM, Nikon A1R HD25), using a 10× 0.45NA

objective and laser lines at 488 nm and 561 nm. The cytotoxicity of the POEGMA-Hzd and POEGMA-Ald polymers was measured over a concentration range of 0.25 to 1 mg/mL using a PrestoBlue Cell Viability Assay (ThermoFisher) after 24 hours of incubation at 37°C. Cells were first plated at a density of $5x10^4$ cells per well in a 96 well plate for 24 hours, after which the polymers were added and incubated with the cells for a subsequent 24 hours. Next, 10 μL of PrestoBlue reagent and 90 μL of media were added to each well and incubated for 2 hours at 37°C. The fluorescence was read using an excitation wavelength of 560 nm and an emission wavelength of 590 nm.

3.2.9 Evaluating Polymer Distribution

The mixing of polymers and cells in the prints was evaluated using three techniques: (1) adding food dyes to the precursor polymer solutions; (2) individually resolvable fluorescent labeling of the two precursor polymers; and (3) pre-staining two different cell lines with different cell dyes and conducting co-culture bioprinting. To evaluate polymer distribution using food dyes, two different colours (yellow for the sheath polymer and blue for the core polymer) were added to the polymers. During extrusion and printing, the color of the construct was evaluated to assess whether the polymers were mixing or if nozzle clogging was occurring. To avoid potential misinterpretations based on the different potential diffusion coefficients of the food dyes relative to the polymers during the printing process and/or within the final prints, POEGMA-Hzd-FITC (stained green, excitation = 491 nm, emission = 516 nm) was used as the core stream and POEGMA-Ald-Rho (stained red, excitation = 546 nm, emission = 568 nm) was used as the sheath stream, with confocal imaging (conducted as described previously) used to identify the independent distribution of both precursor polymers in the 3D prints. To assess the impact of any mixing process on the distribution of co-printed cells, 3T3/NIH fibroblasts were pre-stained using CFSA (green, excitation = 491 nm, emission = 516 nm) and added to the core POEGMA-Hzd stream while Psi2 12S6 epithelial cells were pre-stained with Far-Red stain (red, excitation = 648 nm, emission = 658 nm) and mixed with the sheath POEGMA-Ald stream. The distribution of the two cell lines in the printed scaffold was evaluated after 24 hours of culture in DMEM media supplemented with 10% FBS and 1% penicillin/streptomycin using confocal microscopy.

3.3 Results

3.3.1 Polymer Characterization

Aldehyde and hydrazide functionalized POEGMA polymers (POEGMA-Hzd and POEGMA-Ald) were synthesized via chain transfer radical polymerization with a target degree of hydrazide and aldehyde functionalization 20 mol%, selected based on previous reports to enable gelation on relatively fast timescales (<20 s) while still minimizing the total polymer concentration required for printing. The molecular weights of the polymers were maintained to be <20 kDa, below the renal cut-off, and near-stoichiometric degrees of functionalization were achieved relative to the target (22.8 mol% and 20.1 mol% for hydrazide and aldehyde-functionalized polymers respectively, **Table 3.1**). The polymers are highly non-viscous and exhibit only very slight shear thinning (<1 order of magnitude viscosity change even at a concentration of 20 wt%) over the full range of shear rates tested (**Figure 3.2A**); as such, simulations of the flow polymer precursor solutions themselves could be conducted relatively accurately using a Newtonian-only model. Both precursor polymers maintained high cytocompatibility when exposed to NIH/3T3 fibroblasts and Psi2 12S6 epithelial cells (**Figure 3.2C**), confirming their potential for cell bioprinting. Upon mixing the precursor polymers at concentrations ranging from 10 to 30 wt% (with equivalent mass concentrations used for both precursor materials), hydrazone-crosslinked POEGMA hydrogels were formed with gelation times ranging from instantaneous to 15 seconds (**Table 3.2**), resulting in much more viscous and significantly more shear-thinning printed hydrogels that exhibited a >3 orders of magnitude viscosity change from the highest to lowest shear rates tested (**Figure 3.2B**). While the shear thinning properties of hydrogels prepared at all tested precursor polymer concentrations are similar, the 30 wt% precursor polymer hydrogel was used to estimate the power law exponent given that the zero-shear plateau region is clearly visible with this hydrogel, facilitating power law model fitting; however, based on **Figure 3.2B**, the power law exponent extracted should be broadly relevant to all polymer concentrations tested. Thus, using the dynamic covalent chemistry approach, the initial viscosity to which cells are exposed during the printing remains low, with the post-gelation occurring around the printed cells expected to apply lower shear stresses on the cells than direct printing using a more viscous bioink formulation.

Table 3.1: Characterization of functional precursor polymers used for coaxial printing

Polymer	M_n (kDa)	Đ	Functional monomer (mol%)
POEGMA-Hzd	16.4	3.3	22.8
POEGMA-Ald	14.8	4.1	20.1

Table 3.2: Gelation kinetics of hydrazone crosslinked POEGMA hydrogels for coaxial printing

Polymer Concentration (wt%)	Gelation Time (seconds)
10	15
12	10
14	8
16	6
30	<1

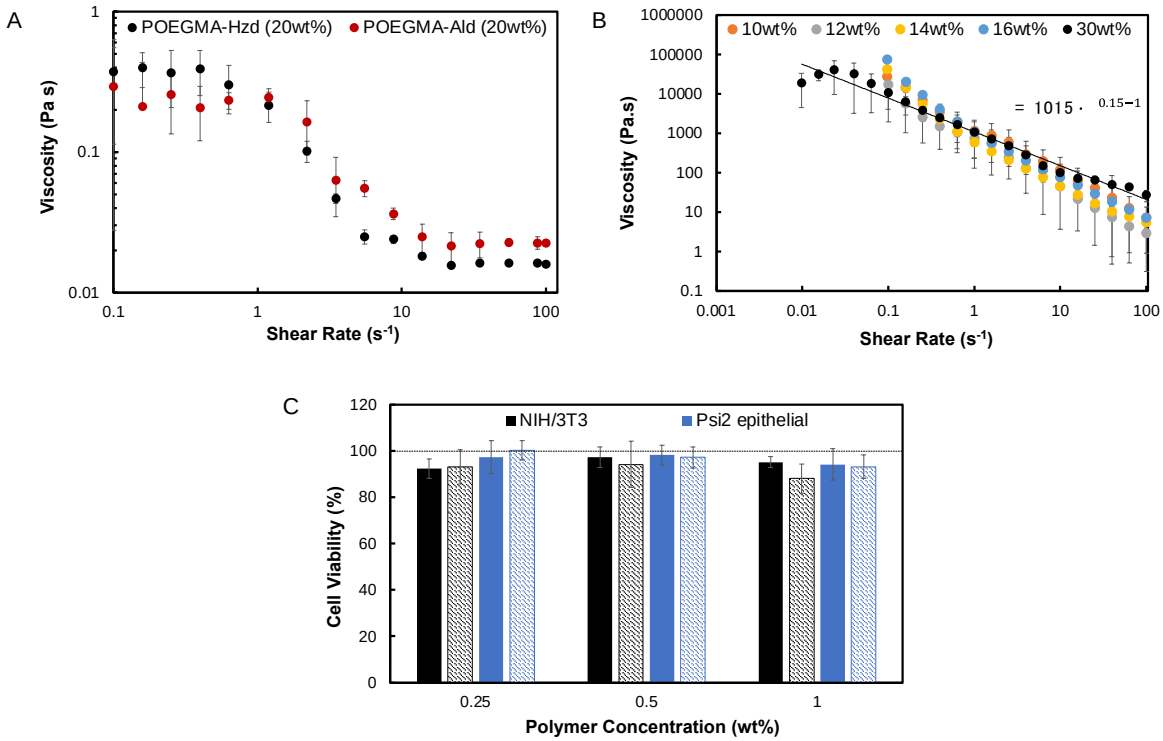

Figure 3.2: Key bioprinting properties of dynamic covalent POEGMA hydrazone-crosslinked hydrogels and precursor polymers: (A) viscosity sweeps of the precursor polymers, POEGMA-Hzd and POEGMA-Ald, at a concentration of 20 wt%; (B) viscosity sweeps of the hydrogel relative to the precursor polymers (10, 12, 14, 16, and 30 wt% precursor polymer concentrations), with the line representing the best-fit of the power law exponent for the 30 wt% precursor polymer solution; (C) cytotoxicity of POEGMA-Hzd (solid) and POEGMA-Ald (shaded) precursor polymers at various concentrations to NIH/3T3 fibroblasts and Psi2 12S6 epithelial cells as measured using the Presto Blue assay.

3.3.2 Coaxial Printing with and without a Mixing Zone

Hydrazone-crosslinked POEGMA hydrogels were first printed using a conventional flush coaxial needle with an inner gauge of 20 and an outer gauge of 16, with POEGMA-Hzd delivered in the core and POEGMA-Ald delivered in the shell at a polymer concentration of 10 wt%; the slowest gelling hydrogel mixture was chosen to minimize the chance of needle clogging. Using the customized printer to print at 200 μL/min, single-layer constructs were successfully printed onto a Petri dish (**Figure S3.1**). Comparing the measured fiber diameter to the theoretical fiber diameter (i.e., the inner diameter of the outer 16 gauge needle, 1.18 mm), significant spreading was observed using the flush coaxial needle, with the printed diameter approximately twice as large as the theoretical diameter and a high standard deviation observed in the measured diameter (**Figure 3.3**). This result is consistent with the relatively slow ~15 second gelation time of the 10 wt% ink (**Table 3.2**) and the lack of contact between the precursor polymers prior to deposition with the flush needle. **Figure S3.2** shows that high viability of NIH/3T3 cells could be maintained both 24 hours and 1-week post-printing; however, significant cell leaching and poor reproducibility between prints were observed.

To improve the mixing and thus the anticipated print fidelity of the coaxially printed fibers, a mixing zone was introduced in the coaxial needles by using an inner needle that was shorter than the outer needle (a "centre-cut" needle design), creating a single bore "mixing zone" at the end of the needle that can allow for diffusion of the functional polymers prior to the extrusion onto the chosen substrate. In contrast to the flush needle, the diameters achieved when introducing a mixing zone were nearly identical to the anticipated diameters based on the outer needle gauge, with very low standard deviations in print feature diameter observed (**Figure 3.3**).

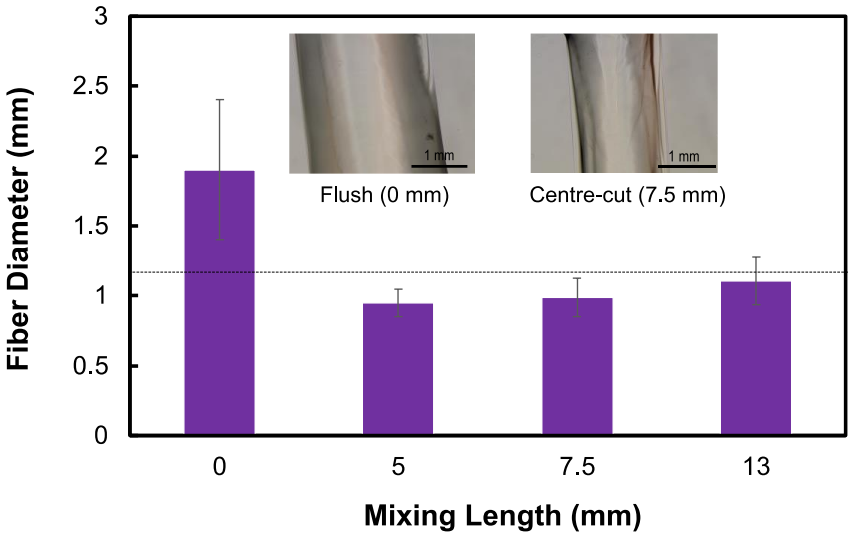

Figure 3.3: Comparison of the average printed fiber diameter using a 10 wt% precursor polymer concentration when printing with the flush coaxial needle (20/16) or a centre-cut coaxial needle resulting in three different mixing lengths prior to the needle outlet. The dotted line represents the theoretical fiber diameter, equal to the inner diameter of the outer needle in the coaxial needle. The inset images show the large spreading observed with the flush coaxial needle.

3.3.3 Fluid Mechanics Analysis of the Mixing Zone

A computational model using non-Newtonian fluid behavior to mimic the shear thinning behaviour of the crosslinked POEGMA hydrogel within the mixing zone was used to assess the degree of precursor polymer mixing enabled by the inclusion of a mixing zone. A power law with the exponent (n) of 0.15 was used in this computational model based on fitting the rheological data from **Figure 3.2B**, allowing the model to mimic the shear-thinning behaviour in the mixing zone assuming the final hydrogel provides an approximation of the shear thinning capacity of the bioink throughout this mixing zone. The resulting mass fractions at the outlet are shown in **Figure 3.4**.

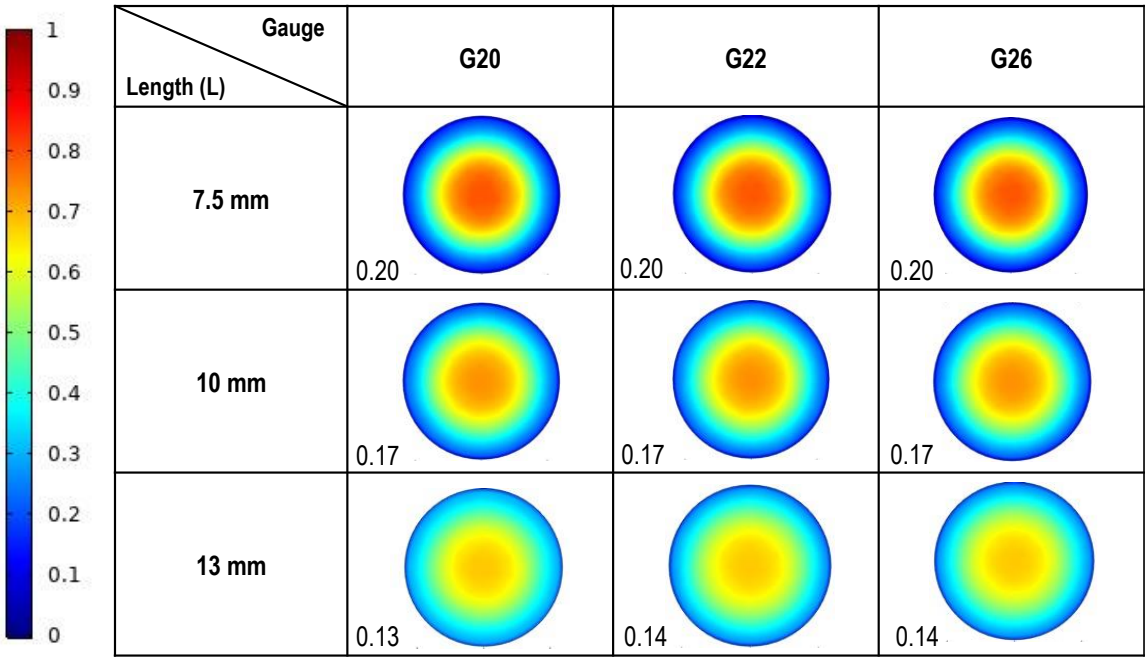

Figure 3.4: COMSOL model results using a non-Newtonian flow model showing the mass fraction of the POEGMA-Hzd polymer as a function of the cross-section of the inner diameter of the outer coaxial needle depending on the inner needle gauge and the length of the mixing zone. The mixing efficiencies (the standard deviation of the pixel intensities) are included underneath each mass fraction profile.

Increasing the length of the mixing zone provides more time for the diffusion of the functional polymers and thus improves mixing between the precursor polymers; in contrast, changing the inner needle gauge from 20 to 26 did not yield any significant change in the precursor polymer mixing. Calculation of the mixing efficiency (representative of the standard deviation of the pixels within the cross-sectional mass fraction profile at the outlet) confirms this result, with the lowest mixing efficiencies achieved with the longest 13 mm mixing zone (~0.13) while the highest mixing efficiencies were recorded at the shortest 7.5 mm mixing zone (~0.20). Interestingly, a similar conclusion is drawn if a Newtonian-only model with four increasing step viscosities along the mixing zone are used (Supporting **Figure S3.3** and **Figure S3.4**), although the mixing efficiencies were consistently (albeit marginally) lower (indicative of improved mixing) for the Newtonian model due to the higher estimated viscosities early in the mixing zone estimated by the non-Newtonian model. It is likely the flow transitions from Newtonian early in the mixing zone to non-Newtonian later in the mixing zone, making the most realistic result likely to lie between these two more extreme estimates; however, the similarity between the two estimates suggests high confidence in using the COMSOL model to understand mixing in these concentric needle systems.

3.3.4 Validating the Mixing Using the Customized Printer

To determine the practical relevance of the computational model, single-layer prints were performed by experimentally varying (1) the length of the mixing zone, (2) the inner core needle diameter, (3) the flow rate, and (4) the polymer concentrations.

Effect of the Length of the Mixing Zone

Three mixing lengths of 5, 7.5, and 13 mm were used to print POEGMA precursor polymers at concentrations of 10 wt% using a 20/16 coaxial needle and a volumetric flow rate of 200 µL/min. **Figure 3.5A** shows the prints achieved using all three mixing zone lengths for 10 wt% polymers, while **Figure 3.5B** quantifies the normalized mean colour intensities from the final prints using the pre-coloured precursor polymers (POEGMA-Hzd = blue food coloring, POEGMA-Ald = yellow food coloring).

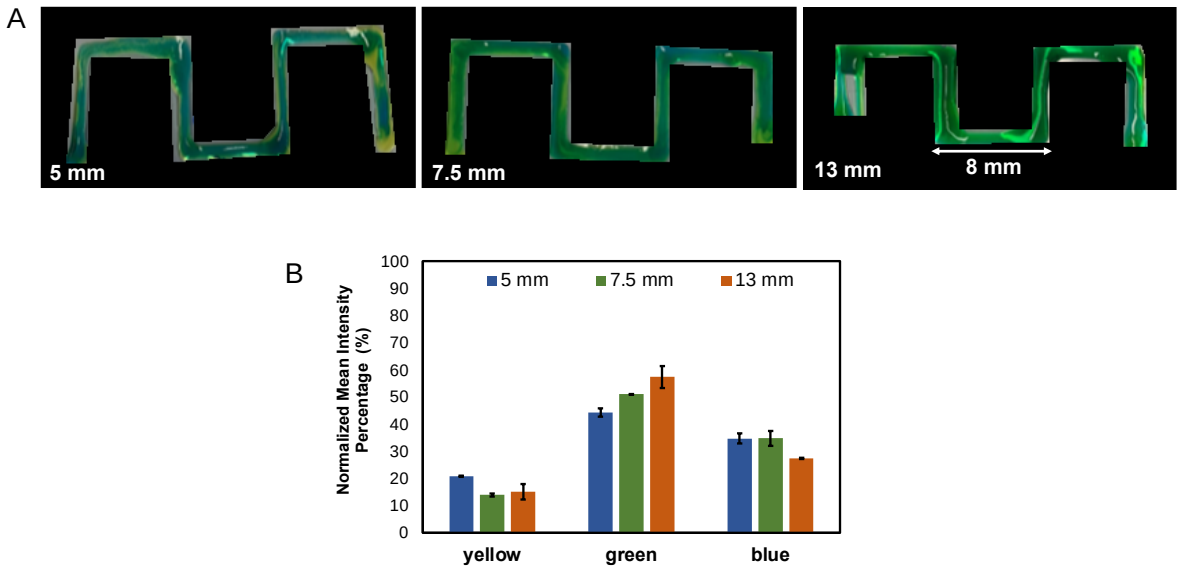

Figure 3.5: Effect of the length of the mixing zone in printing POEGMA hydrogels at 10 wt% precursor polymer concentrations using centre-cut coaxial needles with varying mixing zone lengths: (A) pictures of printed features; (B) normalized (percentage of total) intensity of yellow (POEGMA-Ald), blue (POEGMA-Hzd), and green (mixed) pixels in prints shown in A.

Based on the qualitative and quantitative results in **Figure 3.5**, the longer mixing zone (13 mm vs. 5 mm) showed improved mixing between the two functional polymers at the lower 10 wt% polymer concentration (~15 s gelation time), as evidenced by the continuous green colour observed throughout the printed construct (**Figure 3.5A**) and the higher relative green pixel

fraction in the quantitative analysis (**Figure 3.5B**). However, when the polymer concentration was increased to 12 wt% (~10 s gelation time), fewer clear benefits of increasing mixing zone length were observed; indeed, use of the 13 mm length mixing zone showed an increased risk of clogging relative to the other tested mixing zone lengths, making the 7.5 mm length mixing zone optimal for creating high-quality repeatable prints. As such, the length of the mixing zone optimal for a given print varies based on the gelation kinetics of the bioink, demonstrating the critical importance of balancing contact time with gelation time for effective coaxial printing of *in situ*-gelling hydrogel bioinks.

Effect of Core Needle Diameter

The effect of the core needle diameter was evaluated by changing the inner needle gauge from 20G to 22G, with the resulting qualitative and quantitative results shown in **Figure 3.6**. No significant difference is observed between the homogeneity achieved using either inner needle gauge, with the same filament diameters (1.3 ± 0.20 and 1.3 ± 0.22 mm for gauge 20 and gauge 22, respectively) and similar green pixel intensities (i.e., well-mixed zones) observed in both cases. As such, as predicted by the COMSOL model, the inner gauge does not significantly affect printability.

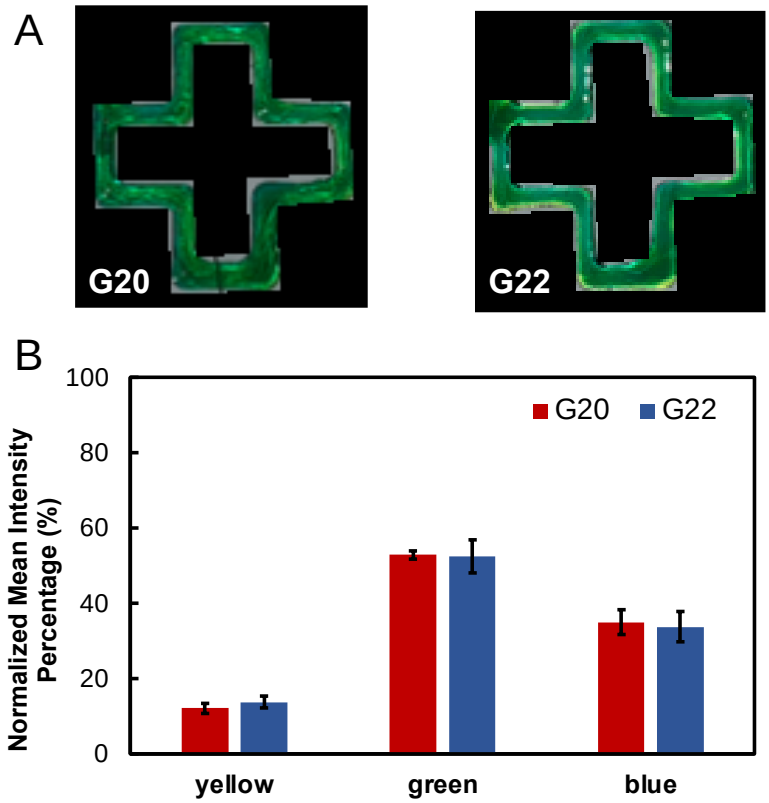

Figure 3.6: Effect of the core needle diameter on the homogeneity of the printed constructs when printing POEGMA hydrogels using 10 wt% polymer concentration and a centre-cut coaxial needle with a mixing length of 7.5 mm: (A) images of prints with an inner 20G and 22G coaxial needle; (B) normalized (percentage of total) intensity of yellow (POEGMA-Ald), blue (POEGMA-Hzd), and green (mixed) pixels in prints shown in A.

Effect of Polymer Concentration and Gelation Time

Polymer concentrations of 10 wt% (~15 s gelation time), 12 wt% (~10 s gelation time), 14 wt % (~8 s gelation time) and 16 wt% (~5 s gelation time) were printed using a 20/16 coaxial needle, a mixing zone of 7.5 mm (chosen based on the result in **Figure 3.5** in which faster gelation induced clogging in the 13 mm mixing length needle) and a volumetric flow rate of 200 µL/min, with printability assessed both for a single layer print as well as a three layer print to demonstrate the potential for building height in the prints. The results of these prints are summarized in **Figure 3.7**.

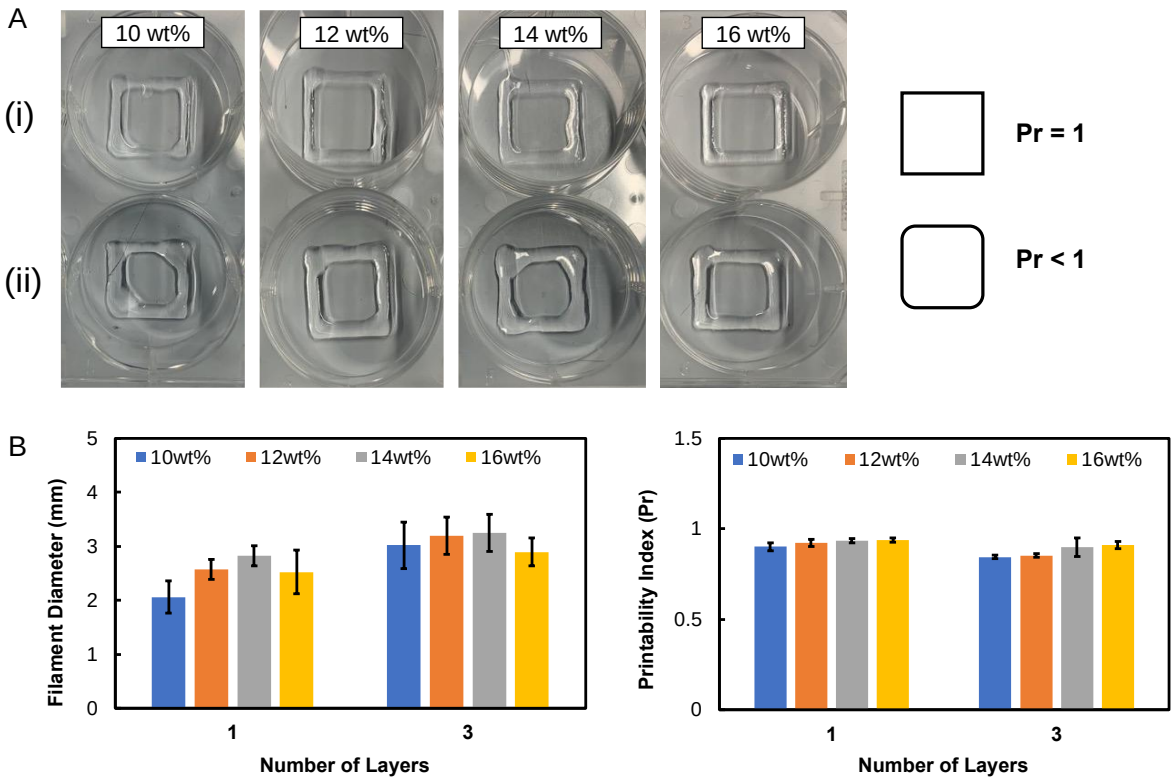

Figure 3.7: Effect of polymer concentration on print fidelity using a 20/16 centre-cut coaxial needle with a mixing zone of 7.5 mm: (A) visual representation of 1-layer (i) and 3-layer (ii) prints; (B) quantitative analysis of filament diameter and printability index.

Across the polymer concentrations evaluated, no significant change in either filament diameter or printability index was observed for both 1-layer and 3-layer prints when a mixing zone was included. Given that varying concentrations of the precursor polymers result in the fabrication of hydrogels with different mechanics (as per our previous work[19]), this result suggests that printed fibers with different mechanics can be effectively printed using the same basic print geometry (including the potential for multi-layer structures). Ultimately, the 14 wt% polymer concentration was identified as the optimal concentration to balance improved mechanics (i.e., higher crosslink densities) with avoiding clogging and thus enabling reproducible prints.

Polymer Distribution Using Optimized Printing Conditions

To better understand the effects of the mixing zone on the distribution of the precursor polymers within the resulting printed gel, POEGMA-Hzd was labelled with FITC (green) while POEGMA-Ald was labelled with rhodamine (red); the two labeled precursor polymers were then printed using the optimized printing parameters (sheath gauge 16, core gauge 20, volumetric flow rate 200 µL/min, and precursor polymer concentration 14 wt%) using both a

flush coaxial needle and a centre-cut coaxial needle with the optimized mixing length of 7.5 mm. Confocal microscopy was then used to assess the polymer distribution before and after immersing the printed structures in phosphate buffered saline, with the results shown in **Figure 3.8**.

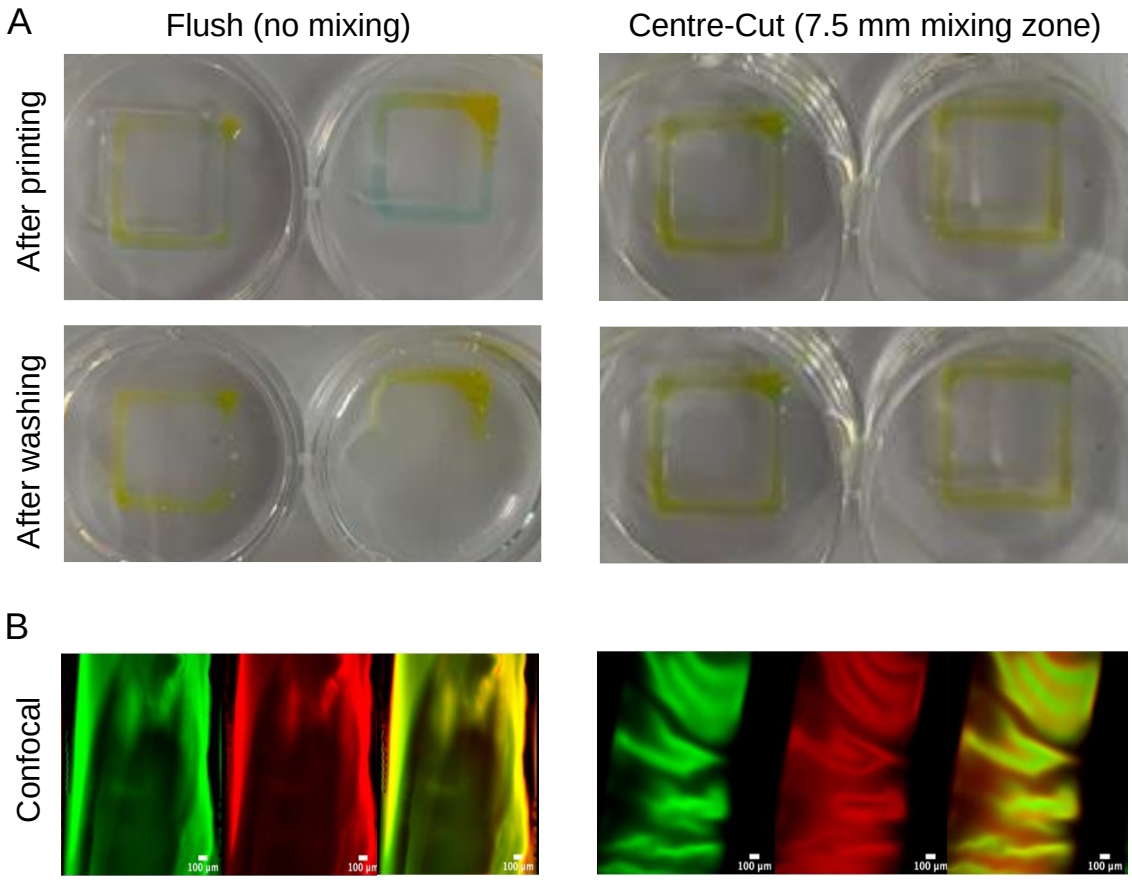

Figure 3.8: Polymer distribution in single-layer prints prepared with a flush coaxial needle (left column) and a centre-cut coaxial needle with a 7.5 mm mixing zone (right column) printed using the same optimized printing parameters and the polymer concentration (14 wt%): (A) optical images of prints before and after washing; (B) confocal images after washing (left = green channel, POEGMA-Hzd-FITC; middle = red channel POEGMA-Ald-Rho; yellow = mixed channel).

Including a mixing zone both significantly improves the stability of the print after washing (**Figure 3.8A**) as well as the uniformity of the two polymers in the resulting print (**Figure 3.8B**); of particular note, while the flush needle resulted in a sequestered nearly core-shell polymer distribution within the printed fiber, the centre-cut coaxial needle resulted in a banded pattern of polymer distribution in which polymer more uniformly filled the entire volume of the printed fiber. This imaging result is consistent with the observed improved stability of both the fiber itself as well as the print geometry in **Figure 3.8A**.

Co-Printing with NIH/3T3 Fibroblast Cells

After optimizing the printing parameters, NIH/3T3 fibroblast cells (~8 million cells/mL) were co-printed to determine the cell viability over a 14-day culture period and the effect of including cells on the optimized printing parameters. Printing was performed using a coaxial needle with a sheath gauge of 16 and a core gauge of 20, a volumetric flow rate of 200 µL/min, a polymer concentration of 14 wt% (identified in **Figure 3.7** to give well-defined prints without clogging but on the upper end of printable polymer concentrations to provide some buffer in case the presence of cells increases the gelation time), and a mixing length of 13 mm. Note that the longer mixing zone was chosen in this experiment due to the inclusion of cells slightly increasing the gelation time. A LIVE/DEAD assay was performed after 1, 7, and 14 days in culture, with the resulting the 2D and 3D confocal images shown in **Figure 3.9**.

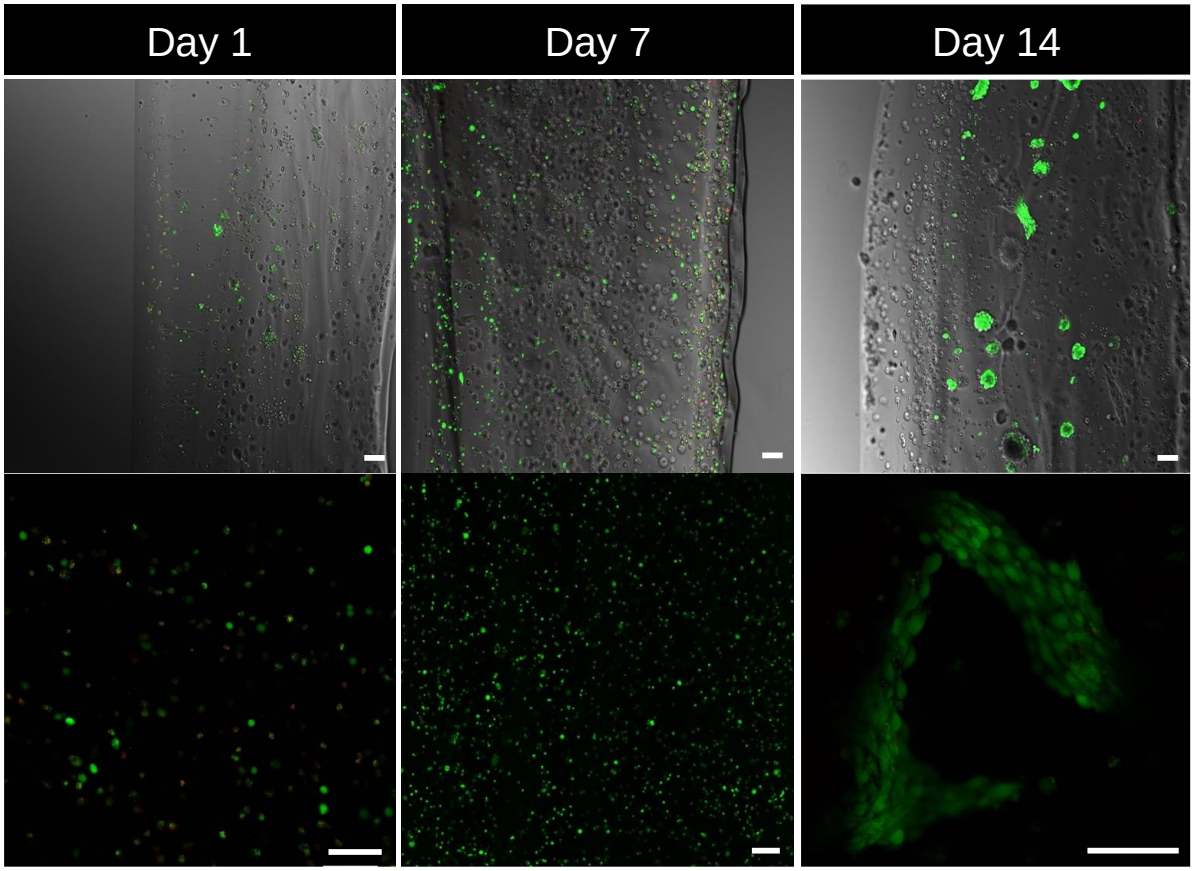

Figure 3.9: Viability of 3T3/NIH fibroblast cells over a 14-day culture period in the single-layer patterning prints using a centre-cut concentric needle with sheath gauge 16, core gauge 20, and mixing length 13 mm (volumetric flow rate 200 µL/min, precursor polymer concentration 14 wt%, cell density 8 million cells/mL). The scale bars represent 100 μm.

High cell viability is observed in the printed scaffolds at all imaged time points, with >85% of the imaged cells remaining viable; furthermore, while a significant decrease in the cell density was observed over time in hydrogels printed using the flush coaxial needle (**Figure S3.2**), no such decrease was observed with the centre-cut needle; indeed, some evidence of cell proliferation is observed between 1 and 7 days. Of interest, after 14 days, cell spreading and resulting spheroid formation were observed, consistent with weak cell-scaffold interactions induced by the POEGMA gels as shown in our previous work[30]; note that the formation of spheroids however made it difficult to quantify cell proliferation as accurate cell counting within the spheroids was challenging. The scaffolds also remain relatively well-defined over the 14-day evaluation period, also suggesting improved scaffold integrity with the inclusion of the mixing zone.

To assess the potential to co-print homogeneous distributions of multiple cell lines, pre-stained 3T3/NIH fibroblasts (CFSA labelled, green) and Psi2 12S6 epithelial cells (Far-Red labelled, red) were incorporated in the core and shell precursor solutions, respectively (**Figure 3.10**). The experiment was performed using a sheath gauge of 16, core gauge of 20, volumetric flow rate of 200 µL/min, polymer concentration of 14 wt% and mixing length of 13 mm, the same conditions used for the single cell (**Figure 3.9**). No significant spatial concentration of either cell line was observed in the images, suggesting that not only the polymers but also the cells can undergo efficient mixing during printing without compromising cell viability. In contrast, performing the same experiment with the flush needle created unstable printed constructs that washed away immediately when exposed to media and thus could not be imaged, consistent with the single cell results as well as the COMSOL model predictions. Indeed, we believe that inclusion of the mixing zone is particularly important for printing the cellularized scaffolds given the role of cells in sterically inhibiting the dynamic covalent gelation process, requiring more intimate mixing between the precursor polymers to create hydrogels with sufficient crosslink density to produce stable printed fibers.

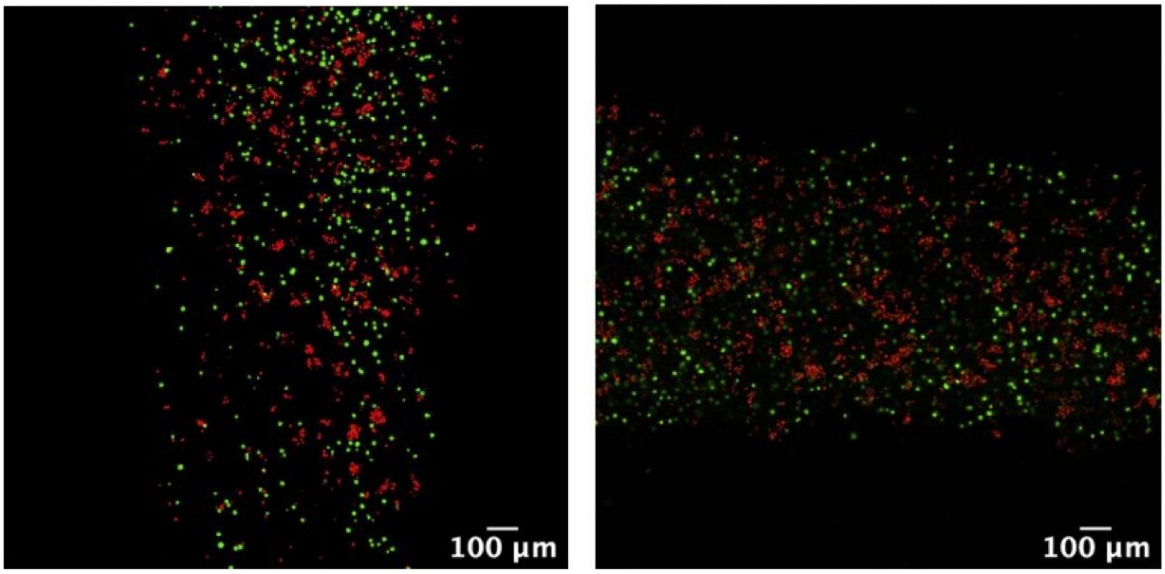

Figure 3.10: Confocal microscopy images of co-culture prints with 3T3/NIH fibroblasts (CFSA labelled, green) loaded in the core solution and Psi2 12S6 epithelial cells (Far-Red labelled, red) loaded in the shell solution (centre-cut concentric needle with sheath gauge 16, core gauge 20, and mixing length 13 mm, volumetric flow rate 200 µL/min, precursor polymer concentration 14 wt%, cell density 10 million cells/mL of each precursor solution).

3.4 Discussion

Coaxial bioprinting conventionally uses the concentric flow patterns to fabricate core-shell fibers that can localize encapsulated cells or provide a way to incorporate sacrificial materials for the fabrication of hollow fibers. Dynamic covalent hydrogel bioinks offer beneficial properties in the context of extrusion bioprinting given that they do not require any additives to facilitate crosslinking, are well-suited for cell encapsulation, and do not need any post-processing. However, printing the functional precursor polymers is not trivial due to the mixing that is required to form a homogeneously crosslinked network. Printing with a coaxial needle design has not been demonstrated for hydrazone chemistry, or any dynamic covalent-based bioink, due to the conventional flush needle design not allowing for sufficient mixing to create stable fibers between the needle end and the print support. In this work, direct free-form printing of hydrazide and aldehyde functionalized POEGMA polymers was made possible using a modified coaxial needle that incorporates a mixing zone in which a shorter inner needle is aligned within a longer outer needle to create a pre-determined distance within the needle for the functional polymers to mix and thereby crosslink prior to deposition. Without this mixing zone, significant spreading (up to 200% of the theoretical fiber diameter, **Figure 3.3**) and poor reproducibility were recorded; using the mixing zone, good correlations between the

actual and theoretical fiber diameters were achieved with much lower fiber-to-fiber variability. To streamline the number of possible needle configurations that would need to be experimentally tested within the printing optimization, a computational model using COMSOL was first developed to determine the mass fraction profile at the outlet for different inner needle gauges (or diameters) and mixing lengths and minimize the number of experimental conditions required to test to optimize print fidelity and stability. Increasing the length of the mixing zone improved the homogeneity of the resulting print using either a Newtonian or non-Newtonian viscosity prediction for the mixing zone, consistent with more efficient the mixing between the two functional polymers leading to better homogeneity and improved crosslinking (**Figure 3.4**); however, the inner needle gauge did not significantly influence mixing, a result we attribute to the laminar flow regime achieved at the relatively low printing flow rates used that make only diffusion the driving force for mixing rather than turbulence at fluid contact points. Both these model predictions were validated using experimental printing trials, with a mixing zone of either 7.5 mm (for <10 seconds in gelation time, 14 wt% polymer concentration or higher) or 13 mm (for >10 seconds in gelation time) (**Figure 3.5**), an inner needle gauge of 20 (**Figure 3.6**), and a polymer concentration of 14 wt% (**Figure 3.7**) identified as the optimal bioink and process conditions for fabricating reproducible, stable, and high-fidelity prints. Of note, when cells were included, a longer mixing length was found to provide improved prints given that the presence of cells increased the gelation time from <10 s (without cells) to >10 s; as such, while the general printing guidelines identified remained consistent with or without cells, the inclusion of cells changed the optimal printing setup at a given polymer concentration. The inclusion of the mixing zone allowed for the fabrication of significantly more homogeneous structures than possible with a flush coaxial needle, as demonstrated using fluorescently labelled polymer precursors (**Figure 3.8**). The printed scaffolds were demonstrated to maintain not only cell viability but also support cell proliferation and cell spreading, leading to spheroid formation at extended culture times (**Figure 3.9**). Furthermore, co-cultures could be printed with high homogeneity of cell distribution without inducing significant cell toxicity (**Figure 3.10**).

3.5 Conclusion

Coaxial bioprinting of hydrazone crosslinked POEGMA hydrogels was enabled with an optimized coaxial needle design that incorporates a mixing zone for the functional polymers to be effectively mixed and crosslinked prior to extrusion. A computational model was developed to determine the effects of the length of mixing and the inner needle diameter on the diffusion (and homogeneity) of the functional polymers that would in turn affect the crosslinking of the printed constructs. Through a combination of computational modeling and experimental validation tests, optimal printing parameters of using a coaxial needle with outer gauge 20 and inner gauge 16, a mixing zone of either 7.5 mm or 13 mm depending on the gelation time, a volumetric flow rate of 200 µL/min, and a polymer concentration of 14 wt% were identified. The final homogeneity of the prints was significantly improved with the mixing zone that could be tracked by fluorescently labelling the precursor polymers and by pre-staining the cells in the core and shell. Further optimization of the needle design is likely to extend this work to printing larger 3D constructs.

3.6 Acknowledgements

The Natural Sciences and Engineering Research Council (Discovery Grant RGPIN-2017-06455 to TH and RG), a Canada Graduate Scholarship (to EM), a NSERC E.W.R. Steacie Memorial Fellowship (for AA), and a Mitacs Globalink (for LK) are acknowledged for funding.

3.7 References

1. Chung, J. H.; Naficy, S.; Yue, Z.; Kapsa, R.; Quigley, A.; Moulton, S. E.; Wallace, G. G., Bio-ink properties and printability for extrusion printing living cells. *Biomater. Sci.* **2013,** *1* (7), 763-773.
2. Ramesh, S.; Harrysson, O. L.; Rao, P. K.; Tamayol, A.; Cormier, D. R.; Zhang, Y.; Rivero, I. V., Extrusion bioprinting: Recent progress, challenges, and future opportunities. *Bioprinting* **2021,** *21*, e00116.
3. Ozbolat, I. T.; Hospodiuk, M., Current advances and future perspectives in extrusion-based bioprinting. *Biomaterials* **2016,** *76*, 321-343.
4. Jiang, T.; Munguia-Lopez, J. G.; Flores-Torres, S.; Kort-Mascort, J.; Kinsella, J. M., Extrusion bioprinting of soft materials: An emerging technique for biological model fabrication. *Appl. Phys. Rev.* **2019,** *6* (1), 011310.
5. Hölzl, K.; Lin, S.; Tytgat, L.; Van Vlierberghe, S.; Gu, L.; Ovsianikov, A., Bioink properties before, during and after 3D bioprinting. *Biofabrication* **2016,** *8* (3), 032002.
6. Kjar, A.; McFarland, B.; Mecham, K.; Harward, N.; Huang, Y., Engineering of tissue constructs using coaxial bioprinting. *Bioact. Mater.* **2021,** *6* (2), 460-471.
7. Liu, W.; Zhong, Z.; Hu, N.; Zhou, Y.; Maggio, L.; Miri, A. K.; Fragasso, A.; Jin, X.; Khademhosseini, A.; Zhang, Y. S., Coaxial extrusion bioprinting of 3D microfibrous constructs with cell-favorable gelatin methacryloyl microenvironments. *Biofabrication* **2018,** *10* (2), 024102.
8. Kim, M. H.; Nam, S. Y., Assessment of coaxial printability for extrusion-based bioprinting of alginate-based tubular constructs. *Bioprinting* **2020,** *20*, e00092.
9. Shao, L.; Gao, Q.; Xie, C.; Fu, J.; Xiang, M.; He, Y., Directly coaxial 3D bioprinting of large-scale vascularized tissue constructs. *Biofabrication* **2020,** *12* (3), 035014.
10. Cooley, J. F., Apparatus for electrically dispersing fluids. *Google Patents*, **1902**.
11. Sefton, M. V.; Dawson, R. M.; Broughton, R. L.; Blysniuk, J.; Sugamori, M. E., Microencapsulation of mammalian cells in a water-insoluble polyacrylate by coextrustion and interfacial precipitation. *Biotech. Bioeng.* **1987,** *29* (9), 1135-1143.
12. Zein, I.; Hutmacher, D. W.; Tan, K. C.; Teoh, S. H., Fused deposition modeling of novel scaffold architectures for tissue engineering applications. *Biomaterials* **2002,** *23* (4), 1169-1185.
13. Kim, G.; Ahn, S.; Kim, Y.; Cho, Y.; Chun, W., Coaxial structured collagen–alginate scaffolds: fabrication, physical properties, and biomedical application for skin tissue regeneration. *J. Mater. Chem.* **2011,** *21* (17), 6165-6172.
14. Gopinathan, J.; Noh, I., Click chemistry-based injectable hydrogels and bioprinting inks for tissue engineering applications. *Tiss. Eng. Regen. Med.* **2018,** *15* (5), 531-546.
15. Mueller, E.; Poulin, I.; Bodnaryk, W. J.; Hoare, T., Click Chemistry Hydrogels for Extrusion Bioprinting: Progress, Challenges, and Opportunities. *Biomacromol.* **2022**. 23 (3), 619-640.
16. Correa, S.; Grosskopf, A. K.; Lopez Hernandez, H.; Chan, D.; Yu, A. C.; Stapleton, L. M.; Appel, E. A., Translational applications of hydrogels. *Chem. Rev.* **2021,** *121* (18), 11385-11457.
17. Hui, E.; Sumey, J. L.; Caliari, S. R., Click-functionalized hydrogel design for mechanobiology investigations. *Mol. Sys. Design Eng.* **2021**, 6, 670-707.

18. Geng, Z.; Shin, J. J.; Xi, Y.; Hawker, C. J., Click chemistry strategies for the accelerated synthesis of functional macromolecules. *J. Polym. Sci.* **2021,** *59* (11), 963-1042.
19. Wang, L. L.; Highley, C. B.; Yeh, Y. C.; Galarraga, J. H.; Uman, S.; Burdick, J. A., Three-dimensional extrusion bioprinting of single- and double-network hydrogels containing dynamic covalent crosslinks. *J. Biomed. Mater. Res A* **2018,** *106* (4), 865-875.
20. Malekpour, A.; Chen, X., Printability and cell viability in extrusion-based bioprinting from experimental, computational, and machine learning views. *J. Funct. Biomater.* **2022,** *13* (2), 40.
21. Chiesa, I.; Ligorio, C.; Bonatti, A. F.; De Acutis, A.; Smith, A. M.; Saiani, A.; Vozzi, G.; De Maria, C., Modeling the three-dimensional bioprinting process of β-sheet self-assembling peptide hydrogel scaffolds. *Front. Med. Tech.* **2020,** *2*, 571626.
22. Mirani, B.; Stefanek, E.; Godau, B.; Hossein Dabiri, S. M.; Akbari, M., Microfluidic 3D printing of a photo-cross-linkable bioink using insights from computational modeling. *Biomater. Sci. Eng.* **2021,** *7* (7), 3269-3280.
23. Reina-Romo, E.; Mandal, S.; Amorim, P.; Bloemen, V.; Ferraris, E.; Geris, L., Towards the experimentally-informed in Silico nozzle design optimization for extrusion-based bioprinting of shear-thinning hydrogels. *Front. Bioeng. Biotech.* **2021,** *9*, 701778.
24. Müller, S. J.; Mirzahossein, E.; Iftekhar, E. N.; Bächer, C.; Schrüfer, S.; Schubert, D. W.; Fabry, B.; Gekle, S., Flow and hydrodynamic shear stress inside a printing needle during biofabrication. *PloS One* **2020,** *15* (7), e0236371.
25. Billiet, T.; Gevaert, E.; De Schryver, T.; Cornelissen, M.; Dubruel, P., The 3D printing of gelatin methacrylamide cell-laden tissue-engineered constructs with high cell viability. *Biomaterials* **2014,** *35* (1), 49-62.
26. Müller, M.; Öztürk, E.; Arlov, Ø.; Gatenholm, P.; Zenobi-Wong, M., Alginate sulfate–nanocellulose bioinks for cartilage bioprinting applications. *Ann. Biomed. Eng.* **2017,** *45* (1), 210-223.
27. Prendergast, M. E.; Davidson, M. D.; Burdick, J. A., A biofabrication method to align cells within bioprinted photocrosslinkable and cell-degradable hydrogel constructs via embedded fibers. *Biofabrication* **2021,** *13* (4), 044108.
28. Silva, C.; Cortes-Rodriguez, C. J.; Hazur, J.; Reakasame, S.; Boccaccini, A. R., Rational design of a triple-layered coaxial extruder system: in silico and in vitro evaluations directed toward optimizing cell viability. *Inter. J. Bioprinting* **2020,** *6* (4), 282.
29. Smeets, N. M.; Bakaic, E.; Patenaude, M.; Hoare, T., Injectable and tunable poly(ethylene glycol) analogue hydrogels based on poly(oligoethylene glycol methacrylate). *Chem. Comm.)* **2014,** *50* (25), 3306-9.
30. Ouyang, L.; Yao, R.; Zhao, Y.; Sun, W., Effect of bioink properties on printability and cell viability for 3D bioplotting of embryonic stem cells. *Biofabrication* **2016,** *8* (3), 035020.

3.8 Supplementary Information

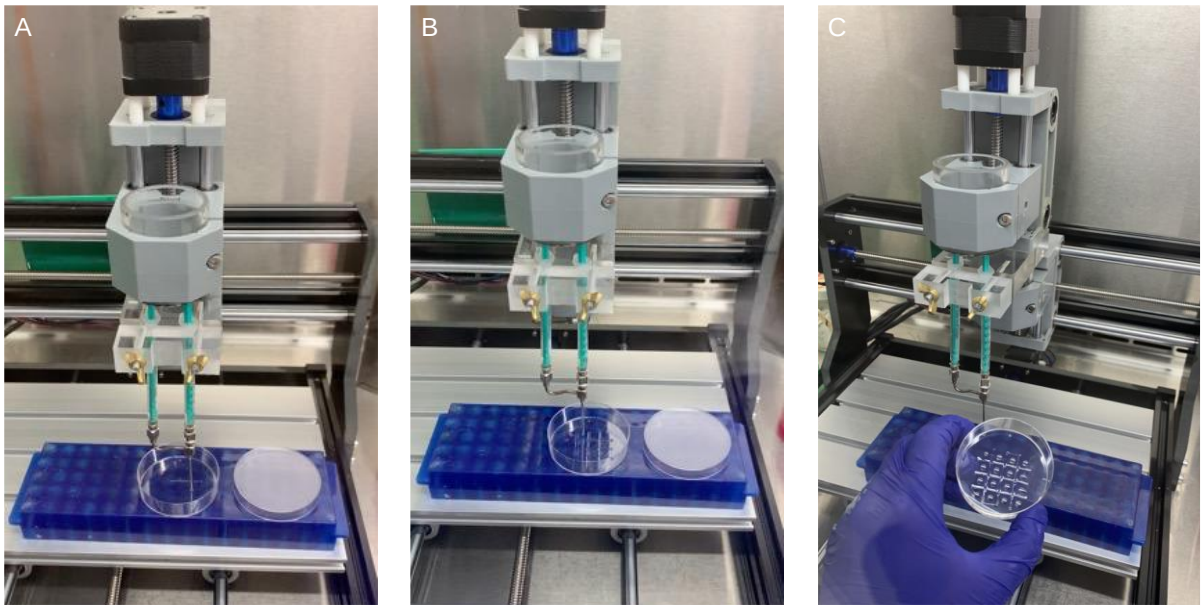

Figure S3.1: Coaxial bioprinting of POEGMA hydrogels using a customized 3D bioprinter

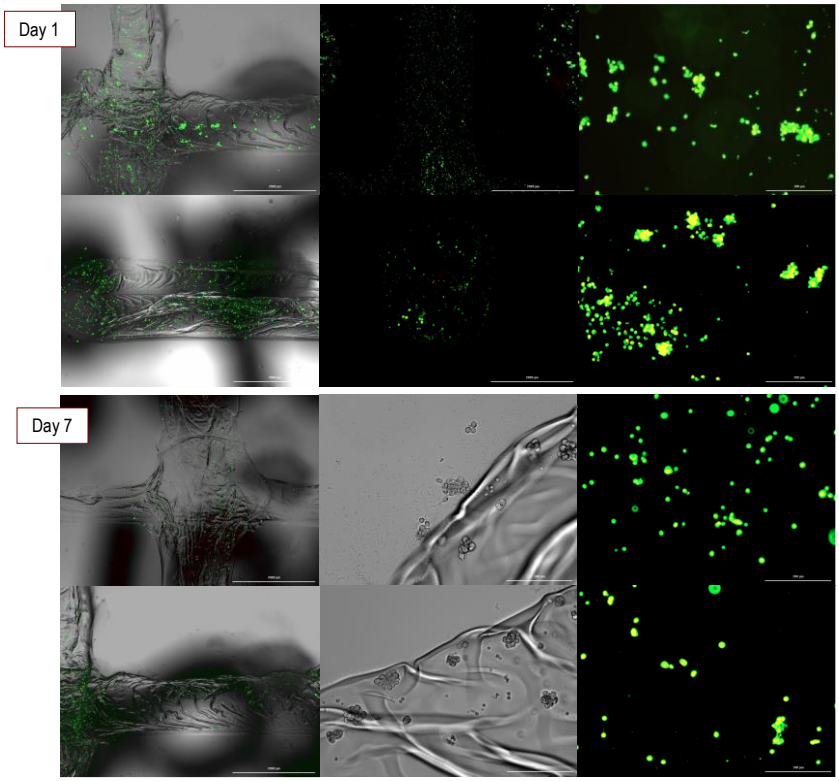

Figure S3.2: Coaxial bioprinting with NIH/3T3 fibroblast cells and POEGMA hydrogel bioink (10 wt% polymer concentration) using a flush 20/16 coaxial needle. Live-dead assay results show high maintained cell viability after one week (due to the absence of red cells), but significant cell leaching; furthermore, significant variation in fiber diameter is observed. These results are in contrast to those obtained using the centre-cut coaxial needls, which led to more stable and much more homogeneous fibers that could retain cells within the printed hydrogel.

Table S3.1: Filament diameter across prints fabricated using different mixing lengths and polymer concentrations

Polymer Concentration	**5 mm Mixing Length**	**7.5 mm Mixing Length**	**13 mm Mixing Length**
10 wt%	0.95±0.10	0.99±0.14	1.11±0.31
12 wt%	1.60 ±0.20	1.18 ±0.19	1.3 ±0.17

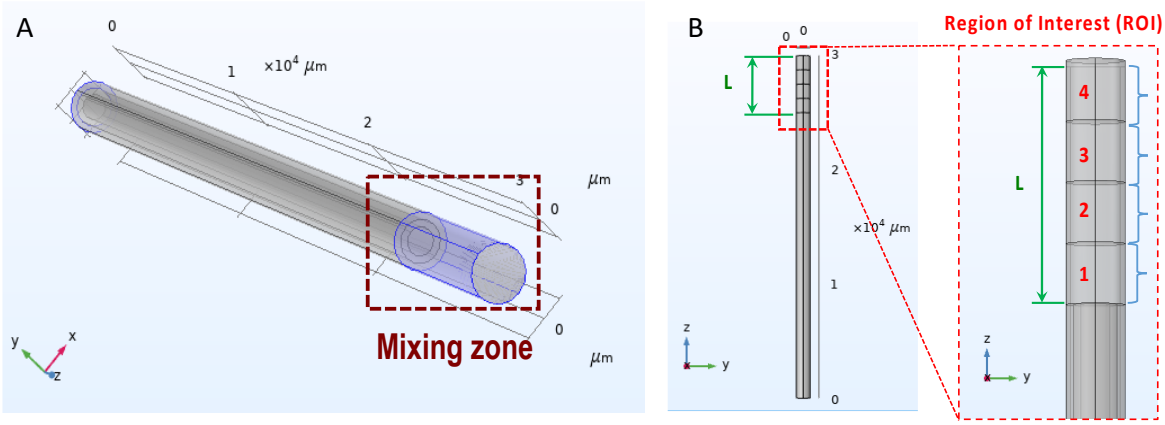

Figure S3.3: First-generation COMSOL model using a mixing zone (A) divided into four distinct regions modeled with different viscosity values (B) to simulate the *in situ* crosslinking process.

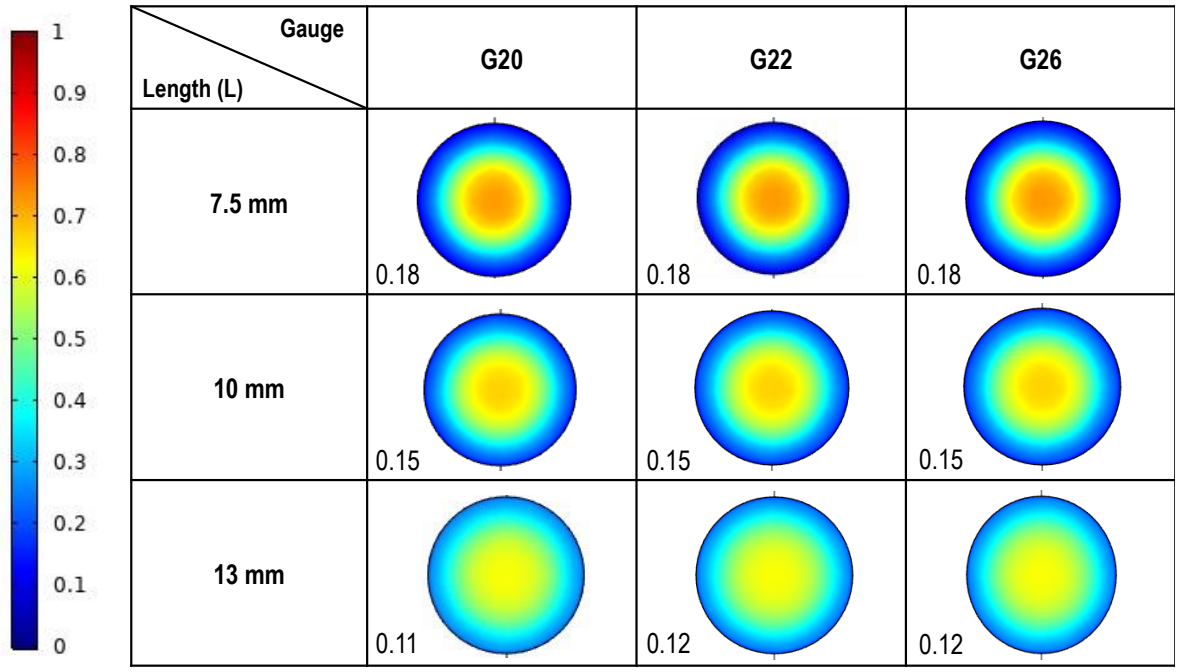

Figure S3.4: COMSOL model results using a four-stage Newtonian flow model showing the mass fraction of the POEGMA-Hzd polymer as a function of the cross-section of the inner diameter of the outer coaxial needle upon changing the inner needle gauge and the length of the mixing zone. The mixing efficiencies (corresponding to the standard deviation of the pixel intensities with lower values indicating higher homogeneity) are included underneath each mass fraction profile.

CHAPTER 4

FRESH Bioprinting of Dynamic Hydrazone-Crosslinked Synthetic Hydrogels

Eva Mueller, Fei Xu, and Todd Hoare

Declaration of Academic Achievement:

This chapter is based on a published paper, with all text and figures/tables reproduced with permission from American Chemical Society (Copyright 2022). Dr. Fei Xu helped with the cell experiments (viability, adhesion) and provided helpful insights in the experimental analysis. All writing and manuscript preparation were done by Eva Mueller and edited with the help of Dr. Todd Hoare.

Mueller, E.; Xu, F.; Hoare, T., FRESH Bioprinting of Dynamic Hydrazone-Crosslinked Synthetic Hydrogels. *Biomacromolecules* 2022, 23 (11), 4883-4896.

FRESH Bioprinting of Dynamic Hydrazone-Crosslinked Synthetic Hydrogels

Eva Mueller, Fei Xu, and Todd Hoare

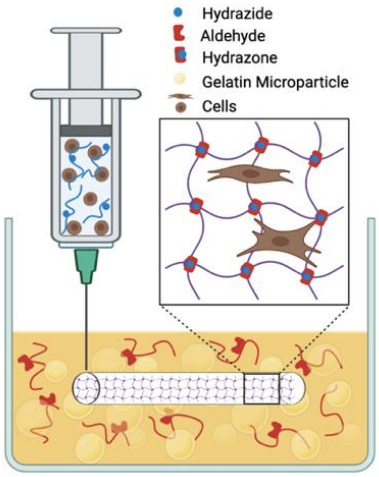

Dynamic covalent chemistry is an attractive crosslinking strategy for hydrogel bioinks due to its ability to mimic the dynamic interactions that are natively present in the extracellular matrix. However, the inherent challenges in mixing the reactive precursor polymers during printing and the tendency of the soft printed hydrogels to collapse during free-form printing have limited the use of such chemistry in 3D bioprinting cell scaffolds. Herein, we demonstrate 3D printing of hydrazone-crosslinked poly(oligoethylene glycol methacrylate) (POEGMA) hydrogels using the freeform reversible embedding of suspended hydrogels (FRESH) technique coupled with a customized low-cost extrusion bioprinter. The dynamic nature and reversibility of hydrazone crosslinks enables reconfiguration of the initially more heterogeneous gel structure to form a more homogeneous internal gel structure, even for more highly crosslinked hydrogels, over a relatively short time (<3 days) while preserving the degradability of the scaffold over longer time frames. POEGMA hydrogels can successfully print NIH/3T3 fibroblasts and human umbilical vein endothelial cells while maintaining high cell viability (>80%) and supporting F-actin-mediated adhesion to the scaffold over a 14-day *in vitro* incubation period, demonstrating their potential use in practical tissue engineering applications.

Keywords: 3D bioprinting, dynamic covalent chemistry, FRESH bioprinting, poly(oligoethylene glycol methacrylate), hydrazone chemistry

4.1 Introduction

The classical tissue engineering paradigm of growing cells in two-dimensions has been largely replaced with three-dimensional (3D) tissue engineering approaches to better mimic native tissues. 3D bioprinting has emerged as a powerful strategy to produce complex functional tissue constructs with precisely patterned cells[1-5] by effectively merging advances in the materials science of cell scaffolds with the ability to computationally control the position at which those materials can be deposited. Soft hydrogels provide a favorable environment for cells to grow, proliferate and differentiate[2, 6, 7]; however, the number of soft hydrogel "bioinks" (comprising both the hydrogel material and the constituent cells) that can be printed is limited within the context of currently reported bioprinting platforms[8]. The most common crosslinking strategies including ionic crosslinking (i.e., alginate/calcium[9, 10]), photocrosslinking (i.e., (meth)acrylated pre-polymer solutions[9, 11]), and post-modification in external conditions (i.e., change in pH for collagen[12-14]) are all specific to a small subset of bioinks, thus limiting the chemical and biological flexibility of printed scaffolds toward engineering targeted 3D cell responses[15, 16]. In particular, control over the scaffold mechanics and degradation kinetics is essential such that the hydrogel can provide a supportive environment for cells to adhere and proliferate but ultimately clear at a rate correlated with functional tissue regeneration. Furthermore, the use of non-physiological calcium levels for ionic crosslinking[17], the use of cytotoxic photoinitiators for photocrosslinking[18, 19], and the non-physiological changes in pH for collagen stabilization[20] can all pose potential risks to cell viability.

To overcome these challenges, click chemistry-based hydrogel bioinks in which *in situ* covalent gelation can occur upon mixing two (or more) precursor polymers functionalized with complementary functional groups under normal physiological conditions represent a promising area of bioink development[21]. Dynamic covalent chemistry-crosslinked hydrogels are especially interesting for tissue engineering applications due to their ability to mimic the dynamic interactions that are natively present in the extracellular matrix[22-24]. While the use of dynamic click chemistry hydrogels to create extrusion bioinks is not well-established, a few papers have shown the potential of this chemistry in the context of 3D bioprinting. For example, Wang et al. reported in 2018 the successful 3D bioprinting of pre-mixed hydrazone crosslinked hyaluronic acid hydrogels that were further stabilized with a second photocrosslinkable interpenetrating network through a thiol-ene reaction[21]. This strategy exploited the shear thinning capacity of the dynamic crosslinks to enable printing, although the relatively limited

mechanics of the gel due to the need extrude the pre-gelled hydrogel required the subsequent photocrosslinking stabilization step for practical 3D printing. More recently, Morgan et al. designed a dynamic covalent hydrogel that mixed both hydrazone and oxime crosslinking to allow for tunable stiffness and stress relaxation over two orders of magnitude; the bioink was formed by pre-crosslinking oxidized alginate using two commercially available crosslinkers (adipic acid dihydrazide and *O,O'*-1,3-propanediylbishydroxylamine) and pre-extruding the bioink through the print needle to transiently rupture the network to enable extrusion printing[22]. However, the use of small molecule crosslinkers and the need for pre-gelation again limits both the *in vivo* practicality and the range of mechanics achievable using this approach. While other types of dynamic click chemistry hydrogel bioinks have been previously reviewed for printing high-resolution structures[21, 25], to date, no soft synthetic hydrogels based on dynamic covalent chemistry have been printed in 3D. While dynamic click chemistry hydrogel bioinks have been previously reviewed as a viable strategy for printing high-resolution structures[21, 25], to date, no soft synthetic hydrogels based on dynamic covalent chemistry have been printed in 3D. This limited success is based on two key challenges associated with such printing. First, rapidly gelling (<1-2 s) polymer precursors are required for freeform 3D printing to maintain shape fidelity following extrusion, resulting in significant challenges around *in situ* mixing the precursor polymers to ensure homogeneous prints but avoid nozzle clogging (particularly over the extended print times required for printing larger constructs). Second, the typical correlation between gelation time and crosslink density in dynamic covalent hydrogels limits the range of potential mechanics of the printed structures if printability is to be preserved, resulting in typically very soft printed structures that have a high tendency to collapse upon free-form printing[25].

The challenge associated with the collapse of soft 3D printed structures was the motivation behind developing gel-based support baths that can physically support the extrusion printing of soft hydrogels into higher-resolution constructs by confining a slower gelation process[23-25]. The support bath thus breaks the correlation between gelation time and mechanics, allowing the printing of stiffer scaffolds that can self-support upon the subsequent removal of the support bath. Of particular interest is the freeform reversible embedding of suspended hydrogels (FRESH) printing technique in which a bioink is printed directly into a gelatin microparticle support bath, crosslinked, and subsequently incubated at physiological temperature to liquify the gelatin support bath and thus release the printed construct[25-28]. Indeed, Heo et al. have demonstrated how FRESH bioprinting can enable printing of soft dynamic covalent hydrogel

bioinks based on natural polymers, exploiting the rapid crosslinking of carbohydrazide-modified gelatin in a support bath of gelatin microparticles suspended in an oxidized alginate solution to create hydrazone-crosslinked 3D scaffolds that can support the viability and growth of human mesenchymal stem cells and human umbilical vein endothelial cells[29]. However, despite the potential of synthetic polymer-based bioinks to enable control over the interfacial, mechanical, and degradation properties of the printed scaffolds[30, 31], few such bioinks have been successfully 3D printed using an embedded printing strategy. Indeed, the only such example to-date is Hull et al.'s work in FRESH bioprinting of UNIversal, Orthogonal Network (UNION) bioinks based on strain-promoted azide-alkyne cycloaddition (SPAAC)[32]; however, SPAAC click chemistry is inherently non-reversible in physiological conditions (resulting in challenges in clearing otherwise non-degradable synthetic polymer-based bioinks over time) and does not allow for dynamic remodeling of the scaffold that mimics the extracellular matrix.

The homogeneity of 3D prints fabricated through an embedded printing strategy can also be a drawback of the use of support bath-based approaches for 3D bioprinting. In particular, embedded printing approaches in which one reactive component is placed in the support bath (to overcome challenges with nozzle clogging) often lead to prints with a heterogeneous highly-crosslinked shell/lightly crosslinked (or still fluid) core structure due to the reliance on diffusion of the crosslinking (bath) polymer into the printed polymer volume to facilitate gelation; such diffusion is significantly slowed by the interfacial crosslinking that occurs rapidly at the printed polymer-support bath interface and the high affinity between the complementary precursor polymers involved in click-based gelation chemistry. The resulting inhomogeneous crosslink distribution may result in easier to fracture hydrogels and/or lower cell viability in the core of the printed structures than observed with a more homogeneous printed gel system. In this context, embedded printing of dynamic covalent chemistry-based bioinks offers the potential to create more homogeneous prints over time by exploiting the reversibility of dynamic covalent hydrazone linkages, offering a potential solution to both the challenges of nozzle clogging (given that the complementary precursor polymer can still be added in the support bath instead of mixed in the nozzle) and print homogeneity (promoting improved mechanics and 3D cell viability).

Herein, we leverage dynamic covalent hydrazone chemistry and the FRESH bioprinting method to report the first demonstration of creating homogeneous synthetic polymer-based dynamic 3D soft hydrogel scaffolds. Hydrazone bond formation via the crosslinking of hydrazide and aldehyde-functionalized poly(ethylene glycol methacrylate) (POEGMA)

precursor polymers occurs quickly upon mixing (in some cases <1 second, as typically required for 3D printing) and is reversible (via hydrolysis over time scales of weeks at acidic pH or months at neutral pH[36, 37]) without requiring any UV crosslinking, templating, or additional catalysts, providing an attractive chemical platform for directly incorporating cells during printing. POEGMA was chosen as the base polymer given its facile functionalization via radical copolymerization, demonstrated non-toxicity, low viscosity to minimize cell shear upon bioprinting, and potential to be tuned in terms of mechanics, gelation time, and cell interactions depending on the chain length of the ethylene oxide repeat units in the side chain, allowing for facile tuning of polymer properties for printing optimization[33, 34]**.** Our previous work has demonstrated that POEGMA hydrogels have significant biological benefits such as low cytotoxicity[38], low inflammation[36], low non-specific adsorption[39] and thermo-reversible cell adhesion suitable for tissue scaffolds[37, 40]; furthermore, the rapid gelation achievable with hydrazone-crosslinked POEGMA hydrogels can enable effective physical entrapment of ECM materials (e.g. collagen) that can mediate effective cell attachment to the printed hydrogels without requiring any additional chemical modification. By combining the beneficial physical and biological properties of POEGMA hydrogels with the supportive mechanical environment enabled by FRESH bioprinting, we demonstrate the fabrication of well-defined 3D printed cell scaffolds suitable for the encapsulation of multiple cell types with high cell viability using a very low-cost customized extrusion bioprinter that can be assembled using off-the-shelf parts (~USD 1000).

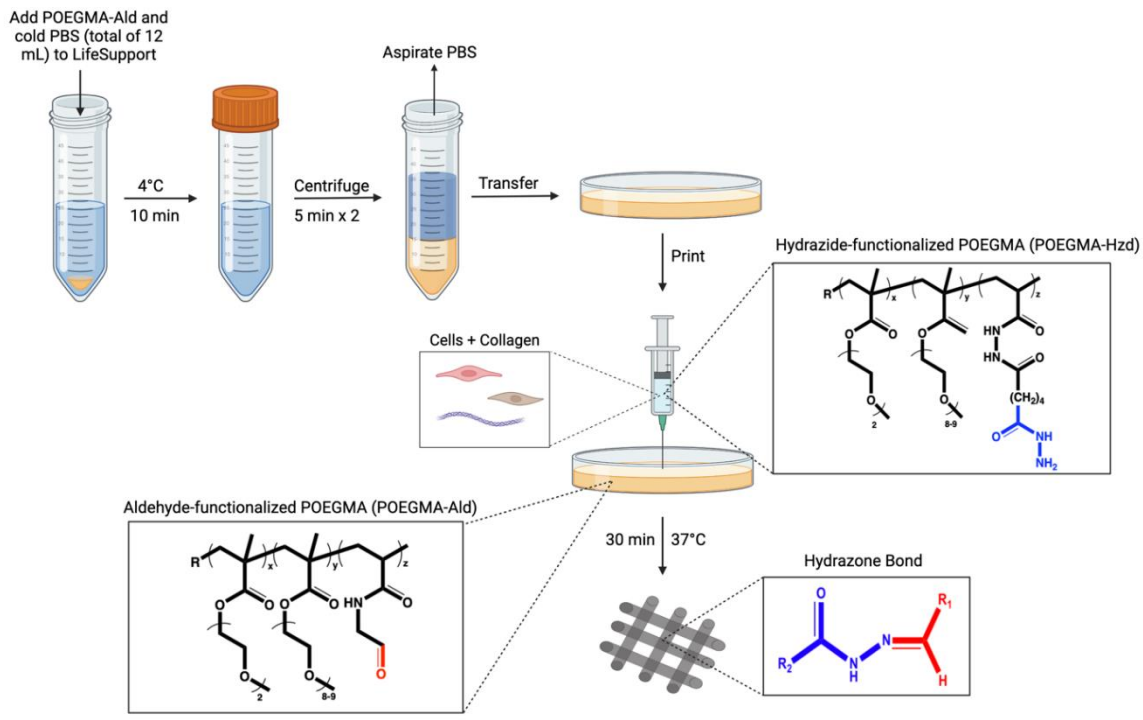

Figure 4.1: FRESH bioprinting process using hydrazone crosslinked poly(ethylene glycol methacrylate) (POEGMA) hydrogel bioinks

4.2 Experimental Section

4.2.1 Materials

Di(ethylene glycol) methyl ether methacrylate ($M(EO)_2MA$, Sigma-Aldrich, 95%) and oligo(ethylene glycol) methyl ether methacrylate ($OEGMA_{500}$, M_n = 500 g/mol, Sigma-Aldrich, 95%) were purified using a basic aluminum oxide-packed column (Sigma-Aldrich, type CG-20) to remove the butylated hydroxytoluene (BHT) and methyl ether hydroquinone (MEHQ) inhibitors before use. Acrylic acid (AA, Sigma-Aldrich, 99%), 2,2-azo-bis-isobutryic acid dimethyl ester (AIBMe, Wako Chemicals, 98.5%), dioxane (Caledon Laboratories, 99%), N′-ethyl-N-(3-(dimethylamino)propyl)-carbodiimide (EDC, Carbosynth, Compton CA, commercial grade), adipic acid dihydrazide (ADH, Alfa Aesar, 98%), and thioglycolic acid (TGA, Sigma-Aldrich, 98%) were all used as received. N-(2,2-Dimethoxyethyl) methacrylamide (DMEMAm) was synthesized as previously reported[33]. Milli-Q grade distilled deionized water (DIW) was used for all experiments. Fluorescein isothiocyanate (FITC) and rhodamine-123 were purchased from Sigma Aldrich and used as received. NIH/3T3 mouse fibroblast cells and GFP-labeled HUVECs cells were all purchased from ATCC (Cedarlane Laboratories, Burlington, ON). Dulbecco's Modified Eagle's Medium (DMEM, ThermoFisher), endothelial-specific growth media (PromoCell), fetal bovine serum (FBS, ThermoFisher), penicillin−streptomycin (ThermoFisher), trypsin−EDTA solution (Sigma-Aldrich), phosphate buffered saline (1× PBS, pH = 7.4, ThermoFisher), and 4′,6-diamidino-2-phenylindole (DAPI, ThermoFisher) were all used as received. Live/dead assay and rhodamine phalloidin (ThermoFisher) were used as per the manufacturer instructions. Collagen type 1 (bovine, 5 mg/mL, ThermoFisher) was neutralized using 1M sodium hydroxide as per manufacturer's instructions. Life Support (FluidForm, Advanced Biomatrix) was used as received.

4.2.2 Synthesis of Hydrazide-Functionalized POEGMA

Hydrazide-functionalized POEGMA precursors were synthesized as previously described[33]. In brief, AIBMe, AA, and a combination of $OEGMA_{500}$ and $M(EO)_2MA$ were dissolved in 20 mL of dioxane and purged with nitrogen for 30 min prior to polymerization. Subsequently, the solution was placed in an oil bath at 75°C for 4 h under magnetic stirring to allow for polymerization to occur. The resulting poly(OEGMA-co-AA) polymer was then redissolved in 100 mL of DIW and functionalized with hydrazide groups by adding a 5-fold molar excess of ADH and a 2.5-fold molar excess of EDC relative to the measured −COOH content of the

prepolymer and maintaining the reaction pH at 4.75 using 0.1 M HCl until the pH stabilized (~4 h). The solution was kept stirring overnight, after which it was purified by dialysis (6+ hours for six cycles). The final polymer (POEGMA-Hzd) obtained after lyophilization was stored as a 30 w/w% solution in DIW at 4 °C. The polymer was filtered using a 0.2 μm filter prior to the printing experiments.

FITC-labeled POEGMA-Hzd (POEGMA-Hzd-FITC) was prepared by reacting fluorescein isothiocyanate (FITC, 5 mg) with POEGMA-Hzd solution (1 g, 15 w/w% in DIW) under magnetic stirring for 12 hours at room temperature. A total of 2 mol% of the available hydrazide groups was targeted for labelling with FITC. The solution was dialyzed (6+ hours for 6 cycles) and lyophilized, with the resulting FITC-labeled POEGMA-Hzd stored at 30 w/w% in DIW at 4°C. All reaction vessels and storage containers were covered by aluminum foil to prevent photobleaching.

4.2.3 Synthesis of Aldehyde-Functionalized POEGMA

Aldehyde-functionalized POEGMA precursors were synthesized as previously reported[33]. AIBMe, DMEMAm, and a combination of $OEGMA_{500}$ and $M(EO)_2MA$ were dissolved in 20 mL of dioxane and purged with nitrogen for 30 min. Polymerization proceeded by placing the mixture in an oil bath at 75 °C for 4 h under magnetic stirring. Subsequently, to cleave the acetal group on DMEMAm monomer residues, the poly(OEGMA-co-DMEMAm) prepolymer was dissolved in 100 mL of 0.25 M HCl and stirred overnight. The final polymer (POEGMA-Ald) was purified by dialysis (6+ hours for six cycles), lyophilized, and stored as a 20 w/w% solution in DIW at 4 °C. The polymer was filtered using a 0.2 μm filter prior to the printing experiments.

Rhodamine 123-labeled POEGMA-Ald (POEGMA-Ald-rho) was prepared by reacting rhodamine 123 (5 mg) with POEGMA-Ald solution (1g, 15 w/w% in DIW) under magnetic stirring for 24 hours. Sodium cyanoborohydride (8.25 mg, 10 mol eq. to rhodamine 123) was then added to the solution to generate a stable conjugate via reductive amination, after which the solution was stirred for another 48 hours. The resulting polymer solution was dialyzed (6+ hours for 6 cycles) and lyophilized to dryness. The rhodamine 123-labeled POEGMA-Ald was stored at 20 w/w% in in DIW at 4 °C. All reaction vessels and storage containers were covered by aluminum foil to prevent photobleaching.

4.2.4 Characterization of Functionalized Polymers

The polymer molecular weight was measured via gel permeation chromatography (GPC) using an Agilent 1260 infinity II GPC system with an Agilent 1260 infinity refractive index detector and a Superpose 6 increase 10/300 GL (GE healthcare) column maintained at 30°C. The solvent was 1× PBS with 0.05% sodium azide at a flow rate of 0.5 mL/min, and the system was calibrated with narrow PEG standards (molecular weights 3-60 kDa). The degree of hydrazide functionalization was determined using ^{1}H NMR (600 MHz, Bruker) by comparing the intensities of the $-CH_2$ group on ADH (0.89−1.06 ppm), the $-OCH_3$ signal on POEGMA (3.45 ppm), and the $-CH_3$ signal on the backbone of POEGMA (0.81 ppm) to obtain the hydrazide content. The degree of aldehyde functionalization was determined by ^{1}H NMR (600 MHz, Bruker) using d6-DMSO by comparing the ratio of aldehyde proton signal at 9.52 ppm to the methyl POEGMA proton signal at 0.81 ppm. The gelation kinetics were tested using a vial inversion test by pipetting 0.25 mL of each precursor polymer into a 2 mL Eppendorf tube and tracking the time required for no flow to be observed within 5 s of flipping the vial upside down.

4.2.5 Cell Culture

NIH/3T3 mouse fibroblast cells (P15) were cultured in DMEM medium with 10% FBS and 1% penicillin−streptomycin to ~80% confluency at 37°C and 5% CO_2 before subsequent use. GFP-labeled HUVECs (P3) were cultured in endothelial-specific growth media (PromoCell) with endothelial growth-specific supplements (as supplied by the manufacturer) to ~80% confluency on a thin layer of gelatin (0.2 wt%, 5 mL for 30 minutes prior to seeding cells).

4.2.6 Customized Extrusion Printer

A low-cost 3D extrusion bioprinter was built consisting of a four-axis stage that controls the printing speed and design of the construct (via G-codes), a control system that regulates the motion of four step motors, and a customized 3D printed clamp system that can hold up to two syringes (see **Figure S4.2** for 3D drawings and **Table S4.1** for a cost breakdown of the components used). The printer was retrofitted from two CNC 2018 PRO Milling Machine 3 Axis machines and connected to a commercial CNC control system (Buildbotics Inc) that allows for the input of four step motors with an easy-to-use interface. The control system can read any G-code and can be easily changed for different prints. The G-code primarily used for

this study defines a 12×12 mm lattice structure with a range of 5 to 25 layers at a layer height of 0.2 mm (see Supporting Information for the full code used).

4.2.7 Preparation of Bioink and Support Bath

The process used to prepare the bioink and the support is summarized in **Figure 4.1**. LifeSupport support bath was prepared by first hydrating the lyophilized LifeSupport (1 g) in 12 mL of cold PBS containing POEGMA-Ald dissolved at a concentration between 3 to 10 wt%. The solution was thoroughly mixed using a vortex and hydrated for 10 min at 4°C. The hydrated slurry was then centrifuged twice at 1000 × g for 5 min (with the removal of the supernatant after each centrifugation) to yield the targeted rheological properties described by the FRESH 2.0 process[12]. The percentage of polymer lost in the two centrifugation steps was quantified using a fluorescent partitioning experiment using the rhodamine-labeled POEGMA-Ald polymer, using excitation and emission wavelengths of 508 nm and 528 nm respectively and a linear calibration curve to calculate the mass of polymer in the supernatant and compare it to the initial mass added to the support bath. The resulting sterile support bath was equally distributed in 2-4 wells within a 12-well plate for printing experiments. Next, the chosen cells (NIH/3T3 fibroblasts, HUVECs) were washed with warm PBS, trypsinized using 5 mL of 0.25% trypsin-EDTA for 5 min and neutralized with 5 mL of cell media in a 15 mL Falcon tube. The cell density was measured using a hemocytometer, and the cell suspension was subsequently centrifuged at 300 RPM for 5 min to remove the media-trypsin supernatant. Cell culture media (0.1 mL), neutralized collagen type I (bovine, 5 mg/ml, 0.1 mL) and POEGMA-Hzd (30 wt%, 0.2 mL) were added directly to the cell pellet and mixed by pipetting up and down to homogenize the bioink prior to printing. The mixed bioink suspension was transferred to a 1 mL syringe for printing. Note that the volumes of each bioink component can be adjusted based on the number and type of prints targeted without modifying any other procedure.

4.2.8 Physical Characterization of Printed Hydrogels

The rheological properties of the polymer precursors and support bath (with and without added polymer) were measured using a dynamic hybrid rheometer (Discovery HR-2, TA Instruments). The flow sweeps were performed over a shear rate range of 0.1 to 100 s^{-1} at room temperature (20°C) using a 1° aluminum cone-plate geometry (d=20 mm) and a volume of ~150 μL. Precursor polymer solutions corresponding to those used for 3D printing (POEGMA-Hzd 15 wt% and 3, 6 and 10wt% POEGMA-Ald, 75 mL of each precursor solution) were

mixed directly on the rheometer stage using a pipette, after which frequency sweeps were performed between 0.1 and 100 rad/s at a strain of 1% to assess the shear storage modulus of the hydrogels. The compressive moduli of the printed lattice structures were measured with the CellScale Microsquisher using a 2×2 mm platen and a 0.56 mm diameter cantilever. Cyclic compression testing was performed at 2.5, 5, 7.5 and 10% strain using sequential compress-hold-recover phases. The average hold force was calculated and divided over the platen area to calculate the stress. The swelling and degradation of the printed hydrogel scaffolds were tested using 3, 6 and 10 wt% embedded polymer concentrations and 0.1 wt% collagen. The hydrogels were placed in pre-weighed cell inserts and submerged in cell media (DMEM, 10% FBS, 1% penicillin/streptomycin), with the weights of the printed lattice structures measured over a period of 2 months at 37°C. All measurements were conducted in triplicate, with error bars representing the standard deviation.

4.2.9 Cell Viability Study

The cytotoxicity of the precursor polymers was measured over a concentration range of 0.25 to 1 mg/mL using a PrestoBlue Cell Viability Assay (ThermoFisher) over a 1-day exposure time. NIH/3T3 fibroblasts and GFP-labeled HUVECs were plated at a density of 1.0×10^4 cells per well in a 96-well plate. Cell viability was assessed by fluorescence (excitation 560 nm, emission 590 nm) using a plate reader and normalized to the cell-only wells in which no polymers were added to estimate relative viability. Cell viability within the printed hydrogel scaffolds was assessed using live/dead staining (ThermoFisher) following the manufacturer's instructions. Briefly, the printed constructs were washed with warm PBS over 3×5-minute intervals before adding the mixture of CFDA/PI and incubating for 30 minutes at room temperature. Following staining, the printed constructs were thoroughly washed with PBS and imaged using confocal microscopy. For GFP-labelled HUVECs, only propidium iodide (PI, 1 mg/mL, 1:1000 dilution in PBS) was added to assess viability given the overlap in emission wavelengths between the GFP and CFDA stains.

4.2.10 Cell Adhesion Study

A cell adhesion assay was performed with DAPI and a rhodamine-phalloidin staining solution to visualize the adhesion of NIH/3T3 fibroblast cells to the printed scaffolds. The media was removed from each well, after which each sample was washed with phosphate buffered saline

(PBS, 1×, 1 mL) using 2×10-minute washes. The encapsulated cells were fixed with 4% formaldehyde (in PBS, methanol-free) for 30 min at room temperature. After washing the samples three times with PBS (3×5 min), the cells were permeabilized with 0.1% Triton X-100 for 15 min, washed with PBS (1×5 min), and then exposed to a blocking solution (10% BSA in PBS) for two hours. Fluorescence staining was performed using rhodamine-labeled phalloidin (4× solution in PBS, or 3-4 drops in 1 mL of PBS using ActinRed™ 555 ReadyProbes™ Reagent Rhodamine phalloidin) overnight at 4℃ followed by DAPI (300 nM solution in PBS) for 5 minutes, with intermediate thorough washing with 1 mL of PBS.

4.2.11 Microscopic Analysis

Confocal laser scanning microscopy (CLSM, Nikon A1R HD25) was used to track cell viability and cell adhesion**.** A 10× 0.45NA objective and laser lines at 488 nm and 561 nm were used to image the live/dead assay results. Large, tiled scans with 10% overlap were acquired to image the 12×12 mm lattice structure. A custom-made FIJI macro was then used that applied user-inputted regions of interest (ROIs) to identify the large structure followed by an overall thresholding method (Triangle) to binarize the different cell populations, allowing for the identification and quantification of all cells with a 50 μm^2 (or higher) area. The total numbers of live and dead cells were added to find the total number of cells present in the printed structure, with the percentage cell viability calculated by dividing the number of live cells by the total number of cells.

4.2.12 Statistical Analysis

All experiments were performed using n=3 replicates (including the printing experiments). For quantitative comparisons between datasets, a two-sided t-test was used to assess significance at 95% confidence.

4.3 Results

4.3.1 Polymer Characterization

Both the hydrazide and aldehyde functionalized POEGMA polymers exhibited number average molecular weights of ~14 kDa, below the renal cut-off to enable clearance after gel degradation. The hydrazide and aldehyde contents of the hydrogels were 20.8 and 19.1 mol% respectively as per ^{1}H NMR (**Figure S4.3**), consistent with previously reported work[35] and the

target reactive functional group concentrations (**Table 4.1**). The hydrazide-functionalized precursor polymer solutions exhibit low viscosity and moderately shear thinning behaviour due to their low molecular weights, making them easy to print via an extrusion process (**Figure 4.2A**). The addition of collagen (to promote cell adhesion to the anti-fouling POEGMA scaffold) into the hydrazide-functionalized polymer solution increases the viscosity and results in more defined shear thinning behaviour; however, the viscosity at any shear rate associated with printing remains <1 Pa s, representing an easily printable precursor polymer solution in an extrusion bioprinting context. The aldehyde-functionalized polymer was directly mixed with the LifeSupport material at three different concentrations (3, 6 and 10 wt%) without significantly altering the shear-thinning behavior of the support bath, as is also essential for successful embedded printing (**Figure 4.2B**). Moreover, the polymers are non-cytotoxic, showing >85% viability towards both NIH/3T3 fibroblast cells and HUVECs after 24 hours at concentrations up to 1 wt% (**Figure S4.4**). Thus, both reactive components of the POEGMA-based dynamic covalent bioink have suitable rheological and cytocompatibility properties for 3D bioprinting applications.

Table 4.1: Characterization of functional precursor polymers used for 3D bioprinting

Polymer	M_n (kDa)	Đ	Functional monomer (mol%)
POEGMA-Hzd	14.4	3.0	20.8
POEGMA-Ald	13.8	4.5	19.1

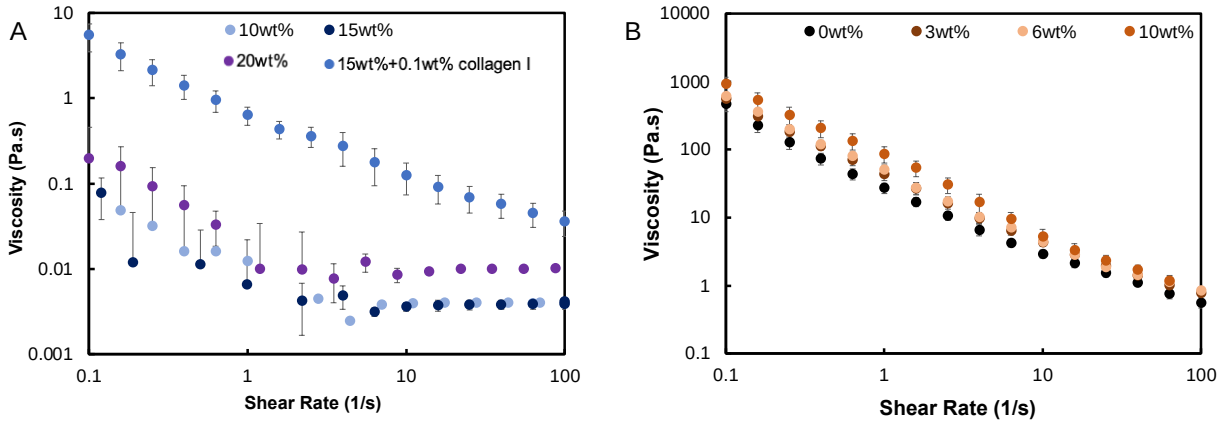

Figure 4.2: Rheological characterization of the bioink and support bath prior to printing: (A) Viscosity sweep of POEGMA-Hzd precursor polymer solutions at the three concentrations used to print and in the presence of 0.1 wt% collagen I additive to promote cell adhesion; (B) Viscosity sweep of the LifeSupport support bath containing three different concentrations of POEGMA-Ald

4.3.2 Printability of Hydrazone-Crosslinked Hydrogels

The functional precursor polymers were next assessed for printability using the customized extrusion printer. Due to the slightly lower cell viability over time observed in our previous work when cells were exposed to very high concentrations of aldehyde-functionalized polymers[35], the aldehyde-functionalized precursor polymer was used as the 'crosslinker' in the support bath while the hydrazide-functionalized precursor polymer was extruded with cells and the collagen additive through a 1 mL syringe and a 25 G needle. Imine crosslinking between the gelatin support bath and the POEGMA-Ald crosslinking polymer was expected to retain most if not all of the crosslinking polymer in the support bath phase during the centrifugation-based preparation process of the support bath, a hypothesis confirmed by a rhodamine-labeled POEGMA-Ald partitioning experiment that showed only 8-14% mass loss of polymer during the centrifugation steps (the lower range corresponding to the higher initial polymer concentrations, see **Table S4.3**).

Printing was then performed by controlling the movement and extrusion rate through the Buildbotics control system using G coding language, maintaining the needle gauge (blunt, 25 G) and printhead speed (6 mm/s) constant over all trials; these constant variables were selected based on preliminary printing trials that indicated potential needle clogging risks with the use of smaller gauge needles as well as no significant effect of the printhead speed (tested range 2.5-15 mm/s) on printability. Printability was assessed by printing a 12×12 mm lattice structure with 3×3 mm theoretical square holes (**Figure 4.3A**, see Supporting Information for the full G code), a structure chosen for its ability to hold shape even for weaker hydrogel bioinks. **Figure 4.3** shows the printability achieved upon varying the embedded POEGMA-Ald concentration (3-10 wt% prior to the centrifugation steps in a 12 mL suspension of gelatin microparticles), the printed POEGMA-Hzd concentrations (10-20 wt%), the number of layers (5-25 layers), the volumetric flow rate of the printed POEGMA-Hzd (100-300 μL/min), and the layer height (0.1-0.3 mm).

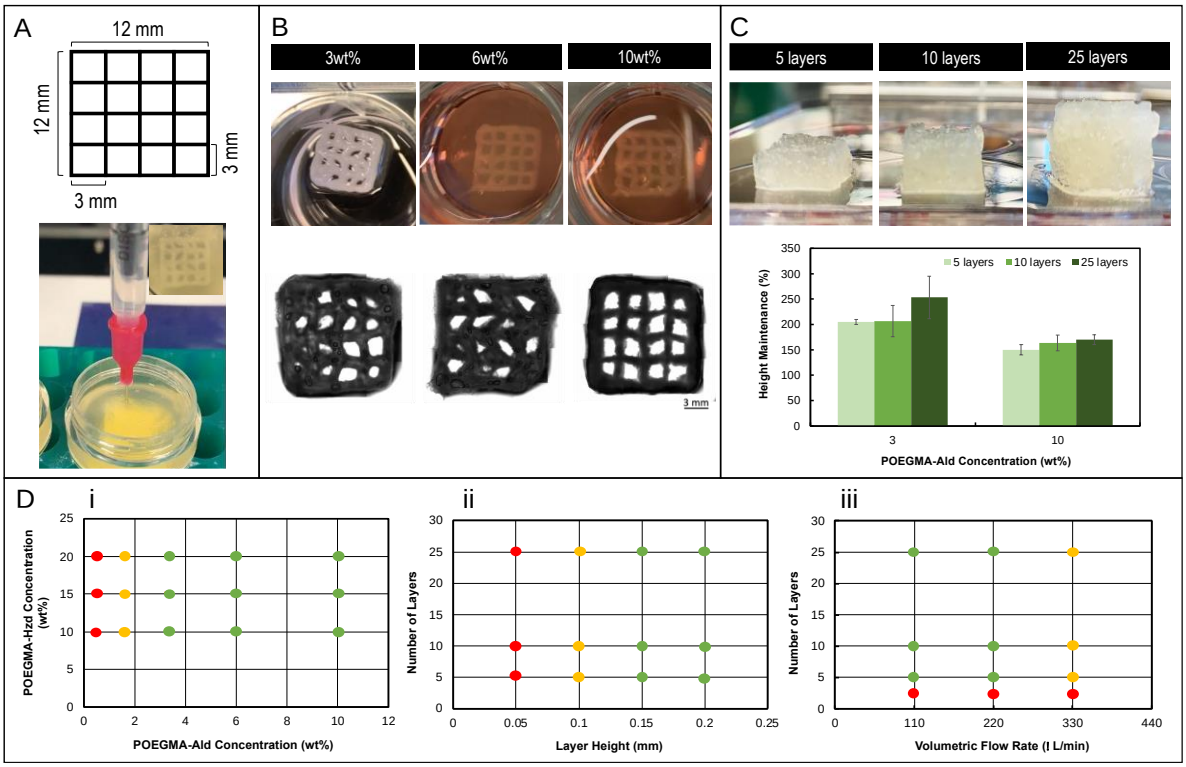

Figure 4.3: Printability analysis of embedded 3D printing using hydrazone crosslinked POEGMA hydrogels and a gelatin support bath: (A) Print geometry using a 12 mm × 12 mm lattice structure compared to the observed lattice structure after printing (inset); (B) The effect of the added POEGMA-Ald (crosslinker) polymer concentration on scaffold printability (blunt 25G needle, printing speed = 6 mm/s, layer thickness = 0.2 mm, POEGMA-Hzd concentration = 15 wt%, volumetric flow rate = 220 mL/min); (C) Z-direction swelling of the printed hydrogels as a function of POEGMA-Ald (crosslinker) concentration and the number of layers printed reported based on the height maintenance (H_M) equation $H_M = \frac{H_A}{H_T} * 100\%$, where H_A is the actual height after printing and H_T is the theoretical height (without any swelling); and (D) Colour printability maps showing the effects of the precursor polymer concentrations, the number of layers printed, the volumetric flow rate, and the layer height. Red points in graph indicate not printable conditions, orange points represent printable but not reproducible conditions, and green points represent printable and reproducible conditions, in which printability is defined as the maintenance of a 3D structure without macroscopic deformation following removal of the support bath and reproducibility is defined as the ability to produce prints with similar dimensions, shape fidelity, and stability over multiple printing cycles.

Increasing the POEGMA-Ald concentration in the support bath results in better print resolution and less swelling due to the higher resulting crosslink density in the printed hydrogel network (**Figure 4.3B**), making the 10 wt% POEGMA-Ald support bath preferable if high shape fidelity to the 2D projection of the grid pattern is prioritized. Similarly, the z-direction resolution, as assessed by the ratio between the actual height of the printed scaffold and the theoretical height of the scaffold based on the crosshead rate and the volumetric flow rate (calculated from the

G-code[36]), indicated a height change of >100% for the 3 wt% embedded POEGMA-Ald printed scaffolds (and >250% for the 25 layer print) but only ~150% for the 10 wt% POEGMA-Ald concentration at various layer heights (**Figure 4.3C**), also reflective of the higher crosslinking density achieved with the higher POEGMA-Ald concentration support bath. However, all printed POEGMA-Ald concentrations could result in stable 3D printed structures that could self-support their own weight upon removal from the support bath (**Figure 4.3C**), suggesting the utility of the crosslinking polymer concentration in the support bath as an adjustable parameter for regulating scaffold mechanics and/or degradation. Printability analyses were then conducted to assess the feasibility of printing under various printing conditions (**Figure 4.3D**). Varying the POEGMA-Hzd concentration between 10-20 wt% did not significantly alter the printability or reproducibility of the scaffolds (**Figure 4.3D-i**), highlighting that the embedded POEGMA-Ald concentration is far more critical to achieving stable prints. Varying the number of layers between 5 (the minimum number of layers observed to give reproducible 3D prints) and 25 (the maximum value tested, although more layers are likely possible to print) did not significantly alter the printability or reproducibility of the scaffolds (**Figure 4.3D-ii**); however, the layer height did affect printability, with thicker layers (0.2 mm) maintaining more distinct interfaces with the underlying print and thus better maintaining print fidelity versus the thinner layers (0.1 mm) that tend to fully wet the pre-existing print and thus lose their shape fidelity. As such, the layer height is the more critical parameter to ensure proper cohesion between the sequentially printed layers. Note that such inter-layer cohesion can be aided by the dynamic nature of the hydrazone chemistry, which can promote bond exchange and thus inter-layer crosslinking to enhance the inter-layer stability of the print. Volumetric flow rates of 110-220 μL/min were determined to be suitable for the printing of the lattice structures over >5 layers (**Figure 4.3D-iii**), with higher flow rates resulting in significant loss in print resolution and lower flow rates resulting in insufficient material deposition for each printed layer (and therefore causing the constructs to collapse or not be printable in some cases). Based on this analysis, **Table 4.2** summarizes the feasible printing conditions that yield both high-fidelity and reproducible prints.

Table 4.2: Summary of tested and constant printing parameters (12×12 mm lattice structure)

Printing Variable	**Tested conditions (*fixed*/varied)**	**Optimal for Printability**
Needle Gauge	*25 G*	*25 G*
Printing Speed	*6 mm/s*	6 *mm/s*
POEGMA-Hzd Concentration	10, 15 and 20 wt%	15 wt%
POEGMA-Ald Concentration	3, 6 and 10 wt%	>3 wt%
Number of layers	5-25	>5
Layer Height	0.1-0.2 mm	0.2 mm
Volumetric Flow Rate	110, 220 and 330 μL/min	110 or 220 μL/min

4.3.3 Mechanics of the Printed Structures

Using the optimal layer height (0.2 mm) and volumetric flow rate (220 µL/min) from the printability screening in **Figure 4.3D**, 5-layer scaffolds were printed with the three POEGMA-Ald concentrations tested previously (3-10 wt%) to assess the compressive moduli of the printed hydrogels as a function of POEGMA-Ald (crosslinker) polymer concentration. To address the limited degree of cell adhesion observed to the POEGMA-based hydrogels[38] and to stay consistent with the subsequent cell experiments, 0.1 wt% type 1 bovine collagen was added into the POEGMA-Hzd bioink solution to introduce specific adhesion motifs for cell immobilization. **Figure 4.4** shows the resulting force versus displacement and compressive modulus results for the printed scaffolds without cells.

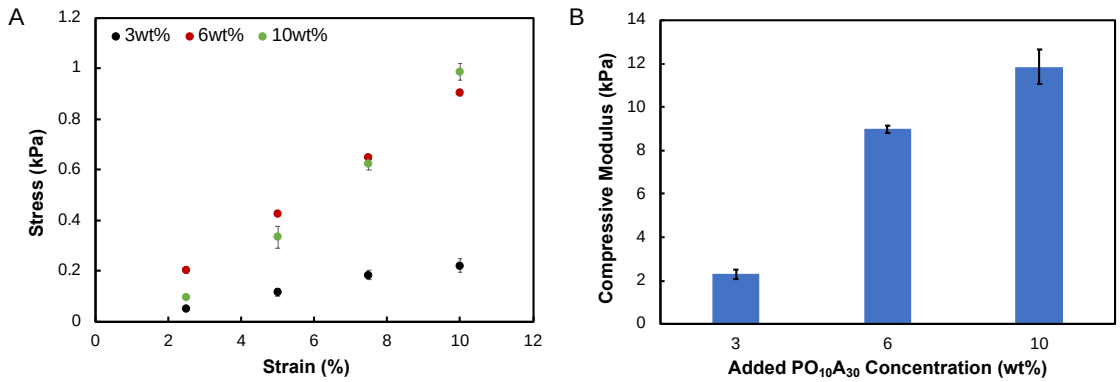

Figure 4.4: Compression testing on printed hydrazone crosslinked structures under uniaxial unconfined compression: (A) stress versus strain data; (B) Compressive modulus of the printed structures calculated based on a linear regression of the data in (A).

Figure 4.4A shows the linear response of the normal force response as a function of strain, illustrating that the printed hydrogel scaffolds show elastic properties. Regression of the linear regime of these stress vs. strain profiles enabled estimation of the compressive moduli of the printed structures, which range from 2 kPa (3 wt% POEGMA-Ald) to 12 kPa (10 wt% POEGMA-Ald) depending on the concentration of the embedded POEGMA-Ald polymer in the print (**Figure 4.4B**). The range of achievable modulus values, coupled with the good dimensional stability of the 3D prints achievable over the same crosslinking polymer concentration range (**Figure 4.3B** and **C**), demonstrates the ability to print 3D hydrogel scaffolds with different mechanics simply by changing the embedded functional polymer concentration in the support bath.

4.3.4 Swelling and Degradation of the Printed Structures

To analyze the degradability of the printed hydrogel structures, a swelling/degradation study was performed by incubating the printed hydrogels in cell media (DMEM, 10% FBS, 1% penicillin/streptocycin) at 37°C. The printed lattice structures using 3, 6 and 10 wt% embedded polymer concentrations and 0.1 wt% collagen were placed in pre-weighed cell inserts and submerged in the cell media over the course of two months (**Figure 4.5**).

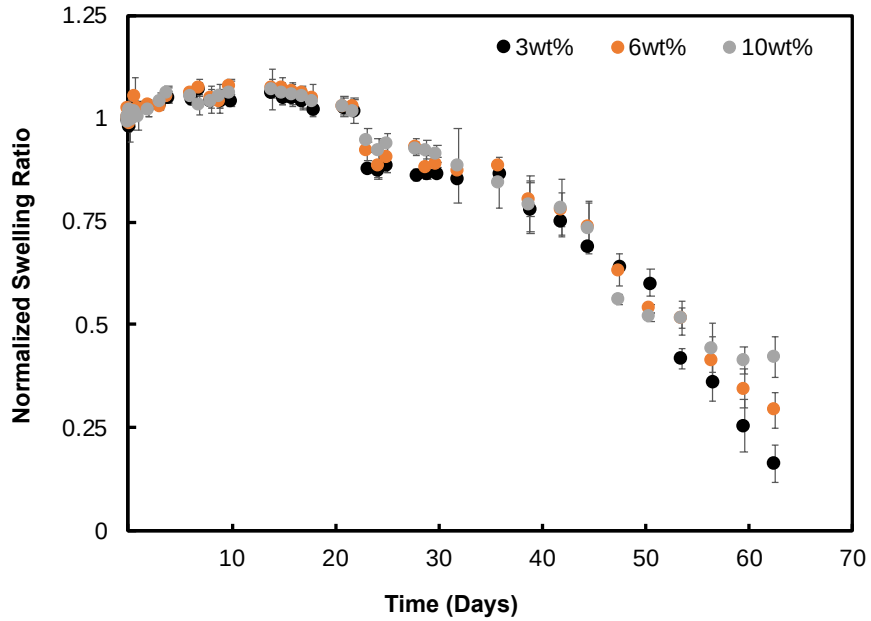

Figure 4.5: Swelling and degradation kinetic study measuring the normalized weight of the printed hydrogel structures in cell media (DMEM, 10% FBS, 1% penicillin/streptomycin) at three embedded polymer concentrations over time.

As seen in **Figure 4.5**, the structures did not undergo significant swelling or degradation over the first three weeks but subsequently started to degrade, with all hydrogels losing >50% of their original mass at 7 weeks post-printing. No significant differences between the three embedded polymer concentrations were observed up to 50 days; however, at the end of the 2-month study period, the 10 wt% prints still retained ~40% of their mass while the 3 wt% prints were almost fully degraded, consistent with the lower crosslink density in the 3 wt% prints. Note that this observed degradation is solely a result of hydrolysis cell media and would likely be accelerated in *in vivo* conditions in which both enzymatic and redox processes can accelerate hydrazone cleavage.

4.3.5 Polymer Distribution

To gain further understanding into how the two reactive polymers mix during the printing process, the hydrazide and aldehyde-functionalized POEGMA polymers were fluorescently labeled with FITC and rhodamine-123 respectively and subsequently printed using the optimal print parameters identified (15wt% POEGMA-Hzd; 5 layers; 220 μL/min; 0.1 wt% collagen) and POEGMA-Ald concentrations of both 3 wt% (the minimum concentration yielding a dimensionally stable print) and 10 wt% (the highest concentration tested). **Figure 4.6** shows the confocal microscopy images of the resulting scaffold over time.

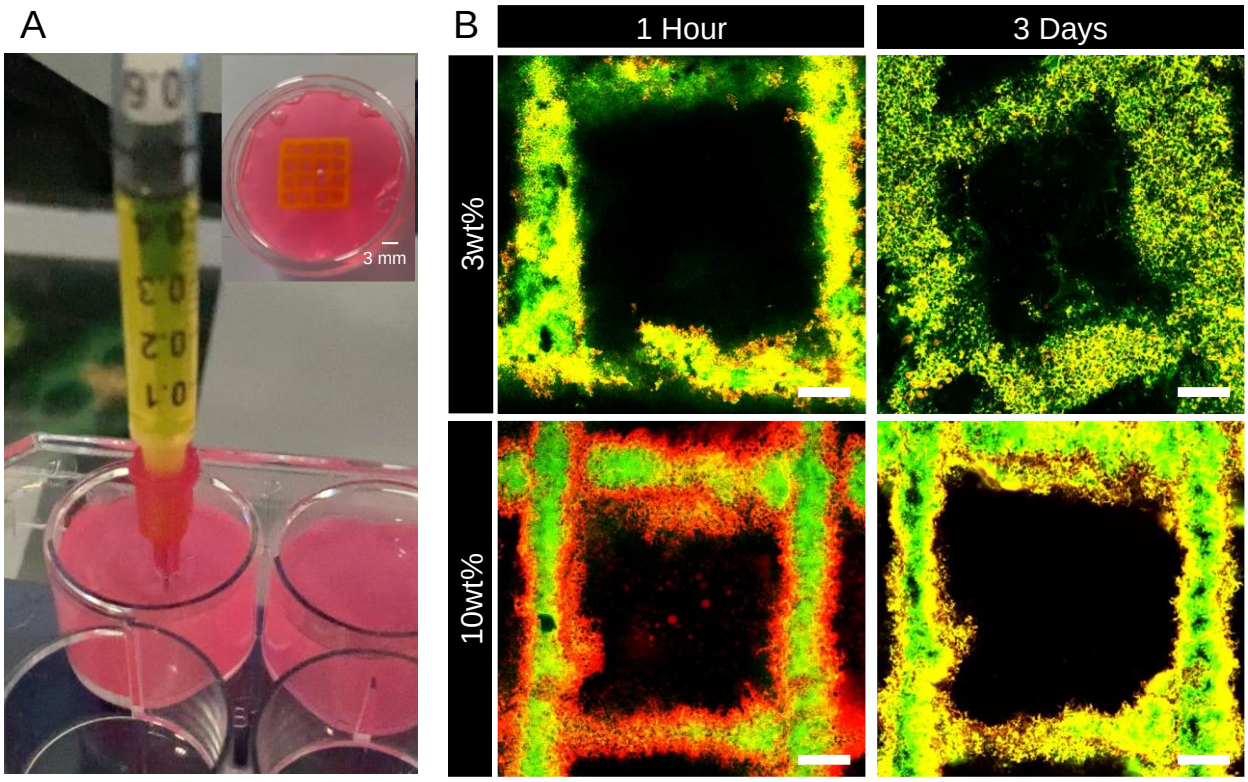

Figure 4.6: Hydrazide (green) and aldehyde (red)-functionalized polymer distributions observed when printing 15wt% POEGMA-Hzd-FITC and 0.1 wt% collagen into a support bath containing either 3 wt% or 10 wt% POEGMA-Ald-rho using the FRESH printing technique: (A) Schematic of the printing geometry and image of printed scaffold within the LifeSupport bath (inset); (B) Confocal laser scanning microscopy images of the distribution of POEGMA-Hzd-FITC (green) and POEGMA-Ald-rho (red) either 1 hour after printing (left column) or 3 days after printing (right column). Scale bar = 500 mm.

Using the lowest embedded POEGMA-Ald concentration (3 wt%), a near-homogeneous polymer distribution was observed even within 1 hour of printing. This result can be attributed to the low crosslink density, high swelling, and relatively slower gelation kinetics (~2-3 min, **Table S4.2**) observed with the lower POEGMA-Ald concentration that allow the crosslinking polymer to diffuse more easily and for a longer period of time into the printed POEGMA-Hzd bioink, resulting in a more homogeneously crosslinked structure over a relatively short time. In contrast, at the highest embedded POEGMA-Ald concentration of 10 wt%, the confocal images demonstrated a clear core-sheath distribution of the two reactive polymers after 1 hour of printing, consistent with the significantly faster gelation time and higher crosslink density of this printed hydrogel limiting in-diffusion of the crosslinking POEGMA-Ald polymer into the interior of the POEGMA-Hzd bioink cylinder printed in the support bath. However, unlike with non-dynamic click chemistries in which such distributions would persist over the lifetime

of the print, the reversible nature of hydrazone crosslinks results in a significant increase in the homogeneity of the printed hydrogel 3 days after printing (**Figure 4.5B**), consistent with the dynamic hydrazone crosslinking chemistry enabling the slow penetration of the POEGMA-Ald crosslinking polymer into the crosslinked hydrogel structures and thus the formation of a more homogeneous internal structure over time. This dynamic crosslinking response is a significant advantage of the use of dynamic covalent chemistry for embedded printing, as it offers an alternative for creating higher crosslink density homogeneous prints while still enabling the incorporation of the crosslinking agent in the support bath rather than requiring *in situ*-mixing of the two reactive precursor polymers in the printer nozzle.

4.3.6 Viability and Adhesion of Encapsulated Cells

To assess the potential of the printed hydrogel scaffolds as a bioink formulation for supporting the long-term viability of cells, two different cell lines were suspended in a 15 wt% POEGMA-Hzd bioink solution and printed into a 3-10 wt% POEGMA-Ald-containing support bath, maintaining all the other variables optimized from previous printing runs (5 layers; 220 μL/min). To address the limited degree of cell adhesion observed to the POEGMA-based hydrogels[35], 0.1 wt% type 1 bovine collagen was added into the POEGMA-Hzd bioink solution to introduce specific adhesion motifs for cell immobilization; note that the amine residues in collagen can (like the gelatin support beads) form imine crosslinks with POEGMA-Ald, providing a mechanism to not only physically entrap but also reversibly chemically bond collagen or any peptide-based adhesion promoter into the hydrogel without requiring any additional chemistry. First, NIH/3T3 mouse fibroblast cells suspended at a cell density of 10^7 cells/mL in the POEGMA-Hzd solution were printed into separate support baths containing three different POEGMA-Ald concentrations (3, 6 and 10 wt%), with the resulting cell viabilities (as measured using the live/dead assay to differentiate between viable (green) and dead (red) cells) after 1, 7 and 14 days post-printing reported in **Figure 4.7**.

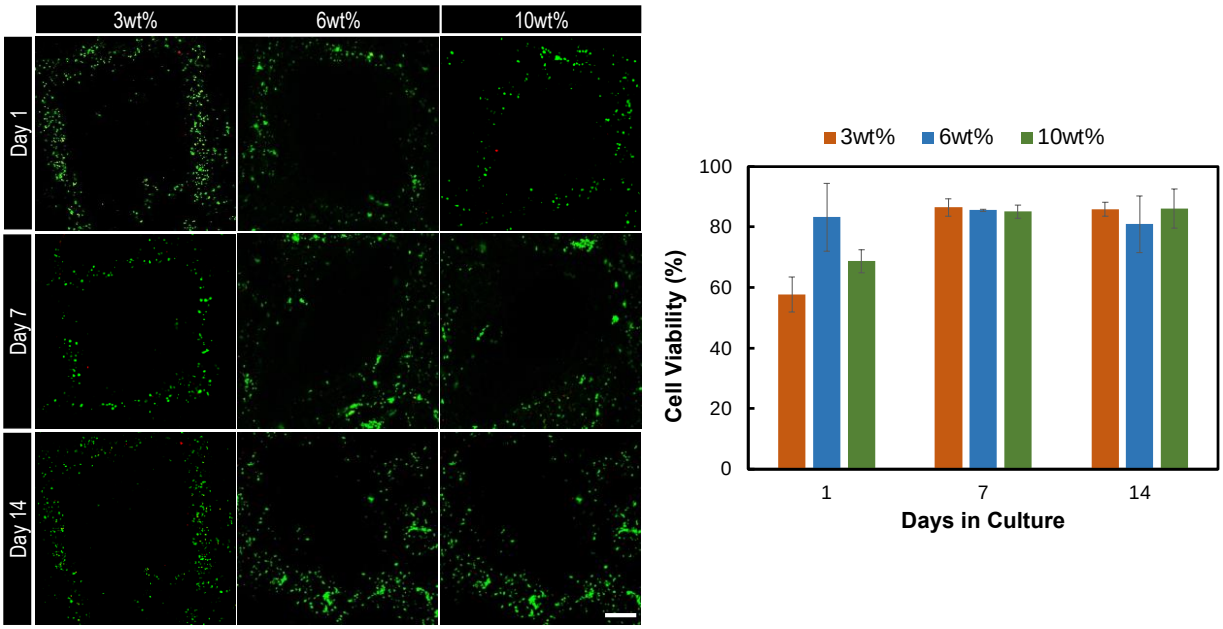

Figure 4.7: Viability of NIH/3T3 fibroblast cells (measured using the live/dead assay) after day 1, 7 and 14 post-printing as a function of the POEGMA-Ald concentration in the support bath. Scale bar = 500 μm

Confocal images indicated high cell viability (>80% after 14 days in culture) for scaffolds printed at all three embedded POEGMA-Ald concentrations. The slightly lower cell viability values observed on day 1, particularly for both the weakest (3 wt% POEGMA-Ald) and stiffest (10 wt% POEGMA-Ald) hydrogels tested, are likely attributable to the moderate shear stress applied on the cells during printing (as is typical in 3D hydrogel printing[37]), the at best moderate cell adhesion to the scaffold achieved after 24 hours, and the potential leakage of some cells out of the slow-gelling print at the lower POEGMA-Ald concentration tested; however, all scaffolds maintained viabilities of >80% after 7 and 14 days in culture regardless of this initial viability result.

To assess the potential of the bioink for printing human cells, GFP-labelled human umbilical vein endothelial cells (HUVECs) were co-printed with cells at a cell density of 10^7 cells/mL into a support bath containing a POEGMA-Ald concentration of 3, 6 and 10 wt%. All other variables were maintained as optimized from previous printing runs (5 layers; 220 μL/min, 15 wt% POEGMA-Hzd). Confocal images of the resulting printed scaffolds at 1-, 7- and 14-days post-printing (green = GFP-labeled cell; red = dead cell) are shown in **Figure 4.8**.

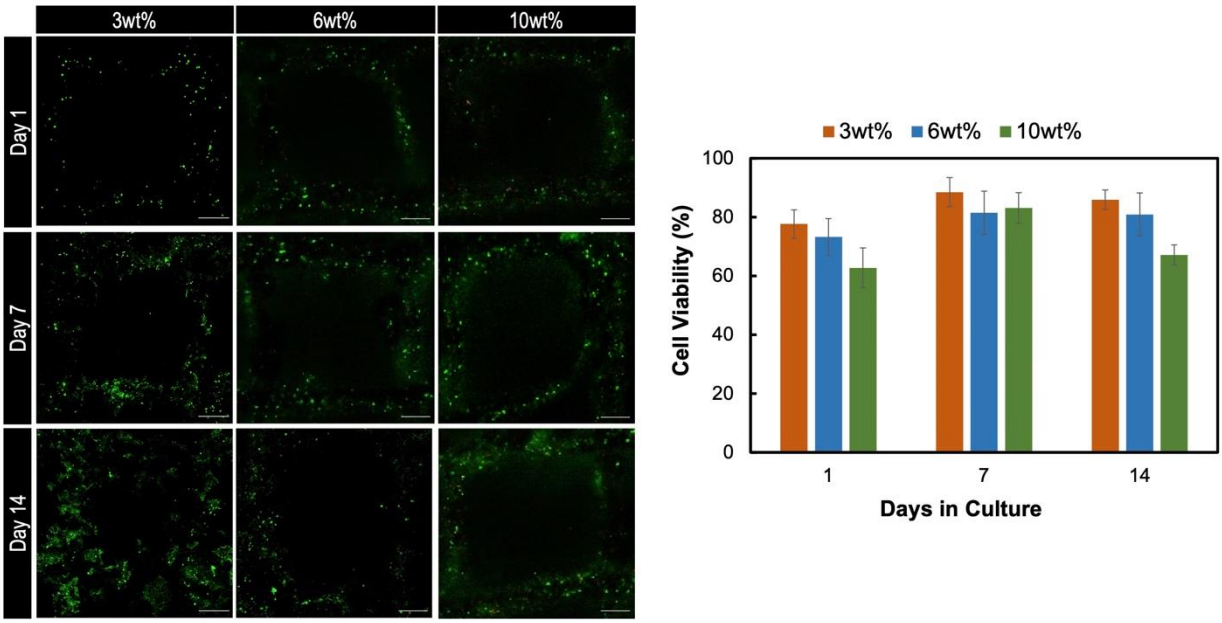

Figure 4.8: Viability of GFP-labeled HUVECs (using a propidium iodide counterstain for dead cells) after day 1, 7 and 14 post-printing as a function of the POEGMA-Ald concentration in the support bath. Scale bar = 500 μm.

Similar to the hardier and less shear-sensitive mouse fibroblast cells tested, encapsulated HUVECs maintain high viability after 14 days in culture. However, unlike with the 3T3 cells, clear differences are observed over time at different embedded polymer concentrations. At 3 and 6 wt% embedded concentrations, the viability stays consistently at >80% after 7 to 14 days, with clear evidence of cell proliferation/spreading observed particularly for the 3 wt% embedded polymer hydrogels over the 14-day culture time. In contrast, at higher embedded polymer concentrations, minimal spreading, and significantly lower cell viability (~60%) is observed after 14 days. We attribute this result to the higher crosslink density in the 10 wt% embedded polymer concentration, with the higher concentration of hydrazone crosslinks formed making it harder for the cells to exploit the dynamic chemistry to remodel the scaffold. As such, while HUVECs can both survive the printing process and grow effectively within the printed scaffolds, they are also significantly more sensitive to higher crosslink density and mechanics of the printed scaffolds

Next, rhodamine-phalloidin staining that allows for the visualization of the F-actin network in the encapsulated cells after 3, 7 and 14 days post-printing was combined with nucleus staining (using DAPI) to visualize the adhesion of the NIH/3T3 fibroblasts to the scaffold over time (**Figure 4.9** for 3T3 cells and Supporting Information **Figure S4.6** for HUVEC cells). Note

that the 3 wt% POEGMA-Ald gel was specifically chosen for this experiment due to: (1) the more dynamic nature of the less crosslinked hydrogel, providing the cells with more opportunity to functionally re-engineer the network to promote cell spreading and proliferation; and (2) the increased fluorescent background observed when applying the rhodamine phalloidin to the 10 wt% POEGMA-Ald crosslinked scaffolds that made interpretation of the adhesion in those gels challenging. A clear progression from the round morphology of the non-adhered NIH/3T3 cells to the presence of cells with elongated F-actin filaments was observed between 3 to 14 days, confirming the desirable phenotypic responses of the cells in the printed hydrogel scaffolds. Phalloidin/DAPI staining of printed HUVEC scaffolds shows a corresponding change in cell morphology from spherical to irregular, indicating that cell-scaffold adhesion can also occur in this case.

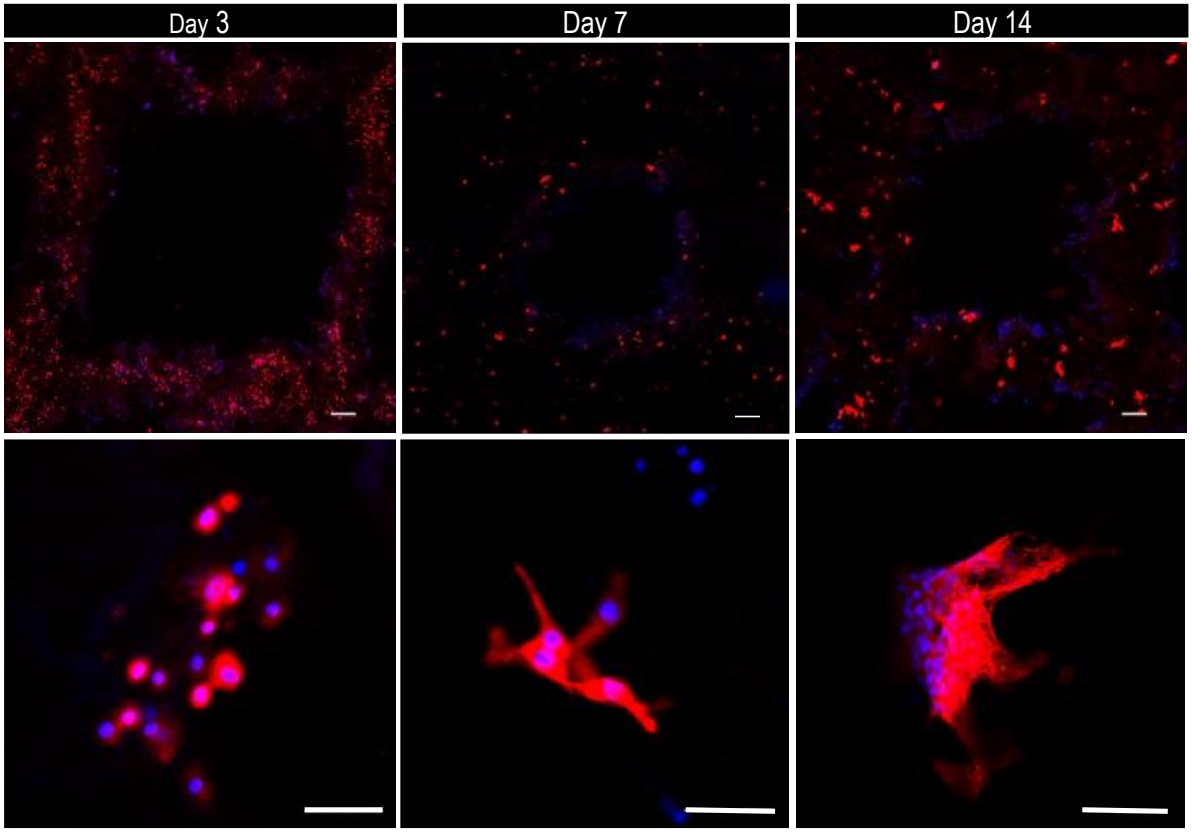

Figure 4.9: Phalloidin (red)-DAPI (blue) staining of NIH/3T3 fibroblasts co-printed in POEGMA-Hzd/ POEGMA-Ald hydrogels prepared with a POEGMA-Ald concentration of 3 wt% in the support bath using FRESH bioprinting after 3 days (left column), 7 days (middle column), and 14 days (right column) in culture. Scale bar = 50 μm.

4.4 Discussion

Hydrazone crosslinked POEGMA hydrogels can be successfully bioprinted using the FRESH bioprinting technique by adding aldehyde functionalized precursor polymer (POEGMA-Ald) into the support bath and printing a bioink based on the hydrazide functionalized precursor polymer (POEGMA-Hzd), optionally containing other bioactive components (i.e., collagen) to promote improved cell adhesion. The functional precursor polymers were chosen due to their low viscosity (making them easy to print and imparting minimum stress on the cells during the printing process), tunable gelation (to evaluate the effect of gelation time on the final printed constructs), and high cytocompatibility towards NIH/3T3 fibroblast cells and HUVECs (**Figure S4.4**). The near-independence of the POEGMA-Hzd concentration relative to the POEGMA-Ald concentration on the resolution and swelling profile of the printed lattice structures (**Figure 4.3D**) is a particularly interesting result. A typical print (even at the lowest 3 wt% POEGMA-Ald concentration tested) contains a large excess of POEGMA-Ald (~400 mg of POEGMA-Ald per ~90 mg of POEGMA-Hzd added); correspondingly, the higher 10 wt% POEGMA-Ald concentrations tested has a nearly 15× stoichiometric excess of aldehyde-functionalized polymer. We hypothesize this result indicates that a significant amount of the POEGMA-Ald polymer is either adsorbed or absorbed to the gelatin microparticle support bath and is thus inaccessible to crosslink the printed hydrazide polymer, such that very large aldehyde polymer excesses still result in significant and measurable changes in the printed scaffold crosslink density and thus scaffold mechanics (2-12 kPa compressive modulus, **Figure 4.4**) and both swelling and print fidelity (Fig. 3). Even so, given the much lower costs of the POEGMA precursor polymers (~$15/g for POEGMA-Hzd and ~$20/g for POEGMA-Ald based on Sigma-Aldrich raw material prices) versus naturally-isolated bioink materials such as gelatin methacrylate (~$300-600/g based on degree of substitution) or collagen (~$1000/g) make this technique economically attractive. The optimal printing ranges for number of layers and volumetric flow rate of POEGMA-Hzd were identified to be 5-25 and 110-220 µL/min respectively, with low layer numbers resulting in poor print resolution, lower volumetric flow rates resulting in insufficient hydrogel deposition, and higher volumetric flow rates resulting in poor print fidelity.

The compressive moduli of the printed hydrogel structures range between 2 and 12 kPa, showcasing the potential to mimic softer tissues found in the human body such as the brain, the liver and/or the pancreas[38, 39]. More specifically, the modulus range achievable with our

embedded extrusion approach are suitable or applications such as neuron regeneration (lower end of range) or muscle regeneration (higher end of range)[40]. Despite the tendency for low viscosity bioinks to also yield less stiff printed scaffolds, printing low viscosity precursor polymers is an effective strategy for maintaining high printed cell viability (including for both mouse and human cells) by reducing the viscosity-driven shear disruption of cells; this result is consistent with those of Matyash et al., who reported that soft alginate hydrogels could more effectively support rat and human neuron growth against oxidative stress[41]. While the mechanical properties of such soft gels create a favorable cellular environment, they also result in the hydrogels being challenging to print into complex scaffolds[42] while avoiding collapse and/or deformation[6]. The use of this reported embedded extrusion printing technique thus allows for high-resolution 3D printing of low concentration bioinks, with potentially significant ramifications for 3D bioink design[43].

The benefits of using dynamic covalent chemistry were also clearly evident based on the polymer distribution results presented (**Figure 4.5**), in which the reversible nature of hydrazone crosslinks significantly improves the homogeneity of the printed hydrogels only three days after printing even at the higher embedded POEGMA-Ald concentration. We hypothesize that the dynamic hydrazone crosslinking chemistry enables the slow penetration of POEGMA-Ald crosslinking polymer into the hydrogel structures as one hydrazone bond is hydrolyzed and another can reform, allowing the POEGMA-Ald polymer to "crawl" into the bulk of the printed structure based on the higher concentration of (unreacted) hydrazide groups present in the core of the printed structure. This result is in direct contrast to irreversible covalent crosslinked hydrogels previously printed with the FRESH bioprinting method (i.e., SPAAC chemistry[32]) in which no such dynamic reconformation of the initially core-shell crosslink density is possible, although the diffusion of a crosslinking polymer from outside the scaffold may still occur at a lower rate if the print is left in the crosslinking solution for an extended period. The dynamic nature of hydrazone click chemistry is thus an attractive strategy to print homogeneous hydrogel structures while still enabling degradation of the gel over time due to the dynamic hydrazone chemistry[33]. Cells would also be expected to also be able to dynamically restructure such a dynamic scaffold in the same way to aid in tasks such as cell proliferation and cell spreading, with the evidence of cell clustering and adhesion presented in this work (**Figure 4.7** and **Figure 4.8**) supporting this advantage of a dynamic gel scaffold. The presence of a dynamic scaffold is particularly beneficial in the absence of macroporosity within the gel, which is difficult to print directly into scaffolds in the context of continuous 3D

bioprinting. Coupled with the very high viabilities maintained over 14 days for both mouse (NIH/3T3) and human (HUVEC) cells (>80% as per **Figure 4.6**, in part facilitated by the avoidance of any chemical or external energy-based crosslinking process) and the desirable phenotypic response of good cell adhesion to the scaffold as indicated by F-actin staining (**Figure 4.9** and **Figure S4.6**), the POEGMA-based dynamic bioink offers advantages versus existing commercial bioinks for long-term 3D cell culture/cell delivery.

4.5 Conclusions

Dynamic synthetic polymer-based 3D cell scaffolds can be fabricated based on hydrazone-crosslinked POEGMA hydrogels using the FRESH bioprinting technique. The covalent hydrazone bond formed by crosslinking hydrazide and aldehyde-functionalized poly(ethylene glycol methacrylate) (POEGMA) precursor polymers, optionally in the presence of collagen to promote cell adhesion, results in a dynamic reversible covalent crosslinked network that can both form quickly (enabling printability) and enable slow reconformation of the hydrogel to increase the homogeneity of the printed structures over time, even in scaffolds with higher crosslink densities. Compressive moduli of up to 12 kPa can be achieved in conjunction with free-standing prints that can maintain their shape fixity over extended periods of time. The hydrazone-crosslinked hydrogel scaffolds can be co-printed with NIH/3T3 mouse fibroblast cells and human umbilical vein endothelial cells (HUVECs) while maintaining high cell viability (>80% after 14 days) and desirable cell morphology (with clear evidence of F-actin-mediated adhesion to the scaffold). We anticipate this printing approach may overcome challenges with both existing FRESH bioprinting approaches (i.e., avoiding the heterogeneity of the printed hydrogel network in the absence of dynamic crosslinking agents) as well as previously reported synthetic polymer-based covalent *in situ*-gelling printable bioinks (i.e., preserving scaffold reversibility to enable dynamic scaffold reconfiguration by cells and ultimate degradation), offering a new bioink design to broaden the 3D printing toolkit.

4.6 Acknowledgements

We gratefully acknowledge Paul Gatt for his help with the customized printer and Joao Pedro Bronze de Firmino for providing the FIJI macro to count the cells in the 3D printed lattice structures. The CALM Institute for Advanced Microscopy is acknowledged for their assistance in the confocal microscopy. The Natural Sciences and Engineering Research Council

(Discovery Grant RGPIN-2017-06455 to TH) and a Canada Graduate Scholarship (to EM) are acknowledged for funding.

4.7 References

1. Murphy, S. V.; Atala, A., 3D bioprinting of tissues and organs. *Nat. Biotechnol.* **2014,** *32* (8), 773-785.
2. Lee, J. M.; Yeong, W. Y., Design and printing strategies in 3D bioprinting of cell-hydrogels: A review. *Adv. Healthcare Mater.* **2016,** *5* (22), 2856-2865.
3. Unagolla, J. M.; Jayasuriya, A. C., Hydrogel-based 3D bioprinting: A comprehensive review on cell-laden hydrogels, bioink formulations, and future perspectives. *Appl. Mater. Today* **2020,** *18*, 100479.
4. Mandrycky, C.; Wang, Z.; Kim, K.; Kim, D.-H., 3D bioprinting for engineering complex tissues. *Biotechnol. Adv.* **2016,** *34* (4), 422-434.
5. Dey, M.; Ozbolat, I. T., 3D bioprinting of cells, tissues and organs. *Nat. Pub. Group* **2020,** 10 (1), 1-3.
6. He, Y.; Yang, F.; Zhao, H.; Gao, Q.; Xia, B.; Fu, J., Research on the printability of hydrogels in 3D bioprinting. *Sci. Rep.* **2016,** *6* (1), 1-13.
7. Ramiah, P.; du Toit, L. C.; Choonara, Y. E.; Kondiah, P. P.; Pillay, V., Hydrogel-based bioinks for 3D bioprinting in tissue regeneration. *Front. Polym. Mater.* **2020,** *7*, 76.
8. Skardal, A., Perspective:"Universal" bioink technology for advancing extrusion bioprinting-based biomanufacturing. *Int. J. Bioprint.* **2018**, 10, e00026.
9. Compaan, A. M.; Song, K.; Huang, Y., Gellan fluid gel as a versatile support bath material for fluid extrusion bioprinting. *Appl. Mater. Interfaces* **2019,** *11* (6), 5714-5726.
10. Lindsay, C. D.; Roth, J. G.; LeSavage, B. L.; Heilshorn, S. C., Bioprinting of stem cell expansion lattices. *Acta Biomater.* **2019,** *95*, 225-235.
11. Ouyang, L.; Highley, C. B.; Sun, W.; Burdick, J. A., A generalizable strategy for the 3D bioprinting of hydrogels from nonviscous photo-crosslinkable inks. *Adv. Mater.* **2017,** *29* (8), 1604983.
12. Lee, A.; Hudson, A.; Shiwarski, D.; Tashman, J.; Hinton, T.; Yerneni, S.; Bliley, J.; Campbell, P.; Feinberg, A., 3D bioprinting of collagen to rebuild components of the human heart. *Science* **2019,** *365* (6452), 482-487.
13. Noor, N.; Shapira, A.; Edri, R.; Gal, I.; Wertheim, L.; Dvir, T., 3D printing of personalized thick and perfusable cardiac patches and hearts. *Adv. Sci.* **2019,** *6* (11), 1900344.
14. Isaacson, A.; Swioklo, S.; Connon, C. J., 3D bioprinting of a corneal stroma equivalent. *Exper. Eye Res.* **2018,** *173*, 188-193.
15. Mabry, K. M.; Lawrence, R. L.; Anseth, K. S., Dynamic stiffening of poly (ethylene glycol)-based hydrogels to direct valvular interstitial cell phenotype in a three-dimensional environment. *Biomaterials* **2015,** *49*, 47-56.
16. Ferreira, S. A.; Faull, P. A.; Seymour, A. J.; Tracy, T.; Loaiza, S.; Auner, H. W.; Snijders, A. P.; Gentleman, E., Neighboring cells override 3D hydrogel matrix cues to drive human MSC quiescence. *Biomaterials* **2018,** *176*, 13-23.
17. Suzuki, Y.; Nishimura, Y.; Tanihara, M.; Suzuki, K.; Nakamura, T.; Shimizu, Y.; Yamawaki, Y.; Kakimaru, Y., Evaluation of a novel alginate gel dressing: Cytotoxicity to fibroblasts in vitro and foreign-body reaction in pig skin in vivo. *J. Biomed. Mater. Res.* **1998,** *39* (2), 317-322.
18. Choi, G.; Cha, H. J., Recent advances in the development of nature-derived photocrosslinkable biomaterials for 3D printing in tissue engineering. *Biomater. Res.* **2019,** *23* (1), 1-7.

19. Zhao, D.; Tie, C.; Cheng, B.; Yang, S.; Wang, X.; Sun, Z.; Yin, M.; Zhu, H.; Yin, M., Effect of altering photocrosslinking conditions on the physical properties of alginate gels and the survival of photoencapsulated cells. *Polym. Degrad. Stability* **2020,** *179*, 109297.
20. Rýglová, Š.; Braun, M.; Suchý, T., Collagen and its modifications—crucial aspects with concern to its processing and analysis. *Macromol. Mater. Eng.* **2017,** *302* (6), 1600460.
21. Wang, L. L.; Highley, C. B.; Yeh, Y. C.; Galarraga, J. H.; Uman, S.; Burdick, J. A., Three-dimensional extrusion bioprinting of single- and double-network hydrogels containing dynamic covalent crosslinks. *J. Biomed. Mater. Res. A* **2018,** *106* (4), 865-875.
22. Morgan, F. L.; Fernández-Pérez, J.; Moroni, L.; Baker, M. B., Tuning Hydrogels by Mixing Dynamic Cross-Linkers: Enabling Cell-Instructive Hydrogels and Advanced Bioinks. *Adv. Healthcare Mater.* **2022,** *11* (1), 2101576.
23. Zhou, K.; Sun, Y.; Yang, J.; Mao, H.; Gu, Z., Hydrogels for 3D embedded bioprinting: a focused review on bioinks and support baths. *J. Mater. Chem. B* **2022**, 10, 1897-1907.
24. Wu, W.; DeConinck, A.; Lewis, J. A., Omnidirectional printing of 3D microvascular networks. *Adv. Mater.* **2011,** *23* (24), H178-H183.
25. Bhattacharjee, T.; Zehnder, S. M.; Rowe, K. G.; Jain, S.; Nixon, R. M.; Sawyer, W. G.; Angelini, T. E., Writing in the granular gel medium. *Sci. Adv.* **2015,** *1* (8), e1500655.
26. Shiwarski, D. J.; Hudson, A. R.; Tashman, J. W.; Feinberg, A. W., Emergence of FRESH 3D printing as a platform for advanced tissue biofabrication. *APL Bioeng.* **2021,** *5* (1), 010904.
27. Hinton, T. J.; Jallerat, Q.; Palchesko, R. N.; Park, J. H.; Grodzicki, M. S.; Shue, H.-J.; Ramadan, M. H.; Hudson, A. R.; Feinberg, A. W., Three-dimensional printing of complex biological structures by freeform reversible embedding of suspended hydrogels. *Sci. Adv.* **2015,** *1* (9), e1500758.
28. Highley, C. B.; Rodell, C. B.; Burdick, J. A., Direct 3D printing of shear-thinning hydrogels into self-healing hydrogels. *Adv. Mater.* **2015,** *27* (34), 5075-5079.
29. Heo, D. N.; Alioglu, M. A.; Wu, Y.; Ozbolat, V.; Ayan, B.; Dey, M.; Kang, Y.; Ozbolat, I. T., 3D bioprinting of carbohydrazide-modified gelatin into microparticle-suspended oxidized alginate for the fabrication of complex-shaped tissue constructs. *ACS App. Mater. Interfaces* **2020,** *12* (18), 20295-20306.
30. Vanaei, S.; Parizi, M.; Salemizadehparizi, F.; Vanaei, H., An overview on materials and techniques in 3D bioprinting toward biomedical application. *Eng. Regen.* **2021,** *2*, 1-18.
31. Liu, F.; Wang, X., Synthetic polymers for organ 3D printing. *Polymers* **2020,** *12* (8), 1765.
32. Hull, S. M.; Lindsay, C. D.; Brunel, L. G.; Shiwarski, D. J.; Tashman, J. W.; Roth, J. G.; Myung, D.; Feinberg, A. W.; Heilshorn, S. C., 3D Bioprinting using UNIversal Orthogonal Network (UNION) Bioinks. *Adv. Funct. Mater.* **2021,** *31* (7), 2007983.
33. Smeets, N. M.; Bakaic, E.; Patenaude, M.; Hoare, T., Injectable and tunable poly(ethylene glycol) analogue hydrogels based on poly(oligoethylene glycol methacrylate). *Chem. Comm.* **2014,** *50* (25), 3306-9.
34. Bakaic, E.; Smeets, N. M. B.; Hoare, T., Injectable hydrogels based on poly(ethylene glycol) and derivatives as functional biomaterials. *RSC Adv.* **2015,** *5* (45), 35469-35486.

35. Smeets, N. M.; Bakaic, E.; Patenaude, M.; Hoare, T., Injectable poly (oligoethylene glycol methacrylate)-based hydrogels with tunable phase transition behaviours: Physicochemical and biological responses. *Acta Biomater.* **2014,** *10* (10), 4143-4155.
36. Seymour, A. J.; Shin, S.; Heilshorn, S. C., 3D printing of microgel scaffolds with tunable void fraction to promote cell infiltration. *Adv. Healthcare Mater.* **2021,** *10* (18), 2100644.
37. Nair, K.; Gandhi, M.; Khalil, S.; Yan, K. C.; Marcolongo, M.; Barbee, K.; Sun, W., Characterization of cell viability during bioprinting processes. *J. Biotech. Healthcare Nutrition Techn.* **2009,** *4* (8), 1168-1177.
38. Singh, G.; Chanda, A., Mechanical properties of whole-body soft human tissues: a review. *Biomed. Mater.* **2021**, 16, 062004.
39. Liu, J.; Zheng, H.; Poh, P. S.; Machens, H.-G.; Schilling, A. F., Hydrogels for engineering of perfusable vascular networks. *Int. J. Mol. Sci.* **2015,** *16* (7), 15997-16016.
40. Banerjee, A.; Arha, M.; Choudhary, S.; Ashton, R. S.; Bhatia, S. R.; Schaffer, D. V.; Kane, R. S., The influence of hydrogel modulus on the proliferation and differentiation of encapsulated neural stem cells. *Biomaterials* **2009,** *30* (27), 4695-4699.
41. Matyash, M.; Despang, F.; Mandal, R.; Fiore, D.; Gelinsky, M.; Ikonomidou, C., Novel soft alginate hydrogel strongly supports neurite growth and protects neurons against oxidative stress. *Tissue Eng. Part A* **2012,** *18* (1-2), 55-66.
42. Luo, Y.; Lode, A.; Akkineni, A. R.; Gelinsky, M., Concentrated gelatin/alginate composites for fabrication of predesigned scaffolds with a favorable cell response by 3D plotting. *RSC Adv.* **2015,** *5* (54), 43480-43488.
43. Udofia, E. N.; Zhou, W., A guiding framework for microextrusion additive manufacturing. *J. Manufact. Sci. Eng.* **2019,** *141* (5), 050801.

4.8 Supplementary Information

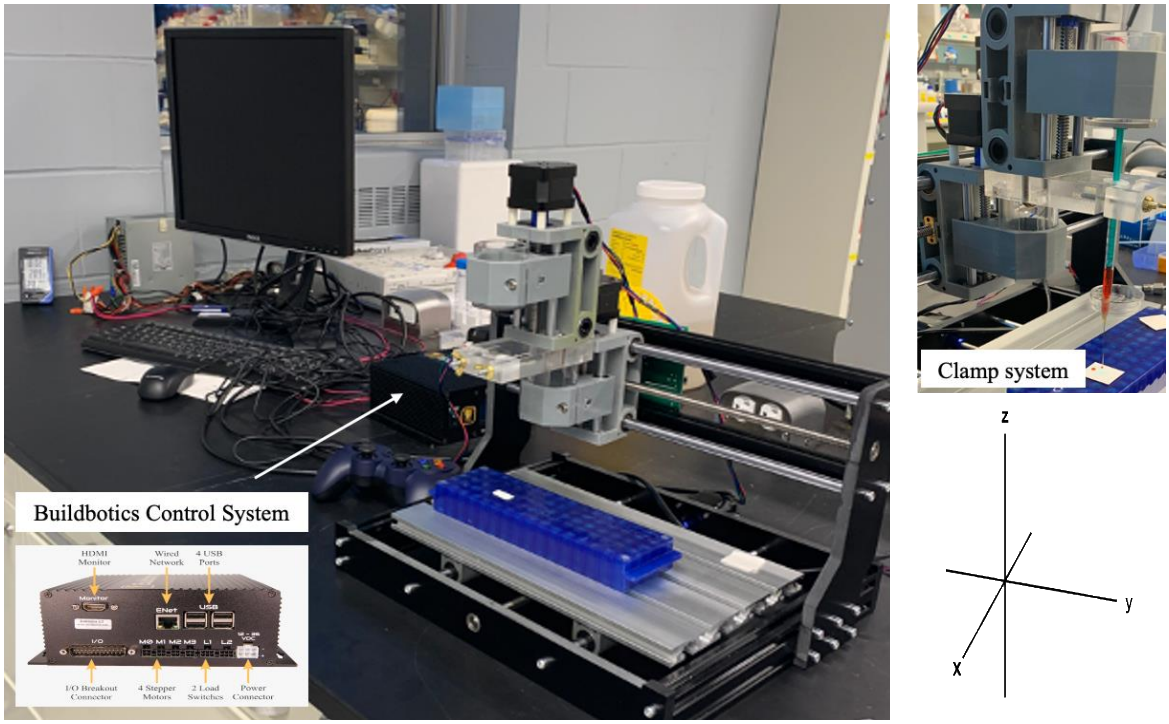

Figure S4.1: Customized extrusion bioprinter using Buildbotics control system to control four step motors (xyz directional control and extrusion axis)

Table S4.1*:* Customized printer components and cost analysis

Component	Source	Cost (USD)
CNC 2018 PRO Milling Machine 3 Axis machines	Amazon	200 x 2 (for fourth step motor + axis)
CNC Control System	Buildbotics Inc	500
3D printed clamp system	In-house	20
		Total ~ USD 1000

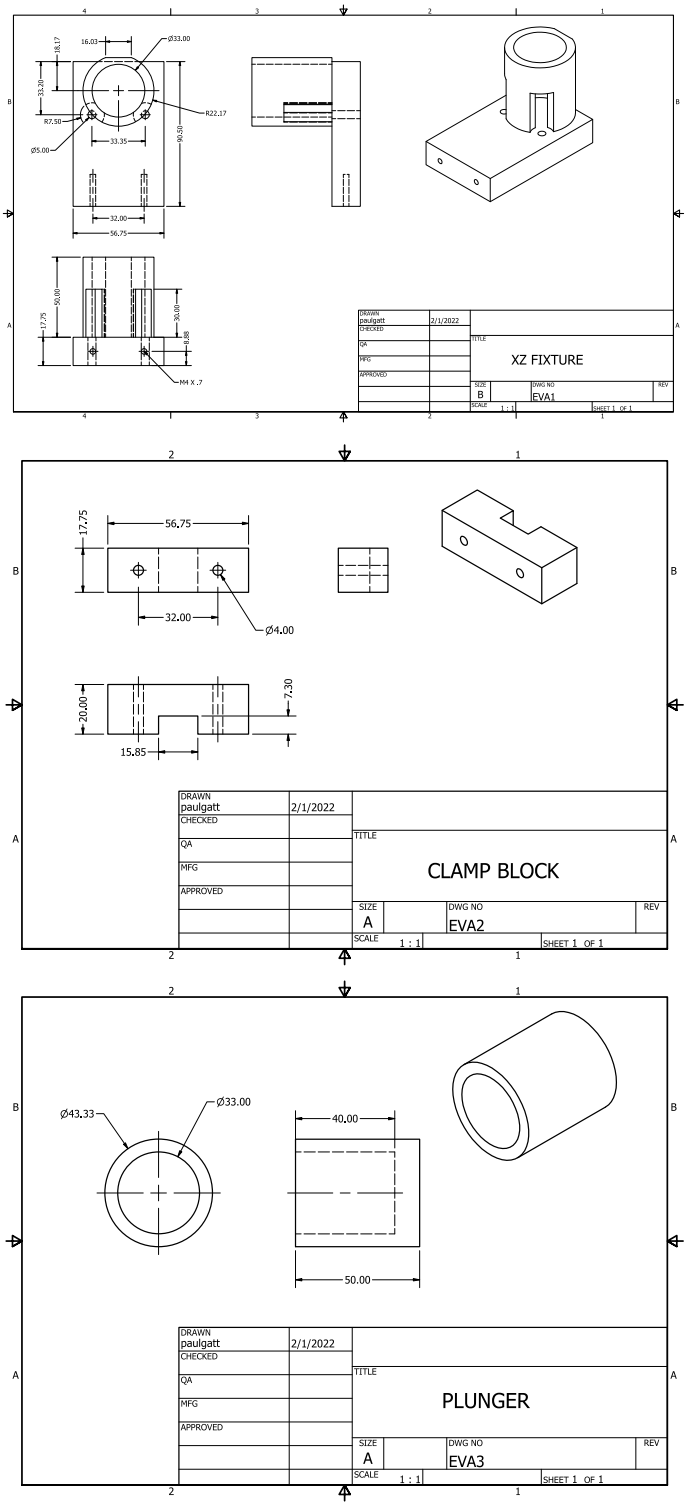

Figure S4.2: Drawings of 3D printed components that make up the extrusion axis in the customized extrusion printer

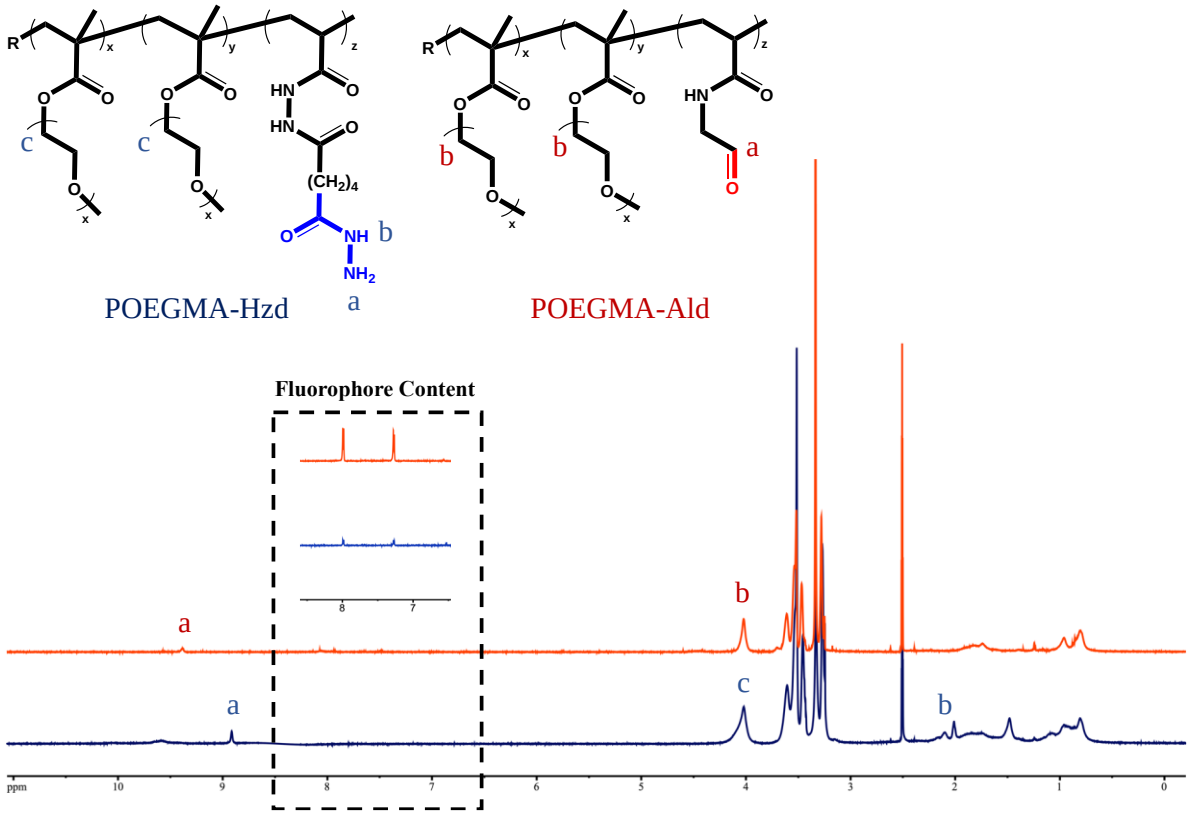

Figure S4.3:[1]H NMR of POEGMA-Hzd and POEGMA-Ald; inset shows the ranges used in each spectrum for integration for quantification of the fluorophore content.

Table S4.2: Gelation kinetics of hydrogel ink formulations used in the printing experiments

POEGMA-Hzd (wt%)	POEGMA-Ald (wt%)	Gelation time
15	3	2-3 min
15	6	<10 seconds
15	10	<5 seconds
20	3	1-2 min
20	6	<5 seconds
20	10	<5 seconds

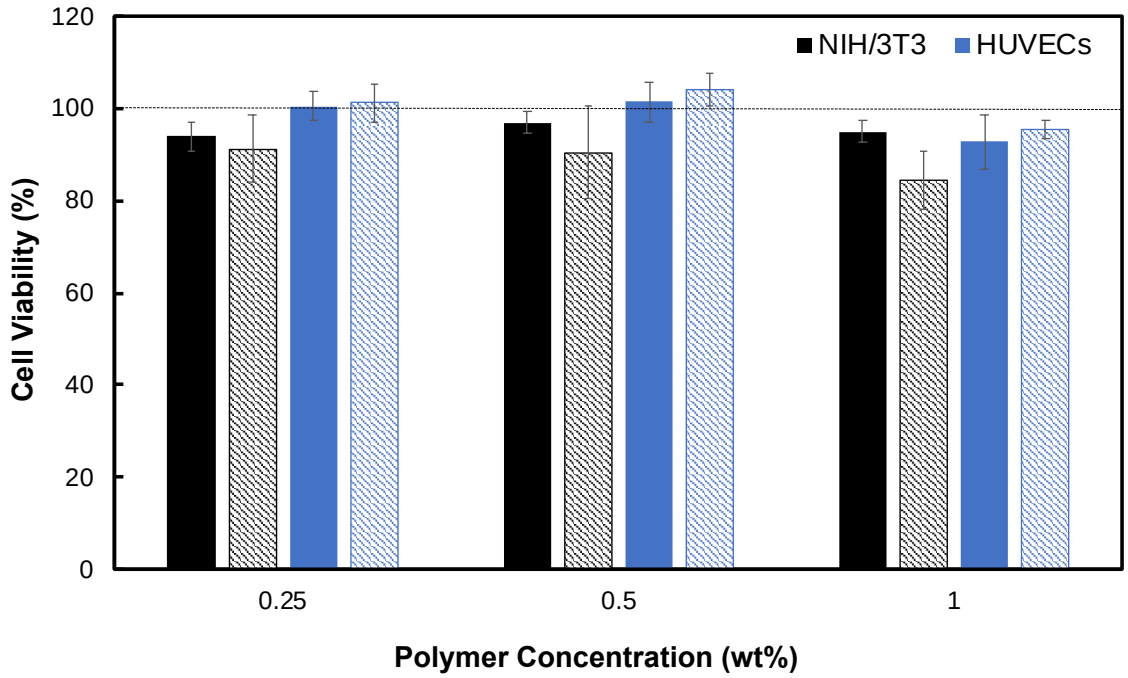

Figure S4.4: Polymer cytotoxicity of POEGMA-Hzd (solid) and POEGMA-Ald (shaded) at three concentrations to NIH/3T3 fibroblasts and human umbilical cord endothelial cells (HUVECs)

G-code for 12×12 mm lattice

Speed 6 mm/s, flow rate = 220 μl/min, layer height 0.2 mm

```
G28 ; home all axes
G21 ; set units to millimeters
G90 ; use absolute coordinates

G1 Z-0.20 F360
G1 X-6 Y-6 F480
G1 F360
G1 X-6 Y-6
G1 X-6 Y6 A+0.2
G1 X-3 Y6
G1 X-3 Y-6 A+0.4
G1 X0 Y-6
G1 X0 Y6 A+0.6
G1 X3 Y6
G1 X3 Y-6 A+0.8
G1 X6 Y-6
G1 X6 Y6 A+1

G1 Z-0.40 F360
G1 X6 Y6
G1 X-6 Y6 A+1.2
G1 X-6 Y3
G1 X6 Y3 A+1.4
G1 X6 Y0
G1 X-6 Y0 A+1.6
G1 X-6 Y-3
G1 X6 Y-3 A+1.8
G1 X6 Y-6
G1 X-6 Y-6 A+2

G1 Z-0.60 F360
G1 X-6 Y-6 F480
G1 F360
G1 X-6 Y-6
G1 X-6 Y6 A+2.2
G1 X-3 Y6
G1 X-3 Y-6 A+2.4
G1 X0 Y-6
G1 X0 Y6 A+2.6
G1 X3 Y6
G1 X3 Y-6 A+2.8
G1 X6 Y-6
G1 X6 Y6 A+3

G1 Z-0.80 F360
G1 X6 Y6
G1 X-6 Y6 A+3.2
G1 X-6 Y3
G1 X6 Y3 A+3.4
G1 X6 Y0
G1 X-6 Y0 A+3.6
```

```
G1 X-6 Y-3
G1 X6 Y-3 A+3.8
G1 X6 Y-6
G1 X-6 Y-6 A+4

G1 Z-1.00 F360
G1 X-6 Y-6 F480
G1 F360
G1 X-6 Y-6
G1 X-6 Y6 A+4.2
G1 X-3 Y6
G1 X-3 Y-6 A+4.4
G1 X0 Y-6
G1 X0 Y6 A+4.6
G1 X3 Y6
G1 X3 Y-6 A+4.8
G1 X6 Y-6
G1 X6 Y6 A+5
```

Table S4.3: Partitioning experiment using POEGMA-Ald-rho in the support bath to assess the percentage of the initially added aldehyde-functionalized POEGMA precursor polymer lost via the centrifugation steps in the preparation of the POEGMA-Ald/LifeSupport support bath

Initial polymer concentration (wt%)	**3.3 wt%**	**6 wt%**	**10 wt%**
Mass loss %	14.3 %	12.0 %	8.5 %

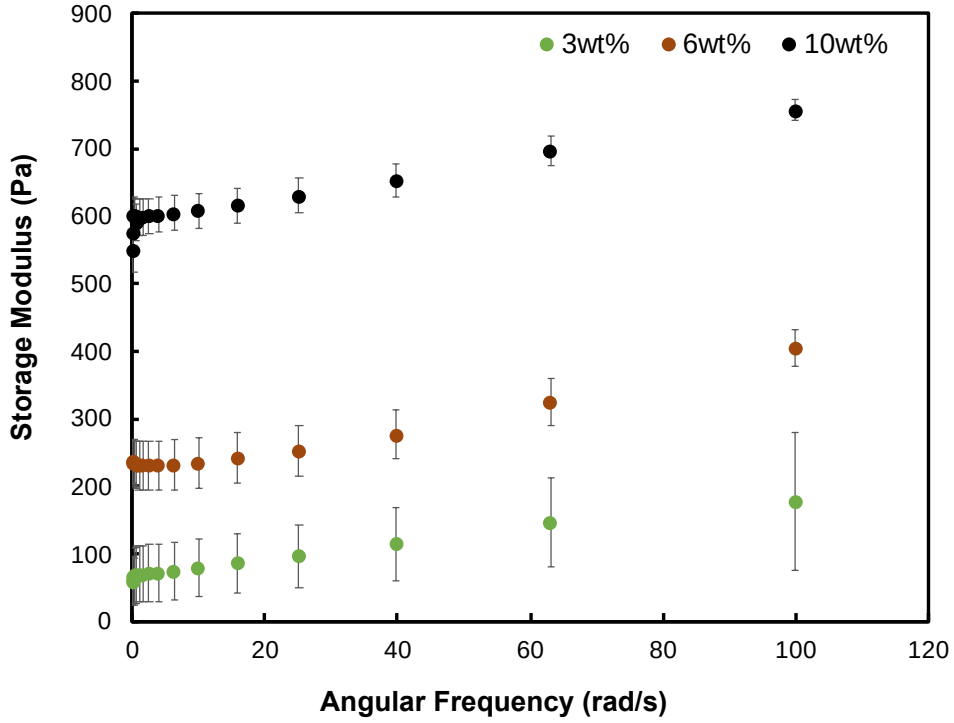

Figure S4.5: Frequency sweeps of hydrogels produced by crosslinking 15 wt% POEGMA-Hzd with 3, 6 or 10 wt% POEGMA-Ald directly on the rheometer stage

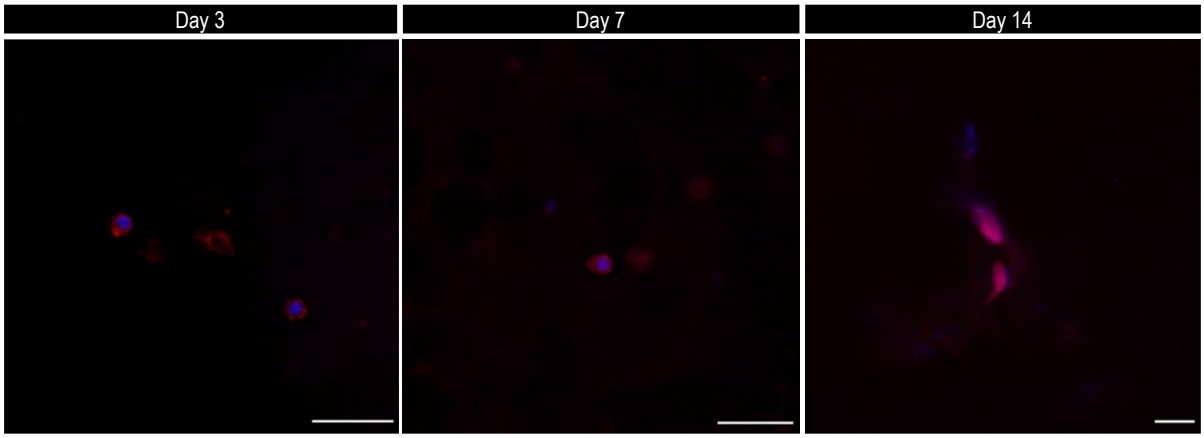

Figure S4.6: Phalloidin (red)-DAPI (blue) staining of HUVECs co-printed in POEGMA-Hzd/ POEGMA-Ald hydrogels prepared with a POEGMA-Ald concentration of 3wt% in the support bath using FRESH bioprinting after 3 days (left column), 7 days (middle column), and 14 days (right column) in culture. Scale bar = 50 μm.

CHAPTER 5

Free-Form Bioprinting using Pre-Mixed Ketone and Hydrazide Functionalized Zwitterionic Polymers

Eva Mueller, Nahieli Preciado, Fei Xu, Thomas Kalab, Todd Hoare

Declaration of Academic Achievement:

Nahieli Preciado is credited with the synthesis and characterization of the ketone monomer. Dr. Fei Xu helped with the cell experiments and provided helpful guidance for the confocal microscopy. Thomas Kalab helped to synthesize and characterize the functional polymers. Eva Mueller performed all other experiments and wrote the manuscript, with help from Dr. Todd Hoare.

Free-Form Bioprinting using Pre-Mixed Ketone and Hydrazide Functionalized Zwitterionic Polymers

Eva Mueller, Nahieli Preciado, Fei Xu, Thomas Kalab, Todd Hoare

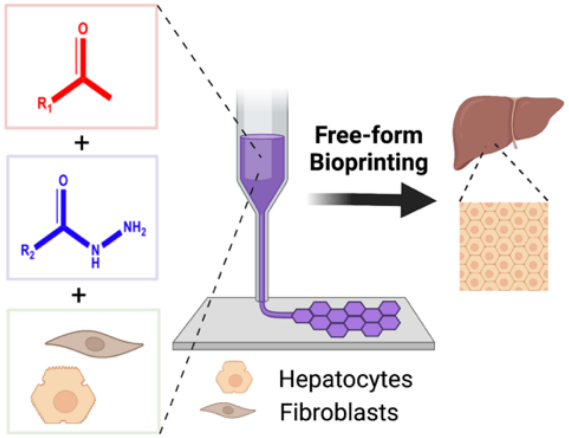

Current hydrogel bioinks often require post-processing strategies to be free-form printed with high print fidelity. Dynamic covalent chemistry provides a promising alternative for hydrogels bioinks to be shear-thinning and reform chemically when high shear rates are applied during the printing process. In this work, a zwitterionic hydrogel bioink based on dynamic hydrazone crosslinking of ketone and hydrazide-functionalized precursor polymers is demonstrated for free-form extrusion-based bioprinting. Pre-mixing the low viscosity precursor polymers allows for easy mixing with cells, well-defined structures upon gelation, and high cell viability (>90%) following co-printing with hepatocytes. Moreover, albumin secretion increased 4-fold when hepatocytes were co-printed with fibroblast cells in a small-scale liver model. Coupled with the inherent high anti-fouling/anti-fibrotic properties of zwitterionic polymers, this zwitterionic hydrogel bioink thus provides a promising strategy for printing functional implantable cell constructs.

Keywords: 3D bioprinting, dynamic covalent chemistry, freeform printing, hydrazone chemistry, liver tissue engineering

5.1 Introduction

Bioprinting is a process that deposits both biomaterials and cells in a precise three-dimensional (3D) architecture, allowing for the fabrication of heterogenous tissue-mimetic constructs that promote cell-cell and cell-extracellular matrix interactions in a 3D environment[1]. Among the different bioprinting strategies that have been studied, including light-induced[2] and inkjet-based[3] methods, extrusion bioprinting has remained the leading bioprinting strategy due to its ease of use and potential to accommodate a wide range of bioink viscosities, cell densities, and crosslinking methods[4]. While there has been a rapid rise in the number of bioprinting methods and printers available for extrusion bioprinting, the major limitation of extrusion bioprinting remains the limited scope of available bioink materials. The ideal bioink must not only be printable but also fulfill properties essential for tissue engineering such as degradability, cell/tissue compatibility, and cell attachment[5]. To prevent clogging and reduce shear stress on the cells, the shear thinning property of a bioink is also typically important given its correlation with gel printability, resolution, and pattern fidelity[6]. The printed bioink must be sufficiently mechanically strong to avoid the collapse of the 3D printed structure while also matching the stiffness of the native tissue to provide the correct interfacial stiffness cues to cells to develop into a tissue[7]. Furthermore, for implantable printed constructs, the ideal hydrogel bioink must suppress non-specific protein adsorption (and ultimately fibrosis[8]) when implanted at the site of injury; such a fibrotic response to an implanted tissue can lead to the failure of the implanted scaffold (particularly if the scaffold is intended as a cell therapeutic in which the printed cells continually produce and release a specific biomolecule) while also causing discomfort to the recipient[9, 10]. However, bioinks based on naturally-occurring matrix polymers may introduce cellular signals that are not ideal for such applications[11], including enhanced protein adsorption and subsequent inflammation/fibrotic responses that may render the implant non-functional and effectively walled from the body[12]. For example, histological analysis of subcutaneously implanted collagen bioinks after one week of implantation showed inflammatory responses that persisted for up to six weeks, at which point the hydrogels were almost fully degraded[13].

Zwitterionic materials are a class of materials containing both negative and positive charges in close proximity. Compared to polyethylene glycol (PEG)-derived materials that are the gold standard for anti-fouling biomaterials[14, 15], zwitterionic materials have much stronger capacity to bind water; for example, each sulfobetaine unit can bind 7-8 water molecules[16], while each ethylene glycol unit in PEG can only bind one[17]. Due to this strong hydration layer, zwitterionic

materials provide a promising route for decreasing non-specific protein adsorption and ultimately reducing immune/inflammatory/fibrotic responses to implanted biomaterials[18]. Zwitterionic hydrogels have been previously studied *in vivo* for their potential to reducing the formation of the fibrous capsule. For example, Chan et al. showed that the complexation of functional carboxylic or sulfonic acid-terminated acrylate monomers with calcium followed by the addition of 30 mol% amino acid-terminated methacryloyl-L-lysine (MLL) resulted in an anti-fouling zwitterionic hydrogel that prevented capsule formation for at least 2 months when subcutaneously implanted in mice[19], while Zhang et al. reported that zwitterionic poly(carboxybetaine methacrylate) hydrogels can prolong the onset of a fibrous capsule for three months compared to <1 month using non-ionic poly(2-hydroxyethyl methacrylate) hydrogels[20]. Furthermore, unlike other anti-fouling materials, zwitterionic materials can better support cell viability and adhesion over extended periods[21].

Despite the significant potential for using zwitterionic hydrogels as implantable biomaterial scaffolds[22, 23], the current methods used for preparation of zwitterionic hydrogels are limited and their potential in the context of innovative biofabrication methods such as bioprinting has not yet been fully explored. Current zwitterionic bioink development has been focused on one of three strategies: (1) 'bottom-up' microsphere assemblies[24]; (2) *in situ* polymerization to fabricate macroporous scaffolds[25]; and (3) stereolithography to create high-resolution zwitterionic scaffolds[26, 27]. As an example of the first approach, Zhang et al. reported a zwitterionic granular hydrogel bioink for stem cell spheroid production and 3D bioprinting in which poly(sulfobetaine methacrylate)-based microspheres were synthesized, concentrated, and then *in situ* polymerized in the presence of N-isopropylacrylamide and sulfobetaine methacrylate to create a composite granular hydrogel[24]. As an example of the second approach, Asadikorayem et al. synthesized a bulk hydrogel via the photopolymerization of zwitterionic carboxybetaine acrylamide monomer using gelatin methacryloyl as crosslinker and tyramine acrylamide as functional comonomers to allow for secondary crosslinking via horseradish peroxidase and hydrogen peroxide[25]. The bulk hydrogel was then mechanically fragmented into microgels of 50-150 µm in size[28] that could be co-printed with human chondrocytes, enabling >90% cell viability and enhanced extracellular matrix production and tissue maturation. As an example of the third approach, Kostina et al. used stereolithography to fabricate zwitterionic hydrogels based on carboxybetaine methacrylamide and a α,ω-methacrylate poly(d,l-lactide-block-ethylene glycol-block-d,l-lactide) telechelic triblock macromer, with the carboxybetaine promoting low non-specific protein adsorption and the

telechelic triblock macromonomer enabling precisely defined gyroid interconnected porosity to allow for fast diffusion of nutrient and waste products[26]. Alternately, Pan et al. quantified the anti-fouling properties by printing both non-ionic and ionic/zwitterionic polyacrylamide hydrogels and determined a 58% reduction in bovine serum albumin absorption in the zwitterionic hydrogels[27]. However, there are drawbacks to these existing methods: (1) microsphere assemblies require multiple ink processing/crosslinking steps to fabricate (both in terms of the ink itself as well as the resulting printed features; (2) stereolithography is more time-consuming and requires UV irradiation (both factors of which can reduce the viability of co-printed cells); and (3) *in situ* crosslinking requires a combination of photoirradiation and post-crosslinking, adding time and technical complexity to the printing process. In contrast, the development of a zwitterionic bioink that can be directly printed with no additional pre/post-processing steps but can still achieve the targeted mechanics and feature resolution required for effective 3D bioprinting would offer significant benefits.

Hydrogels based on dynamic chemistry are promising materials for extrusion bioprinting applications due to the ability to reform rapidly when high shear rates are applied during the printing process. While reports on dynamic chemistry hydrogel bioinks are limited for free-form printing, several examples exist that show the benefits of using such a chemistry. For example, Hafeez et al. studied the printability of oxidized alginate (containing aldehyde groups) with different small molecule crosslinkers (i.e., adipic acid dihydrazide, hexamethylene disemicarbazide, and aminooxy propyl hydroxyl amine dihydrochloride) formed via hydrazone, semicarbazone, and oxime click chemistry, respectively using a pre-mixing approach[29]. The dynamic crosslinking in dual hydrazone and oxime crosslinked hydrogels was further studied by mixing oxidized alginate with dihydrazide and bishydroxlamine cross-linkers, demonstrating that the reversibility of hydrogels with high hydrazone content enables good printability[30]. Wang et al. demonstrated the use of hydrazone-crosslinked hyaluronic acid hydrogels as a viable bioink formulation due to the shear-thinning and self-healing nature of hydrazone bonds, although the addition of a secondary photo-crosslinking step was required to enhance the mechanics[31]. Hydrogels based on imine bonds (using partially oxidized hyaluronic acid and carboxymethyl chitosan[32]) and boronate ester (using boronic acid functionalized laminarin and alginate[33]) have also been reported, although both of these bonds are much more labile in aqueous environments and may not be suitable particularly for fabricating longer-term implantable prints. However, to our knowledge, the

benefits of dynamic chemistry in the context of enabling 3D bioprinting have not been previously demonstrated for zwitterionic hydrogels.

In this work, we synthesized synthetic zwitterionic polymers functionalized with hydrazide and ketone groups that upon mixing form a dynamic hydrazone-crosslinked hydrogel. The rheological and mechanical properties of this synthetic hydrogel bioink were investigated for free-form printing using a customized extrusion printer, with 3D prints achievable without the use of any templating or post-crosslinking based on the combination of hydrazone covalent crosslinking and electrostatic zwitterionic fusion interactions that are shear-responsive but can rapidly reform to retain the shape of the printed structure (**Figure 5.1**). We demonstrate the printability of our bioink and its efficacy in both preserving cell viability as well as mimicking the native cellular microenvironment, the latter by creating small-scale livers with hexagonal lobule patterns by co-printing human carcinoma liver HepG2 cells with and without NIH/3T3 fibroblasts and demonstrating enhanced albumin release from the co-printed constructs, following previous demonstrations of such synergy in other types of hydrogel encapsulation systems[34, 35]. Such *in vitro* liver tissue models, in which the physiological microenvironment of the liver is recreated via the co-culture of hepatocytes with non-parenchymal cells such as fibroblasts[35-38] to understand the signaling pathways of soluble molecules and factors[35] and increase the survival and function of hepatocytes[40], are in great demand for disease modeling, drug discovery, and clinical applications[41, 42]. While other reports have shown the successful fabrication of liver tissues using more complex methods such as dynamic optical projection stereolithography and micro-extrusion bioprinting using bioinks that are not explicitly anti-fouling[43, 44], this report is the first demonstration of a non-fouling synthetic hydrogel bioink that can be directly printed into a free-standing structure using extrusion bioprinting while also maintaining high cell viability and facilitating the functionality of a liver-tissue mimic.

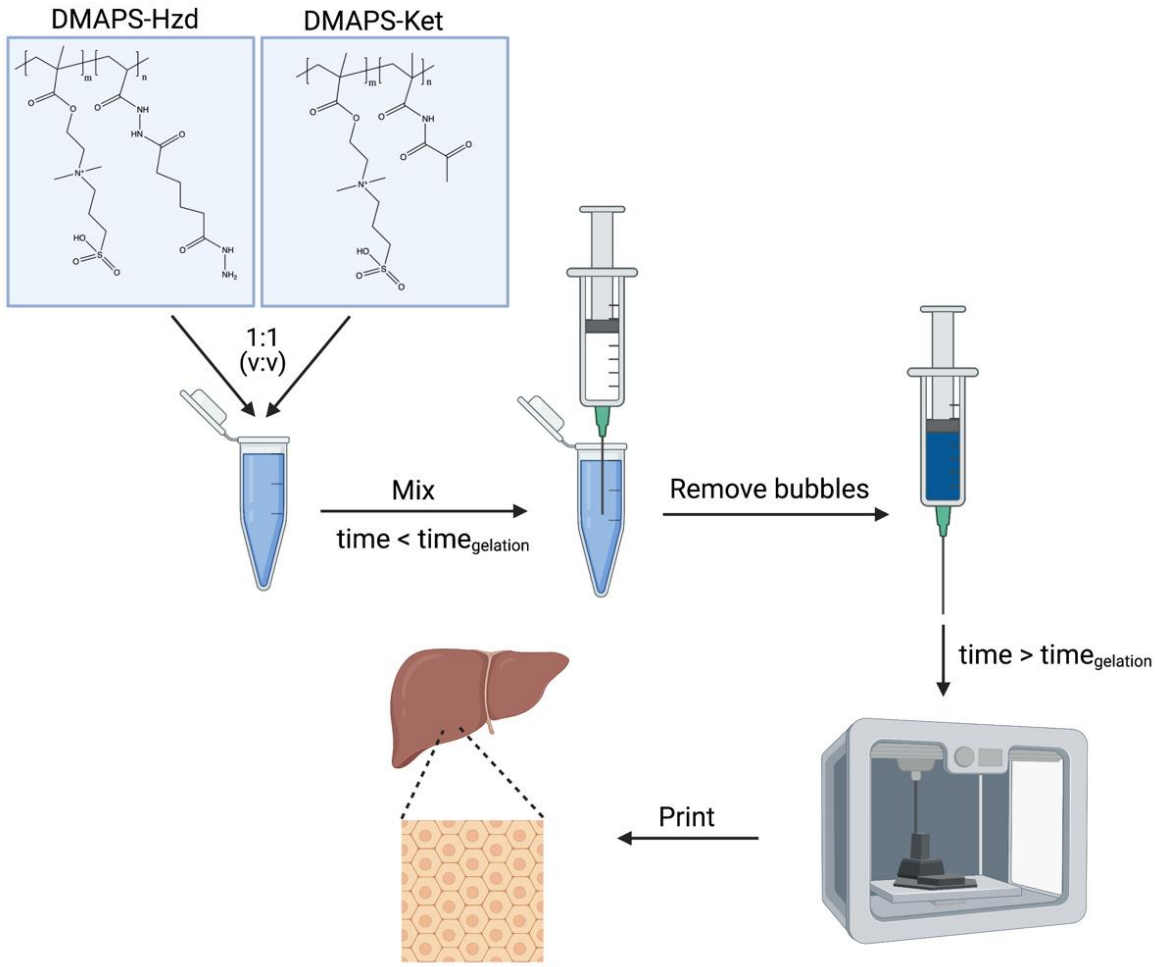

Figure 5.1: Schematic illustration of the bioprinting process

5.2 Experimental Methods

5.2.1 Materials

For the synthesis of the functional polymers, [2-(methacryloyloxy)ethyl]dimethyl-(3-sulfopropyl)ammonium hydroxide (DMAPS, Sigma-Aldrich), acrylic acid (AA, Sigma-Aldrich, 99%), thioglycolic acid (TGA, Sigma-Aldrich, 98%), ammonium persulfate (APS, Sigma-Aldrich), N′-ethyl-N-(3-(dimethylamino)propyl)-carbodiimide (EDC, Carbosynth, Compton CA, commercial grade), and adipic acid dihydrazide (ADH, Alfa Aesar, 98%) were all used as received. Milli-Q grade distilled deionized water (DIW) was used for all experiments.

NIH/3T3 mouse fibroblast cells and HepG2 cells were purchased from ATCC (Cedarlane Laboratories, Burlington, ON). Dulbecco's Modified Eagle's Medium (DMEM, ThermoFisher), fetal bovine serum (FBS, ThermoFisher) and penicillin−streptomycin (ThermoFisher), trypsin−EDTA solution (Sigma-Aldrich), and phosphate buffered saline (1× PBS, pH = 7.4, ThermoFisher) were all used as received. The live/dead assay and human albumin ELISA kits (ThermoFisher) were used as per the manufacturer instructions.

5.2.2 Synthesis of Ketone Monomer

The ketone precursor monomer 2-methyl-N-[(2-methyl-1,3-dioxolan-2-yl)methyl]-2-propenamide was synthesized via a four-step process of a nucleophilic substitution reaction, ketone protection, hydrolysis reaction, and acyl substitution. Refer to the Supporting Information for full synthesis and characterization information, including the synthesis pathway summary in **Figure S5.1**, and a ^{1}H NMR spectrum confirming the final structure in **Figure S5.2**.

5.2.3 Synthesis of Functionalized DMAPS Polymers

The functional DMAPS polymers were synthesized via free-radical polymerization using thioglycolic acid (TGA) as the chain transfer agent to control the molecular weight and ammonium persulfate (APS) as the initiator. The reactions were performed in Milli-Q water at 75℃ overnight to allow for polymerization to occur.

For the hydrazide-functionalized DMAPS polymer, DMAPS (4 g) was pre-dissolved in 10 mL of Milli-Q water in a 100 mL round bottom flask. Acrylic acid (0.44 g), TGA (10 μL) and APS

(40 mg) were added to the flask, after which 20 mL of Milli-Q water was added (total volume = 30 mL). The contents in the flask were stirred for 10 minutes at room temperature to ensure complete dissolution. The flask was then purged with nitrogen for 45 minutes under constant stirring, after which the flask was placed into a pre-heated 75℃ oil bath overnight to ensure full conversion of the reactants to the final polymer. Next, the flask was removed from the oil bath, cooled to room temperature, and ADH (5.35 g) and EDC (2.38 g) were added to convert the acrylic acid moieties to hydrazide groups. An additional 70 mL of Milli-Q water was added to fully dissolve the ADH and EDC, after which the reaction was maintained at a pH of 4.75 using 1 M HCl until the pH stabilized (~4 hours). The solution was kept stirring overnight, after which it was purified by dialysis (6+ hours for six cycles). The final polymer (DMAPS-Hzd) obtained after lyophilization was stored dry at room temperature. The polymer was filtered using a 0.2 μm filter prior to the printing experiments.

For the ketone-functionalized DMAPS polymer, DMAPS (4 g) was pre-dissolved in 10 mL of Milli-Q water in a 100 mL round bottom flask. The synthesized ketone monomer (2-methyl-N-[(2-methyl-1,3-dioxolan-2-yl)methyl]-2-propenamide, 1.14 g), TGA (10 μL) and APS (40 mg) were added to the flask, after which 20 mL of Milli-Q water was added (total volume = 30 mL). The contents in the flask were stirred for 10 minutes at room temperature to ensure complete dissolution. The flask was then purged with nitrogen for 45 minutes under constant stirring, after which the flask was placed into a pre-heated 75℃ oil bath overnight to complete the polymerization. The polymer solution was cooled to room temperature, after which 100 mL of 1 M HCl was added and the reaction was stirred for 24 hours. The final polymer (DMAPS-Ket) was purified by dialysis (6+ hours for six cycles), lyophilized, and stored dry at room temperature. The polymer was filtered using a 0.2 μm filter prior to the printing experiments.

5.2.4 Characterization of Functionalized Polymers

Polymer molecular weights were measured using an Agilent 1260 infinity II gel permeation chromatography (GPC) system with an Agilent 1260 infinity refractive index detector and a Superpose 6 increase 10/300 GL (GE Healthcare) column maintained at a temperature of 30°C and calibrated with PEG standard ranging from 3 to 60 kDa in molecular weights. The solvent used for this GPC characterization was 1× PBS with 0.05% sodium azide at a flow rate of 0.5 mL/min. The gelation kinetics were tested using a vial inversion test by pipetting 0.25 mL of

each precursor polymer into a 2 mL Eppendorf tube and tracking the time required for no flow to be observed within 5 s of flipping the vial upside down.

5.2.5 Bioink Preparation

Equal volumes of hydrazide (0.4 mL) and ketone (0.4 mL) functionalized DMAPS polymers dissolved at concentrations of either 6, 8 or 10 wt% in 0.9% saline were pre-mixed in a 2 mL Eppendorf tube by pipetting up and down for 30 to 60 seconds, loaded into a 1 mL syringe, and allowed to gel in the syringe for 15 minutes prior to printing. When printing with cells, the same preparation steps were followed but with the chosen cells suspended in the functional precursor polymer solutions. Specifically, the hydrazide functionalized DMAPS polymer solution was added to a pellet of HepG2 cells to create a cell suspension of ~8 million cells/mL, without adding any additional cell media or PBS to minimize any changes in gelation kinetics in the presence of cells; the remainder of the cell-free bioink preparation protocol was then followed. For the co-culture prints, each cell type was pre-mixed (again using a cell pellet as the starting point, without any additional media or PBS) with one of the functional polymers; specifically, HepG2 cells were resuspended in 0.4 mL of hydrazide-functionalized DMAPS polymer while NIH/3T3 cells were resuspended in 0.4 mL of ketone-functionalized DMAPS polymer, with the bioink subsequently prepared using the same protocol used for cell-free printing.

5.2.6 Measuring the Bioink Rheological Properties

The rheological properties of the polymer precursors and the crosslinked hydrogels were measured using a Modular Compact Rheometer (Anton Paar, MCR 302). The viscosity sweeps were performed over a shear rate range of 0.1 to 100 s^{-1} at 25°C. The frequency sweeps were performed at 25°C between 0.1 and 100 rad/s at a strain of 1% to assess the shear storage modulus of the hydrogels. The thixotropic study was performed at 25°C with a pre-shear of 0.1 s^{-1} for 20 seconds, followed by the experimental sequence of 10 seconds of testing at low shear (0.1 s^{-1}), 5 seconds of testing at high shear (100 s^{-1}), and an additional 10 seconds of testing at low shear (0.1 s^{-1}).

5.2.7 3D Printer and Printing Procedure

A low-cost home-built 3D extrusion bioprinter was used for the printing experiments that controls the printing speed and design of the construct by reading customized G-codes[44]. The

printer operates using mechanical extrusion and is connected to a commercial CNC control system (Buildbotics Inc) with an easy-to-use interface that directly reads the G-codes generated through conventional slicer software (PrusaSlicer). See Chapter 3 (**Figure S4.1**) for more information on the customized extrusion bioprinter.

5.2.8 Measuring Scaffold Compressive Modulus and Swelling Profile

The compressive moduli of the printed lattice structures were measured using the CellScale Microsquisher using a 6×6 mm platen and a 0.56 mm diameter cantilever. Cyclic compression testing was performed at 2.5, 5, 7.5 and 10% strain using sequential compress-hold-recover steps. The average hold force was calculated and divided over the platen area to calculate the stress. The swelling and degradation of the printed hydrogel scaffolds were tested by placing the hydrogels into pre-weighed cell inserts and submerging them in cell media (DMEM, 10% FBS, 1% penicillin/streptomycin), with the weights of the printed structures measured at 37°C. All measurements were conducted in triplicate, with error bars representing the standard deviation.

5.2.9 Cell Culture and Characterization

HepG2 cells (P14) were cultured in DMEM medium with 10% FBS and 1% penicillin-streptomycin to ~80% confluency at 37°C and 5% CO_2 before subsequent use. NIH/3T3 fibroblasts (P15) were cultured in DMEM medium with 10% FBS and 1% penicillin-streptomycin to ~80% confluency at 37°C and 5% CO_2 before subsequent use.

The cytotoxicity of the functional DMAPS polymers was measured over a concentration range of 0.25 to 1 mg/mL using a PrestoBlue Cell Viability Assay (ThermoFisher) after 24 hours of incubation at 37°C. HepG2 and NIH/3T3 cells were plated at a density of 1 x 10^4 cells per well in a 96-well plate, and the cell viability was assessed by fluorescence (excitation 560 nm, emission 590 nm) using a plate reader and normalized to the cell-only wells. Cell viability within the printed hydrogel scaffolds was assessed using a live/dead staining assay (ThermoFisher) based on the manufacturer's instructions. Briefly, the printed constructs were washed with warm PBS over 3×5-minute intervals before adding the live-dead assay and incubating for 30 minutes at room temperature. Following staining, the printed constructs were thoroughly washed with PBS and imaged via confocal microscopy (CLSM, Nikon A1R HD25) using a 10× 0.45 NA objective and excitation wavelengths of 488 nm and 561 nm to image the live/dead assay results.

5.2.10 Measurement of Albumin Production

Printed cell-laden liver structures were cultured in 6-well plates and incubated in 4 mL cell media per well. Cell media from each well was collected on days 1, 3, 7, 10, 14 and 21 and stored at -20°C for subsequent analysis. The cell media was replaced with fresh media after each collection period. Following the experiment, albumin release was tracked on the frozen samples using a human albumin ELISA kit (Invitrogen, ThermoFisher) used as per the manufacturer's guidelines.

5.3 Results

5.3.1 Zwitterionic Hydrogel Formulation and Properties

Functional DMAPS polymers were synthesized via free-radical polymerization with number average molecular weights of ~15 kDa, significantly lower than the renal clearance. The hydrazide and ketone contents of the polymers on a total monomer basis were 26 mol% and 25 mol% respectively as measured using ^{1}H NMR (**Table 5.1**, **Figure S5.3**), similar to (albeit marginally lower) than the target 30 mol% degree of functionalization; however, the matched functionalization in the two precursor polymers ensure stoichiometric functional group ratios when the polymers are mixed at equal mass concentrations. The polymers are non-cytotoxic, showing >90% viability towards both HepG2 cells and NIH/3T3 after 24 hours at concentrations up to 1 mg/mL (**Figure S5.6**). The polymer solutions exhibit low viscosity, making them easy to pre-mix with cells without inducing significant interfacial stress on the cells (**Figure S5.4**). The gelation times of the hydrazide and ketone functionalized DMAPS polymers were 2 min (10 wt% precursor polymer concentration), 3 min (8 wt% precursor polymer concentration), or 5 min (6 wt% precursor polymer concentration) (see **Table S5.1** and the visualization of the gelation process in **Figure S5.5**); to ensure complete gelation and thus consistent printing results, a minimum wait time of 10 min was used between mixing the precursor polymers and printing the pre-gelled bioink.

Table 5.1: Characterization of functional precursor polymers

Polymer	M_n (kDa)	Đ	Functional monomer (mol%)
DMAPS-Hzd-30mol%	16.9	3.8	26
DMAPS-Ket-30mol%	15.1	3.6	25

5.3.2 Rheological Properties of Zwitterionic Hydrogel Bioink

To assess the printability of the pre-gelled DMAPS-based bioink, the rheological properties were tested. As shown in **Figure 5.2A**, the DMAPS hydrogels exhibit highly shear thinning behaviour across all three concentrations used, with a >3 order of magnitude decrease in viscosity observed between the low shear (0.1 s^{-1}) to the high shear (100 s^{-1}) test conditions. The addition of HepG2 cells (8 million cells/mL in 10 wt% DMAPS hydrogel, as used in the printing experiments) increased the viscosity by a multiple of three at low shear rates but did not significantly alter the shear thinning behavior of the hydrogel; indeed, the viscosity of the bioink with and without cells was identical at shear rates between 1 and 10 s^{-1} (**Figure 5.2B**). Frequency sweeps of the crosslinked DMAPS hydrogels (**Figure 5.2C**) showed that hydrogels prepared with 8 wt% and 10 wt% precursor polymer concentrations exhibited an elastic modulus of ~1000 Pa in the linear viscoelastic range while the 6 wt% precursor polymer hydrogel elastic modulus was significantly lower (~800 Pa) but still sufficiently stiff to be self-supporting. Of critical importance for supporting a pre-gelled bioink approach, the thixotropic behaviour of the crosslinked DMAPS hydrogels (**Figure 5.2D**) showed excellent reversible switching between the low shear (0.1 s^{-1}) and high shear (100 s^{-1}) conditions at all three precursor polymer concentrations tested, showing the rapid structure recovery required for maintaining a 3D printed shape.

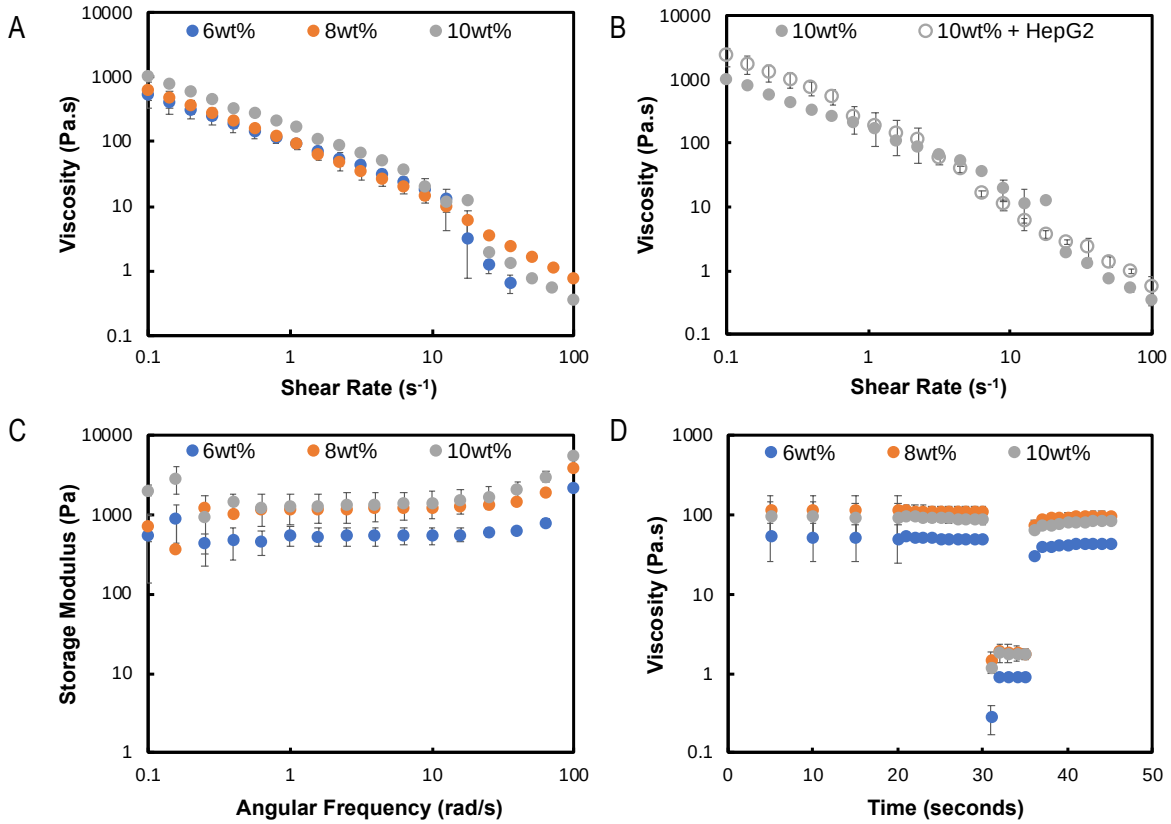

Figure 5.2: Rheological characterization of DMAPS bioinks prepared using 6 wt% (blue points), 8 wt% (orange points), and 10 wt% (grey points) hydrazide and ketone precursor polymer concentrations: (A) viscosity sweeps; (B) viscosity sweep of the 10 wt% precursor polymer concentration gel with (filled points) or without (unfilled points) the addition of HepG2 cells (~8 million cells/mL); (C) frequency sweeps; and (D) thixotropic study switching between low ($0.1 s^{-1}$) and high ($100 s^{-1}$) shear rates showing structure recovery. Error bars represent the standard deviation of three independent replicates.

5.3.3 Printability of Zwitterionic Hydrogel Ink

Printing parameters were optimized for the DMAPS hydrogel inks to evaluate the suitability of the hydrogel ink for printing 3D structures in terms of resolution, pattern fidelity and geometrical aspect ratio. A 10 wt% polymer concentration was used for optimization given the highest modulus (and thus highest mechanical stability of the resulting print) but still high shear reversibility achievable at this concentration (**Figure 5.2**). The optimized printing parameters for free-form printing of DMAPS hydrogels are summarized in **Table 5.2**. The smallest diameter needle that could successfully print the pre-mixed DMAPS hydrogel inks was gauge 22 (corresponding to a nozzle diameter of 0.41 mm); the smaller gauge 26 needle had too high of a back pressure to enable continuous extrusion printing. The extrusion cross-sectional area ($4.78 mm^2$) is directly related to the 1 mL syringe used for printing, which was kept constant throughout all printing experiments herein but could be changed for printing larger constructs.

The extrusion multiplier is a specific material-dependent value within the PrusaSlicer software that allows for more or less material to be extruded during the printing to ensure the filaments are deposited continuously, with a value of 1.5 (a 50% increase in volume from the conventional value of 1) was found to be optimal for the pre-mixed DMAPS hydrogels. The layer height was adjusted because of this increase in overall extrusion rate, resulting in the layer height also increasing by an additional 50% compared to the conventional 'rule of thumb' of 40% of the nozzle diameter. Finally, while it is possible to print at a slower speed of 180 mm/min (3 mm/s), a faster speed of 10 mm/s was not favorable for continuous fiber deposition; as such, the intermediate printing speed of 6 mm/s was chosen to maximize print speed while preserving high print fidelity.

Table 5.2: Optimized printing parameters for free-form printing of DMAPS hydrogels

Printing Parameter	Optimized Value
Needle Gauge	G22
Nozzle Diameter	0.41 mm
Extrusion cross-sectional area	4.78 mm^2
Extrusion multiplier	1.5
Layer Height	60% of nozzle diameter = 0.246 mm
Speed	F360 = 360 mm/min = 6 mm/s

To study the effect of polymer concentration on the printed constructs, a hollow cube structure was printed at a structure height of 10 mm using the optimized printing parameters; **Figure 5.3A** shows the resulting printed structures for bioinks prepared at 6 wt%, 8 wt%, and 10 wt% precursor polymer concentrations. Only the 10 wt% polymer concentration allowed for good structure fidelity without any degree of structure collapse at this height, which can be further demonstrated in the successful prints in **Figure 5.3B** using this 10 wt% precursor polymer concentration showing other types of structures (imaged at different observation angles for clarity).

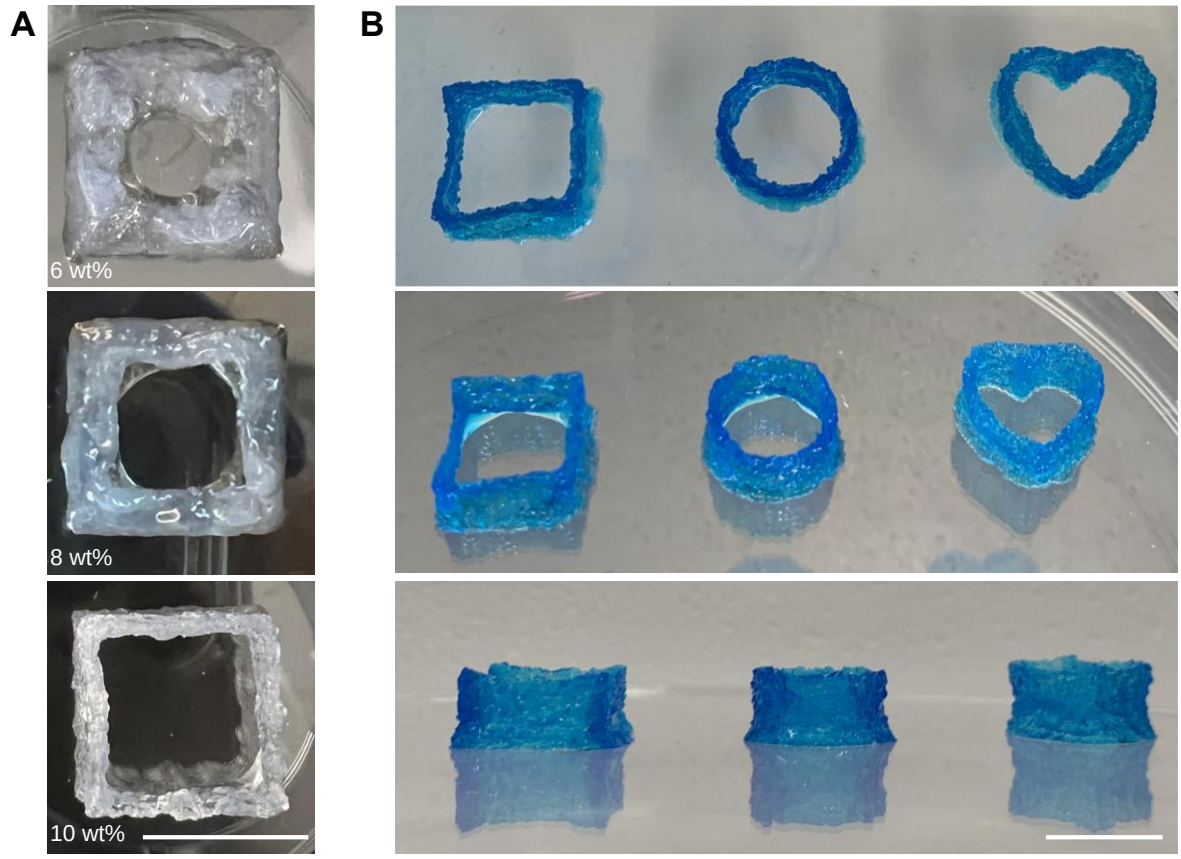

Figure 5.3: Printability study using pre-crosslinked hydrazide/ketone DMAPS hydrogel inks: (A) 3D structure stability for 10 mm tall prints performed using 6 wt% (top), 8 wt% (middle), and 10 wt% (bottom) precursor polymer concentrations. The prints show partial collapse of the structure at the lower polymer concentrations but good shape fidelity at the 10 wt% polymer concentration; (B) varying prints showing the stable and free-standing nature of printed structures prepared with pre-gelled bioinks containing 10 wt% DMAPS precursor polymers. Scale bar = 10 mm.

To evaluate the printability with more complex shapes, small-scale liver models were printed using hydrogel bioinks prepared at all three tested precursor polymer concentrations to determine the suitability of the hydrogel for a liver tissue engineering application (see the Supplementary Video for the STL file). The fill density was kept at 20% with a rectangular infill pattern, providing the mini liver mimics with a pre-determined internal porosity that was patterned into the 3D construct through the layer-by-layer printing. The small-scale livers could be successfully printed at all three polymer concentrations; however, consistent with the printability results in **Figure 5.3**, only the 10 wt% precursor polymer concentration prints could remain fully free-standing after printing (**Figure 5.4A**). This high print fidelity and geometrical aspect ratio of the 10 wt% prints are further evidenced in **Figure 5.4B**, using food colouring to enhance the visualization of the print quality. Furthermore, the 10 wt% precursor polymer

DMAPS hydrogels enabled printing of high-fidelity free-standing hexagonal patterns consistent with the geometry of the liver lobule (**Figure 5.4C**).

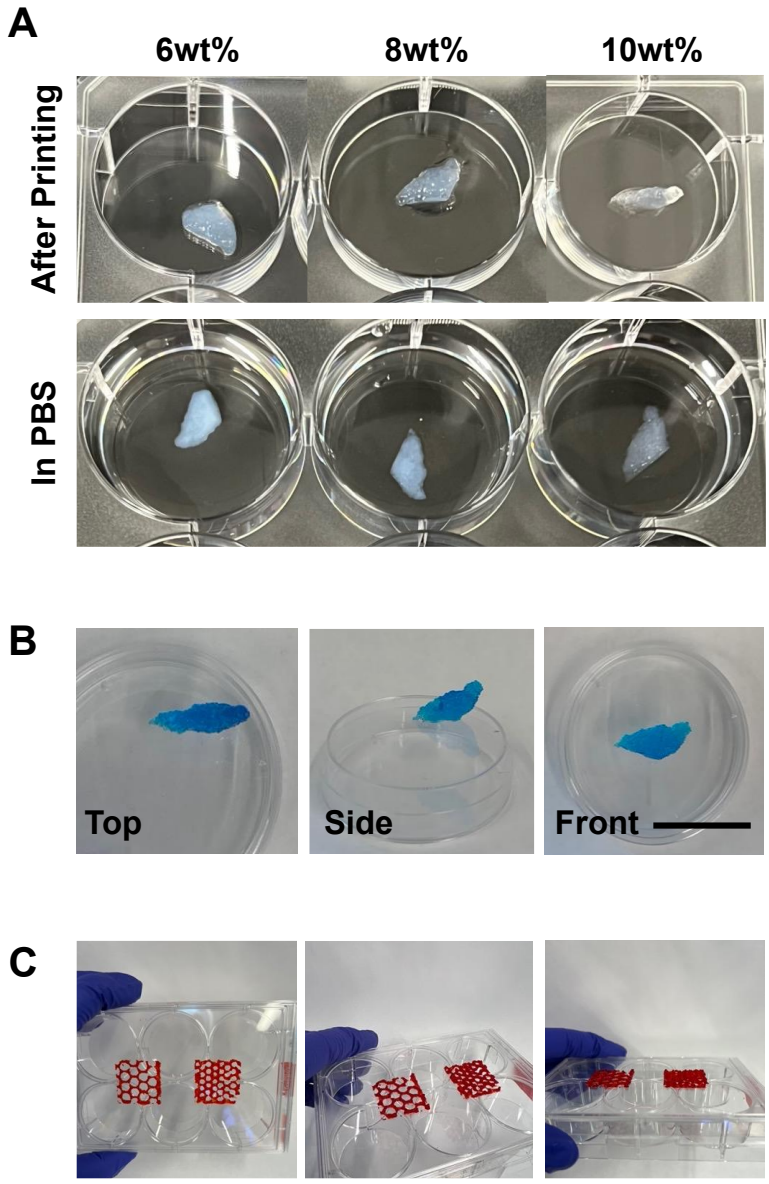

Figure 5.4: Printed small-scale livers and hexagonal structures (mimicking the liver nodules) with pre-crosslinked hydrazide/ketone DMAPS hydrogel inks: (A) prints immediately after printing (top row) and following x hours of incubation in PBS (bottom concentration) for bioinks prepared at 6 wt% (left), 8 wt% (middle), and 10 wt% (right) precursor polymer concentrations; (B) free-standing small-scale livers printed using 10 wt% precursor polymer DMAPS hydrogel inks with added blue food colouring to assist with visualization; (C) printed hexagonal patterns using 10 wt% precursor polymer DMAPS hydrogel inks. Scale bar = 15 mm.

5.3.4 Mechanics, Swelling and Degradation of the Printed Structures

To assess the mechanics of the printed bioinks over time, the compressive moduli of the printed liver models were tested following swelling in PBS after 24 hours and after 14 days; the results are shown in **Figure 5.5**.

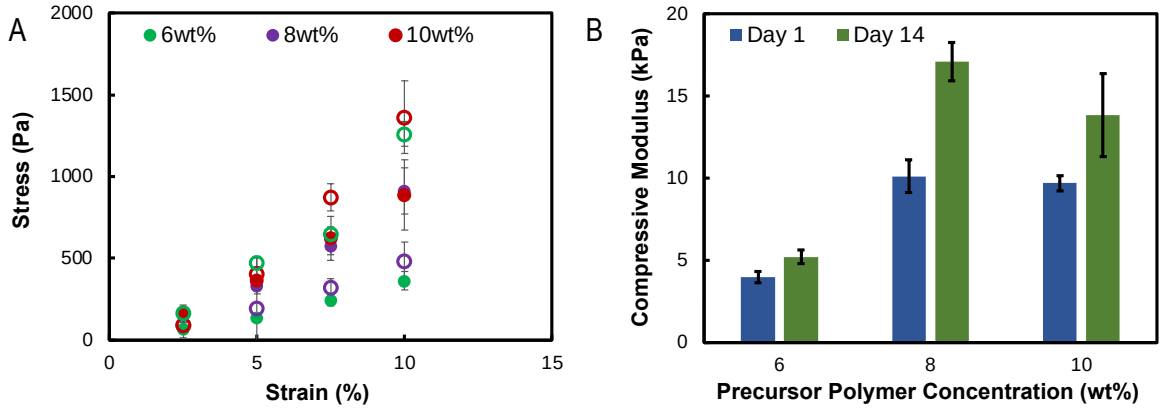

Figure 5.5: Compression testing on printed DMAPS structures under uniaxial unconfined compression: (A) raw stress versus strain data (solid circles represent data after 1 day; hollow circles represent data after 14 days of incubation in PBS); (B) compressive moduli of the printed structures calculated based on a linear regression of the data in (A). Error bars are based on the standard deviation of three independent replicates.

The compressive moduli ranged between 4 ± 1 kPa (for hydrogels prepared with 6 wt% precursor polymer concentration) to 10 ± 1 kPa (for hydrogels prepared with 8 wt% or 10 wt% polymer concentrations) after 24 hours. After two weeks of incubation in phosphate buffered saline at room temperature, the compressive moduli slightly but significantly increased to 5 ± 0.4 kPa (6 wt% precursor polymer concentration), 17 ± 1 kPa (8 wt% precursor polymer concentration), and 14 ± 3 kPa (10 wt% precursor polymer concentration) respectively, all of which represent significant increases in modulus relative to those measured in the short-term (24 hour) swelling experiment (p<0.05 for each pairwise comparisons). We hypothesize this time-dependent stiffening of the matrix can be attributed to: (1) the slow kinetics of the hydrazide-ketone crosslinking reaction (which is hindered by the alkyl group on the ketone) relative to the much faster hydrazide-aldehyde crosslinking reaction that we have studied in our previous work[46]; and (2) zwitterion fusion interactions between adjacent zwitterion groups that can reconform over time as the gel relaxes to a more equilibrium structure[47]. Based on the work of Ma et al., stiffnesses between 0.5 kPa and 5 kPa tend to lead to desirable HepG2 cell aggregation and ultimate spheroid formation[48], a modulus value achievable with the lower

concentration 6 wt% precursor polymer pre-crosslinked DMAPS hydrogel ink. While the higher concentrations are on the higher end of this optimal range reported for HepG2 cells, these stiffer scaffolds are still suitable for reproducing biological function, as the encapsulated cells are likely to soften the mechanics.

The high stability of the printed structures assessed in the compressive modulus data was also reflected in the swelling profiles of the printed small-scale liver models in cell media (DMEM, 10% FBS, 1% penicillin/streptomycin) (**Figure 5.6**). At each tested precursor polymer concentration, only limited swelling (<20% mass gain) and no evidence of degradation was observed over the full 21-day incubation period, with no significant differences observed between the three tested polymer concentrations. The dual crosslinking of these hydrogels by both dynamic covalent (hydrazone) and physical (zwitterionic fusion) mechanisms accounts for the very slow degradation times observed, allowing the printed structures can maintain high mechanical and dimensional stability over extended incubation times (as is desired for cell therapeutics such as implantable liver models).

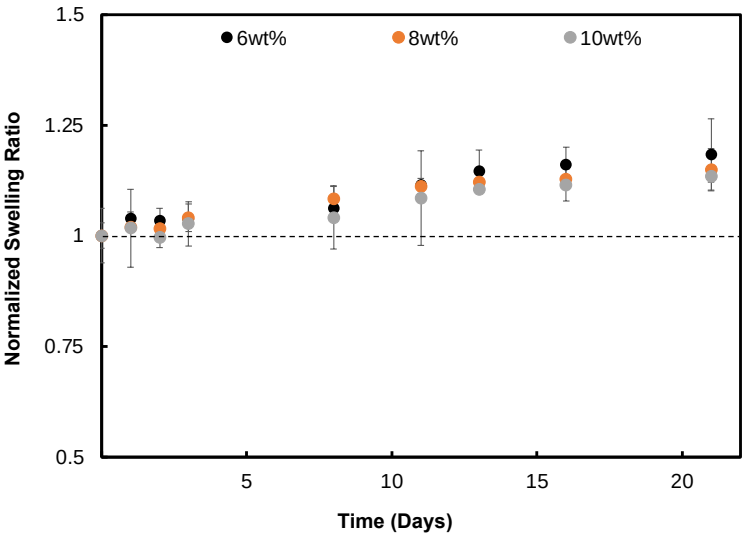

Figure 5.6: Swelling kinetics study measuring the normalized weight (relative to day 0) of the printed hydrogel structures in cell media (DMEM, 10% FBS, 1% penicillin/streptomycin) prepared at 6 wt%, 8 wt%, and 10 wt% hydrazide and ketone precursor polymer concentrations as a function of time. Error bars are based on the standard deviation of three independent replicates.

5.3.5 Cell Viability in Bioprinted Small-Scale Livers

A mono-cellular liver structure with HepG2 cells (8 million cells/mL) was first printed, using the 10 wt% precursor polymer pre-gelled DMAPS hydrogel as the bioink given its significantly higher shape fidelity/3D stability relative to the other concentrations tested (**Figure 5.3**). Cell viability over a 14-day culture period was evaluated using a live-dead assay, with the results shown in **Figure 5.7**. The cells remained highly viable (>90%) both immediately after printing (Day 1, suggesting that the higher viscosity of the pre-formed hydrogel bioink does not result in excessive shear on the cells during the printing process) as well as after a full 14-day incubation period (see **Figure S5.7** for the cell viability quantification). Note that the slight decrease observed in cell viability (~85%) and cell number after 14 days is likely attributed to the slight swelling observed in the scaffold over that period (**Figure 5.6**) that may result in limited cell leakage from the scaffold.

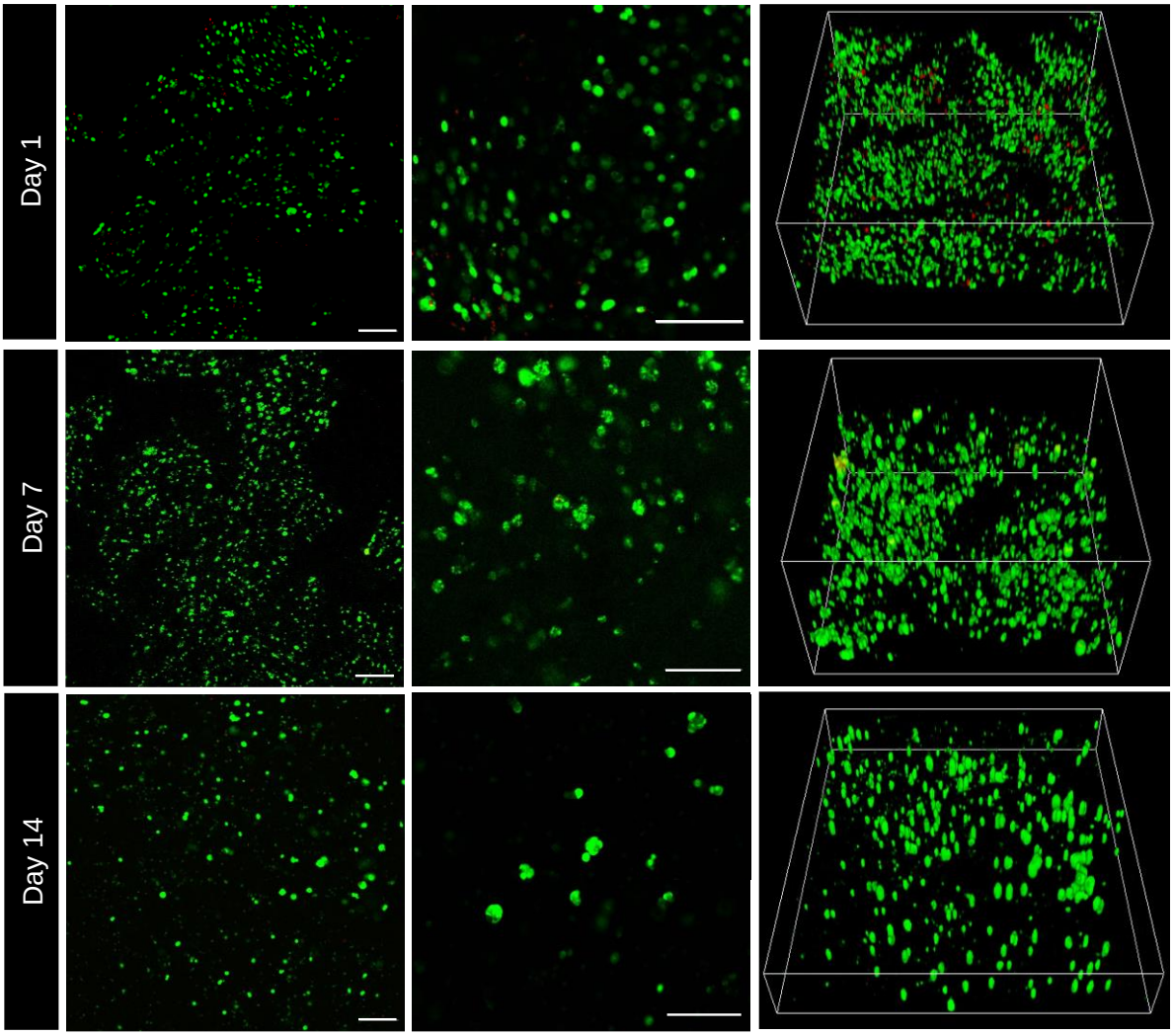

Figure 5.7: Live/dead assay results for HepG2 cells printed in mini liver structures using a pre-crosslinked 10 wt% hydrazide/ketone precursor polymer bioink 1 day (top), 7 days (middle), and 14 days (bottom) after printing. Scale bar = 200 μm.

Next, NIH/3T3 cells were co-printed with HepG2 cells in the bioprinted small-scale livers to study the effect of non-parenchymal cells such as fibroblasts on the survival and function of hepatocytes. Both cells were added at a concentration 8 million cells/mL into separate bioinks, with the NIH/3T3 cells added to the aldehyde-functionalized precursor polymer and the HepG2 cells added to the hydrazide-functionalized precursor polymer. **Figure 5.8** shows the resulting live/dead images (top) and the depth profile of live cells (bottom) within the printed liver mimics. The depth profiles were generated to clearly illustrate the internal porosity (as designed by the fill density inputted in the G-code used for the layer-by-layer printing); cells shown in pink are located deeper into the structure while blue cells are located toward the surface of the prints.

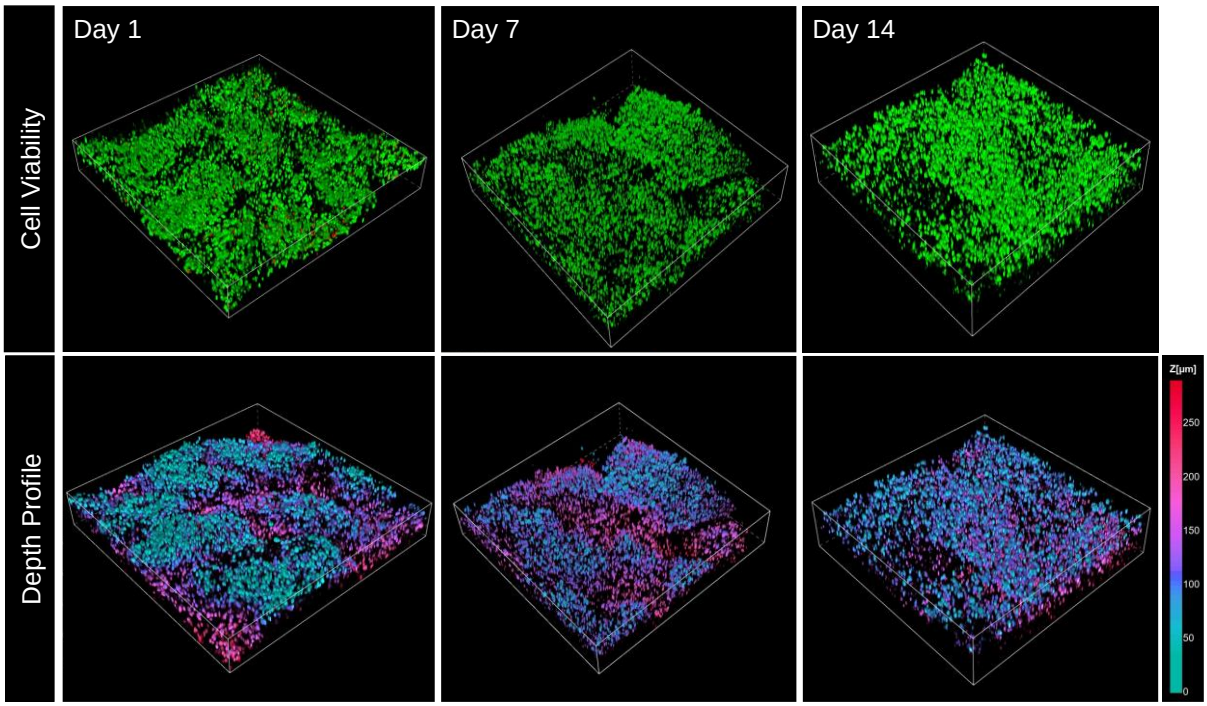

Figure 5.8: Viability and depth profiles of HepG2 and NIH/3T3 cells printed in mini liver structures using a pre-crosslinked 10 wt% hydrazide/ketone precursor polymer bioink 1 day (top), 7 days (middle), and 14 days (bottom) after printing. Green/blue in the depth map shows the top of the imaged section, while purple/pink ranges between 150 to 300 μm in depth.

The co-culture of HepG2 and NIH/3T3 in the printed liver structures showed extremely high cell viability during the two-week culture period (>90%, **Figure S5.7**), with only very minimal dead cells found after 24 hours of printing. Moreover, the slight decrease in cell number observed after 14 days for the HepG2-only prints could be avoided by co-printing with fibroblast cells. Cells were also observed to conform to the internal structure of the livers printed, as can be seen by the depth maps generated from the viability images in **Figure 5.8**. The cells elongated along the internal 'holes' that generated with the pre-defined infill density and structure after day 1 and 7. After 14 days, the depth profile showed a more homogenous distribution, likely due to the slight swelling of the DMAPS hydrogel scaffolds that allows cells to proliferate into the void spaces. These depth profiles combined with the viability results can be further visualized in Supplementary Videos S1-S3.

5.3.6 Albumin Secretion

To assess the albumin secretion function of HepG2 cells printed in both single-cell and co-culture liver prints, the cumulative albumin production (normalized per 10^6 HepG2 cells in each printed structure) was assessed using two printing strategies. First, to mimic the spatial

organization of the liver and take advantage of the tunable mechanics of the zwitterionic bioinks, the NIH/3T3 cells were printed in a hexagonal pattern using a 10 wt% precursor polymer pre-crosslinked DMAPS hydrogel bioink (layer height 2.5 mm) while HepG2 cells were droplet printed using a single layer using a 6 wt% precursor polymer pre-crosslinked DMAPS hydrogel bioink in the void spaces of the hexagonal pattern (**Figure 5.9**). The droplet printing is facilitated by the slower gelation achievable with hydrazide-ketone crosslinking, with the 6 wt% concentration chosen due to its longer gelation time (for ease of printing in well-defined dots) and its lower compressive modulus (**Figure 5.5**) that is more suitable for HepG2 cells.

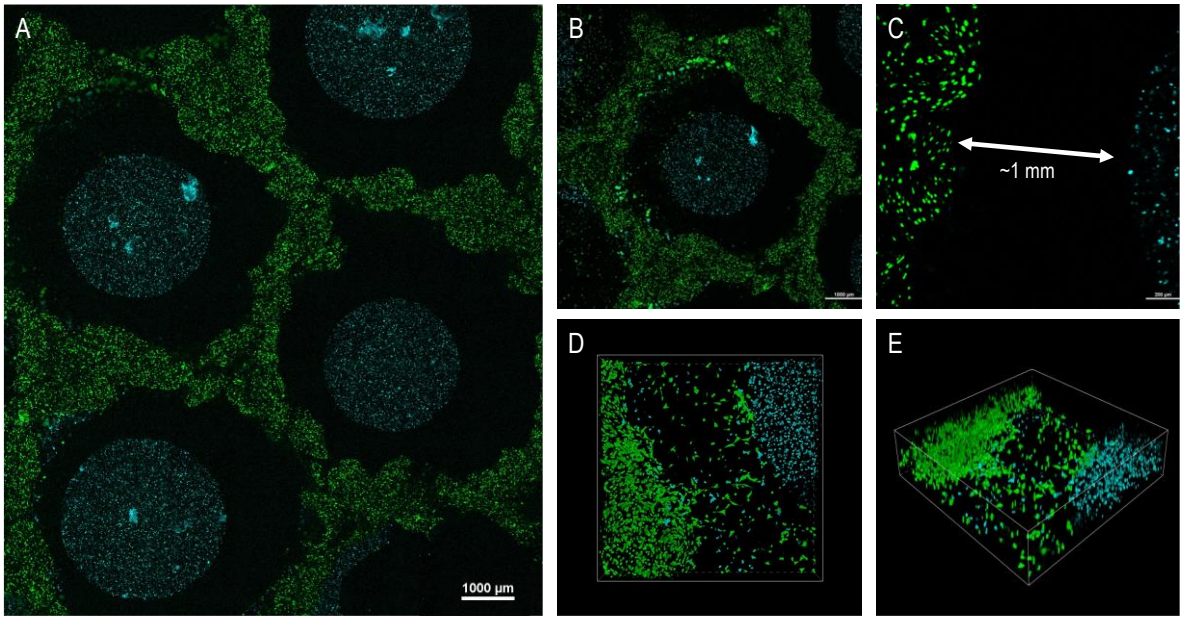

Figure 5.9: Localization of pre-stained HepG2 cells (blue coloration; Far-Red stain) printed in 6 wt% precursor polymer DMAPS bioink and localized in droplets and NIH/3T3 cells (green coloration; CFDA stain) printed in pre-crosslinked 10 wt% precursor polymer DMAPS bioink and localized in hexagonal liver lobule mimics after day 1: (A) large scan image; (B) close-up on one hexagon structure; (C) close-up on interface between the printed hexagons and droplets, indicating that the distance between the printed hexagon and the droplet is ~1 mm; (D and E) front and side views of a z-stack showing the migration of NIH/3T3 cells to the HepG2 droplets.

Immediately after the day 1 measurements, higher amounts of albumin were secreted from the printed co-culture system, with the co-printing of NIH/3T3 cells resulting in a 150% increase in albumin secretion over the 21 days compared to printing with HepG2 cells alone (**Figure 5.10**). This result is consistent with reports of other spatially separated printing strategies in which the functionality of liver cells due to the release of soluble factors from parenchymal

cells that directly affect the release of albumin[35,49-50], although the exact mechanism is still not fully understood. However, the optimal distance between the cell types to drive this enhanced albumin release has previously been reported to be 100-300 μm[49,51], significantly closer than the 1 mm distance achieved in the localized pattern shown in **Figure 5.9** despite the significant cell spreading that is observed in the printed construct. In contrast, when the two cells were co-printed in intimate contact using 3D printing in a single matrix (i.e., in the mini-liver mimic structures shown in **Figure 5.4**), ~2-fold higher albumin secretion was observed (**Figure 5.10**). This result, facilitated by the capacity to load different cells in different low viscosity precursor polymers to form a bio-orthogonal gel around those cells that preserves high cell viability, is ideally facilitated by the dynamic covalent zwitterionic bioink.

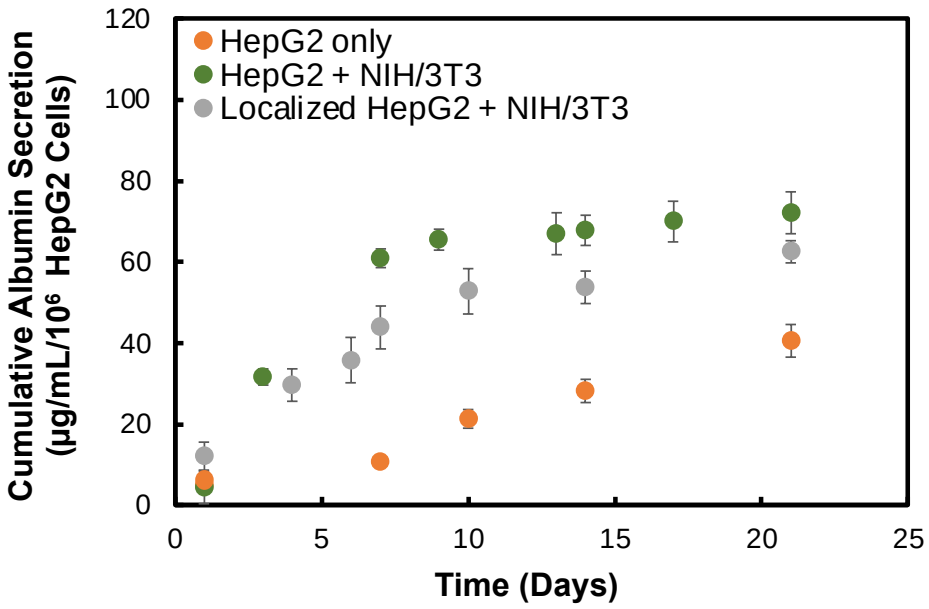

Figure 5.10: Cumulative albumin production (normalized to one million HepG2 cells) of HepG2-only and HepG2-NIH/3T3 co-cultures (both homogeneously mixed – green points and printed in sequestered hexagonal/droplet pattern – grey points) printed in DMAPS hydrogel bioinks over a 21-day period. Error bars represent the standard deviation of three independent replicates.

5.4 Discussion

DMAPS hydrogels were successfully free-form printed using pre-mixed ketone and hydrazide functionalized precursor polymers that could be directly mixed with cells and printed through a nozzle, exploiting the highly shear-thinning and self-healing properties of dynamic covalent chemistry. Combining this pre-mixing technique with a conventional and inexpensive extrusion printer enables the effective 3D printing that does not require UV, heating, or any

other type of crosslinking stimulus, providing an easy, cell-friendly strategy to print stable, covalently crosslinked constructs in a single step. Small-scale liver mimics were successfully printed with good print fidelity using a precursor polymer concentration of 10 wt% (**Figure 5.3** and **Figure 5.4**). The DMAPS hydrogels have suitable mechanics for HepG2 and fibroblast encapsulation, ranging from 4 kPa (using 6 wt% precursor polymers) to 18 kPa (using 10 wt% precursor polymers), and remain stable with minimal swelling and no onset of degradation over 21 days (**Figure 5.5** and **Figure 5.6**). While the higher polymer concentrations yield moduli values on the higher end of this 0.5-5 kPa optimal modulus range reported for HepG2 cells[47], these stiffer scaffolds are still shown to be suitable for reproducing biological function based on the role of the encapsulated cells in reducing the modulus[51-52]. This result is consistent with previous literature; for example, Wu et al. reported a decrease of ~50% in compressive modulus for their gelatin methacryloyl (GelMA) bioinks when mixed with both HepG2 and NIH/3T3 cells[38]. The synthetic zwitterionic hydrogel bioink maintained high cell viability and adhesion over time with multiple cell types (HepG2 cells, NIH/3T3 fibroblast cells) despite having no specific biological affinity to cells (i.e., binding domains in natural polymer-based scaffolds), with cells remaining highly viable (>90%) both immediately after printing as well as after a full 14-day incubation period (**Figure 5.7** and **Figure 5.8**). The slow-gelling ketone-hydrazide crosslinking chemistry allows for simple mixing of the bioink with cells while imparting minimal shear stress, thus likely contributing to the high cell viability in the printed structures. Interestingly, while the number of encapsulated cells slightly decreased after 14 days for the HepG2-only prints, the homogeneous co-culture print with both HepG2 and fibroblast cells maintained high cell density at all tested timepoints, potentially due to the role of the fibroblasts in producing more native ECM within the hydrogel to reduce porosity and increase cell adhesion. Consistent with literature results that co-culturing hepatocytes with parenchymal cells increases the overall functionality of the hepatocytes[35, 39, 50], co-culturing the HepG2 cells with fibroblast cells increased the cumulative albumin production by 3 to 4 times compared to the monoculture, with the intimate mixing of the two cell types in the 3D co-print (**Figure 5.10**) resulting in higher albumin secretion than was observed within a hexagonal/droplet pattern with sequestered cells in which the ~1 mm distance between the cells resulted in slower transport of secreted factors between the two cell types (**Figure 5.9**). The ability to sequester the cells individually in the hydrazide and ketone-functionalized precursor polymer of the bioinks (both of which are chemically orthogonal with other biomolecules) but then create prints with near-homogeneous cell distributions upon pre-gelation thus offers potential benefits for practical bioink translation.

5.5 Conclusion

A synthetic zwitterionic hydrogel bioink suitable for free-from extrusion bioprinting with high print fidelity was developed. Due to the highly shear-thinning properties of the hydrogel ink, various structures with high shape fidelity and shape stability could be successfully printed without requiring any post-crosslinking step (or indeed any crosslinking step whatsoever aside from the *in situ*-gelation of the ketone and hydrazide-functionalized precursor polymers). The slower gelling ketone-hydrazide crosslinking method allows for simple mixing with cells while imparting minimal shear stress, resulting in extremely high cell viability in the printed structures. The compressive moduli of the printed small-scale liver models range between 4 and 18 kPa, comparable to the native liver tissue. Hepatocytes (HepG2) were successfully printed, showing excellent viability (>85%) over 14 days; furthermore, when co-printed with fibroblast cells, improved cell retention (>90%) and significantly enhanced albumin secretion (3-4x higher than monoculture) were observed. Coupling these results with the minimal swelling or mechanical changes observed in the hydrogel over at least three weeks of incubation as well as the inherently anti-fibrotic nature of DMAPS-based materials, these printed scaffolds offer significant potential as liver mimics for *in vitro* testing as well as implantable liver constructs for use as cell therapeutics.

5.6 Acknowledgements

The CALM Institute for Advanced Microscopy is acknowledged for its assistance in the confocal microscopy. The Natural Sciences and Engineering Research Council (Discovery Grant RGPIN-2017-06455 to TH, NP, FX) and a Canada Graduate Scholarship (to EM) are acknowledged for funding. Dr. Boyang Zhang is thanked for helpful discussions about the cell co-culture work.

5.7 References

1. Kang, H.-W.; Lee, S. J.; Ko, I. K.; Kengla, C.; Yoo, J. J.; Atala, A., A 3D bioprinting system to produce human-scale tissue constructs with structural integrity. *Nat. Biotechnol.* **2016,** *34* (3), 312-319.
2. Zheng, Z.; Eglin, D.; Alini, M.; Richards, G. R.; Qin, L.; Lai, Y., Visible light-induced 3D bioprinting technologies and corresponding bioink materials for tissue engineering: a review. *Engineering* **2021,** *7* (7), 966-978.
3. Li, X.; Liu, B.; Pei, B.; Chen, J.; Zhou, D.; Peng, J.; Zhang, X.; Jia, W.; Xu, T., Inkjet bioprinting of biomaterials. *Chem. Rev.* **2020,** *120* (19), 10793-10833.
4. Boularaoui, S.; Al Hussein, G.; Khan, K. A.; Christoforou, N.; Stefanini, C., An overview of extrusion-based bioprinting with a focus on induced shear stress and its effect on cell viability. *Bioprinting* **2020,** *20*, e00093.
5. Retting, K.; Carter, D.; Crogan-Grundy, C.; Khatiwala, C.; Norona, L.; Paffenroth, E.; Hanumegowda, U.; Chen, A.; Hazelwood, L.; Lehman-McKeeman, L., Modeling liver biology and the tissue response to injury in bioprinted human liver tissues. *Appl. In Vitro Toxicol.* **2018,** *4* (3), 288-303.
6. Schwab, A.; Levato, R.; D'Este, M.; Piluso, S.; Eglin, D.; Malda, J., Printability and shape fidelity of bioinks in 3D bioprinting. *Chem. Rev.* **2020,** *120* (19), 11028-11055.
7. Skardal, A.; Devarasetty, M.; Kang, H.-W.; Mead, I.; Bishop, C.; Shupe, T.; Lee, S. J.; Jackson, J.; Yoo, J.; Soker, S., A hydrogel bioink toolkit for mimicking native tissue biochemical and mechanical properties in bioprinted tissue constructs. *Acta Biomater.* **2015,** *25*, 24-34.
8. Anderson, J. M.; Rodriguez, A.; Chang, D. T. In *Foreign body reaction to biomaterials*, Seminars in immunology, *Elsevier* **2008,** 86-100.
9. Xu, F.; Dawson, C.; Lamb, M.; Mueller, E.; Stefanek, E.; Akbari, M.; Hoare, T., Hydrogels for Tissue Engineering: Addressing Key Design Needs Toward Clinical Translation. *Front. Bioeng. Biotechnol.* **2022,** *10*, 849831.
10. Langer, R., Perspectives and challenges in tissue engineering and regenerative medicine. *Adv. Mater.* **2009,** *21* (32-33), 3235-3236.
11. Pati, F.; Jang, J.; Ha, D.-H.; Won Kim, S.; Rhie, J.-W.; Shim, J.-H.; Kim, D.-H.; Cho, D.-W., Printing three-dimensional tissue analogues with decellularized extracellular matrix bioink. *Nat. Comm.* **2014,** *5*, 3935.
12. Roche, C. D.; Brereton, R. J.; Ashton, A. W.; Jackson, C.; Gentile, C., Current challenges in three-dimensional bioprinting heart tissues for cardiac surgery. *European J. Cardio Thoracic Surg.* **2020,** *58* (3), 500-510.
13. Drzewiecki, K. E.; Malavade, J. N.; Ahmed, I.; Lowe, C. J.; Shreiber, D. I., A thermoreversible, photocrosslinkable collagen bio-ink for free-form fabrication of scaffolds for regenerative medicine. *Technology* **2017,** *5* (04), 185-195.
14. Sanchez-Cano, C.; Carril, M., Recent developments in the design of non-biofouling coatings for nanoparticles and surfaces. *Int. J. Mol. Sci.* **2020,** *21* (3), 1007.
15. Lowe, S.; O'Brien-Simpson, N. M.; Connal, L. A., Antibiofouling polymer interfaces: poly (ethylene glycol) and other promising candidates. *Polym. Chem.* **2015,** *6* (2), 198-212.
16. Wu, J.; Lin, W.; Wang, Z.; Chen, S.; Chang, Y., Investigation of the hydration of nonfouling material poly (sulfobetaine methacrylate) by low-field nuclear magnetic resonance. *Langmuir* **2012,** *28* (19), 7436-7441.
17. Wu, J.; Chen, S., Investigation of the hydration of nonfouling material poly (ethylene glycol) by low-field nuclear magnetic resonance. *Langmuir* **2012,** *28* (4), 2137-2144.

18. Grainger, D. W., All charged up about implanted biomaterials. *Nat. Biotechnol.* **2013,** *31* (6), 507-509.
19. Chan, H.-M.; Erathodiyil, N.; Wu, H.; Lu, H.; Zheng, Y.; Ying, J. Y., Calcium cross-linked zwitterionic hydrogels as antifouling materials. *Mater. Today Comm.* **2020,** *23*, 100950.
20. Zhang, L.; Cao, Z.; Bai, T.; Carr, L.; Ella-Menye, J.-R.; Irvin, C.; Ratner, B. D.; Jiang, S., Zwitterionic hydrogels implanted in mice resist the foreign-body reaction. *Nat. Biotechnol.* **2013,** *31* (6), 553-556.
21. Pan, Z.; Dorogin, J.; Preciado Rivera, N.; Hoare, T. In Situ Gelling Zwitterionic Hydrogel Compositions, and Methods of Use Thereof. *PCT Priority Patent Application PCT/CA2021/050731*, filed May 28, 2021.
22. Bai, T.; Li, J.; Sinclair, A.; Imren, S.; Merriam, F.; Sun, F.; O'Kelly, M. B.; Nourigat, C.; Jain, P.; Delrow, J. J., Expansion of primitive human hematopoietic stem cells by culture in a zwitterionic hydrogel. *Nat. Med.* **2019,** *25* (10), 1566-1575.
23. Liu, Q.; Chiu, A.; Wang, L.; An, D.; Li, W.; Chen, E. Y.; Zhang, Y.; Pardo, Y.; McDonough, S. P.; Liu, L., Developing mechanically robust, triazole-zwitterionic hydrogels to mitigate foreign body response (FBR) for islet encapsulation. *Biomaterials* **2020,** *230*, 119640.
24. Zhang, J.; Xin, W.; Qin, Y.; Hong, Y.; Xiahou, Z.; Zhang, K.; Fu, P.; Yin, J., "All-in-one" zwitterionic granular hydrogel bioink for stem cell spheroids production and 3D bioprinting. *Chem. Eng. J.* **2022,** *430*, 132713.
25. Asadikorayem, M.; Surman, F.; Weber, P.; Zenobi-Wong, M. In *Enzymatically crosslinked zwitterionic microgels for bioprinting of macroporous scaffolds*, Tiss. Eng. Part A, **2022**; S521-S522.
26. Kostina, N. Y.; Blanquer, S.; Pop-Georgievski, O.; Rahimi, K.; Dittrich, B.; Höcherl, A.; Michálek, J.; Grijpma, D. W.; Rodriguez-Emmenegger, C., Zwitterionic functionalizable scaffolds with gyroid pore Architecture for tissue engineering. *Macromol. Biosci.* **2019,** *19* (4), 1800403.
27. Pan, W.; Wallin, T. J.; Odent, J.; Yip, M. C.; Mosadegh, B.; Shepherd, R. F.; Giannelis, E. P., Optical stereolithography of antifouling zwitterionic hydrogels. *J. Chem. B* **2019,** *7* (17), 2855-2864.
28. Kessel, B.; Lee, M.; Bonato, A.; Tinguely, Y.; Tosoratti, E.; Zenobi-Wong, M., 3D bioprinting of macroporous materials based on entangled hydrogel microstrands. *Adv. Sci.* **2020,** *7* (18), 2001419.
29. Hafeez, S.; Ooi, H. W.; Morgan, F. L.; Mota, C.; Dettin, M.; Van Blitterswijk, C.; Moroni, L.; Baker, M. B., Viscoelastic oxidized alginates with reversible imine type crosslinks: self-healing, injectable, and bioprintable hydrogels. *Gels* **2018,** *4* (4), 85.
30. Morgan, F. L.; Fernández-Pérez, J.; Moroni, L.; Baker, M. B., Tuning hydrogels by mixing dynamic cross-linkers: enabling cell-instructive hydrogels and advanced bioinks. *Adv. Healthc. Mater.* **2021**, 2101576.
31. Wang, L. L.; Highley, C. B.; Yeh, Y. C.; Galarraga, J. H.; Uman, S.; Burdick, J. A., Three-dimensional extrusion bioprinting of single- and double-network hydrogels containing dynamic covalent crosslinks. *J. Biomed. Mater. Res. A* **2018,** *106* (4), 865-875.
32. Puertas-Bartolomé, M.; Włodarczyk-Biegun, M. K.; Del Campo, A.; Vázquez-Lasa, B.; San Román, J., 3D printing of a reactive hydrogel bio-ink using a static mixing tool. *Polymers* **2020,** *12* (9), 1986.
33. Amaral, A. J.; Gaspar, V. M.; Lavrador, P.; Mano, J. F., Double network laminarin-boronic/alginate dynamic bioink for 3D bioprinting cell-laden constructs. *Biofabrication* **2021,** *13* (3), 035045.

34. Ito, A.; Jitsunobu, H.; Kawabe, Y.; Kamihira, M., Construction of heterotypic cell sheets by magnetic force-based 3-D coculture of HepG2 and NIH3T3 cells. *Journal of Biosci. Bioeng.* **2007,** *104* (5), 371-378.
35. Lee, H. W.; Kook, Y.-M.; Lee, H. J.; Park, H.; Koh, W.-G., A three-dimensional co-culture of HepG2 spheroids and fibroblasts using double-layered fibrous scaffolds incorporated with hydrogel micropatterns. *RSC Adv.* **2014,** *4* (105), 61005-61011.
36. He, Q.; Okajima, T.; Onoe, H.; Subagyo, A.; Sueoka, K.; Kuribayashi-Shigetomi, K., Origami-based self-folding of co-cultured NIH/3T3 and HepG2 cells into 3D microstructures. *Sci. Rep.* **2018,** *8*, 4556.
37. Mittal, N.; Li, H.; Ananthanarayanan, A.; Yu, H., Complex interplay between serum and fibroblasts in 3D hepatocyte co-culture. *BioRxiv* **2018**, 286088.
38. Wu, Y.; Wenger, A.; Golzar, H.; Tang, X. S., 3D bioprinting of bicellular liver lobule-mimetic structures via microextrusion of cellulose nanocrystal-incorporated shear-thinning bioink. *Sci. Rep.* **2020,** *10*, 20648.
39. Taymour, R.; Kilian, D.; Ahlfeld, T.; Gelinsky, M.; Lode, A., 3D bioprinting of hepatocytes: Core–shell structured co-cultures with fibroblasts for enhanced functionality. *Scientific Reports* **2021,** *11*, 5130
40. Kook, Y.-M.; Jeong, Y.; Lee, K.; Koh, W.-G., Design of biomimetic cellular scaffolds for co-culture system and their application. *J. Tiss. Eng.* **2017,** *8*, 2041731417724640.
41. Banaeiyan, A. A.; Theobald, J.; Paukštyte, J.; Wölfl, S.; Adiels, C. B.; Goksör, M., Design and fabrication of a scalable liver-lobule-on-a-chip microphysiological platform. *Biofabrication* **2017,** *9* (1), 015014.
42. Khetani, S. R.; Bhatia, S. N., Microscale culture of human liver cells for drug development. *Nat. Biotechnol.* **2008,** *26* (1), 120-126.
43. Ma, X.; Qu, X.; Zhu, W.; Li, Y.-S.; Yuan, S.; Zhang, H.; Liu, J.; Wang, P.; Lai, C. S. E.; Zanella, F., Deterministically patterned biomimetic human iPSC-derived hepatic model via rapid 3D bioprinting. *Proc. Nat. Acad. Sci.* **2016,** *113* (8), 2206-2211.
44. Nguyen, D. G.; Funk, J.; Robbins, J. B.; Crogan-Grundy, C.; Presnell, S. C.; Singer, T.; Roth, A. B., Bioprinted 3D primary liver tissues allow assessment of organ-level response to clinical drug induced toxicity in vitro. *PloS One* **2016,** *11* (7), e0158674.
45. Mueller, E.; Xu, F.; Hoare, T., FRESH Bioprinting of Dynamic Hydrazone-Cross-Linked Synthetic Hydrogels. *Biomacromol.* **2022**, 23 (11), 4883-4895.
46. Patenaude, M.; Campbell, S.; Kinio, D.; Hoare, T., Tuning Gelation Time and Morphology of Injectable Hydrogels Using Ketone–Hydrazide Cross-Linking. *Biomacromol.* **2014,** *15* (3), 781-790.
47. Doncom, K. E.; Willcock, H.; O'Reilly, R. K., The direct synthesis of sulfobetaine-containing amphiphilic block copolymers and their self-assembly behavior. *Euro. Polym. J.* **2017,** *87*, 497-507.
48. Ma, X.; Yu, C.; Wang, P.; Xu, W.; Wan, X.; Lai, C. S. E.; Liu, J.; Koroleva-Maharajh, A.; Chen, S., Rapid 3D bioprinting of decellularized extracellular matrix with regionally varied mechanical properties and biomimetic microarchitecture. *Biomaterials* **2018,** *185*, 310-321.
49. Hui, E. E.; Bhatia, S. N., Micromechanical control of cell–cell interactions. *Proc. Nat. Acad. Sci.* **2007,** *104* (14), 5722-5726.
50. Stevens, K.; Ungrin, M.; Schwartz, R.; Ng, S.; Carvalho, B.; Christine, K.; Chaturvedi, R.; Li, C.; Zandstra, P.; Chen, C., InVERT molding for scalable control of tissue microarchitecture. *Nat. Comm.* **2013,** *4*, 1847.

51. Cui, J.; Wang, H.; Zheng, Z.; Shi, Q.; Sun, T.; Huang, Q.; Fukuda, T., Fabrication of perfusable 3D hepatic lobule-like constructs through assembly of multiple cell type laden hydrogel microstructures. *Biofabrication* **2018,** *11* (1), 015016.
52. Solon, J.; Levental, I.; Sengupta, K.; Georges, P. C.; Janmey, P. A., Fibroblast adaptation and stiffness matching to soft elastic substrates. *Biophys. J.* **2007,** *93* (12), 4453-4461.
53. Duan, B.; Yin, Z.; Kang, L. H.; Magin, R. L.; Butcher, J. T., Active tissue stiffness modulation controls valve interstitial cell phenotype and osteogenic potential in 3D culture. *Acta Biomater.* **2016,** *36*, 42-54.

5.8 Supplementary Information

5.8.1 Synthesis of Ketone Monomer

For the synthesis of the ketone monomer, the following chemicals were used as received: chloroacetone (Sigma-Aldrich, 95%), potassium salt of phthalimide (Sigma-Aldrich, 98%), acetone (Sigma-Aldrich, 99.5%), dichloromethane (Sigma-Aldrich, ACS reagent 99.5%), sodium chloride (BioShop, Reagent grade), magnesium sulfate (Sigma-Aldrich, reagent plus 99.5%), diethyl ether (Sigma-Aldrich, ACS reagent 99%), toluene (Sigma-Aldrich, ACS reagent 99.5%), ethylene glycol (Sigma-Aldrich, Reagent Plus 99%), p-toluenesulfonic acid (Sigma-Aldrich, ACS reagent 98%), sodium bicarbonate (EMD, GR ACS), ethanol (Commercial Alcohols, anhydrous), sodium hydroxide (Sigma-Aldrich, ACS reagent 97%), TEMPO methacrylate (Sigma-Aldrich, 98%), methacryloyl chloride (Sigma-Aldrich, 97%), petroleum ether (Caledon, ACS grade), and ter-butyl methyl ether (Sigma-Aldrich, Chromosol HPLC 99.8%).

Step 1: Chloroacetone (45 g) and potassium phthalimide (100 g) were mixed with acetone (600 mL) and placed in an oil bath (80°C) for 24 hours under a reflux condenser. Afterwards, acetone was removed using a rotary evaporator, redissolved in dichloromethane, and cleaned with saturated sodium chloride solution. The organic layer was dried with magnesium sulfate and placed in the rotary evaporator to remove the dichloromethane. The product was washed with diethyl ether until a white powder was obtained, after which the phthalate ketone product was dried under vacuum.

Step 2: The phthalate ketone (43.89 g) was mixed with toluene (660 mL), ethylene glycol (24.43 g) and dry p-toluenesulfonic acid (4.6 g) and heated to 130°C for 24 hours in a round bottom flask using a Dean-Stark apparatus filled with toluene and a condenser attached to the Dean-Stark apparatus. Following, the solution was allowed to cool, mixed with diethyl ether, and cleaned with saturated sodium bicarbonate. The organic layer (diethyl ether/toluene) was dried and removed using a rotary evaporator. The product was then recrystallized using ethanol under an ice bath, filtered, and allowed to dry under a vacuum to obtain the acetal-protected product.

Step 3: The acetal-protected material (40 g) was mixed with concentrated NaOH solution (400 mL) and allowed to mix at 80°C for 2 days using a reflux condenser. The product was then allowed to cool and extracted with dichloromethane (~200 mL), after which the organic layer was dried using magnesium sulfate and then removed using a rotary evaporator. The resulting product was dried overnight using an in-house vacuum to obtain the primary amine product, a clear liquid with a faint yellow color.

Step 4: The primary amine product (30 g) was mixed with 50 wt% NaOH solution (100 mL) and TEMPO methacrylate (100 mg) under an ice bath and nitrogen. Methacryloyl chloride (47.08 mL) was then added dropwise over 2 hours and left to stir overnight in darkness. The product was cleaned with petroleum ether (disposed) and then extracted using *t*-butyl methyl ether. The organic layer (*t*-butyl methyl ether) was dried and removed using a rotary evaporator to obtain an orange oil final product. The acetal monomer was stored at -20°C in darkness until use.

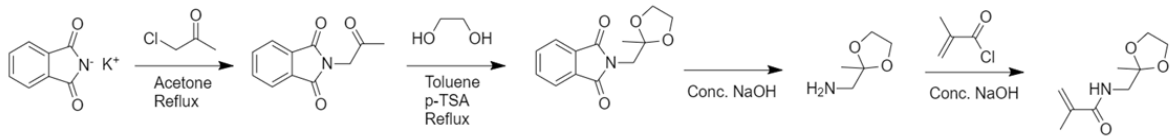

Figure S5.1: Synthesis scheme for the 2-methyl-N-[(2-methyl-1,3-dioxolan-2-yl)methyl]-2-propenamideketone monomer

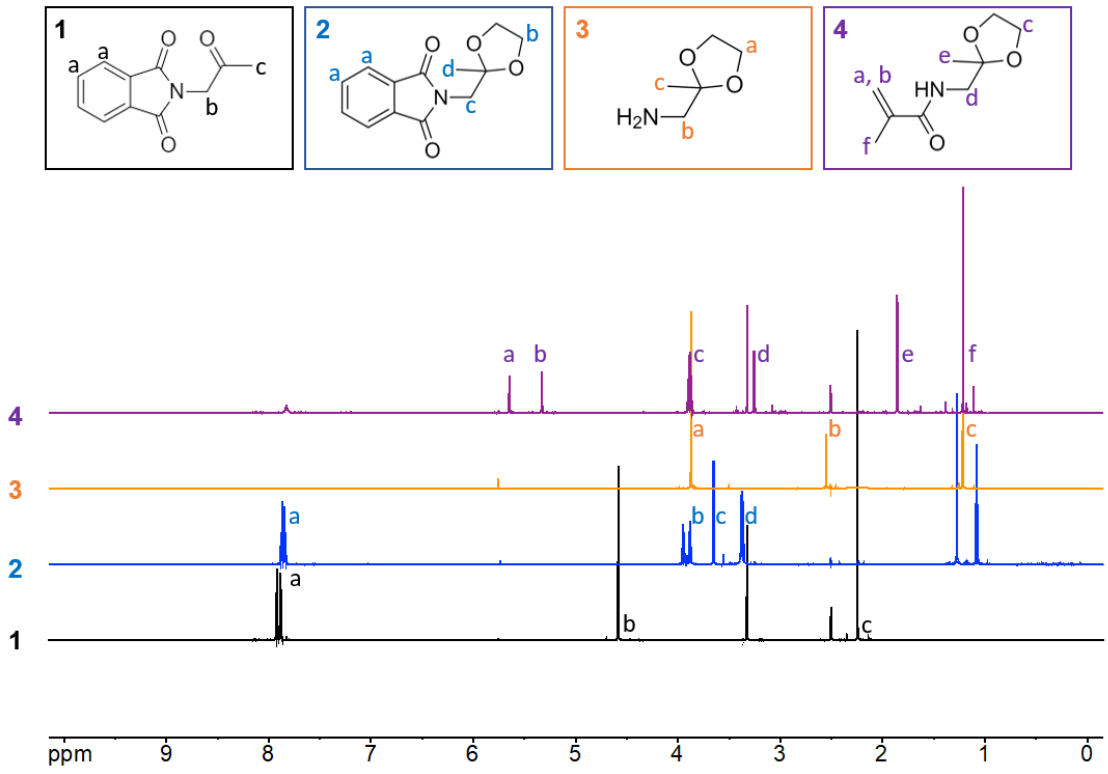

Figure S5.2: ^{1}H NMR spectra of the 2-methyl-N-[(2-methyl-1,3-dioxolan-2-yl)methyl]-2-propenamide ketone monomer and the precursor materials produced in each step of the synthesis. H-NMR (DMSO, 600 MHz): δ = 1.22 (s, 3H, -CH3, f), δ = 1.86 (t, 3H, -CH3, e), δ = 3.25 (d, 2H, -CH2, d), δ = 3.91 (m, 4H, -CH2, c), δ = 5.33 (s, 1H, =CH2, b) , δ = 5.65 (s, 1H, =CH2, a).

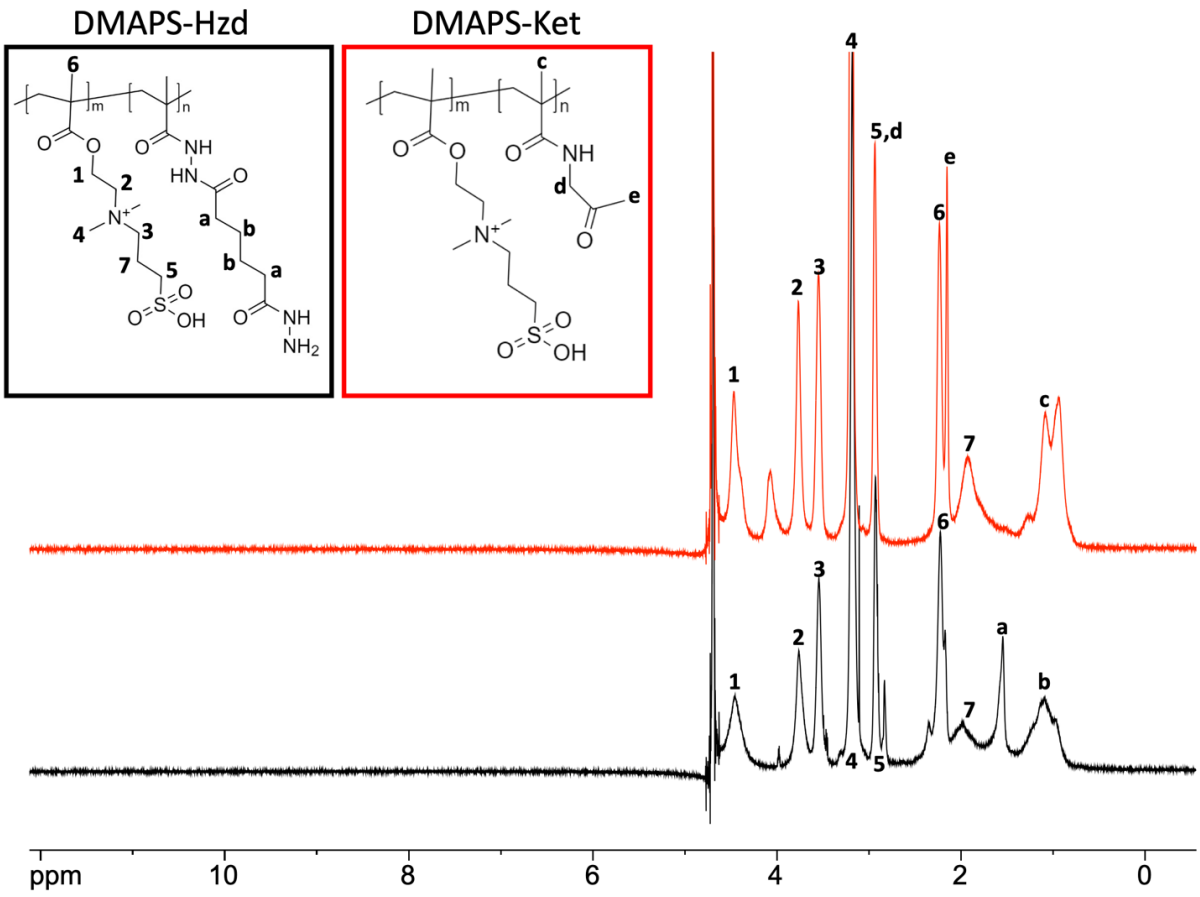

Figure S5.3: ^{1}H NMR of hydrazide-functionalized DMAPS (DMAPS-Hzd, black) and ketone-functionalized DMAPS (DMAPS-Ket, red) precursor polymers. Hydrazide and aldehyde functional group contents were quantified based on the intensity of using peaks ‘a’ and ‘e’ respectively relative to peak ‘1’ from the DMAPS repeat units.

Table S5.1: Gelation kinetics of hydrogel ink formulations used in the printing experiments

Polymer concentrations (wt%)	Gelation time (min)
6	5
8	3
10	2

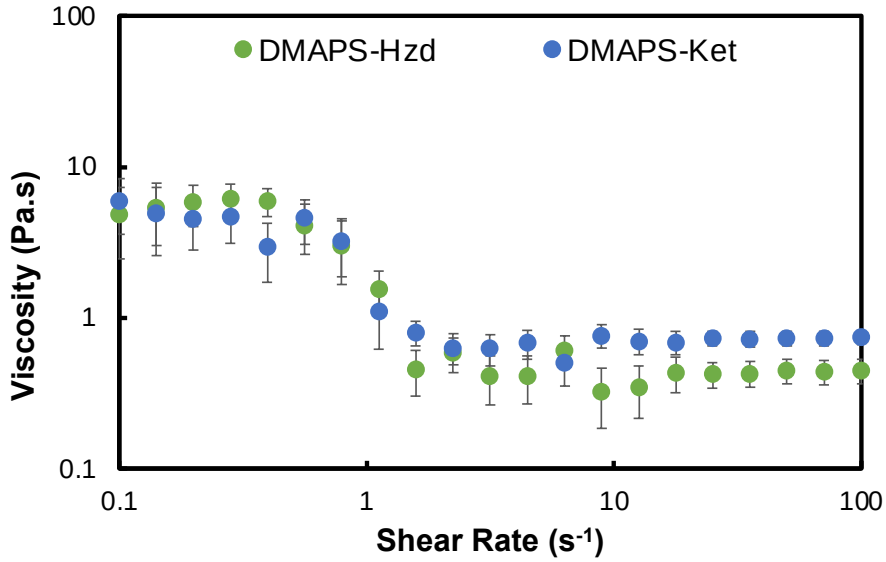

Figure S5.4: Viscosity sweep of the hydrazide and ketone functionalized DMAPS precursor polymers prior to crosslinking and printing

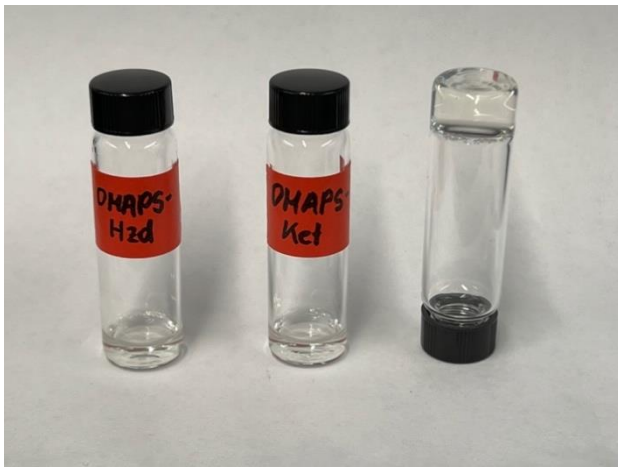

Figure S5.5: Photographs of hydrazide (DMAPS-Hzd) and ketone (DMAPS-Ket) precursor polymers and the resulting hydrazone-crosslinked DMAPS hydrogel (10 wt% precursor polymer, after 2 minutes).

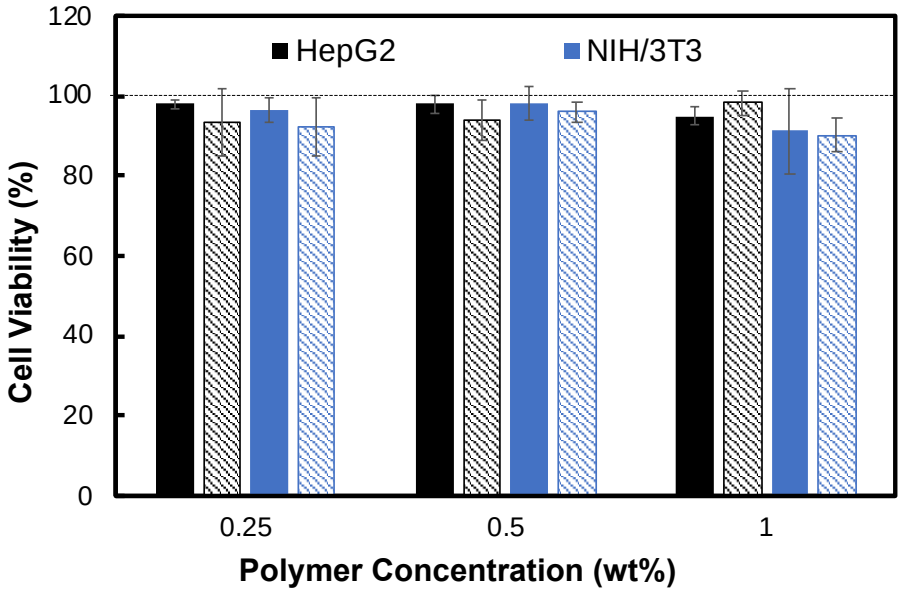

Figure S5.6: Cytotoxicity of hydrazide-functionalized (DMAPS-Hzd, solid) and ketone-functionalized (DMAPS-Ket, shaded) precursor polymers at various concentrations to HepG2 and NIH/3T3 cells. Data was collected using the PrestoBlue assay and normalized to a cell-only (no materials treatment) well.

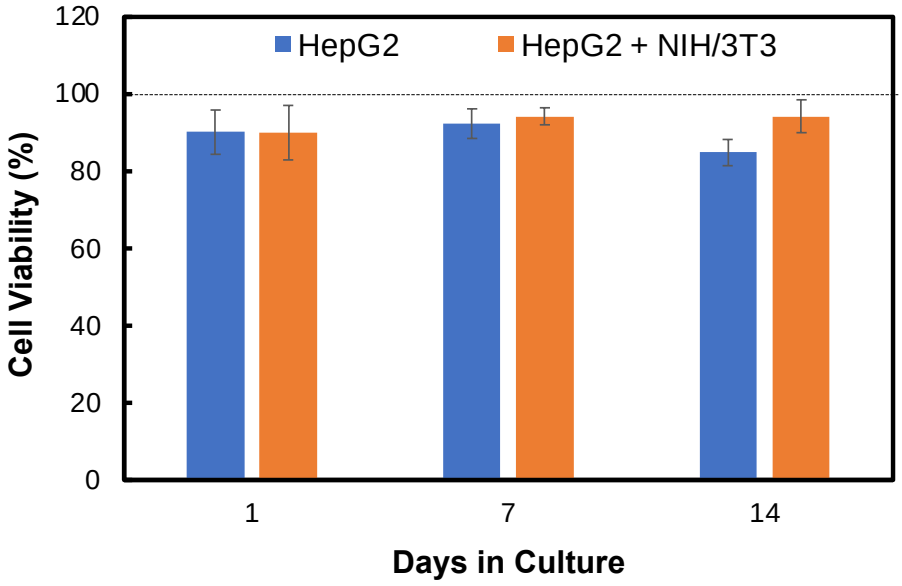

Figure S5.7: Cell viability in liver mimics printed with DMAPS hydrogels encapsulating HepG2 and HepG2 + NIH/3T3 cells

CHAPTER 6

Polysulfobetaine-Poly(Oligoethylene Glycol Methacrylate) Copolymers with Improved Anti-Fouling and Anti-Coagulant Properties

Eva Mueller, Hugo Lopez, Zheng Fu Zhou, Ruiqi Yin, Jim Fredenburgh, Jeff Weitz, Todd Hoare

Declaration of Academic Achievement:

Hugo Lopez and Zheng Fu Zhou are credited for synthesizing and characterizing the functional co-polymers and conducting the protein uptake studies. Zheng Fu Zou performed the kinetic polymerization experiment, with feedback from Dr. James Bodnaryk. Ruiqi Yin, Jim Fredenburgh and Jeff Weitz are thanked for their support and guidance on the coagulation studies. The remaining experiments, analyses and written discussions were completed by Eva Mueller, with help from Dr. Todd Hoare.

Polysulfobetaine-Poly(Oligoethylene Glycol Methacrylate) Copolymers with Improved Anti-Fouling and Anti-Coagulant Properties

Eva Mueller, Hugo Lopez, Zheng Fu Zhou, Ruiqi Yin, Jim Fredenburgh, Jeff Weitz, Todd Hoare

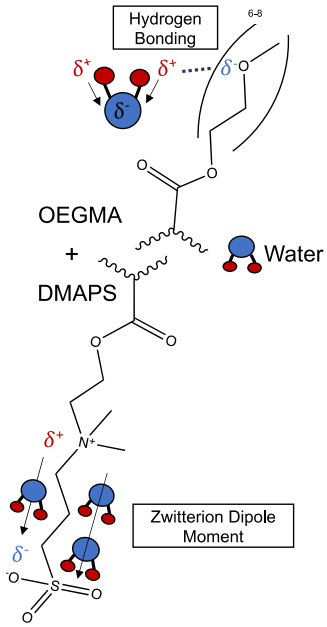

Zwitterionic polymers such as poly(sulfobetaines) and polyether polymers such as poly(ethylene glycol) (PEG) have both been reported as promising anti-fouling materials for various biomedical applications based on their high water binding capacity through hydrogen bonding (PEG) or ion-dipole interactions (zwitterionic polymers). Herein, to assess whether synergistic anti-fouling properties can be achieved when poly(sulfobetaine) and PEG moieties are combined, linear co-polymers were fabricated by the chain transfer radical polymerization of [2-(methacryloyloxy) ethyl] dimethyl-(3-sulfopropyl) ammonium hydroxide (DMAPS) and poly(ethylene glycol) methyl ether methacrylate (OEGMA), functionalized with aldehyde or hydrazide functional groups to enable *in situ* gelation via hydrazone crosslinking. In general, hydrogels prepared with more OEGMA resulted in longer gelation times, increased protein adsorption (and absorption due to the higher degree of swelling observed), and faster plasma clotting times; however, hydrogels prepared with precursor polymers containing a 90:10 ratio of DMAPS:OEGMA exhibited significantly lower protein adsorption as well as lower peak thrombin upon exposure to blood plasma than either single-component gel, suggesting a potential benefit of introducing multiple types of water binding mechanisms into an anti-fouling biomaterial.

Keywords: anti-fouling, anti-clotting, *in situ*-gelling hydrogels, copolymerization, poly(sulfobetaine), poly(oligoethylene glycol methacrylate)

6.1 Introduction

Non-specific protein adsorption is widely recognized as the first step to the inflammatory cascade that can ultimately trigger fibrosis and/or rejection of implanted biomaterials[1-4]. Biofouling via protein adsorption is driven by a combination of charge interactions, hydrogen bonding, hydrophobic interactions, and van der Waals forces between plasma proteins and an interface[5, 6]. On this basis, multiple techniques have been developed to try to minimize or eliminate protein adsorption to biomaterials, including manipulating surface hydrophobicity[7, 8], texture[9, 10], and surface functionalization[11, 12] of the implants. Functionalization of an interface with a highly water-binding polymer has emerged as the most popular strategy for fabricating anti-fouling biomaterials, with the strong hydrogen bonding capacity of water to such polymers resulting in the formation of hydrogen-bonded water "cages" that can sterically inhibit protein deposition on a surface[13]. Among such water-binding polymers, polyethylene glycol (PEG) is considered as the gold standard due to its ability to direct water assembly via hydrogen bonding with the oxygens in its ether repeat unit[14]. However, PEG also has drawbacks as an anti-fouling material since it can undergo oxidation in biological medium[15] and still interacts with proteins weakly[16]. Recent studies have also confirmed the relatively wide-spread existence of PEG antibodies[17], prompting renewed efforts to identify alternative anti-fouling polymers.

Zwitterionic materials are a class of materials that contain both negative and positive charges. As previously discussed in **Chapter 5**, zwitterionic materials exhibit much stronger hydrophilicity, when compared to PEG, due to the dipole-induced dipole interactions with water[18]. Polymeric betaines are a class of zwitterionic polymer of particular interest that have cationic and anionic functional groups are located on the same monomer unit[19], with sulfobetaines[20], phosphobetaines[21], and carboxybetaines[22] all commercially available with varying anionic groups. From an anti-fouling perspective, the number of water molecules that a betaine polymer can bind to is significantly higher than that of PEG; for example, polysulfobetaine can bind 7-8 water molecules per repeat unit[23], while PEG only binds one[24]. Sulfobetaines have been shown to be tissue compatible[25, 26], to reduce bacterial adhesion and protein fouling[27], and to play an important role in the development of blood-inert surfaces and wound care dressings[28, 29]. Zwitterionic fusion interactions between complementary charges on adjacent sulfobetaine groups have also more recently been investigated as a means of micellar

formation via self-assembly, with high-molecular weight sulfobetaines having been shown to exhibit upper critical solution temperature thermoresponsive behavior[30].

Due to the diverse chemical and anti-fouling properties of the zwitterionic polymers, the fabrication of crosslinked hydrogel networks based on these polymers has attracted significant interest. The preparation of zwitterionic hydrogels can be achieved through radical polymerization, polymer coupling, or self-assembly through physical interactions[31], leading to the development of a range of hydrogels with improved properties for anti-fouling coatings[32], membrane separations[33], biosensing devices[34], drug delivery vehicles[35], and tissue engineering matrices[36]. The potential of zwitterionic polymers to reduce thrombosis, infection, and foreign body responses of biomedical implants has been an area of particular interest[37-38]. "Click" chemistry-based zwitterionic hydrogels are of particular emerging interest given that the *in situ* gelation facilitated with such materials eliminates the need for surgical implantation. Zwitterionic "click" hydrogels with anti-fouling/anti-fibrotic properties have been fabricated using thiol-ene chemistry (thiol-functionalized zwitterionic carboxybetaine methacrylate + methacrylated hyaluronic acid[39]) or amine-epoxy chemistry[40]; we have also recently reported hydrazone-crosslinked polysulfobetaine polymers fabricated by *in situ* mixing of hydrazide- and aldehyde-functionalized precursor polymers that exhibited long-term stability and effective anti-fouling properties[41].

Despite the multiple advantages of zwitterionic hydrogels as anti-fouling biomaterials, two key limitations remain to their practical use. First, while non-specific protein adsorption is significantly suppressed with zwitterionic materials, it is still not completely eliminated; as such, the identification of methods that can further reduce non-specific protein adsorption and thrombotic responses is necessary to improve biological performance. Second, the interaction between the zwitterionic polymer chains is highly dependent on the salt concentration and the types of salts in the environment, including the high ionic strength *in vivo* environment[42]. The presence of low salt concentrations can break zwitterion fusion interactions and promote hydrogel swelling; conversely, at higher ion contents and/or in the presence of higher valence ions[44] (particularly anions[45]), ion bridging between zwitterionic chains can occur to collapse the extended polymer chains into a network structure, resulting in phase separation[43]. Such a transition can significantly reduce the anti-fouling potential of zwitterionic polymers in certain ionic environments in addition to making it challenging to mix zwitterionic polymers with other types of ionic biomaterials (i.e., proteins or many bioactive carbohydrates) that may have

other favorable properties in the context of tissue engineering applications such as promoting secondary gelation, cell spreading, or cell adhesion. As such, developing a zwitterionic-based hydrogel formulation that can further reduce non-specific protein adsorption while also being more broadly miscible with other types of commonly used biomaterials (i.e., carbohydrates or PEG) may offer attractive application advantages.

In this work, we report a linear co-polymer system based on [2-(methacryloyloxy)ethyl]dimethyl-(3-sulfopropyl)ammonium hydroxide (DMAPS) and poly(ethylene glycol) methyl ether methacrylate (OEGMA) functionalized with either aldehyde or hydrazide functional groups to enable efficient *in situ* gelation via the formation of hydrazone crosslinks. In particular, we hypothesize that free radical copolymerization of both zwitterionic and PEG-based moieties into a single covalently linked polymer chain offers the potential to: (1) introduce multiple water binding mechanisms (hydrogen bonding and permanent dipole-induced dipole interactions) into a single polymer, with the potential to further improve water binding and thus protein repellency and (2) dilute the zwitterionic component of the polymer to reduce the salt sensitivity of the polymer and promote improved miscibility with other biomaterials with favorable biological responses, offering potential to improve the bioactivity of the hydrogels without compromising the anti-fouling/anti-thrombotic/anti-fibrotic properties of the overall material. We demonstrate that the gelation kinetics, protein adsorption, and coagulation responses of the hydrogels can be strongly influenced by the ratio of DMAPS:OEGMA, with a 90:10 DMAPS:OEMGA ratio exhibiting both reduced non-specific protein adsorption and reduced peak thrombin relative to either polyDMAPS-only or polyOEGMA-only hydrogels. In addition, we demonstrate that the 90:10 DMAPS:OEGMA polymers are directly miscible with a range of biologically-relevant carbohydrates, opening the door to form multi-component hydrogels with both anti-fouling and bioactive properties.

6.2 Experimental Methods

6.2.1 Materials

[2-(Methacryloyloxy)ethyl]dimethyl-(3-sulfopropyl)ammonium hydroxide (DMAPS, Sigma-Aldrich), poly(ethylene glycol) methacrylate (OEGMA, M_n = 500 g/mol, Sigma-Aldrich), acrylic acid (AA, Sigma-Aldrich, 99%), thioglycolic acid (TGA, Sigma-Aldrich, 98%), ammonium persulfate (APS, Sigma-Aldrich), N′-ethyl-N-(3-(dimethylamino)propyl)-carbodiimide (EDC, Carbosynth, Compton CA, commercial grade), and adipic acid dihydrazide (ADH, Alfa Aesar, 98%) were all used as received. Milli-Q grade distilled deionized water (DIW) was used for all experiments. NIH/3T3 mouse fibroblast cells and C2C12 myoblasts were all purchased from ATCC (Cedarlane Laboratories, Burlington, ON). Dulbecco's Modified Eagle's Medium (DMEM, ThermoFisher), fetal bovine serum (FBS, ThermoFisher) and penicillin−streptomycin (ThermoFisher), trypsin−EDTA solution (Sigma-Aldrich), and phosphate buffered saline (1× PBS, ThermoFisher) were all used as received. For the coagulation assays, the pooled normal plasma (PNP) was generously donated from the lab of Dr. Jeffrey Weitz. Calcium chloride ($CaCl_2$, Sigma Aldrich), HEPES buffer (Gibco, pH 7.4) and z-GGR-AMC thrombin substrate (Z-Gly-Gly-Arg-AMC, Bachem, Switzerland) were used as received. For the miscibility experiments, sodium carboxymethyl cellulose (CMC, Sigma Aldrich, 250,000 g/mol, substitution=0.7), dextran (Dex, Sigma Aldrich, from *Leuconostoc. spp*), sodium alginate (Alg, Sigma Aldrich), sodium hyaluronate (HA, LifeCore Biomedical) and poly(ethylene glycol) (PEG, Sigma Aldrich, 10,000 g/mol were used as received.

6.2.2 Polymer Synthesis

Hydrazide-functionalized and aldehyde-functionalized DMAPS-OEGMA polymers were synthesized targeting 10 mol% hydrazide or aldehyde functionality in Milli-Q water overnight at 75℃, using DMAPS-OEGMA molar ratios of 100:0 (polyDMAPS-only hydrogel), 90:10, 80:20, 70:30, 50:50, 30:70, 10:90, or 0:100 (polyOEGMA-only gel), as per recipes in **Table 6.1** for hydrazide-functionalized polymers and **Table 6.2** for aldehyde-functionalized polymers. In each case, the reaction mixture was purged with nitrogen for 30 minutes prior to heating and kept under continuous nitrogen purge during the 24-hour reaction time. Following polymerization, the polymers were purified via 6 x 6-hour cycles of dialysis (3.5 kDa molecular weight cut-off membrane), lyophilized to dryness, and stored at 4℃ until use.

Table 6.1: DMAPS-OEGMA-Hzd polymer synthesis recipes

	100:0	**90:10**	**80:20**	**70:30**	**50:50**	**30:70**	**10:90**	**0:100**
DMAPS (g)	4.0	3.6	3.2	2.8	2.0	1.2	0.4	-
OEGMA (g)	-	0.72	1.43	2.15	3.58	5.01	6.44	4.0
AA (g)	0.115	0.115	0.115	0.115	0.115	0.115	0.115	0.115
APS (mg)	40	40	40	40	40	40	40	40
TGA (*μ*L)	10	10	10	10	10	10	10	10
Milli-Q (mL)	20	20	20	20	40	40	40	40
ADH (g)	1.38	1.38	1.38	1.38	1.38	1.38	1.38	1.38
EDC (g)	0.62	0.62	0.62	0.62	0.62	0.62	0.62	0.62

Table 6.2: DMAPS-OEGMA-Ald polymer synthesis recipes

	100:0	**90:10**	**80:20**	**70:30**	**50:50**	**30:70**	**10:90**	**0:100**
DMAPS (g)	4.0	3.6	3.2	2.8	2	1.2	0.4	-
OEGMA (g)	-	0.72	1.43	2.15	3.58	5.01	6.44	4.0
DMEM (g)	0.28	0.28	0.28	0.28	0.28	0.28	0.28	0.28
APS (mg)	42	42	42	42	42	42	42	42
TGA (*μ*L)	10	10	10	10	10	10	10	10
Milli-Q (mL)	20	20	20	20	40	40	40	40

6.2.3 Polymer Characterization

Aqueous size exclusion chromatography (SEC) was performed on a system consisting of a Waters 515 HPLC pump, a Waters 717 Plus autosampler, three Ultrahydrogel columns (30 cm × 7.8 mm i.d.; exclusion limits: 0–3 kDa, 0–50 kDa, 2–300 kDa) and a Waters 2414 refractive index detector. A mobile phase consisting of 0.3 M sodium nitrate and 0.05 M phosphate buffer (pH 7) running at a flow rate of 0.8 mL/min was used for all polymers analyzed. All polymers were also characterized using ^{1}H NMR to quantify the mol% functionalization of the aldehyde or hydrazide groups and compare the theoretical and experimental incorporation values of DMAPS:OEGMA.

6.2.4 Copolymerization Kinetics

The reactivity ratios (r_1 and r_2) of DMAPS and OEGMA within the copolymer were measured by tracking the relative changes in intensity of the vinyl protons of each monomer (4.2 ppm for OEGMA and 4.5 ppm for DMAPS) from ^{1}H NMR spectra collected from samples taken at specific time points. More specifically, the reagents to synthesize polymers with ratios of 90:10 DMAPS-OEGMA (large DMAPS excess) and 10:90 DMAPS-OEGMA (large OEGMA excess) were first added to a 250 mL round-bottom flask, without the initiator. The oil bath was heated to 75°C and the flask was submerged. The reaction mixtures were purged with nitrogen for 30-40 min, after which the required amount of initiator was added through a long nitrogen needle. The first sample (~100 μL) was taken right away (t=0), with subsequent samples taken at 2, 5, 10, 20, 30, 60, 120, 240, 360 and 1440 min after the initiator injection time through along needle under the pressure of the sparged nitrogen, ensuring a continuous air-free environment inside the reaction vessel. Each sample was immediately quenched by exposing the solution to air, placing it in an ice bath, and adding 500 ppm of mono methyl ether hydroquinone (MEQH) to stop the polymerization. Each sample was then analyzed using NMR with deuterium oxide (D_2O) as the solvent, with the resulting conversion versus time data analyzed using the Jaacks method (Eq. 6.1).

$$\boldsymbol{log\frac{[M_1]_t}{[M_1]_0} = r_1 log\frac{[M_2]_t}{[M_2]_0}} \tag{6.1}$$

Here, $[M_1]_t$ represents the instantaneous monomer concentration of the monomer in large excess, $[M_1]_0$ represents the initial monomer concentration of the monomer in large excess, r_1 represents the copolymerization ratio of the monomer in large excess, $[M_2]_t$ represents the instantaneous concentration of the minor comonomer, and $[M_2]_t$ represents the initial concentration of the minor comonomer. A plot of $log\frac{[M_1]_t}{[M_1]_0}$ versus $log\frac{[M_2]_t}{[M_2]_0}$ should yield a line with a slope corresponding to the copolymerization ratio r_1. Repeating the process for the DMAPS-excess and OEGMA-excess copolymers yields both copolymerization ratios.

6.2.5 Polymer Cytotoxicity

NIH/3T3 and C2C12 myoblasts were cultured in DMEM medium with 10% FBS and 1% penicillin−streptomycin to ~80% confluency at 37°C and 5% CO_2 before subsequent use. The cytotoxicity of the functional DMAPS-OEGMA polymers was measured over a concentration

range of 0.25 to 1 mg/mL using a PrestoBlue Cell Viability Assay (ThermoFisher) after 24 hours of incubation at 37°C. Cells were first plated at $5x10^4$ cells per well using a 96 well plate for 24 hours, after which the polymers were added and incubated with the cells for a subsequent 24 hours. 10 μL of PrestoBlue reagent and 90 μL of media were then added to each well and incubated for 2 hours at 37°C. The resulting fluorescence was read using a Tecan Infinite M200 Pro plate reader using an excitation wavelength of 560 nm and an emission wavelength of 590 nm.

6.2.6 Hydrogel Fabrication

Hydrogels were prepared via co-extrusion of aldehyde or hydrazide functionalized precursors. The precursor polymers were loaded into separate barrels of a double barrel syringe fitted with a static mixer at the outlet (Medmix Systems, L-series) to ensure thorough mechanical mixing. Hydrogel disks were prepared using precursor polymer concentrations of 20 and 10 wt% for hydrazide and aldehyde functionalized precursors, respectively. The polymers were extruded into cylindrical silicone rubber molds (diameter 7 mm and height 3 mm) and incubated at room temperature for at least 12 hours to ensure complete gelation. Gelation time was investigated by extruding 250 μL of the precursor solution at various concentration into a 2 mL Eppendorf tube and inverting the tube every 5 s; the gelation time was measured as the time after which the material does not flow following 5 s of inversion.

6.2.7 Swelling Kinetics

The swelling ratio of hydrogels was determined by gravimetric measurements in 10 mM PBS at pH = 7.4. Hydrogels were placed into cell culture inserts, weighed (W_0), placed into a 6-well cell culture plate, and completely submerged in 5 mL PBS. At predetermined time intervals, the cell culture inserts were removed from the well, the PBS was drained, and the hydrogels were gently wicked with a Kimwipe to remove the unabsorbed PBS. The hydrogel disks were then weighed (W_t), after which the hydrogels were resubmerged into a fresh PBS solution for subsequent measurements over a total of 100 hours. Error bars represent the standard deviation of independent replicate measurements (n = 3). The swelling ratio (SR) was determined according to Eq. 6.2:

$$\boldsymbol{SR = \frac{W_t}{W_0}} \tag{6.2}$$

6.2.8 In Vitro Protein Adsorption

To assess protein adsorption to the hydrogels, thin film hydrogels were first fabricated in 96-well plates. Precursor polymer solutions were prepared at concentrations of 10 and 20 wt% for aldehyde and hydrazide functionalized precursors, respectively, after which 60 μL of each precursor solution was sequentially extruded into 96 well plate and left overnight to ensure complete gelation. Following, 200 μL of the 10 mM PBS was added and the hydrogels were incubated for 2 hours to achieve equilibrium swelling. Excess PBS was removed, and 100 μL of either BSA-FITC, lysozyme-FITC or fibrinogen-FITC solution at concentrations of 250, 500, or 1000 μg/mL in PBS was added and incubated for 4 hours at 37°C. The hydrogels were then rigorously rinsed five times with PBS to remove any unadsorbed protein. Protein adsorption/absorption was measured using two strategies: (1) The fluorescence signal from the interface of the gel was quantified using a Tecan Infinite M200 Pro plate reader operating at an excitation wavelength of 495 nm and an emission wavelength of 520 nm, using a linear calibration curve in the concentration range of 1 to 100 μg/mL to relate the fluorescence signal to the total protein concentration; (2) confocal laser scanning microscopy (CLSM, Nikon) was used to probe the fluorescence intensity both on the hydrogel surface and in the hydrogel bulk to semi-quantitatively assess both adsorbed and absorbed protein. The error bars represent the standard deviation of three independent replicates.

6.2.9 Clotting Assay and Thrombin Generation Assay

Precursor polymer solutions were prepared at concentrations of 10 and 20 wt% for aldehyde and hydrazide functionalized precursors, respectively. To form the hydrogels for testing, 25 μL of each precursor solution was pipetted into 96 well plate, mixed manually (to avoid introducing any bubbles), and left overnight to ensure complete gelation. For the plasma clotting assays, 80 μL of 20 mM HEPES pH 7.4 buffer was added to each well followed by 100 μL of pooled normal plasma (PNP), after which the entire plate was incubated at 37℃ for 15 minutes without any shaking. Finally, 20 μL of 260 mM $CaCl_2$ was added simultaneously using a multi-channel pipette to all wells. After briefly shaking the plate to ensure homogeneous mixing of the $CaCl_2$ in each well, the absorbance was tracked at a wavelength of 405 nm for 1 hour at 37℃. For the thrombin generation assay, 100 μL of PNP was added and the plate was incubated at 37℃ for 15 minutes without any shaking. Following, 100 μL of a master mix including $CaCl_2$ (15 mM), z-GGR-AMC thrombin substrate (1 mM) and pH 7.4

HEPES buffer (20 mM) was simultaneously added to each well using a multi-channel pipette and the plate was briefly shaken to ensure mixing. The resulting fluorescence signal (corresponding to substrate-to-thrombin complexation) was tracked using a fluorescence plate reader (excitation: 360 nm, emission: 460 nm) over 90 min at 37℃ at 1 min intervals. Thrombograms were generated based on the readings, from which the peak thrombin (i.e., the highest measured thrombin concentration) and time to peak (i.e., the time to maximum thrombin concentration) were extracted.

6.3 Results

6.3.1 Polymer Characterization

DMAPS-OEGMA copolymers with both hydrazide and aldehyde functional groups were successfully synthesized via free-radical polymerization over the full range of DMAPS:OEGMA molar ratios. Each polymer solution prepared at either 10 or 20 wt% in 0.9% saline was clear and showed no sign of phase separation. The molecular weights of the resulting copolymers are summarized in **Table 6.3**. Copolymers prepared with 50 mol% or less of OEGMA all showed M_n values in the 8-12 kDa range; however, at 30:70 and 10:90 DMAPS:OEGMA molar ratios, the molecular weights significantly increased (M_n ~30 kDa) and the dispersities of the polymers were significantly higher. We attribute this increase in molecular weight to the solvent effects during free-radical polymerization. The DMAPS monomer was only soluble in water, whereas OEGMA is conventionally polymerized in dioxane to improve control over molecular weight[46]. To compromise between miscibility of the DMAPS monomer and control of the polymerization rate at lower DMAPS:OEGMA ratios, the high OEGMA reactions were still performed in water but using a higher solvent volume (40 mL instead of the conventional 20 mL that was used for all other polymers).

Table 6.3: Molecular weights for different DMAPS-OEGMA polymers

Molar Ratio (DMAPS: OEGMA)	Functionality	M_n (kDa)	Đ
100:0	Hzd	12	2.9
	Ald	8	1.7
90:10	Hzd	7	2.1
	Ald	7	2.2
80:20	Hzd	13	3.5
	Ald	16	4.5
70:30	Hzd	10	2.6
	Ald	8	1.9
50:50	Hzd	12	2.6
	Ald	11	2.3
30:70	Hzd	29	7.1
	Ald	29	7.7
10:90	Hzd	34	8.0
	Ald	25	6.9
0:100	Hzd	28	3.3
	Ald	26	3.1

To assess the actual DMAPS:OEGMA ratio as well as the degree of functionalization of the different copolymers, the polymers were analyzed using ^{1}H NMR (see **Figure S6.1** and **Figure S6.2** for the relevant ^{1}H NMR spectra). **Table 6.4** compares the experimental andtheoretical compositions of the copolymers.The experimentally measured functional group molar ratios for hydrazide or aldehyde groups ranged between 7 and 12 mol%, with the lower incorporations reported for the aldehyde functionalized DMAPS-OEGMA polymers; this compares favorably with the target 10 mol% functionalization of all the polymers, allowing us to directly compare the performance of hydrogels prepared with different DMAPS:OEGMA ratios. Similarly, the DMAPS:OEGMA ratios were similar to the target ratios, suggesting relatively random copolymerization kinetics between DMAPS and OEGMA.

Table 6.4: Experimental versus theoretical molar ratios of functional DMAPS-OEGMA polymers prepared with different DMAPS:OEGMA molar ratios

Theoretical Molar Ratios (DMAPS: OEGMA: Hzd/Ald)*	Functionality	DMAPS Molar Ratio	OEGMA Molar Ratio	Functional Group Molar Ratio
90:0:10 (100:0)	Hzd	92	-	8
	Ald	93	-	7
81:9:10 (90:10)	Hzd	82	7	11
	Ald	81	11	8
72:18:10 (80:20)	Hzd	67	22	11
	Ald	69	21	7
63:27:10 (70:30)	Hzd	65	24	11
	Ald	60	32	8
45:45:10 (50:50)	Hzd	45	43	12
	Ald	43	47	10
27:63:10 (30:70)	Hzd	33	56	11
	Ald	26	66	8
9:81:10 (10:90)	Hzd	12	76	12
	Ald	10	79	11
0:90:10 (0:100)	Hzd	-	88	12
	Ald	-	89	11

6.3.2 Kinetic Polymerization Study

To assess the relative reactivity of DMAPS and OEGMA (and thus their anticipated chain distributions within the copolymers), the reactivity ratios of DMAPS and OEGMA (r_1 and r_2) were determined experimentally using ^{1}H NMR to track the relative changes in the intensity of the vinyl protons of each monomer. **Figure 6.1A** shows the plot of $\log\frac{[M_1]_t}{[M_1]_o}$ versus $\log\frac{[M_2]_t}{[M_2]_o}$ for the copolymerization of 90% DMAPS/10% OEGMA, yielding a line with a slope of r_1; **Figure 6.1B** shows the corresponding plot for the copolymerization of 10% DMAPS/90% OEGMA, yielding a line with a slope of r_2. From this analysis, the calculated reactivity ratios for DMAPS (r_1) and OEGMA (r_2) were 1.22 and 1.05, respectively. These very similar reactivity ratios, anticipated given the common methacrylate backbone of the two monomers and the high correlation observed in **Table 6.2** between the actual and theoretical DMAPS:OEGMA ratios across the whole range of ratios tested, indicate that the two monomers have no significant preference for self-propagation versus cross-propagation (r_1r_2 = 1.28) and should thus be randomly distributed within the copolymer backbone.

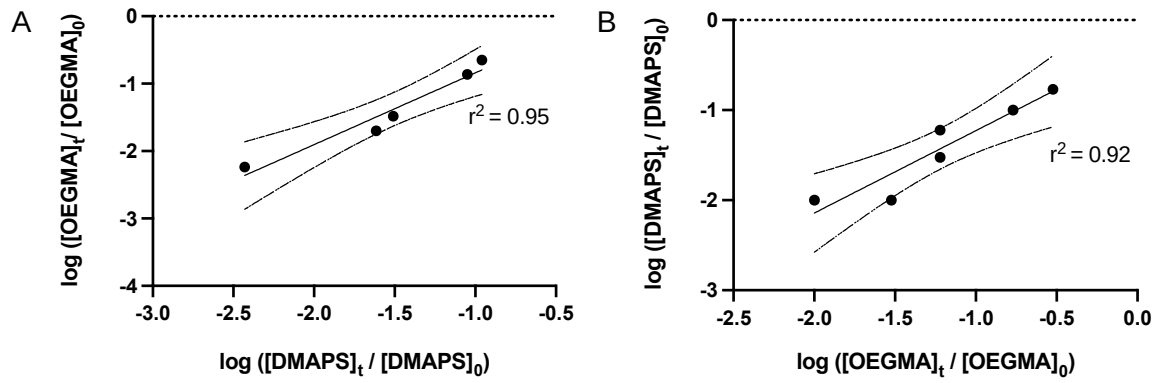

Figure 6.1: Jaacks plots to calculate the reactivity ratios for DMAPS (A, 90% DMAPS/10% OEGMA copolymer) and OEGMA (B, 10% DMAPS/90% OEGMA copolymer). The dotted lines reflect the upper and lower range of the 95% confidence interval.

6.3.3 Polymer Cytotoxicity

DMAPS-OEGMA-Hzd polymers with varying DMAPS:OEGMA ratios were tested for cytotoxicity against NIH/3T3 mouse fibroblast cells (**Figure 6.2A**) and C2C12 myoblast cells (**Figure 6.2B**). None of the tested polymers show any cytotoxic effects on either cell type after 24 hours of exposure up to relatively high polymer concentrations (1 mg/mL), highlighting their potential application in biomedical applications.

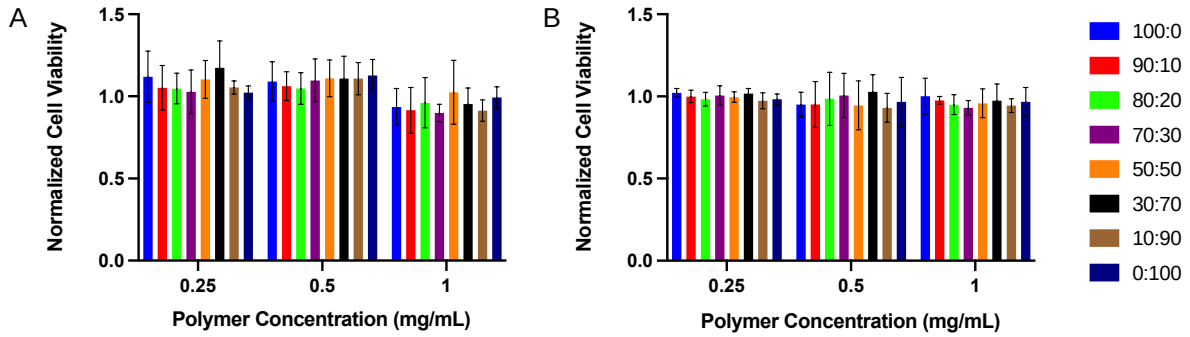

Figure 6.2: Cytotoxicity of DMAPS-OEGMAHzd copolymers prepared with varying DMAPS:OEGMA ratios following 24 hours of exposure to NIH/3T3 fibroblast (A) or C2C12 myoblast (B) cells as assessed using the PrestoBlue assay.

6.3.4 Hydrogel Characterization

Hydrogels were next fabricated by mixing hydrazide and aldehyde-functionalized DMAPS-OEGMA polymers using a double barrel syringe equipped with a static mixer to form

hydrazone-crosslinked hydrogels. The gelation kinetics of the hydrogels were first assessed in 0.9% saline using a vial inversion test by mixing equal concentrations (20 wt%) of precursor polymers with the same DMAPS:OEGMA ratio. While gelation times with the all-DMAPS precursor polymers were rapid (<5 min), gelation times of polymer pairs with higher OEGMA mole fractions were impractically slow and did not gel within 24 hours when >50 mol% OEGMA was incorporated into the precursor polymers (**Table S6.1**). As such, to ensure that all gelation times are comparable and can be achieved within a few minutes at the same concentrations (and same mol% of functional groups) across the entire range of DMAPS:OEGMA ratios tested, a common aldehyde-functionalized crosslinker (100:0 DMAPS-OEGMA-Ald) was used to prepare all hydrogels. The resulting gelation times achieved are summarized in **Table 6.5**. Consistent with the results observed with the matched DMAPS:OEGMA ratio gels, the gelation time significantly increased as the OEGMA mole fraction was increased, consistent with both the higher steric hindrance to crosslinking presented by the OEGMA monomers as well as the dilution of potential zwitterion fusion interactions between DMAPS-rich polymers that can assist in creating rapid physical crosslinks in DMAPS-rich systems[47]. Indeed, to compensate for the slow gelation observed with OEGMA-rich copolymers if the matched 10 wt% concentration of DMAPS-Ald was used, a hydrazide polymer concentration of 20 wt% was used for all gelation experiments.

Table 6.5: Gelation kinetics for hydrogels prepared by mixing 100:0 DMAPS-OEGMA-Ald (10 wt%) with different ratios of DMAPS-OEGMA-Hzd (20 wt%)

Hydrogel Formulation	**Gelation Time (min)**
100:0 DMAPS-OEGMA-Ald (10 wt%) + 100:0 DMAPS-OEGMA-Hzd (20 wt%)	<1
100:0 DMAPS-OEGMA-Ald (10 wt%) + 90:10 DMAPS-OEGMA-Hzd (20 wt%)	1
100:0 DMAPS-OEGMA-Ald (10 wt%) + 80:20 DMAPS-OEGMA-Hzd (20 wt%)	2
100:0 DMAPS-OEGMA-Ald (10 wt%) + 70:30 DMAPS-OEGMA-Hzd (20 wt%)	2
100:0 DMAPS-OEGMA-Ald (10 wt%) + 50:50 DMAPS-OEGMA-Hzd (20 wt%)	4
100:0 DMAPS-OEGMA-Ald (10 wt%) + 30:70 DMAPS-OEGMA-Hzd (20 wt%)	4
100:0 DMAPS-OEGMA-Ald (10 wt%) + 10:90 DMAPS-OEGMA-Hzd (20 wt%)	8
100:0 DMAPS-OEGMA-Ald (10 wt%) + 0:100 DMAPS-OEGMA-Hzd (20 wt%)	10

6.3.5 Swelling Kinetics

The swelling kinetics of DMAPS-OEGMA hydrogels prepared with varying DMAPS:OEGMA ratios in the hydrazide functionalized polymer and a fixed 100:0 DMAPS-OEGMA-Ald gelling polymer are shown in **Figure 6.3A** while representative pictures of DMAPS-rich and OEGMA-rich hydrogels following 100 hours of swelling are shown in **Figure 6.3B**. Polymers prepared with a high fraction of OEGMA swelled significantly more than DMAPS-rich polymers, again consistent with the steric hindrance of the OEGMA side chains that slow (**Table 6.5**) and ultimately limit the crosslinking density as well as the occurrence of fewer physical crosslinks via zwitterionic fusion. Slight decreases in swelling at longer times were observed for hydrogels prepared with 30:70 and 50:50 DMAPS:OEGMA ratios, suggestive of potential onset of degradation in more OEGMA-rich hydrogels that imbibe more water; however, no bulk degradation of any hydrogel was observed on the timescale of this swelling study.

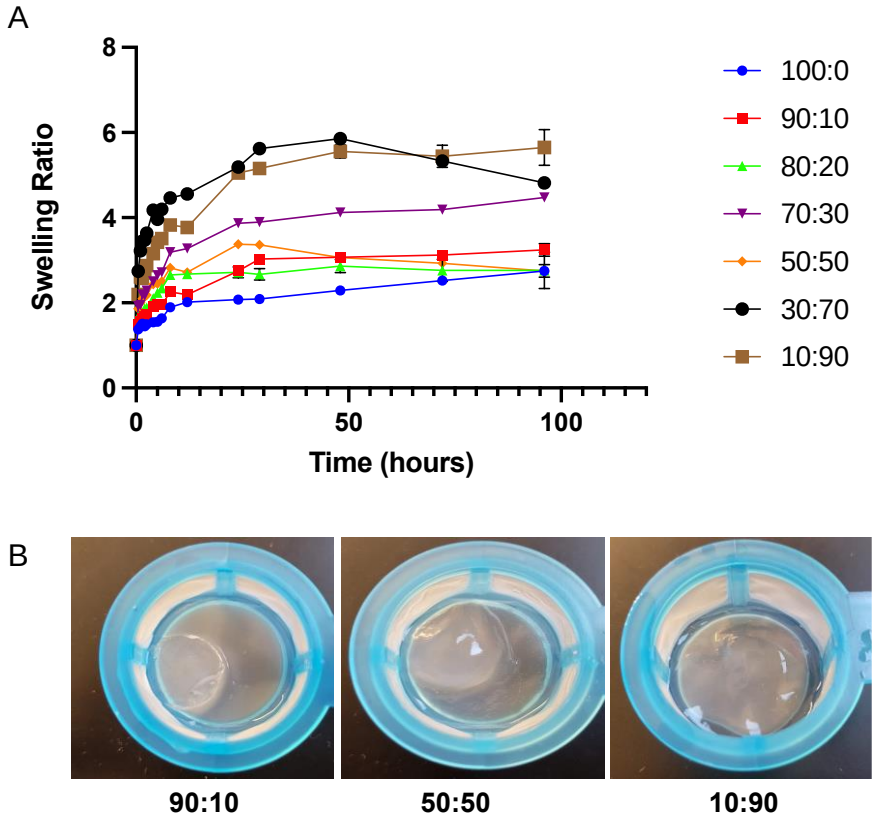

Figure 6.3: Swelling kinetics of DMAPS-OEGMA hydrogels prepared with 20 wt% hydrazide polymers containing varying DMAPS:OEGMA ratios crosslinked with 10 wt% 100:0 DMAPS-OEGMA-Ald over 100 hours (A) and representative images of the range of hydrogel swelling properties observed (B).

6.3.6 Single Protein Uptake Studies

Three different fluorescein-labelled proteins (albumin, lysozyme, fibrinogen) were incubated with the DMAPS-OEGMA hydrogels to assess the resistance of hydrogels with different DMAPS:OEGMA ratios to the adsorption and/or absorption of proteins. For both albumin (**Figure 6.4A**) and lysozyme (**Figure 6.4B**), hydrogels containing higher fractions of OEGMA generally bound more protein, consistent with the enhanced swelling of OEGMA-rich hydrogels (**Figure 6.3**) that would be expected to drive increased protein absorption into the gel network. The uptake of fibrinogen was more variable between different DMAPS:OEGMA ratios (**Figure 6.4C**), likely attributable to the higher molecular weight of fibrinogen limiting the degree of protein absorption possible even when the gels swell as well as the higher baseline amount of protein uptake observed relative to that observed with albumin and lysozyme; however, the lowest protein uptake was consistently observed for DMAPS-only hydrogels at each fibrinogen concentration tested. Interestingly, the 50:50 DMAPS:OEGMA ratio resulted in significantly lower protein uptake values across the full range of albumin and fibrinogen concentrations tested relative to hydrogels prepared with somewhat higher or somewhat lower DMAPS:OEGMA ratios while no analogous effect was observed for lysozyme; the physical reason for this observation is not clear but may be related to different phase separation patterns within these gels upon crosslinking. However, even with this analogous result, the DMAPS-rich hydrogels (100:0 or 90:10 DMAPS:OEGMA ratios) consistently matched or outperformed the protein repellency observed with the 50:50 DMAPS:OEGMA ratio hydrogels over all proteins and protein concentrations tested.

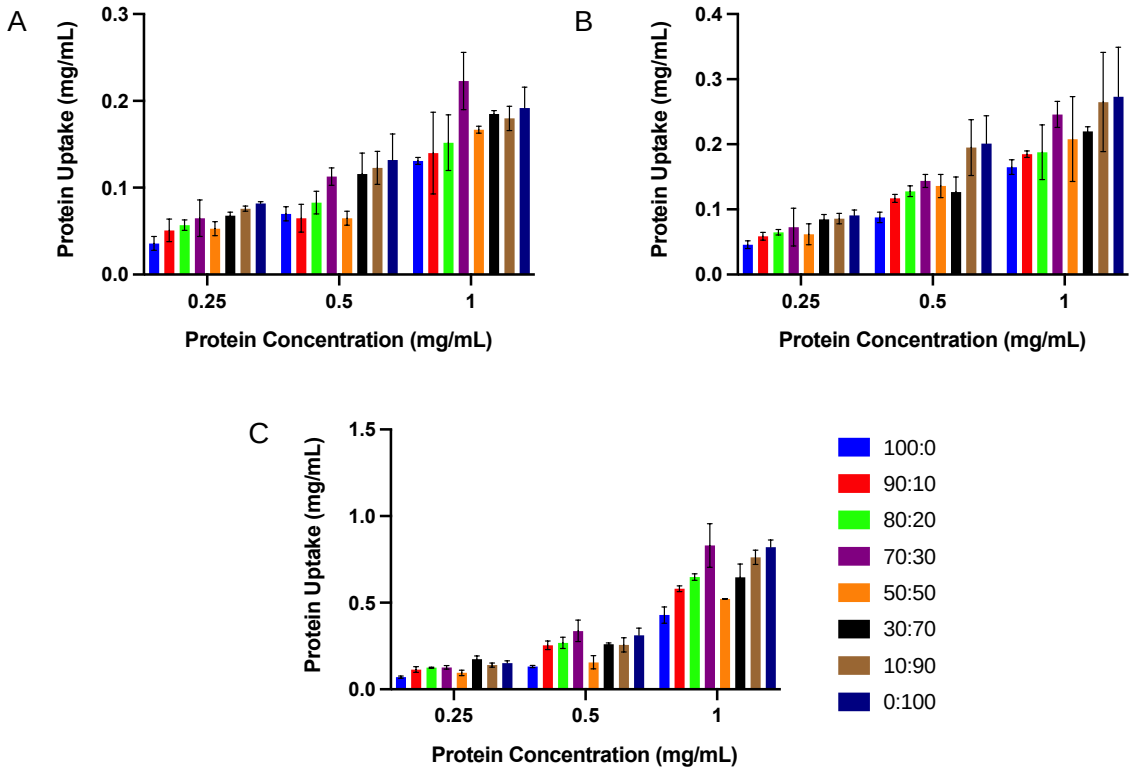

Figure 6.4: Protein uptake of FITC-albumin (A), FITC-lysozyme (B), and FITC-fibrinogen (C) into DMAPS-OEGMA hydrogels prepared with 20 wt% hydrazide polymers containing varying DMAPS:OEGMA ratios crosslinked with 10 wt% 100:0 DMAPS-OEGMA-Ald. Error bars represent the standard deviation of five independent replicates.

To attempt to differentiate interfacial protein adsorption (which is particularly problematic for biomaterials fouling[48]) and protein absorption into the bulk of the hydrogel, confocal microscopy was used to image the cross-section of the thin film hydrogels following interaction with FITC-albumin (**Figure 6.5**). The confocal images in general showed significantly more FITC-albumin absorption in the high OEGMA fraction hydrogels, consistent with the protein uptake results (**Figure 6.4**) and the increased swelling observed in these hydrogels (**Figure 6.3**). However, hydrogels prepared with precursor polymers containing a 90:10 DMAPS:OEGMA ratio exhibited both very minimal fluorescence at both the interface of the hydrogel (significantly lower than that observed even with the 100% DMAPS hydrogel) as well as within the bulk, suggesting some potential benefit of mixing DMAPS and OEGMA precursors for promoting protein adsorption.

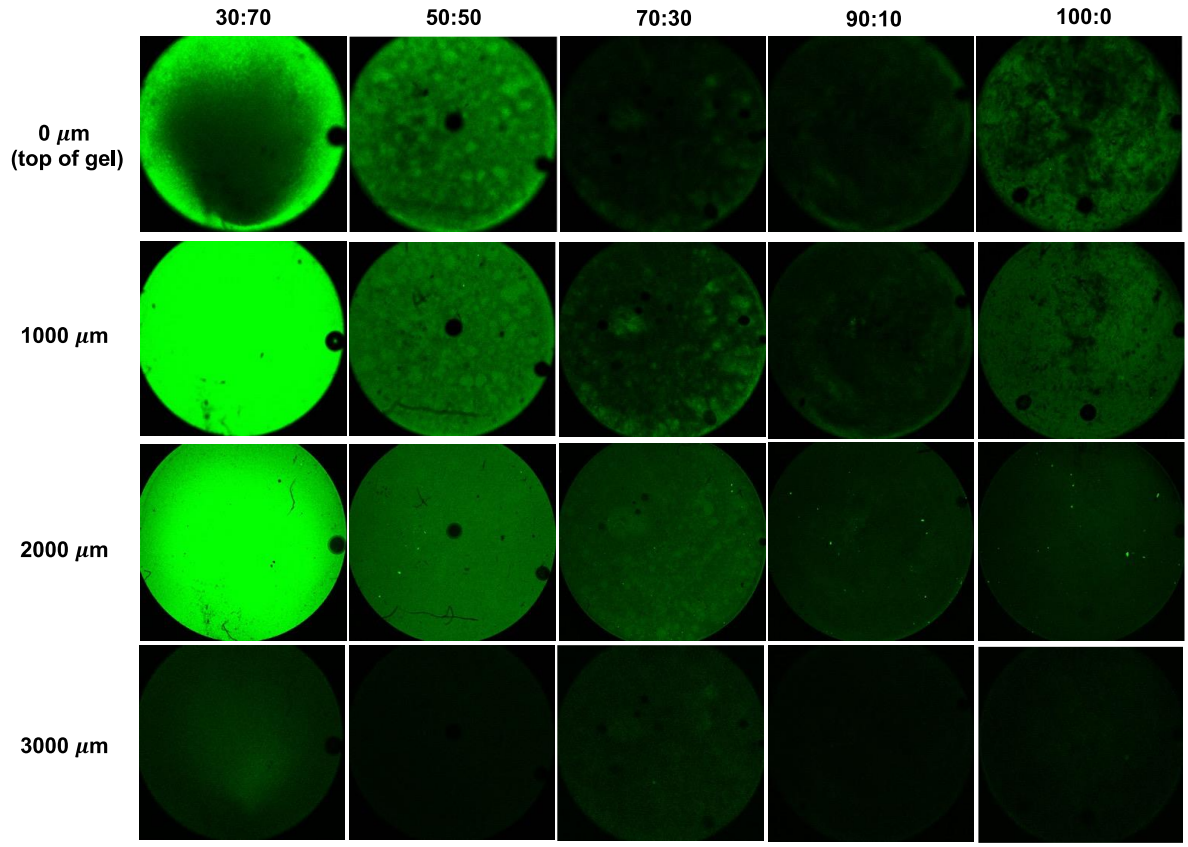

Figure 6.5: Confocal microscopy of images of DMAPS-OEGMA hydrogels prepared with 20 wt% hydrazide polymers containing varying DMAPS:OEGMA ratios crosslinked with 10 wt% 100:0 DMAPS-OEGMA-Ald following 4 h of incubation with 1 mg/mL FITC-albumin.

6.3.7 Coagulation Studies

To assess if this apparent reduced interfacial protein adsorption observed with the 90:10 DMAPS:OEGMA hydrogel correlated with improved practical anti-fouling performance, the time to clot formation (**Figure 6.6A**) and the kinetics of thrombin generation (**Figure 6.6B**) were assessed by exposing pooled normal human plasma to thin film DMAPS-OEGMA hydrogels; the thrombograms in **Figure 6.6B** were then used to assess the peak thrombin (**Figure 6.6C**) and time to peak thrombin (**Figure 6.6D**) to quantitatively compare the materials responses.

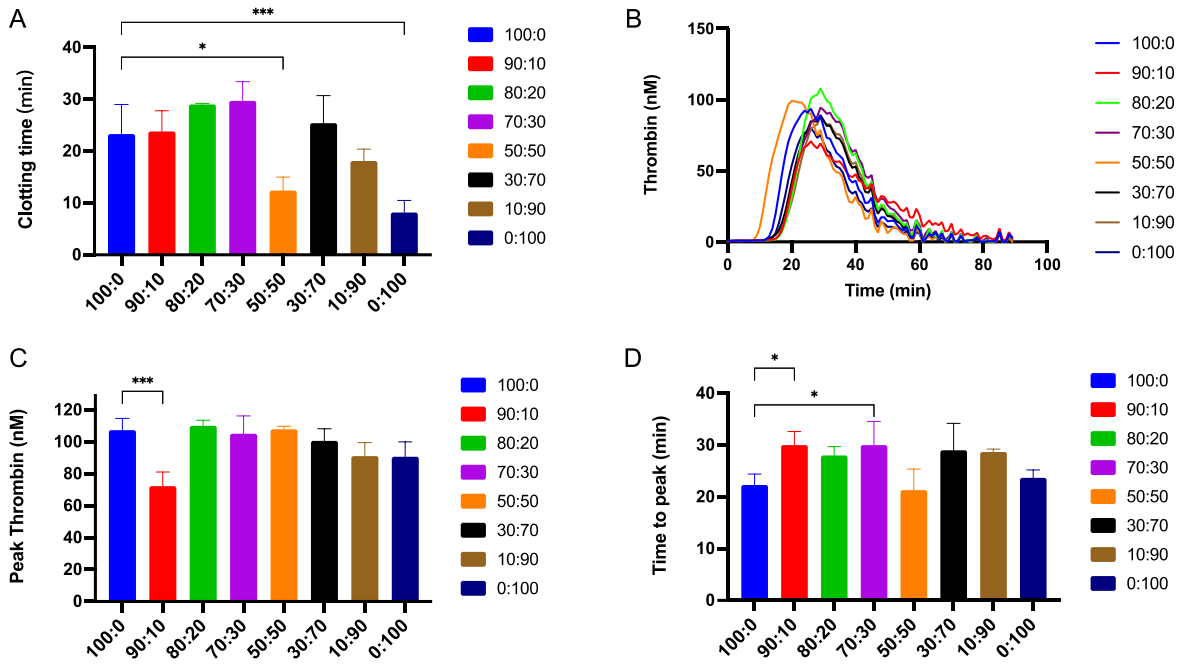

Figure 6.6: Responses of DMAPS-OEGMA hydrogels prepared with 20 wt% hydrazide polymers containing varying DMAPS:OEGMA ratios crosslinked with 10 wt% 100:0 DMAPS-OEGMA-Ald when exposed to pooled human blood plasma: (A) clotting time; (B) thrombograms from the thrombin generation assay; (C) peak thrombin analysis (maximum thrombin level from panel (B)); and (D) time to peak thrombin analysis (time at which peak thrombin was expressed from panel (B)). Error bars represent the standard deviations of three independent replicates. One-way ANOVA was performed at 95% confidence to assess significance in comparisons.

Hydrogels prepared with higher DMAPS:OEGMA ratios showed no significant differences in clotting times; however, hydrogels prepared with 50:50 or 0:100 DMAPS:OEGMA ratios induced clotting significantly faster than the DMAPS-rich hydrogels, with the general trend being faster coagulation as the OEGMA fraction in the hydrogel was increased (**Figure 6.6A**). From the thrombograms (**Figure 6.6B**), the 90:10 DMAPS:OEGMA ratio hydrogels showed significantly lower peak thrombin level compared to all other hydrogel formulations (**Figure 6.6C**); furthermore, the 90:10 (and the 70:30) DMAPS:OEGMA ratios showed significant increases in the time to the peak thrombin compared to the control DMAPS hydrogels (**Figure 6.6D**). Both these results indicate that the 90:10 DMAPS:OEGMA ratio hydrogels have significantly better anticoagulant properties compared to DMAPS-only or OEGMA-only hydrogels. Coupling these results with the confocal microscopy results showing the lower interfacial protein adsorption facilitated by the 90:10 DMAPS:OEGMA hydrogel, the results collectively suggest that introducing a small fraction of OEGMA monomers into a zwitterionic polymer can enhance anti-fouling properties. We speculate that this improvement is due to the

introduction of functional groups that can structure water molecules both by hydrogen bonding (OEGMA) as well as dipole-induced dipole interactions (DMAPS), resulting in improved interfacial water binding and thus anti-fouling; at the same time, the still dominant zwitterion mole fraction can promote zwitterion fusion interactions that minimize hydrogel swelling and thus suppress total protein uptake.

6.3.8 Miscibility Enhancement

To assess whether the incorporation of small OEGMA fractions can not only improve anti-fouling properties but also address the phase separation challenges associated with mixing highly salt-responsive zwitterionic polymers with other water-soluble polymers (particularly ionic polymers), miscibility tests were performed by mixing hydrazide-functionalized 90:10 DMAPS:OEGMA or 100:0 DMAPS:OEGMA (at a concentration of 10 wt% in 0.9% saline) with multiple carbohydrates (at a concentration of 2 wt% in 0.9% saline) of potential interest for fabricating tissue scaffolds (**Figure 6.7**): sodium hyaluronate (HA, a key glycosaminoglyan that can promote cell spreading[52]), dextran (Dex, commonly used as an anticoagulant[53]), sodium carboxymethyl cellulose (CMC, commonly incorporated due to its ability to enhance scaffold mechanics[54]), and sodium alginate (Alg, commonly used to facilitate cell-compatible gels upon mixing with calcium[55]). The miscibility of linear poly(ethylene glycol (PEG, broadly used to form protein-repellant tissue scaffolds with varying mechanics[56]) was also included for reference.

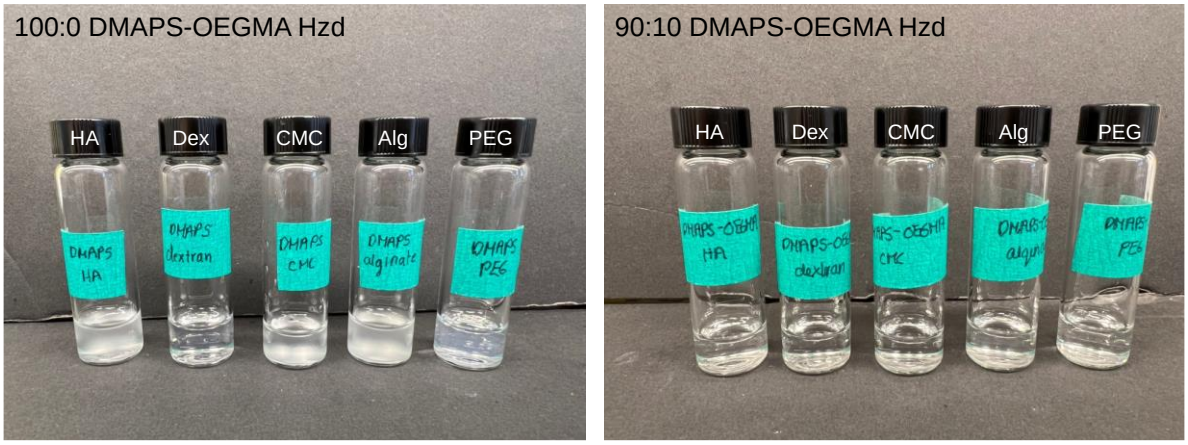

Figure 6.7: Comparison of the miscibility of common building blocks of tissue scaffolds (HA = sodium hyaluronate, Dex = dextran, CMC = sodium carboxymethyl cellulose, Alg = sodium alginate, and PEG = poly(ethylene glycol), all at 2 wt%) with 100:0 DMAPS-OEGMA Hzd (10 wt%) or 90:10 DMAPS-OEGMA Hzd (10 wt%).

As seen qualitatively in **Figure 6.7**, the miscibility of ionic carbohydrate salts such as sodium hyaluronate, sodium carboxymethyl cellulose and sodium alginate significantly improved when mixed with the 90:10 DMAPS:OEGMA polymer compared to the DMAPS-only polymer; in comparison, no significant phase separation was observed for the neutral dextran and poly(ethylene glycol) polymers, although the slight opacity observed in the PEG mixture with DMAPS-only polymer was fully resolved upon mixing with the 90:10 DMAPS:OEGMA polymer consistent with the introduction of a small number of miscible ethylene oxide repeat units in the copolymer. As such, incorporating a small fraction of OEGMA into a zwitterionic polymer backbone not only improves anti-fouling/anti-clotting properties but also significantly reduces the salting out of zwitterionic polymers when mixed with ionic polysaccharides. Coupling this result with the reduced peak thrombin and significantly lower protein adsorption/absorption achievable, the 90:10 DMAPS:OEGMA hydrogel offers key benefits to the fabrication of more biofunctional hydrogels for tissue engineering applications.

6.4 Conclusions

Hydrazide and aldehyde-functionalized random copolymers of zwitterionic DMAPS and PEG-based OEGMA can be successfully synthesized and used as building blocks for anti-fouling *in situ*-gelling hydrogel fabrication. High-OEGMA hydrazone-crosslinked hydrogels showed more pronounced swelling and increased protein adsorption compared to the high-DMAPS hydrogels, attributed to the steric hindrance of the longer side chains within the polymer backbone. Combining the results from the single protein adsorption assay, confocal microscopy probing the absorption versus adsorption properties of the different hydrogels, and coagulation studies using human plasma, hydrogels produced from precursor polymers with a 90:10 DMAPS:OEGMA ratio showed significant benefits relative to DMAPS-only and OEGMA-only hydrogels in terms of reducing protein adsorption/absorption as well as suppressing coagulation, a result attributed to potential synergy between the different mechanisms OEGMA (hydrogen bonding) and DMAPS (dipole-induced dipole interactions) use to bind interfacial water. Furthermore, the incorporation of even the small 10 mol% fraction of OEGMA into the polymer backbones significantly improved the miscibility of a range of ionic carbohydrates with the zwitterionic DMAPS-based precursor polymers, a significant benefit for introducing biological cues for directing cell behavior into the anti-fouling and long-lasting DMAPS-based hydrogels. In this context, we anticipate this work to have potential

benefits in creating cell-based therapeutics in which both maintaining high cell viability as well as avoiding fibrotic responses are critical.

6.5 Acknowledgements

The Natural Sciences and Engineering Research Council (Discovery Grant RGPIN-2017-06455 to TH) and a Canada Graduate Scholarship (to EM) are acknowledged for funding. Fei Xu is acknowledged for her help with the confocal microscopy images.

6.6 References

1. Chung, L.; Maestas Jr, D. R.; Housseau, F.; Elisseeff, J. H., Key players in the immune response to biomaterial scaffolds for regenerative medicine. *Adv. Drug Deliv. Rev.* **2017,** *114*, 184-192.
2. Franz, S.; Rammelt, S.; Scharnweber, D.; Simon, J. C., Immune responses to implants–a review of the implications for the design of immunomodulatory biomaterials. *Biomaterials* **2011,** *32* (28), 6692-6709.
3. Anderson, J. M.; Rodriguez, A.; Chang, D. T. Foreign body reaction to biomaterials, Seminars in immunology. *Elsevier*, **2008**, 86-100.
4. Mariani, E.; Lisignoli, G.; Borzì, R. M.; Pulsatelli, L., Biomaterials: foreign bodies or tuners for the immune response? *Int. J. Mol. Sci.* **2019,** *20* (3), 636.
5. Brash, J. L.; Horbett, T. A.; Latour, R. A.; Tengvall, P., The blood compatibility challenge. Part 2: Protein adsorption phenomena governing blood reactivity. *Acta Biomater.* **2019,** *94*, 11-24.
6. Kalasin, S.; Santore, M. M., Non-specific adhesion on biomaterial surfaces driven by small amounts of protein adsorption. *Coll. Surfaces B: Biointerfaces* **2009,** *73* (2), 229-236.
7. Sugiura, S.; Edahiro, J.-i.; Sumaru, K.; Kanamori, T., Surface modification of polydimethylsiloxane with photo-grafted poly (ethylene glycol) for micropatterned protein adsorption and cell adhesion. *Coll. Surfaces B: Biointerf.* **2008,** *63* (2), 301-305.
8. Wang, M. S.; Palmer, L. B.; Schwartz, J. D.; Razatos, A., Evaluating protein attraction and adhesion to biomaterials with the atomic force microscope. *Langmuir* **2004,** *20* (18), 7753-7759.
9. Deligianni, D. D.; Katsala, N.; Ladas, S.; Sotiropoulou, D.; Amedee, J.; Missirlis, Y., Effect of surface roughness of the titanium alloy Ti–6Al–4V on human bone marrow cell response and on protein adsorption. *Biomaterials* **2001,** *22* (11), 1241-1251.
10. Lord, M. S.; Foss, M.; Besenbacher, F., Influence of nanoscale surface topography on protein adsorption and cellular response. *Nano Today* **2010,** *5* (1), 66-78.
11. VandeVondele, S.; Vörös, J.; Hubbell, J. A., RGD-grafted poly-l-lysine-graft-(polyethylene glycol) copolymers block non-specific protein adsorption while promoting cell adhesion. *Biotechnol. Bioeng.* **2003,** *82* (7), 784-790.
12. Huang, N.-P.; Michel, R.; Voros, J.; Textor, M.; Hofer, R.; Rossi, A.; Elbert, D. L.; Hubbell, J. A.; Spencer, N. D., Poly (L-lysine)-g-poly (ethylene glycol) layers on metal oxide surfaces: surface-analytical characterization and resistance to serum and fibrinogen adsorption. *Langmuir* **2001,** *17* (2), 489-498.
13. Latour, R. A., Fundamental principles of the thermodynamics and kinetics of protein adsorption to material surfaces. *Coll. Surfaces B: Biointerf.* **2020,** *191*, 110992.
14. Rosso, M.; Nguyen, A. T.; de Jong, E.; Baggerman, J.; Paulusse, J. M.; Giesbers, M.; Fokkink, R. G.; Norde, W.; Schroën, K.; Rijn, C. J. v., Protein-repellent silicon nitride surfaces: UV-induced formation of oligoethylene oxide monolayers. *Appl. Mater. Interfaces* **2011,** *3* (3), 697-704.
15. Chen, S.; Li, L.; Zhao, C.; Zheng, J., Surface hydration: Principles and applications toward low-fouling/nonfouling biomaterials. *Polymer* **2010,** *51* (23), 5283-5293.
16. Li, L.; Wang, N.; Jin, X.; Deng, R.; Nie, S.; Sun, L.; Wu, Q.; Wei, Y.; Gong, C., Biodegradable and injectable in situ cross-linking chitosan-hyaluronic acid based hydrogels for postoperative adhesion prevention. *Biomaterials* **2014,** *35* (12), 3903-3917.
17. Zhang, P.; Sun, F.; Liu, S.; Jiang, S., Anti-PEG antibodies in the clinic: Current issues and beyond PEGylation. *J. Control. Rel.* **2016,** *244*, 184-193.

18. Ladd, J.; Zhang, Z.; Chen, S.; Hower, J. C.; Jiang, S., Zwitterionic polymers exhibiting high resistance to nonspecific protein adsorption from human serum and plasma. *Biomacromol.* **2008,** *9* (5), 1357-1361.
19. Lowe, A. B.; McCormick, C. L., Synthesis and solution properties of zwitterionic polymers. *Chem. Rev.* **2002,** *102* (11), 4177-4190.
20. Hart, R.; Timmerman, D., New polyampholytes: The polysulfobetaines. *J. Polym. Sci.* **1958,** *28* (118), 638-640.
21. Nakai, S.; Nakaya, T.; Imoto, M., Polymeric phospholipid analog, 10. Synthesis and polymerization of 2-(methacryloyloxy) ethyl 2-aminoethyl hydrogen phosphate. *Macromol. Chem. Phys.* **1977,** *178* (10), 2963-2967.
22. Ladenheim, H.; Morawetz, H., A new type of polyampholyte: Poly (4-vinyl pyridine betaine). *J. Polym. Sci.* **1957,** *26* (113), 251-254.
23. Wu, J.; Lin, W.; Wang, Z.; Chen, S.; Chang, Y., Investigation of the hydration of nonfouling material poly (sulfobetaine methacrylate) by low-field nuclear magnetic resonance. *Langmuir* **2012,** *28* (19), 7436-7441.
24. Wu, J.; Chen, S., Investigation of the hydration of nonfouling material poly (ethylene glycol) by low-field nuclear magnetic resonance. *Langmuir* **2012,** *28* (4), 2137-2144.
25. Yuan, J.; Huang, X.; Li, P.; Li, L.; Shen, J., Surface-initiated RAFT polymerization of sulfobetaine from cellulose membranes to improve hemocompatibility and antibiofouling property. *Polym. Chem.* **2013,** *4* (19), 5074-5085.
26. Chang, Y.; Liao, S.-C.; Higuchi, A.; Ruaan, R.-C.; Chu, C.-W.; Chen, W.-Y., A highly stable nonbiofouling surface with well-packed grafted zwitterionic polysulfobetaine for plasma protein repulsion. *Langmuir* **2008,** *24* (10), 5453-5458.
27. Seetho, K.; Zhang, S.; Pollack, K. A.; Zou, J.; Raymond, J. E.; Martinez, E.; Wooley, K. L., Facile synthesis of a phosphorylcholine-based zwitterionic amphiphilic copolymer for anti-biofouling coatings. *Macro Lett.* **2015,** *4* (5), 505-510.
28. Chang, Y.; Shih, Y. J.; Lai, C. J.; Kung, H. H.; Jiang, S., Blood-inert surfaces via ion-pair anchoring of zwitterionic copolymer brushes in human whole blood. *Adv. Funct. Mater.* **2013,** *23* (9), 1100-1110.
29. Huang, K.-T.; Fang, Y.-L.; Hsieh, P.-S.; Li, C.-C.; Dai, N.-T.; Huang, C.-J., Zwitterionic nanocomposite hydrogels as effective wound dressings. *J. Mater. Chem. B* **2016,** *4* (23), 4206-4215.
30. Doncom, K. E.; Willcock, H.; O'Reilly, R. K., The direct synthesis of sulfobetaine-containing amphiphilic block copolymers and their self-assembly behavior. *Euro. Polym. J.* **2017,** *87*, 497-507.
31. Liu, S.; Tang, J.; Ji, F.; Lin, W.; Chen, S., Recent Advances in Zwitterionic Hydrogels: Preparation, Property, and Biomedical Application. *Gels* **2022,** *8* (1), 46.
32. Wen, C.; Guo, H.; Yang, J.; Li, Q.; Zhang, X.; Sui, X.; Cao, M.; Zhang, L., Zwitterionic hydrogel coated superhydrophilic hierarchical antifouling floater enables unimpeded interfacial steam generation and multi-contamination resistance in complex conditions. *Chem. Eng. J.* **2021,** *421*, 130344.
33. Tran, T.; Pan, S.; Chen, X.; Lin, X.-C.; Blevins, A. K.; Ding, Y.; Lin, H., Zwitterionic hydrogel-impregnated membranes with polyamide skin achieving superior water/salt separation properties. *Appl. Mater. Interfaces* **2020,** *12* (43), 49192-49199.
34. Yang, W.; Xue, H.; Carr, L. R.; Wang, J.; Jiang, S., Zwitterionic poly (carboxybetaine) hydrogels for glucose biosensors in complex media. *Biosens. Bioelectr.* **2011,** *26* (5), 2454-2459.
35. Fang, K.; Wang, R.; Zhang, H.; Zhou, L.; Xu, T.; Xiao, Y.; Zhou, Y.; Gao, G.; Chen, J.; Liu, D., Mechano-responsive, tough, and antibacterial zwitterionic hydrogels

with controllable drug release for wound healing applications. *Appl. Mater. Interfaces* **2020,** *12* (47), 52307-52318.
36. He, H.; Xiao, Z.; Zhou, Y.; Chen, A.; Xuan, X.; Li, Y.; Guo, X.; Zheng, J.; Xiao, J.; Wu, J., Zwitterionic poly (sulfobetaine methacrylate) hydrogels with optimal mechanical properties for improving wound healing in vivo. *J. Mater. Chem. B* **2019,** *7* (10), 1697-1707.
37. Chan, H.-M.; Erathodiyil, N.; Wu, H.; Lu, H.; Zheng, Y.; Ying, J. Y., Calcium cross-linked zwitterionic hydrogels as antifouling materials. *Mater. Today Comm.* **2020,** *23*, 100950.
38. Zhang, L.; Cao, Z.; Bai, T.; Carr, L.; Ella-Menye, J.-R.; Irvin, C.; Ratner, B. D.; Jiang, S., Zwitterionic hydrogels implanted in mice resist the foreign-body reaction. *Nat. Biotechnol.* **2013,** *31* (6), 553-556.
39. Zhang, Y.; Liu, S.; Li, T.; Zhang, L.; Azhar, U.; Ma, J.; Zhai, C.; Zong, C.; Zhang, S., Cytocompatible and non-fouling zwitterionic hyaluronic acid-based hydrogels using thiol-ene "click" chemistry for cell encapsulation. *Carbohydr. Polym.* **2020,** *236*, 116021.
40. Oh, J.; Jung, K. I.; Jung, H. W.; Khan, A., A modular and practical synthesis of zwitterionic hydrogels through sequential amine-epoxy "click" chemistry and n-alkylation reaction. *Polymers* **2019,** *11* (9), 1491.
41. Pan, Z.; Dorogin, J.; Preciado Rivera, N.; Hoare, T. "In Situ Gelling Zwitterionic Hydrogel Compositions, and Methods of Use Thereof". PCT Priority Patent Application PCT/CA2021/050731, filed May 28, 2021
42. Hildebrand, V.; Laschewsky, A.; Päch, M.; Müller-Buschbaum, P.; Papadakis, C. M., Effect of the zwitterion structure on the thermo-responsive behaviour of poly (sulfobetaine methacrylates). *Polym. Chem.* **2017,** *8* (1), 310-322.
43. Chen, H.; Wang, Z. M.; Ye, Z. B.; Han, L. J., The solution behavior of hydrophobically associating zwitterionic polymer in salt water. *J. Appl. Polym. Sci.* **2014,** *131* (1), 39707.
44. Leng, C.; Han, X.; Shao, Q.; Zhu, Y.; Li, Y.; Jiang, S.; Chen, Z., In situ probing of the surface hydration of zwitterionic polymer brushes: structural and environmental effects. *J. Phys. Chem. C* **2014,** *118* (29), 15840-15845.
45. Zhang, Z.; Moxey, M.; Alswieleh, A.; Morse, A. J.; Lewis, A. L.; Geoghegan, M.; Leggett, G. J., Effect of salt on phosphorylcholine-based zwitterionic polymer brushes. *Langmuir* **2016,** *32* (20), 5048-5057.
46. Smeets, N. M.; Bakaic, E.; Patenaude, M.; Hoare, T., Injectable and tunable poly(ethylene glycol) analogue hydrogels based on poly(oligoethylene glycol methacrylate). *Chem. Comm.* **2014,** *50* (25), 3306-3309.
47. Clark, A.; Taylor, M. E.; Panzer, M. J.; Cebe, P., Interactions between ionic liquid and fully zwitterionic copolymers probed using thermal analysis. *Thermo. Acta.* **2020,** *691*, 178710.
48. Jesmer, A. H.; Wylie, R. G., Controlling Experimental Parameters to Improve Characterization of Biomaterial Fouling. *Front. Chem.* **2020,** *8*, 604236.
49. Estephan, Z. G.; Schlenoff, P. S.; Schlenoff, J. B., Zwitteration as an alternative to PEGylation. *Langmuir* **2011,** *27* (11), 6794-6800.
50. Racovita, S.; Trofin, M.-A.; Loghin, D. F.; Zaharia, M.-M.; Bucatariu, F.; Mihai, M.; Vasiliu, S., Polybetaines in biomedical applications. *Int. J. Molec. Sci.* **2021,** *22* (17), 9321.
51. Laschewsky, A., Structures and synthesis of zwitterionic polymers. *Polymers* **2014,** *6* (5), 1544-1601.

52. Mandal, K.; Raz-Ben Aroush, D.; Graber, Z. T.; Wu, B.; Park, C. Y.; Fredberg, J. J; Janmey, P. A. Soft hyaluronic gels promote cell spreading, stress fibers, focal adhesion, and membrane tension by phosphoinositide signaling, not traction force. *Nano* **2018**, *13*(1), 203-214.
53. Nehal, F.; Sahnoun, M.; Smaoui, S.; Jaouadi, B.; Bejar, S.; Mohammed, S., Characterization, high production and antimicrobial activity of exopolysaccharides from Lactococcus lactis F-mou. *Microb. Pathogenesis*, **2019,** *132*, 10-19.
54. Zennifer, A.; Senthilvelan, P.; Sethuraman, S.; Sundaramurthi, D., Key advances of carboxymethyl cellulose in tissue engineering & 3D bioprinting applications. *Carbohyd. Polym.*, **2021,** *256*, 117561.
55. Axpe, E.; Oyen, M. L; Applications of alginate-based bioinks in 3D bioprinting. *Int. J. Mol. Sci.*, **2016,** *17*(12), 1976.
56. Patel, N. R.; Whitehead, A. K.; Newman, J. J.; Caldorera-Moore, M. E., Poly (ethylene glycol) hydrogels with tailorable surface and mechanical properties for tissue engineering applications. *Biomater. Sci. Eng.*, **2017,** *3*(8), 1494-1498.

6.7 Supplementary Information

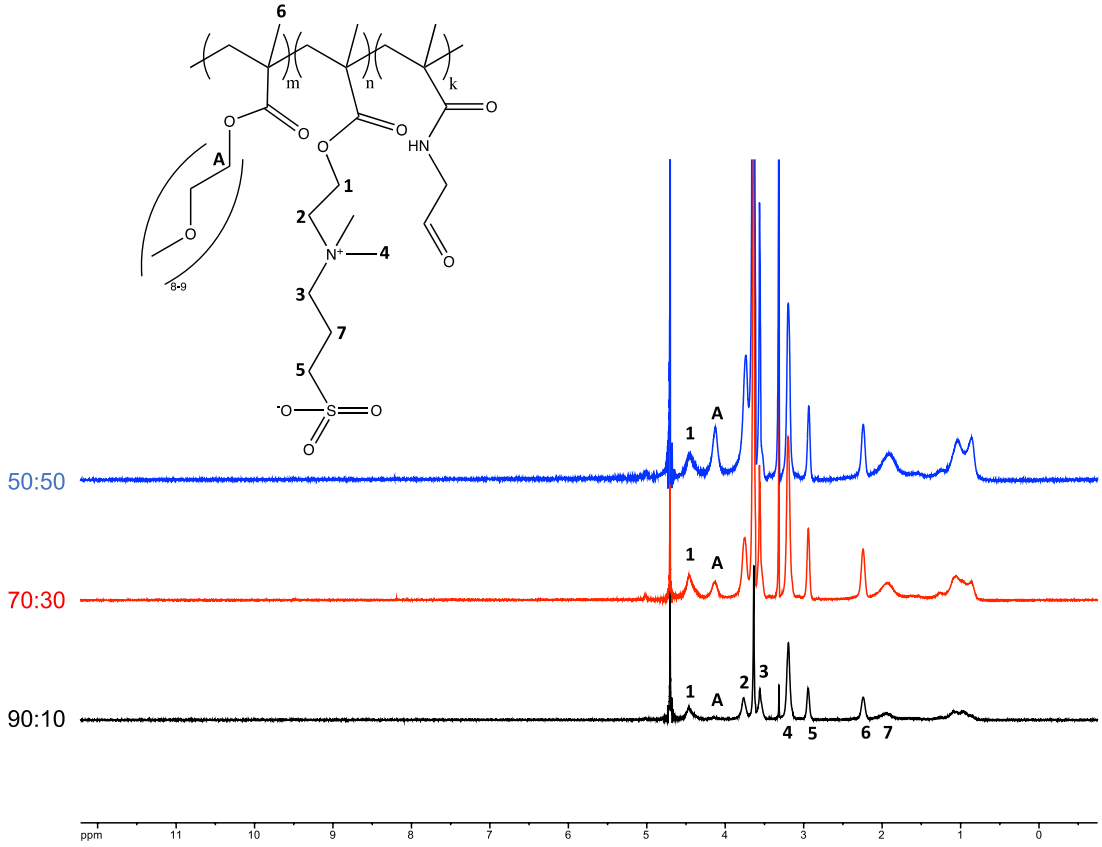

Figure S6.1: Representative ^{1}H NMR of aldehyde-functionalized DMAPS-OEGMA polymers prepared at different DMAPS:OEGMA ratios

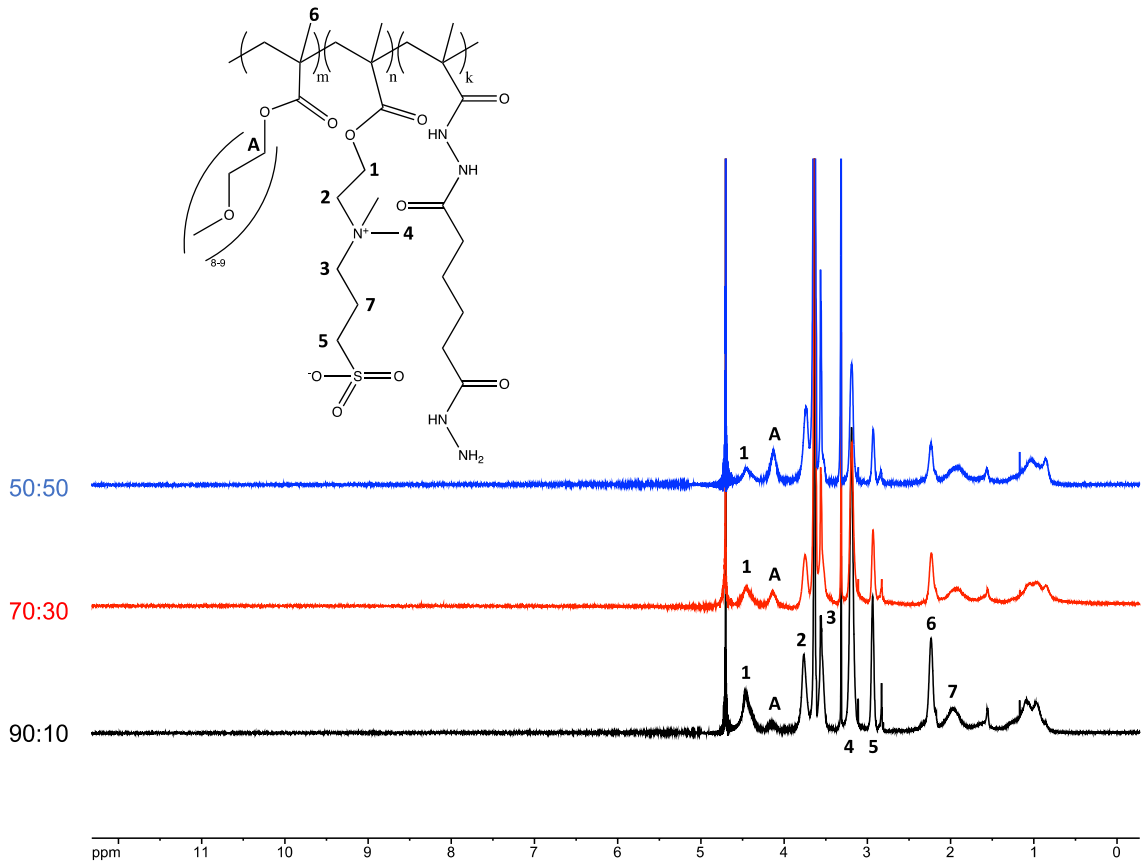

Figure S6.2: Representative ^{1}H NMR of hydrazide-functionalized DMAPS-OEGMA polymers prepared at different DMAPS:OEGMA ratios

Table S6.1: Gelation kinetics for hydrogels prepared by mixing 20 wt% DMAPS-OEGMA Ald/Hzd (24 hours total testing time)

Hydrogel Formulation	Gelation Time (min)
100:0 DMAPS-OEGMA-Ald + 100:0 DMAPS-OEGMA-Hzd	<1
90:10 DMAPS-OEGMA-Ald + 90:10 DMAPS-OEGMA-Hzd	3
80:20 DMAPS-OEGMA-Ald + 80:20 DMAPS-OEGMA-Hzd	4
70:30 DMAPS-OEGMA-Ald + 70:30 DMAPS-OEGMA-Hzd	4
50:50 DMAPS-OEGMA-Ald + 50:50 DMAPS-OEGMA-Hzd	Did not gel
30:70 DMAPS-OEGMA-Ald + 30:70 DMAPS-OEGMA-Hzd	Did not gel
10:90 DMAPS-OEGMA-Ald + 10:90 DMAPS-OEGMA-Hzd	Did not gel
0:100 DMAPS-OEGMA-Ald + 0:100 DMAPS-OEGMA-Hzd	Did not gel

CHAPTER 7

3D Printing of Interpenetrating Zwitterionic Dynamic Covalent Hydrogels and Calcium-Alginate Hydrogels for the Fabrication of Longer-Lasting Implants

Eva Mueller, Norma Garza, Melaina del Grosso, Todd Hoare

Declaration of Academic Achievement:

Norma Garza helped with the experimental design and printability experiments. Melaina del Grosso conducted the mechanical comparison study and printability experiments. The analysis and manuscript preparation were completed by Eva Mueller, with help from Dr. Todd Hoare.

3D Printing of Interpenetrating Zwitterionic Dynamic Covalent Hydrogels and Calcium-Alginate Hydrogels for the Fabrication of Longer-Lasting Implants

Eva Mueller, Norma Garza, Melaina del Grosso, Todd Hoare

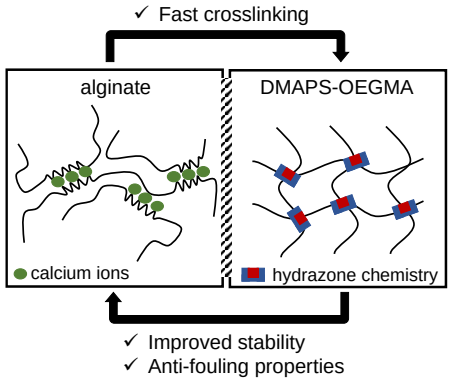

Alginate hydrogels have been used extensively in extrusion bioprinting applications due to their low cost, low toxicity, and mild gelation with calcium that is harmless to cells. However, for implantable tissue constructs, calcium-alginate based inks offer insufficient stability and anti-fouling properties. Herein, we report hydrazide and aldehyde-functionalized copolymers based on a zwitterionic sulfobetaine monomer and a poly(ethylene glycol) analogue that are miscible with sodium alginate, facilitating the fabrication of an interpenetrating network hydrogel that can provide both increased stability (due to the *in situ* covalent hydrazone crosslinking facilitated upon mixing the two functional copolymers) and improved anti-fouling properties (due to the zwitterionic polymer composition) to 3D printed tissue constructs. The resulting interpenetrating network hydrogels maintained a compressive modulus of 6-8 kPa over 7 days, an optimal range for liver tissue engineering. Furthermore, the hydrogel is shown to be useful as a bioink for extrusion-based 3D printing in which the rapid gelation of calcium-alginate gives sufficient time for the hydrazone copolymer interpenetrating network to form; co-printing with HepG2 carcinoma cells maintained high cell viability (>85%) over a two-week culture period without significant reductions in the structural or mechanical integrity of the printed structure. As such, the zwitterionic/alginate interpenetrating bioink can address the gelation time challenges with synthetic polymer-based bioinks while potentially improving fibrotic responses.

Keywords: hydrogels, anti-fouling, 3D bioprinting, dynamic covalent chemistry, FRESH bioprinting

7.1 Introduction

3D printing of hydrogel scaffolds with well-defined shapes and dimensions offers significant potential to custom-print soft scaffolds with mechanics, chemistries, and micro/nanostructures that better mimic native extracellular matrix (ECM) and thus better enable the functional regeneration of diseased tissues. Hydrogel-based bioinks can be based on natural or synthetic polymers (or a combination thereof) and are most typically crosslinked using photocrosslinking[1] (i.e., gelatin methacrylate, poly(ethylene glycol diacrylate)), thermoresponsive gelation[2] (i.e., gelatin, collagen, Pluronics), or ionic crosslinking[3] (i.e., alginate) (or combinations thereof). 3D bioinks based on ionic alginate-calcium crosslinking chemistry have been widely applied for *in vitro* screening (i.e., drug discovery) applications[4, 5] based on the low cost, low toxicity, and mild cytocompatible gelation conditions required for ionic alginate crosslinking[6]. However, for implantable tissue constructs, calcium-alginate based bioinks offer significant drawbacks in terms of both stability and anti-fouling properties[7, 8]. In the former case, ion exchange of calcium from the gel in the high salt *in vivo* environment can lead to significant and often rapid degradation of the gel[6, 9]; while the use of heavier divalent ions (i.e., barium, strontium) and/or higher divalent cation concentrations can slow this exchange and thus the gel degradation process[10], there is a limit to the stability of any small divalent cation crosslinked hydrogel upon implantation. In the latter case, non-specific protein adsorption activates the inflammatory cascade that ultimately can trigger fibrosis and/or rejection of implanted biomaterials[11], a particular challenge in implantable cell therapeutics in which even a mild fibrotic response can sufficiently suppress the transport of nutrients in (and cell metabolites out) of the implanted scaffold and thus render the cell therapeutic non-functional. As such, developing strategies to leverage the excellent printability of calcium-alginate bioinks to create more stable and anti-fouling hydrogels are an urgent need in 3D bioink development.

Zwitterionic materials are a class of materials containing both negative and positive charges (typically in close proximity)[12, 13] that exhibit exceptionally high water binding capacity due to the potential of the fixed and proximate charges in the material to locally structure water and thus inhibit protein adsorption[14, 15]. Zwitterionic hydrogels have been demonstrated to show beneficial properties in the contexts of antifouling coatings[16], membrane separations[17], biosensing[18], drug delivery[19], and tissue engineering[20] based on this key property. More recently, zwitterionic hydrogels have become an attractive biomaterial choice for 3D

bioprinting applications due to their high water retention, tunable soft mechanics, and low-fouling properties[21, 22]. Nevertheless, the lack of a facile crosslinking strategy to enable the rapid gelation of zwitterionic hydrogels akin to the calcium-alginate interaction (as is required for effective extrusion-based bioprinting) as well as the brittleness of most zwitterionic hydrogels have limited their practical use as bioinks[23, 24]. Indeed, the successful 3D printing strategies involving zwitterionic hydrogels (summarized in **Table 7.1**) have focused on blending zwitterionic polymers with other polymers and/or copolymerizing with a different monomer to balance the mechanical stability with the desired anti-fouling and anti-fibrotic properties, leading to bioinks showing evidence of good printability, mechanical strength, and adequate anti-fouling properties *in vitro*[21, 25-28]. However, each of the previously reported zwitterionic polymer-based bioinks require non-physiological crosslinking conditions (*i.e.*, the use of low-wavelength light) and the use of potentially cytotoxic photoinitiators and/or photopolymerizable functional groups to induce gelation and/or achieve the necessary mechanical strength[29, 30]. In addition, the long-term and *in vivo* anti-fibrotic effects of such bioinks have in most cases yet to be elucidated.

Table 7.1: Summary of literature reports of the use of zwitterionic hydrogels for modulating foreign body responses in 3D bioprinting applications

Bioink composition	Crosslinking mechanism	Printing technique	Application	Results	Ref.
Poly (carboxybetaine acrylamide) + tyramine acrylamide	Enzymatic + Photo-crosslinking	Extrusion	Encapsulation of human chondrocytes	• Facilitated diffusion and cell-cell interactions • 90% cell viability maintained • Enhanced ECM production and tissue maturation • *In vitro* (21 days)	25
Poly(sulfobetaine methacrylate microspheres, N-isopropylacrylamide	Photo-crosslinking	Extrusion	Regeneration of articular cartilage defects	• Shear-thinning and self-healing properties • High cell viability and maintenance of stemness • Efficient chondrogenic, osteogenic and adipogenic differentiation • *In vivo* (8 weeks)	21
Carboxybetaine methacrylamide + α,ω-methacrylate poly(d,l-lactide-block-ethylene glycolblock-d,l-lactide)	Photo-crosslinking	Stereolithography	Protein immobilization to induce specific cell adhesión	• Fast diffusion of nutrient and waste product • Bovine serum albumin-specific immobilization in hydrogel pores • *In vitro* (14 h)	26
Acrylamide + [2-(methacryloyloxy)ethyl] dimethyl(3-sulfopropyl) ammonium hydroxide	Ionic- + photo-crosslinking	Optical stereolithography	N/A, proof-of-concept study	• Enhanced moduli, ultimate strain, and rapid gelation • Decreased BSA adsorption • *In vitro* (6 h)	27
Laponite clay + (N-(3-sulfopropyl)-Nmethacroyloxyethyl-N,N-dimethylammonium betaine	Photo-crosslinking	Extrusion	Development of neuronal scaffolds	• Thixotropic and shear thinning behaviour • Material showed cues for axonal guidance • No cytotoxicity to a neuroblastoma cell line • *In vitro* (72 h)	28

As an alternative, click chemistry-based hydrogel bioinks have attracted extensive recent attention in extrusion bioprinting applications[31, 32]. Click (or click-like) chemistries including hydrazone chemistry[33], imine chemistry[34], boronate esters[35], and strain-promoted azide-alkyne cycloaddition (SPAAC)[36] have attracted particular interest for bioink design. In this context, we have recently reported FRESH bioprinting of poly(oligoethylene glycol methacrylate) (POEGMA)-based oligomers with molecular weights below the renal filtration limit (<40 kDa) functionalized with hydrazide or aldehyde/ketone groups, with the resulting hydrazone-crosslinked networks offering the advantages of tunable gelation times and (slow) degradation of the hydrazone bond over time to regenerate the oligomeric starting materials and thus allow the hydrogel to be excreted[37, 38]. Hydrogels of this type based on zwitterionic-based materials thus may offer particularly attractive properties as bioinks as they induce low inflammation

and non-specific adsorption while being simple to chemically modify; however, the common salting-out of zwitterionic polymers, as described in **Chapter 6**, when mixed with ionic polymers such as sodium alginate represents a significant limitation to combining the fast-gelation of calcium-alginate with the beneficial anti-fouling properties of zwitterionic polymers. **Chapter 6** described the fabrication of copolymers of oligo(ethylene glycol methacrylate) and 2-(methacryloyloxy)ethyl]dimethyl-(3-sulfopropyl)ammonium hydroxide (DMAPS-OEGMA) in which we demonstrated the miscibility of alginate with a 90 mol% DMAPS/10 mol% OEGMA copolymer, offering a potential solution to this dichotomy and enabling the potential combination of the fast calcium-alginate ionic interactions with anti-fouling and covalent hydrazone-crosslinked DMAPS-OEGMA networks to create an improved functional bioink.

Herein, we leverage this miscibility of DMAPS-OEGMA copolymers with sodium alginate to fabricate a dual dynamic covalent/ionic crosslinked hydrogel bioink that can be successfully printed using the embedded bioprinting approach. The fast ionic crosslinking and good cytocompatibility of calcium chloride-crosslinked sodium alginate hydrogels combined with the increased stability and the improved anti-fouling properties of hydrazone dynamic covalent DMAPS-OEGMA copolymers are demonstrated to result in a bioink capable of meeting multiple key requirements for practical *in vivo* use.

7.2 Experimental Section

7.2.1 Materials

Poly(ethylene glycol) methacrylate (OEGMA, M_n = 500 g/mol, Sigma-Aldrich) [2-(methacryloyloxy)ethyl]dimethyl-(3-sulfopropyl)ammonium hydroxide (DMAPS, Sigma-Aldrich), , thioglycolic acid (TGA, Sigma-Aldrich, 98%), acrylic acid (AA, Sigma-Aldrich, 99%), ammonium persulfate (APS, Sigma-Aldrich), adipic acid dihydrazide (ADH, Alfa Aesar, 98%), N′-ethyl-N-(3-(dimethylamino)propyl)-carbodiimide (EDC, Carbosynth, Compton CA, commercial grade), and sodium alginate (Sigma Aldrich) were all used as received. The aldehyde[38] and ketone monomer syntheses (**Chapter 5, Figure S5.1**) were conducted as previously described. Milli-Q grade distilled deionized water (DIW) was used for all experiments. HepG2 carcinoma cells were purchased from ATCC (Cedarlane Laboratories, Burlington, ON). Dulbecco's Modified Eagle's Medium (DMEM, ThermoFisher), penicillin−streptomycin (ThermoFisher), fetal bovine serum (FBS, ThermoFisher),

trypsin−EDTA solution (Sigma-Aldrich), and phosphate buffered saline (1× PBS, ThermoFisher) were all used as received. For the coagulation assays, the pooled normal plasma (PNP) was generously donated from the lab of Dr. Jeffrey Weitz. Calcium chloride ($CaCl_2$, Sigma Aldrich), HEPES buffer (Gibco, pH 7.4) and z-GGR-AMC thrombin substrate (Z-Gly-Gly-Arg-AMC, Bachem, Switzerland) were used as received. LifeSupport (#5244, Advanced Biomatrix) was purchased and used as per the manufacturer's instructions.

7.2.2 Polymer Synthesis

The functional copolymers based on DMAPS and OEGMA were synthesized at a theoretical molar ratio of 90:10 (DMAPS: OEGMA), with 30 mol% of the total number of monomers bearing either a hydrazide or aldehyde/ketone functional group. Briefly, hydrazide functionalized DMAPS-OEGMA precursor polymers (DMAPS-OEGMA-Hzd) were synthesized by dissolving DMAPS (3.6 g), OEGMA (0.72 g), AA (0.44 g), APS (40 mg), and TGA (10 μL) in 20 mL Milli-Q water and polymerizing at 75℃ overnight under nitrogen and magnetic stirring. The conversion of acrylic acid moieties to hydrazide was facilitated by adding ADH (1.38 g) and EDC (0.62 g) and mixing the resulting solution for 4 hours at a constant pH of ~4.7. The final polymer was then dialyzed against a 3.5 kDa molecular weight cut-off (MWCO) membrane over 6 cycles (6+ hours), lyophilized, and stored dry at room temperature. Aldehyde- and ketone-functionalized DMAPS-OEGMA precursor polymers (DMAPS-OEGMA-Ald and DMAPS-OEGMA-Ket) were synthesized by dissolving DMAPS (3.6 g), OEGMA (0.72 g), aldehyde monomer (N-(2,2-dimethoxyethyl)methacrylamide, DMEMAm, 1.06 g) or ketone monomer (2-methyl-N-[(2-methyl-1,3-dioxolan-2-yl)methyl]-2-propenamide,1.14 g), APS (40 mg) and TGA (10 μL) in 20 mL Milli-Q water and polymerizing at 75℃ overnight under nitrogen and magnetic stirring. The resulting DMAPS-OEGMA-Ald and DMAPS-OEGMA-Ket polymers were then exposed to 100 mL 1 M HCl for 24 hours to hydrolyze the acetal protecting group and expose the active aldehyde or ketone group, after which the final polymer was dialyzed against a 3.5 kDa MWCO membrane over 6 cycles (6+ hours), lyophilized, and stored dry at room temperature.

7.2.3 Polymer Characterization

The polymers were characterized using aqueous size exclusion chromatography and ^{1}H NMR. Aqueous size exclusion chromatography (SEC) was performed on a system consisting of a Waters 515 HPLC pump, a Waters 717 Plus autosampler, three Ultrahydrogel columns (30 cm × 7.8 mm i.d.; exclusion limits: 0–3 kDa, 0–50 kDa, 2–300 kDa), and a Waters 2414 refractive

index detector. A mobile phase consisting of 0.3 M sodium nitrate and 0.05 M phosphate buffer (pH 7) at a flow rate of 0.8 mL/min was used for all polymers analyzed.

7.2.4 Rheological Properties

The rheological properties of the polymer precursors and the crosslinked hydrogels were measured using a DHR Rheometer (TA Instruments). Viscosity sweeps were performed over a shear rate range of 0.1 to 100 1/s at 25°C. Frequency sweeps were performed at 25°C between 0.1 and 100 rad/s at a strain of 1% (conditions confirmed via an initial stress sweep to lie within the linear viscoelastic range) to assess the shear storage modulus of the hydrogels. For each of the tested hydrogel formulations (DMAPS-OEGMA-Hzd/Ket, calcium-crosslinked hydrogels, and the dual-crosslinked DMAPS-OEGMA-alginate), the hydrogel formulations were pre-mixed in an Eppendorf tube, mixed manually for 30 seconds, pipetted onto the rheometer stage, and allowed to gel for30 minutes to ensure complete crosslinking has occurred prior to the rheological testing.

7.2.5 Anti-Fouling Properties

Plasma clotting and thrombin generation assays were performed on three hydrogel formulations to compare the anti-clotting properties: (1) DMAPS-OEGMA-only hydrogels prepared by mixing 0.2 mL of 7 wt% ketone and hydrazide functionalized precursor polymer solutions prepared in 0.9% saline in an Eppendorf vial for 30 seconds and then adding 50 μL of the pre-mixed uncrosslinked hydrogel to each well of a 96 well plate; (2) calcium-crosslinked sodium alginate hydrogel prepared by crosslinking 50 μL of 2 wt% sodium alginate with 150 μL of 0.1 wt% calcium chloride directly in the well; and (3) dual-crosslinked DMAPS-OEGMA-alginate prepared using 14 wt% solutions of ketone and hydrazide-functionalized DMAPS-OEGMA in xxxx and 4 wt% of sodium alginate, which when mixed in equal volume ratios create a hydrogel in which each polymer concentration was equal to that used in the single-component hydrogels). The dual-crosslinked hydrogel was formed by pre-mixing 0.2 mL of 4 wt% sodium alginate, 0.1 mL of 14 wt% hydrazide functionalized DMAPS-OEGMA, and 0.1 mL of 14 wt% ketone functionalized DMAPS-OEGMA in an Eppendorf tube, mixing manually for 30 seconds, and then adding 50 μL of the pre-mixed formulation to each well, after which 150 μL of 0.1 wt% calcium chloride was added to induce ionic crosslinking. All hydrogels were then left overnight to ensure equilibrium gelation, after which 200 μL of 0.9% saline was added to allow the hydrogels to fully swell prior to conducting the plasma clotting and thrombin generation assays. For the plasma clotting assay, 80 μL of 20

mM HEPES pH 7.4 buffer was added to each well containing the samples. 100 μL of human plasma was then added, and the entire plate was incubated at 37℃ for 15 minutes without shaking. Finally, 20 μL of 260 mM $CaCl_2$ was added simultaneously to each well in the multi-well plate using a multi-channel pipette. The absorbance was subsequently tracked at 405 nm for 1 hour at 37℃. For the thrombin generation assay, 100 μL of human plasma was added, and the plate was incubated at 37℃ for 15 minutes without any shaking. During this incubation period, a master mix was prepared that included $CaCl_2$ (15 mM), z-GGR-AMC thrombin substrate (1 mM) and HEPES buffer, pH 7.4 (20 mM). Following incubation, 100 μL of the master mix was then added simultaneously to each well using a multi-channel pipette and the fluorescence was tracked (excitation: 360 nm, emission: 460 nm) over 90 min at 37℃ with 1 min intervals. From the collected data points, a thrombogram was generated from which both the peak thrombin concentration as well as the time required to reach that peak could be extracted.

7.2.6 Printing Experiments

12x12 mm lattice structures with 16 square holes were printed with and without cells using the FRESH printing method. The gelation bath was first prepared by hydrating lyophilized LifeSupport (1 g) in 12 mL of either cold PBS or a PBS solution containing the crosslinking agents (0.1 wt% calcium chloride and/or 2 mL of 20 wt% DMAPS-OEGMA-Ald). The resulting suspension was thoroughly mixed by vigorous shaking and then hydrated for 10 min at 4℃. The hydrated slurry was centrifuged twice at 1000 x *g* for 5 min to yield the targeted rheological properties for successful 3D printing. The resulting sterile support bath was equally distributed in 2-4 wells of a 12-well plate for printing experiments. Printing trials were conducted using three approaches that are summarized in **Figure 7.1** using the ink combinations summarized in **Table 7.2**: 1) full embedded printing in which either alginate and DMAPS-OEGMA-Hzd are extruded into a support bath containing calcium chloride or functional DMAPS-OEGMA-Ald, respectively; 2) pre-mixed printing in which the slower-gelling pair of DMAPS-OEGMA-Hzd and DMAPS-OEGMA-Ket is pre-mixed in a single syringe and printed prior to gelation, resulting a single hydrazone-crosslinked network; and 3) a combined approach with embedded printing in which an ink formulation comprised of the DMAPS-OEGMA-Hzd and DMAPS-OEGMA-Ket gelling pair mixed together with sodium alginate is printed into a calcium chloride-containing support bath, creating a dual-crosslinked network based on both ionic and dynamic covalent crosslinks.

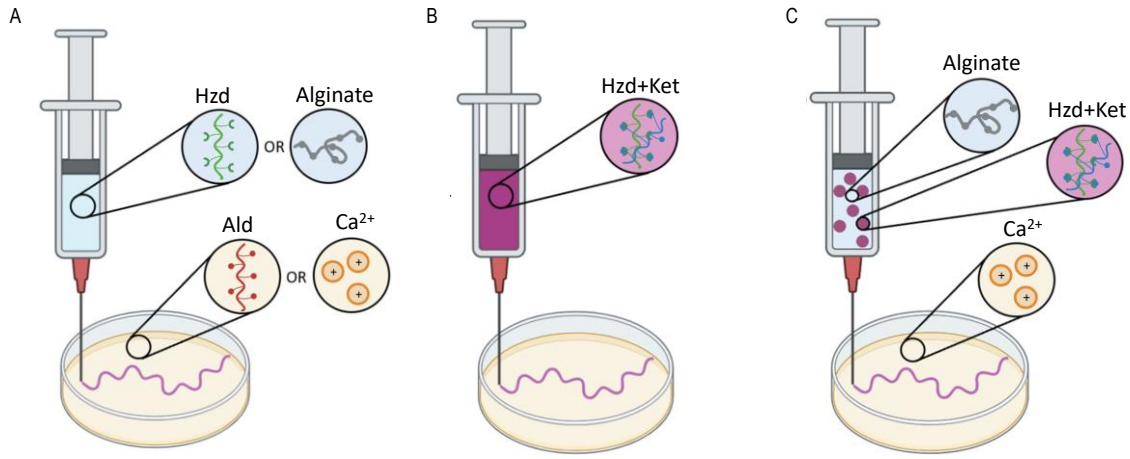

Figure 7.1: Schematic of the printing experiments using the gelatin support bath: (A) embedded printing with the aldehyde-functionalized polymer and/or calcium chloride in the support bath; (B) pre-mixed printing in which the slow-gelling DMAPS-OEGMA-Ket/Hzd pair are pre-mixed and extruded into the unmodified support bath; (C) pre-mixed printing in which the DMAPS-OEGMA-Ket/Hzd gelling pair is mixed with alginate and extruded into a support bath supplemented with calcium chloride.

Table 7.2: Ink formulations used for FRESH printing with the gelatin support bath

Printing Method	Dual Crosslinking	Ionic Crosslinking	Covalent Crosslinking
Embedded	No	--	DMAPS-OEGMA-Hzd/Ald
Embedded	No	2wt% Alginate 0.1wt% $CaCl_2$	--
Pre-Mixed	No	--	DMAPS-OEGMA-Hzd/Ket
Embedded + Pre-Mixed	Yes	2wt% Alginate 0.1wt% $CaCl_2$	DMAPS-OEGMA-Hzd/Ket
Embedded	Yes	2wt% Alginate 0.1wt% $CaCl_2$	DMAPS-OEGMA-Hzd/Ald

7.2.7 Mechanical Analysis

The compressive moduli of the printed lattice structures were measured with the CellScale Microsquisher using a 6×6 mm platen and a 0.56 mm diameter cantilever. Cyclic compression testing was performed at 2.5, 5, 7.5 and 10% strain using sequential compress-hold-recover steps. The average hold force was calculated and divided over the platen area to calculate the stress. All measurements were conducted in triplicate, with error bars representing the standard deviation of three independently printed scaffolds.

7.2.8 Cell Culture and Cytocompatibility Evaluation

HepG2 cells were cultured in DMEM medium with 10% FBS and 1% penicillin−streptomycin to ~80% confluency at 37°C and 5% CO_2 before subsequent use. The cytotoxicity of the functional DMAPS-OEGMA polymers was measured over a concentration range of 0.25 to 1 mg/mL using a PrestoBlue Cell Viability Assay (ThermoFisher) after 24 hours of incubation of the polymers at 37°C. HepG2 cells were plated at a density of 1.0 x 10^4 cells per well in a 96-well plate, and the cell viability was assessed by fluorescence (excitation 560 nm, emission 590 nm) using a plate reader; results were normalized to metabolism measured in the cell-only (no material exposure) wells. Cell viability within the printed hydrogel scaffolds was assessed using a live/dead staining assay (ThermoFisher) based on the manufacturer's instructions.

7.2.9 Microscope Analysis

Confocal laser scanning microscopy (CLSM, Nikon A1R HD25) was used to track the viability of printed cells within the 3D printed structures over time. A 10× 0.45 NA objective and laser lines at 488 nm and 561 nm were used to image the live/dead assay results.

7.3 Results and Discussion

7.3.1 Polymer Characterization

Three functional polymers based on DMAPS and OEGMA were synthesized with either hydrazide, aldehyde, or ketone functional groups (20 mol% target degree of functionalization in each case). The molar ratio of DMAPS:OEGMA was kept constant at 90:10 due to the improved miscibility with carbohydrates such as alginate that was observed at this DMAPS:OEGMA ratio coupled with the improved anti-fouling/anti-thrombotic properties of this hydrogel formulation, as discussed in **Chapter 6**. The DMAPS-OEGMA polymers exhibited consistent molecular weights (M_n ~ 10 kDa, as measured via gel permeation chromatography, **Table 7.3**) and DMAPS:OEGMA ratios and functional group concentrations close to the 90:10 and 20 mol% theoretical targets from the recipes (as measured via ^{1}H NMR spectroscopy, **Figure S7.1**). None of the precursor polymers exhibited significant cytotoxicity upon exposure of HepG2 carcinoma cells to the precursor polymers at concentrations up to 1 mg/mL (**Figure 7.2**), showing the high cytocompatibility of all the potential precursor polymers. Gelation kinetics (as measured via the vial inversion test, **Table 7.4**) could be varied significantly depending on the concentration of the precursor polymers as well as the type of

electrophile (aldehyde or ketone) used for gelation, with gelation times ranging from <1 minute (for hydrazide-aldehyde crosslinking) to ~12 minutes (for hydrazide-ketone crosslinking) easily achievable using starting polymer concentrations in the range of 7-10 wt%. Such a range of gelation kinetics, possible given the control over the polymer properties enabled with synthetic polymer chemistry, is highly beneficial for optimizing different types of printing strategies; a slower gelation time (>10 minutes) is required for the pre-mixed printing strategy to give sufficient time to mix the precursors, load the syringe on the printer, and print the desired print volume while a faster gelation time is preferred for the embedded printing strategy as it prohibits the printed ink from spreading into the support bath. The inclusion of sodium alginate in the bioink significantly slows the gelation kinetics as it sterically inhibits the hydrazone crosslinking chemistry; as such, to achieve reasonable gelation times for pre-mixed printing in the presence of 2 wt% or 4 wt% alginate (<15 minutes), hydrazide and ketone polymer concentrations of 14 wt% were required.

Table 7.3: Polymer characterization

Theoretical Molar Ratios (DMAPS: OEGMA: Hzd/Ald/Ket	Functionality	DMAPS Molar Ratio	OEGMA Molar Ratio	Functional Group mol%	M_n (kDa)	Đ
72:8:20	Hzd	75	7	18	8.2	2.3
	Ald	73	11	16	7.1	2.2
	Ket	75	10	15	9.3	2.5

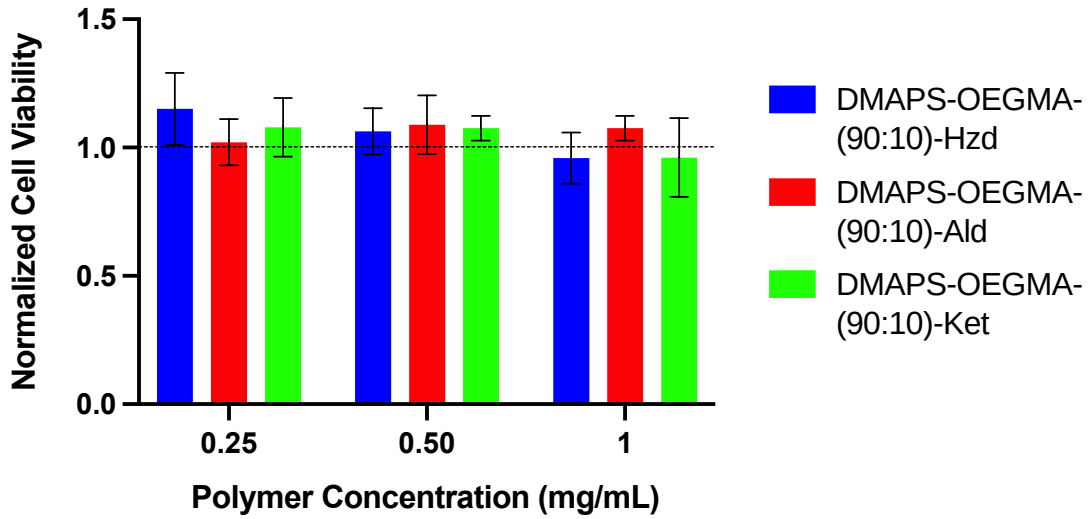

Figure 7.2: Polymer cytotoxicity of DMAPS-OEGMA (90:10)-Hzd, DMAPS-OEGMA (90:10)-Ald and DMAPS-OEGMA (90:10)-Ket at three concentrations to HepG2 cells.

Table 7.4: Gelation kinetics of (alginate)-DMAPS-OEGMA hydrogel ink formulations

Polymer Concentration (wt%)	Sodium Alginate (wt%)	DMAPS-OEGMA (90:10)-Hzd	DMAPS-OEGMA (90:10)-Ald	DMAPS-OEGMA (90:10)-Ket	Gelation Time (min)
10	x	✓	✓	x	<1
7	x	✓	x	✓	11
8	x	✓	x	✓	8
9	x	✓	x	✓	6
10	x	✓	x	✓	5
14	✓	✓	x	✓	14
14	✓	✓	x	✓	15

7.3.2 Rheological Properties of Hydrogel Bioinks

The rheological properties of the double network hydrogel ink formulations were tested to analyze how the addition of DMAPS-OEGMA-Hzd/Ket would change the rheological properties of alginate hydrogels crosslinked with 0.1 wt% $CaCl_2$ alone. **Figure 7.3** shows the viscosity sweeps and frequency sweeps of hydrogels produced using alginate alone (2 wt%), DMAPS-OEGMA-Hzd/Ket alone (7 wt%) and the double network hydrogel (DMAPS-OEGMA-alginate) prepared using 4 wt% alginate and 14 wt% DMAPS-OEGMA-Hzd/Ket polymers (concentrations that keep the final concentrations of each component in final hydrogel the same as the single-crosslinked hydrogels upon mixing of the two precursor solutions). The viscosity profiles (**Figure 7.3A**) were not significantly different between the alginate-only and DMAPS-OEGMA-only hydrogels; however, the double network hydrogel was less shear thinning over the range of shear rates tested, likely attributed to the interpenetrating nature of the ionic crosslinks mixed with the chemical hydrazone crosslinks. However, the elastic modulus of the DMAPS-OEGMA-only or DMAPS-OEGMA-alginate hydrogels was approximately one order of magnitude higher than that observed with the alginate-only hydrogel, highlighting that even at low polymer concentrations (7 wt% of the functional precursor polymers in the final double network formulation), the dynamic covalent network can add significant mechanical strength to the prints. In addition, the interpenetrating DMAPS-OEGMA/alginate hydrogel showed significantly less frequency dependence in its response relative to either the alginate-only or DMAPS-OEGMA-only hydrogels, showing the potential of the interpenetrating network to better absorb applied stress without undergoing significant structural changes (consistent with the shear thinning result in **Figure 7.3A**).

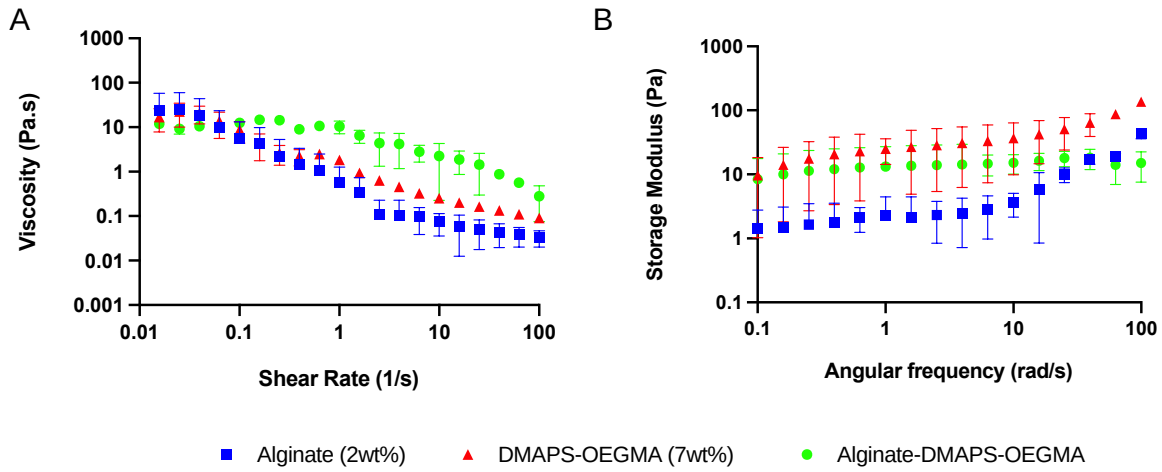

Figure 7.3: Rheological characterization of the three hydrogel inks used in the printing experiments (2 wt% alginate only, 7 wt% DMAPS-OEGMA Hzd/Ket only, and an interpenetrating network of 2 wt% alginate/7 wt% DMAPS-OEGMA Hzd/Ket): (A) viscosity sweeps; and (B) frequency sweeps in the linear viscoelastic range. Error bars represent the standard deviation of measurements on three independent replicate samples.

7.3.3 Improving the Anti-Fouling Properties

The anti-fouling and anti-coagulation properties of the three hydrogel inks (i.e., the DMAPS-OEGMA-Ket/Hzd hydrogel, the calcium-crosslinked sodium alginate, and the dual-crosslinked alginate-DMAPS-OEGMA) were compared and analyzed using blood plasma clotting and thrombin generation assays, the results of which are shown in **Figure S7.3**. While the DMAPS-OEGMA-only bioink significantly increased the clotting time, lowered the peak thrombin, and increased the time to the peak coagulation relative to alginate-only hydrogels, the combination alginate-DMAPS-OEGMA performed similarly to the alginate-only hydrogel, with only a slight (and not statistically significant) increase observed in the clotting time and no significant change in the thrombin expression. As such, based on clotting results alone, the interpenetrating DMAPS-OEGMA phase does not significantly suppress the inherent pro-clotting activity of the alginate hydrogel. However, when performing a single protein uptake experiment using FITC-labelled albumin (**Figure 7.4**), significantly lower protein uptake was recorded for the dual-crosslinked hydrogel, especially at the highest exposed protein concentration (1 mg/mL). Thus, while further experiments are required to further investigate the anti-fouling properties, the inclusion of the DMAPS-OEGMA interpenetrating hydrogel phase has apparent benefits in suppressing interfacial protein adsorption as is desired for creating anti-fouling implants.

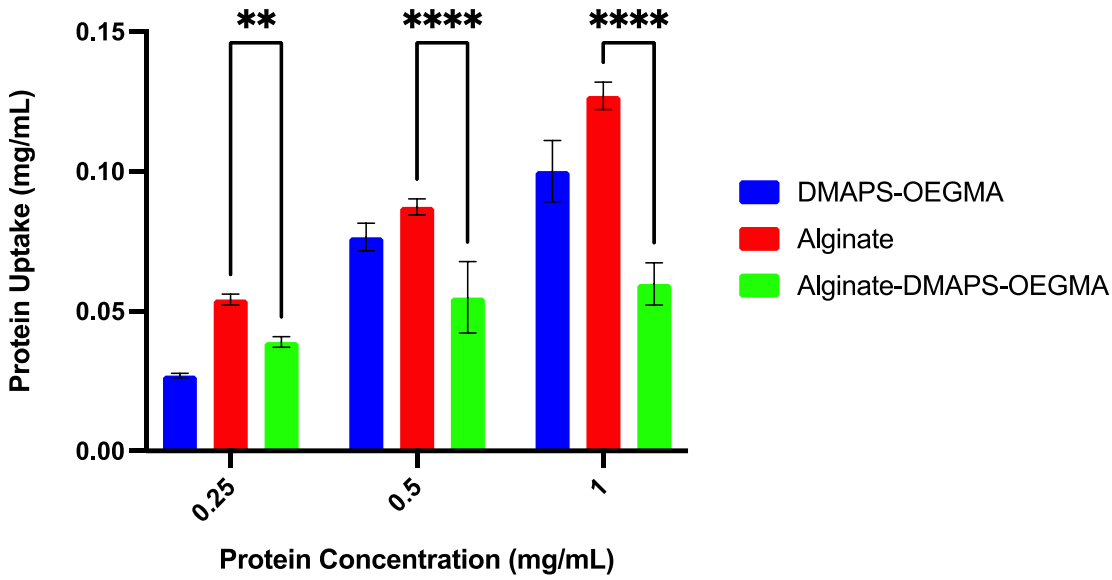

Figure 7.4: Protein uptake study using FITC-albumin to assess the anti-fouling properties of the three hydrogel inks used in the printing experiments (2 wt% alginate only, 7 wt% DMAPS-OEGMA Hzd/Ket only, and an interpenetrating network of 2 wt% alginate/7 wt% DMAPS-OEGMA Hzd/Ket). Error bars represent the standard deviation of three independent replicates. One-sided ANOVA is used at 95% confidence to assess statistical significance.

7.3.4 Printability of Dual-Crosslinked Hydrogels

The printability of the dual-crosslinked hydrogels based on the ionic crosslinking of calcium-crosslinked sodium alginate and covalent hydrazone crosslinking between hydrazide and ketone/aldehyde-functionalized DMAPS-OEGMA polymers was next investigated. As a preliminary study (**Figure S7.2**), three ratios of alginate:DMAPS-OEGMA-Hzd (3:1, 1:1, and 1:3) were selected and printed into a support bath containing both $CaCl_2$ and DMAPS-OEGMA-Ald. The printability results showed significantly better printability when higher ratios of sodium alginate were used, consistent with the alginate primarily driving gelation on a shorter time scale to prevent leaching of uncrosslinked polymer into the support bath prior to gelation. Next, the printability studies were extended to investigate the effect of printing strategy (**Table 7.2**) on the printability and stability of a printed grid pattern over one week of storage in cell media, with the resulting prints shown in **Figure 7.5**. Printing DMAPS-OEGMA-Hzd into a bath of DMAPS-OEGMA-Ald (column 1, Embedded DMAPS-OEGMA) achieves relatively poor print fidelity, with the gelation time insufficiently fast to prevent significant diffusion of the low viscosity printed DMAPS-OEGMA-Hzd bioink into the support bath. Direct printing of alginate into a calcium-supplemented support bath (column 2, Embedded alginate) yields much better initial print fidelity but is not stable over the one-week

observation period despite supplementing the media with 5 mM $CaCl_2$. Pre-mixing the DMAPS-OEGMA-Hzd and DMAPS-OEGMA-Ket polymers (column 3, Pre-mixed) yields much better shape fixity compared to printing the polymers using an embedded approach and the printed scaffold remains stable over the one week observation period, albeit with significant swelling. In comparison, when alginate is added to the pre-mixed DMAPS-OEGMA-Hzd/Ald ink and printed into a calcium-supplemented support bath (column 4, Embedded + Pre-mixed), significantly better shape fixity is achieved that can be sustained over the full 7 day observation period without significant swelling occurring, showing the benefits of using the dual ionic/covalent network crosslinking strategy. Significant improvements in shape fixity and scaffold stability could also be achieved using an all-embedded printing approach in which alginate and DMAPS-OEGMA-Hzd were printed into a calcium + DMAPS-OEGMA-Ald support bath (column 5, Embedded), albeit with imperfect print fidelity of the inner squares. As such, mixing calcium-alginate gelation with covalent dynamic crosslinking (irrespective of the print strategy) can improve the quality and stability of the prints relative to either hydrogel alone.

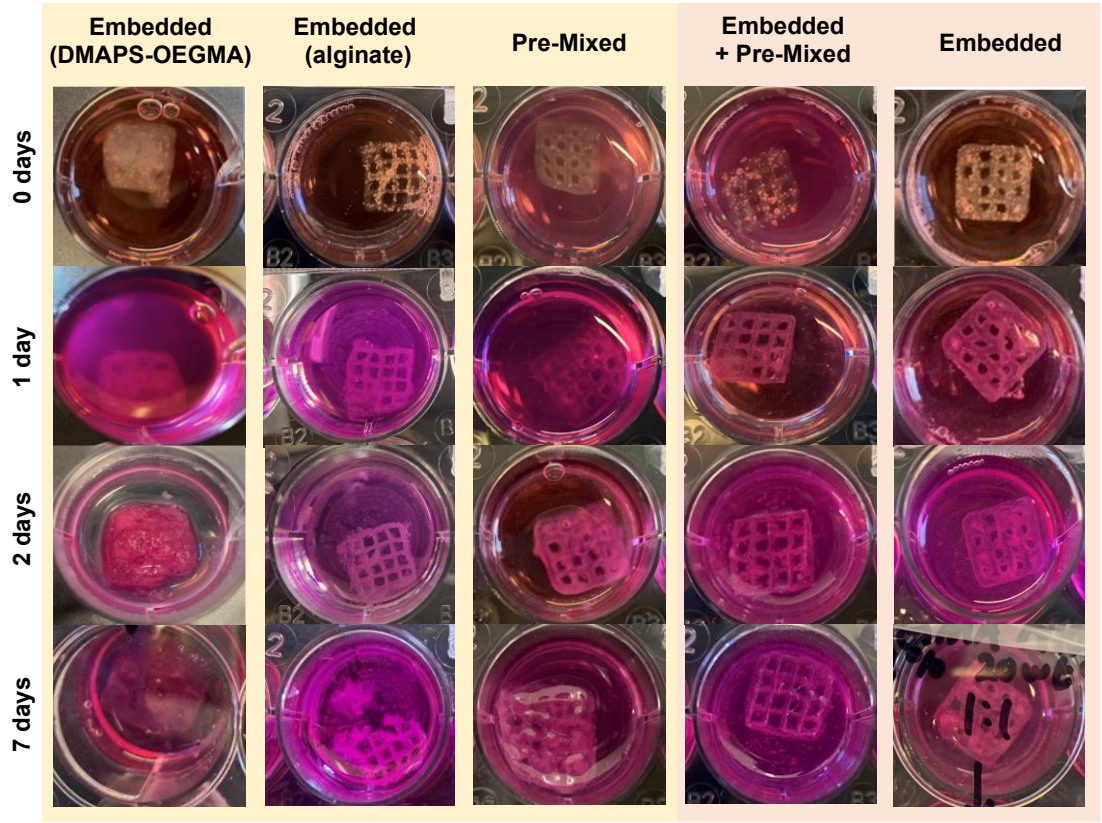

Figure 7.5: Printability and stability comparison for the different printing strategies (yellow = single crosslinked; orange = dual crosslinked) over 7 days of incubation in cell media supplemented with 5 mM $CaCl_2$.

7.3.5 Mechanics of Printed Lattice Structures

The mechanics of the printed lattice structures were analyzed and compared between the five printing strategies (embedded (DMAPS-OEGMA), embedded (alginate), control pre-mixed with DMAPS-OEGMA-Hzd/Ket, embedded and pre-mixed using both sodium alginate/calcium chloride with DMAPS-OEGMA-Hzd/Ket, and the dual-crosslinked embedded strategy using calcium-crosslinked sodium alginate with DMAPS-OEGMA-Hzd/Ald). The resulting compressive moduli of the printed scaffolds after 1, 2, and 7 days of incubation in cell media supplemented with 5 mM $CaCl_2$ are summarized in **Figure 7.6**.

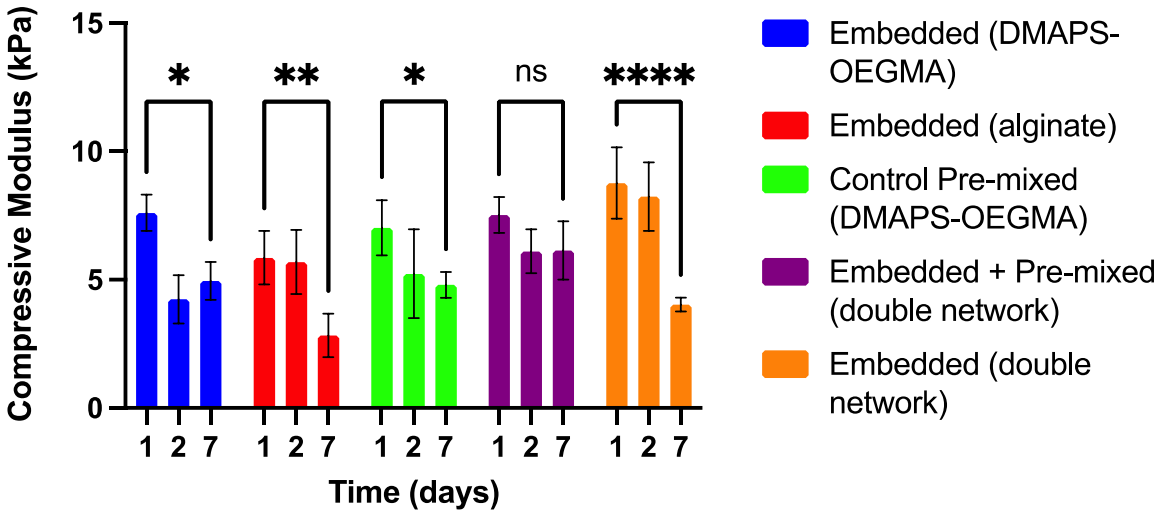

Figure 7.6: Compressive modulus of the hydrogel prints before and after 7 days of incubation in cell media supplemented with 5 mM $CaCl_2$. Error bars represent the standard deviation of three independent samples. One-sided ANOVA is used at 95% confidence to assess statistical significance.

All printed hydrogels had compressive moduli in the range of 2 to 10 kPa, highlighting the relevance of these printed constructs for application in liver tissue engineering[39]. However, significant differences in the compressive modulus development could be observed over the seven-day incubation period between prints fabricated using the different printing strategies. The alginate-only embedded hydrogels exhibited a ~50% decrease in compressive modulus from 1 to 7 days despite the addition of 5 mM $CaCl_2$ in the media which is not directly mimetic to a practical *in vivo* condition; this mechanical change is consistent with the poor print stability observed over this same time in the qualitative analysis in **Figure 7.6**. The DMAPS-OEGMA-only embedded and pre-mixed print showed a 30% decrease over the 7 days, although the final modulus was still ~5 kPa. The double network embedded strategy showed the highest initial

modulus (consistent with the high-density crosslinking observed at the print-support bath interface) but exhibited a similar ~50% decrease in modulus by day 7. In contrast, the alginate-DMAPS-OEGMA double network pre-mixed strategy resulted in a much more consistent modulus over time, showing both the highest modulus at day 7 (~7 kPa) and no significant change in the modulus over the full one-week incubation period consistent with the improved shape fixity observed with this strategy in the visual observations in **Figure 7.6**. As such, using the dual network strategy avoids the mechanical property degradation observed over time using either single network bioink, critical for providing proper long-term mechanical cues to cells and/or maintaining consistent porosities for ensuring continual immunoisolation of cells used for cell therapeutics.

7.3.6 Cell Viability in Bioprinted Constructs

To ensure that the dual-crosslinked hydrogel ink is a viable bioink for extrusion bioprinting applications, HepG2 carcinoma cells were co-printed using the pre-mixed/embedded double network strategy that showed the best shape fidelity, fixity, and mechanical stability in the printability screening trials (i.e., DMAPS-OEGMA-Hzd/Ket polymers pre-mixed with sodium alginate and extruded into a calcium chloride-supplemented gelatin support bath). 8 million cells/mL were co-printed and stained using a live/dead assay after day 1, 7 and 14, with the results shown in **Figure 7.7**. The results showcased not only the good printability of the lattice structure but also the high cytocompatibility of the scaffold, with >85% of live cells observed at day 1 following printing; furthermore, good cell proliferation and spreading were observed over the 14-day incubation period, suggesting the printed scaffolds were not only cell compatible but also supportive of cell growth.

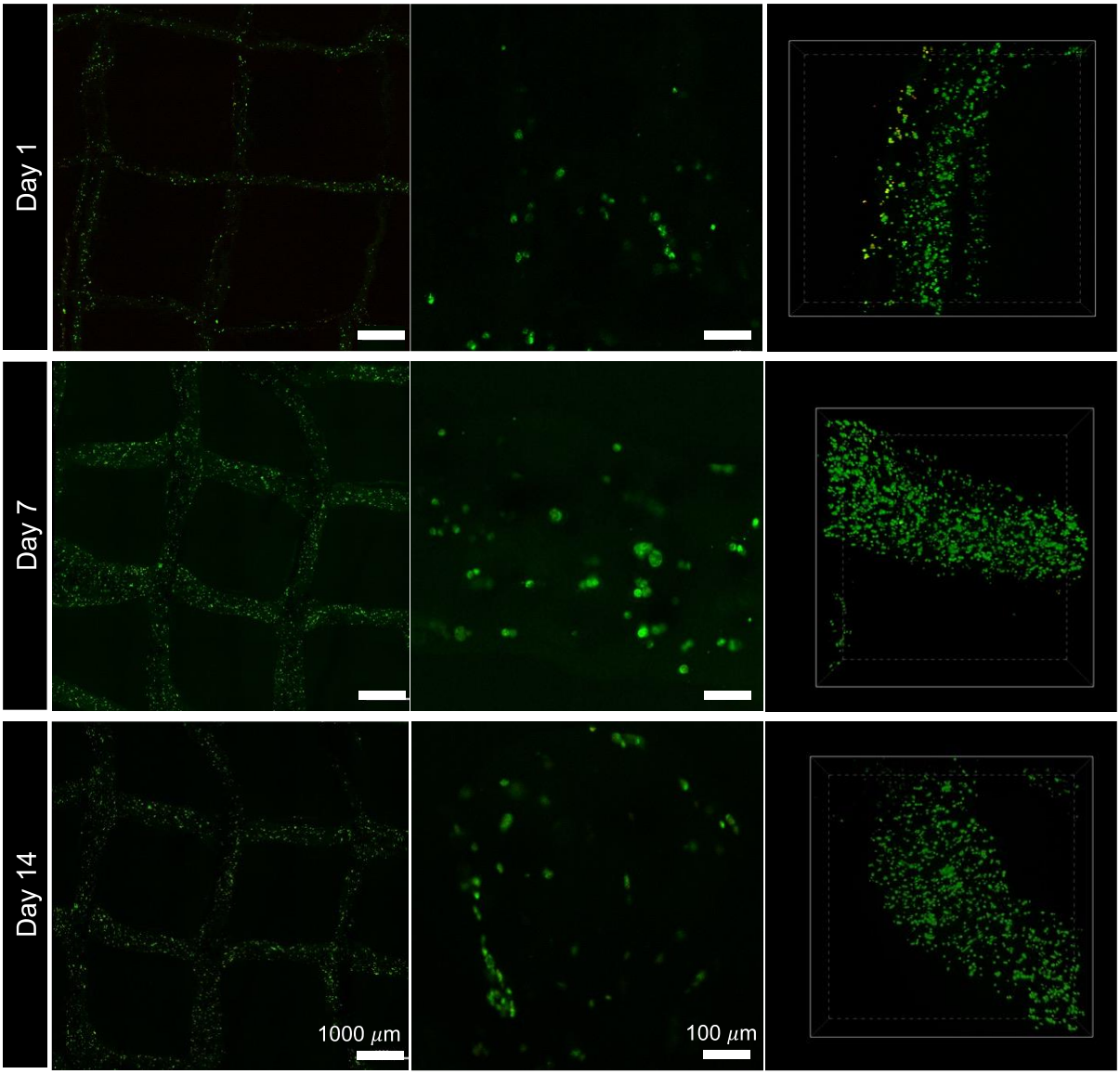

Figure 7.7: Live/dead assay showing cytocompatibility and cell proliferation of HepG2 cells printed in pre-mixed/embedded alginate-DMAPS-OEGMA hydrogel bioinks at day 1, 7 and 14 post-printing. The first column shows zoomed-out images (scale bar = 1000 μm), the second column shows zoomed-in images (scale bar = 100 μm), and the third column shows 3D stacks showcasing the density of the encapsulated HepG2 cells within the printed lattice structures.

7.4 Discussion

Double network hydrogels based on calcium-crosslinked alginate and hydrazone-crosslinked DMAPS-OEGMA hydrogels were fabricated to overcome two limitations that are present with conventional alginate hydrogels (i.e., poor stability over time and limited anti-fouling properties) while leveraging the fast crosslinking that occurs between calcium ions and sodium alginate to facilitate zwitterionic hydrogel bioprinting. While all hydrogels tested were shear-thinning (**Figure 7.3A**), the double network hydrogel was not as shear thinning over the range

of shear rates tested, likely attributed to the interpenetrating nature of the ionic crosslinks mixed with the chemical hydrazone crosslinks. However, the elastic modulus of the double network hydrogels was approximately one order of magnitude higher than that observed with the alginate-only hydrogel, highlighting that even at low polymer concentrations (7 wt% of the functional precursor polymers in the final double network formulation), the dynamic covalent network can add significant mechanical strength to the prints (**Figure 7.3B**). While the clotting assays did not show a significant improvement in terms of anti-coagulant behaviour compared to the alginate-only hydrogel (**Figure S7.3**), a significant decrease in albumin uptake was reported for the double network hydrogels (**Figure 7.4**). While this result is not completely unambiguous in demonstrating the potential of the interpenetrating network bioink in promoting long-term anti-fibrotic properties, future work (see **Chapter 8**) will focus on implanting the optimal prints in mouse models to track the in vivo fibrotic response over time in a more realistic use case than direct continuous exposure to blood plasma. However, from a bioprinting perspective, use of the double network bioink was shown to significantly improve print fidelity and print stability under two printing strategies: (1) pre-mixing ketone and hydrazide functionalized DMAPS-OEGMA with or without sodium alginate and printing the pre-mixed formulation pre-gelation; and (2) using the embedded approach (described in detail in **Chapter 3**) by incorporating either the aldehyde functionalized DMAPS-OEGMA or calcium chloride, or both, in the gelatin support bath, and printing with hydrazide functionalized DMAPS-OEGMA, sodium alginate, or both (exploiting the miscibility improvement of the 90:10 DMAPS to OEGMA ratio with sodium alginate as described in **Chapter 6**). In particular, the pre-mixed double network hydrogel resulted in the highest print fidelity and most consistent mechanics (~7 kPa) over 7 days (**Figure 7.6**) and maintained high viability of encapsulated HepG2 cells over 14 days (>85%, **Figure 7.7**). This dual network strategy avoids not only the mechanical degradation observed over time using the single network alginate-calcium hydrogels but also provides a suitable (mechanical) environment for encapsulated liver cells that require consistent porosities for their phenotypic responses (i.e., release of albumin). Compared to existing literature around anti-fouling hydrogel bioinks (**Table 7.1**), this double network hydrogel strategy is the first demonstration of using a covalent click chemistry-based hydrogel in combination with the conventional ionic crosslinking of sodium alginate to provide the desired mechanics and stability for the long-term encapsulation of liver cells.

7.5 Conclusions

Double network hydrogels based on dual ionic crosslinking and hydrazone dynamic covalent chemistry were successfully printed using the FRESH printing method. Sodium alginate, a common choice for bioprinting applications due to its fast ionic gelation with calcium chloride and good cytocompatibility, lacks *in vivo* stability and anti-fouling properties; interpenetration with a dynamic covalent network based on hydrazide and aldehyde/ketone-functionalized copolymers of DMAPS and OEGMA (two highly anti-fouling monomers) thus offers potential to address both drawbacks. The gelation time could be tuned from instantaneous (<10 seconds) to 15 minutes, depending on the polymer concentration and the choice of aldehyde or ketone functionality. The double network hydrogels showed significantly reduced non-specific protein adsorption, improved stability, and improved printability, with stable compressive moduli of 6-8 kPa maintained over at least a two-week period and high compatibility maintained with co-printed HepG2 carcinoma cells (including the facilitation of cell proliferation) over a 14-day observation period. The dual benefit of improved print stability and high cell compatibility highlights the potential for using alginate-DMAPS-OEGMA double network hydrogels for liver tissue engineering applications.

7.6 Acknowledgements

The CALM Institute for Advanced Microscopy is acknowledged for their assistance with the confocal microscopy. The Natural Sciences and Engineering Research Council (Discovery Grant RGPIN-2017-06455 to TH), Mitacs (Accelerate Grant IT27833), the NSERC Undergraduate Student Research Award (MG), and a Canada Graduate Scholarship (to EM) are acknowledged for funding.

7.7 References

1. Lim, K. S.; Galarraga, J. H.; Cui, X.; Lindberg, G. C.; Burdick, J. A.; Woodfield, T. B., Fundamentals and applications of photo-cross-linking in bioprinting. *Chemical reviews* **2020,** *120* (19), 10662-10694.
2. Suntornnond, R.; An, J.; Chua, C. K., Bioprinting of thermoresponsive hydrogels for next generation tissue engineering: a review. *Macromolecular Materials and Engineering* **2017,** *302* (1), 1600266.
3. GhavamiNejad, A.; Ashammakhi, N.; Wu, X. Y.; Khademhosseini, A., Crosslinking strategies for 3D bioprinting of polymeric hydrogels. *Small* **2020,** *16* (35), 2002931.
4. Freeman, F. E.; Kelly, D. J., Tuning alginate bioink stiffness and composition for controlled growth factor delivery and to spatially direct MSC fate within bioprinted tissues. *Sci. Rep.* **2017,** *7*, 17042.
5. Pahlevanzadeh, F.; Mokhtari, H.; Bakhsheshi-Rad, H. R.; Emadi, R.; Kharaziha, M.; Valiani, A.; Poursamar, S. A.; Ismail, A. F.; RamaKrishna, S.; Berto, F., Recent trends in three-dimensional bioinks based on alginate for biomedical applications. *Materials* **2020,** *13* (18), 3980.
6. Lee, K. Y.; Mooney, D. J., Alginate: properties and biomedical applications. *Progr. Polym. Sci.* **2012,** *37* (1), 106-126.
7. King, A.; Sandler, S.; Andersson, A., The effect of host factors and capsule composition on the cellular overgrowth on implanted alginate capsules. *J. Biomed. Mater. Res.* **2001,** *57* (3), 374-383.
8. Manoury, B.; Caulet-Maugendre, S.; Guénon, I.; Lagente, V.; Boichot, E., TIMP-1 is a key factor of fibrogenic response to bleomycin in mouse lung. *Inter. J. Immunopath. Pharmacol.* **2006,** *19* (3), 471-487.
9. Thu, B.; Bruheim, P.; Espevik, T.; Smidsrød, O.; Soon-Shiong, P.; Skjåk-Bræk, G., Alginate polycation microcapsules: I. Interaction between alginate and polycation. *Biomaterials* **1996,** *17* (10), 1031-1040.
10. Haug, A., Affinity of some divalent metals to different types of alginates. *Acta Chem. Scand.* **1961**, 5 (8), 1794.
11. Mariani, E.; Lisignoli, G.; Borzì, R. M.; Pulsatelli, L., Biomaterials: foreign bodies or tuners for the immune response? *Inter. J. Mol. Sci.* **2019,** *20* (3), 636.
12. Blackman, L. D.; Gunatillake, P. A.; Cass, P.; Locock, K. E., An introduction to zwitterionic polymer behavior and applications in solution and at surfaces. *Chem. Soc. Rev.* **2019,** *48* (3), 757-770.
13. Shao, Q.; Jiang, S., Molecular understanding and design of zwitterionic materials. *Adv. Mater.* **2015,** *27* (1), 15-26.
14. He, M.; Gao, K.; Zhou, L.; Jiao, Z.; Wu, M.; Cao, J.; You, X.; Cai, Z.; Su, Y.; Jiang, Z., Zwitterionic materials for antifouling membrane surface construction. *Acta Biomater.* **2016,** *40*, 142-152.
15. Zhang, Y.; Liu, Y.; Ren, B.; Zhang, D.; Xie, S.; Chang, Y.; Yang, J.; Wu, J.; Xu, L.; Zheng, J., Fundamentals and applications of zwitterionic antifouling polymers. *J. Phys. Appl. Phys.* **2019,** *52* (40), 403001.
16. Leigh, B. L.; Cheng, E.; Xu, L.; Derk, A.; Hansen, M. R.; Guymon, C. A., Antifouling photograftable zwitterionic coatings on PDMS substrates. *Langmuir* **2018,** *35* (5), 1100-1110.
17. Zhu, Y.; Wang, J.; Zhang, F.; Gao, S.; Wang, A.; Fang, W.; Jin, J., Zwitterionic nanohydrogel grafted PVDF membranes with comprehensive antifouling property and superior cycle stability for oil-in-water emulsion separation. *Adv. Funct. Mater.* **2018,** *28* (40), 1804121.

18. Yang, W.; Xue, H.; Carr, L. R.; Wang, J.; Jiang, S., Zwitterionic poly (carboxybetaine) hydrogels for glucose biosensors in complex media. *Biosens. Bioelectron.* **2011,** *26* (5), 2454-2459.
19. Fang, K.; Wang, R.; Zhang, H.; Zhou, L.; Xu, T.; Xiao, Y.; Zhou, Y.; Gao, G.; Chen, J.; Liu, D., Mechano-responsive, tough, and antibacterial zwitterionic hydrogels with controllable drug release for wound healing applications. *Appl. Mater. Interfaces* **2020,** *12* (47), 52307-52318.
20. Zhang, L.; Cao, Z.; Bai, T.; Carr, L.; Ella-Menye, J.-R.; Irvin, C.; Ratner, B. D.; Jiang, S., Zwitterionic hydrogels implanted in mice resist the foreign-body reaction. *Nat. Biotechnol.* **2013,** *31* (6), 553-556.
21. Zhang, J.; Xin, W.; Qin, Y.; Hong, Y.; Xiahou, Z.; Zhang, K.; Fu, P.; Yin, J., "All-in-one" zwitterionic granular hydrogel bioink for stem cell spheroids production and 3D bioprinting. *Chem. Eng. J.* **2022,** *430*, 132713.
22. Zhang, J.; Chen, L.; Chen, L.; Qian, S.; Mou, X.; Feng, J., Highly antifouling, biocompatible and tough double network hydrogel based on carboxybetaine-type zwitterionic polymer and alginate. *Carbohydr. Polym.* **2021,** *257*, 117627.
23. Liu, Q.; Chiu, A.; Wang, L.; An, D.; Li, W.; Chen, E. Y.; Zhang, Y.; Pardo, Y.; McDonough, S. P.; Liu, L., Developing mechanically robust, triazole-zwitterionic hydrogels to mitigate foreign body response (FBR) for islet encapsulation. *Biomaterials* **2020,** *230*, 119640.
24. Carr, L. R.; Zhou, Y.; Krause, J. E.; Xue, H.; Jiang, S., Uniform zwitterionic polymer hydrogels with a nonfouling and functionalizable crosslinker using photopolymerization. *Biomaterials* **2011,** *32* (29), 6893-6899.
25. Asadikorayem, M.; Surman, F.; Weber, P.; Zenobi-Wong, M. In Enzymatically crosslinked zwitterionic microgels for bioprinting of macroporous scaffolds, *Tiss. Eng. Part A*, **2022**; S521-S522.
26. Kostina, N. Y.; Blanquer, S.; Pop-Georgievski, O.; Rahimi, K.; Dittrich, B.; Höcherl, A.; Michálek, J.; Grijpma, D. W.; Rodriguez-Emmenegger, C., Zwitterionic functionalizable scaffolds with gyroid pore Architecture for tissue engineering. *Macromol. Biosci.* **2019,** *19* (4), 1800403.
27. Pan, W.; Wallin, T. J.; Odent, J.; Yip, M. C.; Mosadegh, B.; Shepherd, R. F.; Giannelis, E. P., Optical stereolithography of antifouling zwitterionic hydrogels. *J. Mater. Chem. B* **2019,** *7* (17), 2855-2864.
28. Sällström, N.; Capel, A.; Lewis, M. P.; Engstrøm, D. S.; Martin, S., 3D-printable zwitterionic nano-composite hydrogel system for biomedical applications. *J. Tiss. Eng.* **2020,** *11*, 2041731420967294.
29. Zhao, D.; Tie, C.; Cheng, B.; Yang, S.; Wang, X.; Sun, Z.; Yin, M.; Zhu, H.; Yin, M., Effect of altering photocrosslinking conditions on the physical properties of alginate gels and the survival of photoencapsulated cells. *Polym. Degrad. Stab.* **2020,** *179*, 109297.
30. Choi, G.; Cha, H. J., Recent advances in the development of nature-derived photocrosslinkable biomaterials for 3D printing in tissue engineering. *Biomater. Res.* **2019,** *23*, 18.
31. Gopinathan, J.; Noh, I., Click chemistry-based injectable hydrogels and bioprinting inks for tissue engineering applications. *Tiss. Eng. Regen. Med.* **2018,** *15* (5), 531-546.
32. Mueller, E.; Poulin, I.; Bodnaryk, W. J.; Hoare, T., Click Chemistry Hydrogels for Extrusion Bioprinting: Progress, Challenges, and Opportunities. *Biomacromol.* **2022**, 23 (3), 619-640.
33. Wang, L. L.; Highley, C. B.; Yeh, Y. C.; Galarraga, J. H.; Uman, S.; Burdick, J. A., Three-dimensional extrusion bioprinting of single- and double-network hydrogels

containing dynamic covalent crosslinks. *J. Biomed. Mater. Res. A* **2018,** *106* (4), 865-875.
34. Puertas-Bartolomé, M.; Włodarczyk-Biegun, M. K.; Del Campo, A.; Vázquez-Lasa, B.; San Román, J., 3D printing of a reactive hydrogel bio-ink using a static mixing tool. *Polymers* **2020,** *12* (9), 1986.
35. Amaral, A. J.; Gaspar, V. M.; Lavrador, P.; Mano, J. F., Double network laminarin-boronic/alginate dynamic bioink for 3D bioprinting cell-laden constructs. *Biofabrication* **2021,** *13* (3), 035045.
36. Hull, S. M.; Lindsay, C. D.; Brunel, L. G.; Shiwarski, D. J.; Tashman, J. W.; Roth, J. G.; Myung, D.; Feinberg, A. W.; Heilshorn, S. C., 3D Bioprinting using UNIversal Orthogonal Network (UNION) Bioinks. *Adv. Funct. Mater.* **2021,** *31* (7), 2007983.
37. Smeets, N. M.; Bakaic, E.; Patenaude, M.; Hoare, T., Injectable and tunable poly(ethylene glycol) analogue hydrogels based on poly(oligoethylene glycol methacrylate). *Chem. Comm.* **2014,** *50* (25), 3306-3309.
38. Smeets, N. M.; Bakaic, E.; Patenaude, M.; Hoare, T., Injectable poly (oligoethylene glycol methacrylate)-based hydrogels with tunable phase transition behaviours: Physicochemical and biological responses. *Acta Biomater.* **2014,** *10* (10), 4143-4155.
39. Evans, D. W.; Moran, E. C.; Baptista, P. M.; Soker, S.; Sparks, J. L., Scale-dependent mechanical properties of native and decellularized liver tissue. *Biomech. Model. Mechanobio.* **2013,** *12* (3), 569-580.

7.8 Supplementary Information

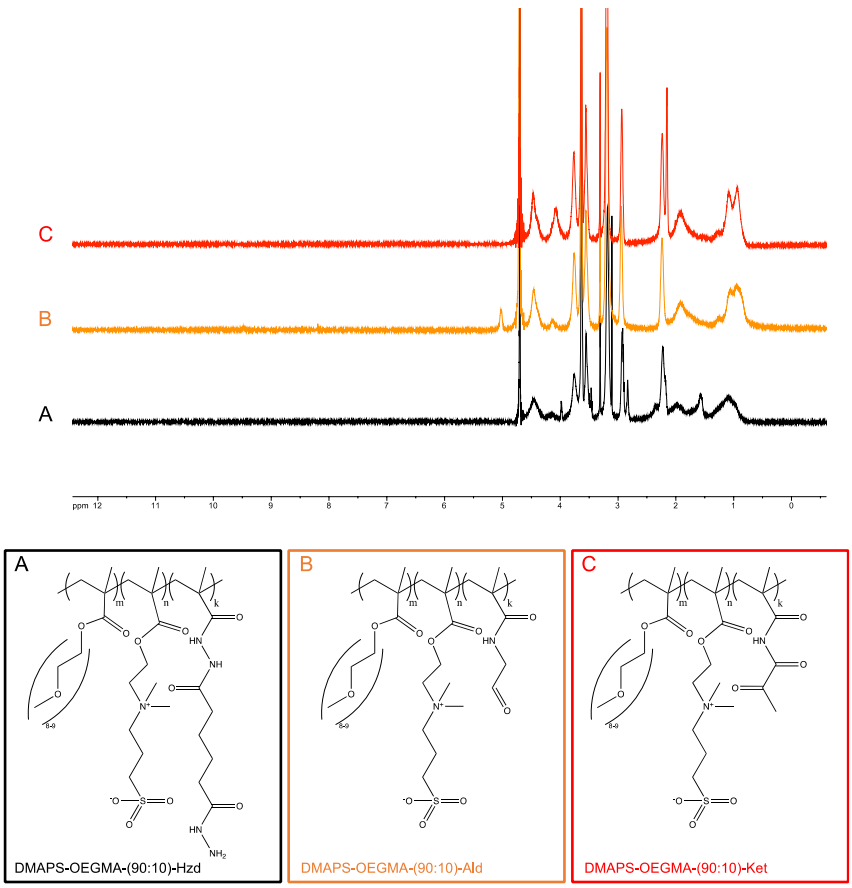

Figure S7.1: ^{1}H-NMR spectra for DMAPS-OEGMA-(90:10)-Hzd (A), DMAPS-OEGMA-(90:10)-Ald (B), and DMAPS-OEGMA-(90:10)-Ket (C) precursor polymers and related structures

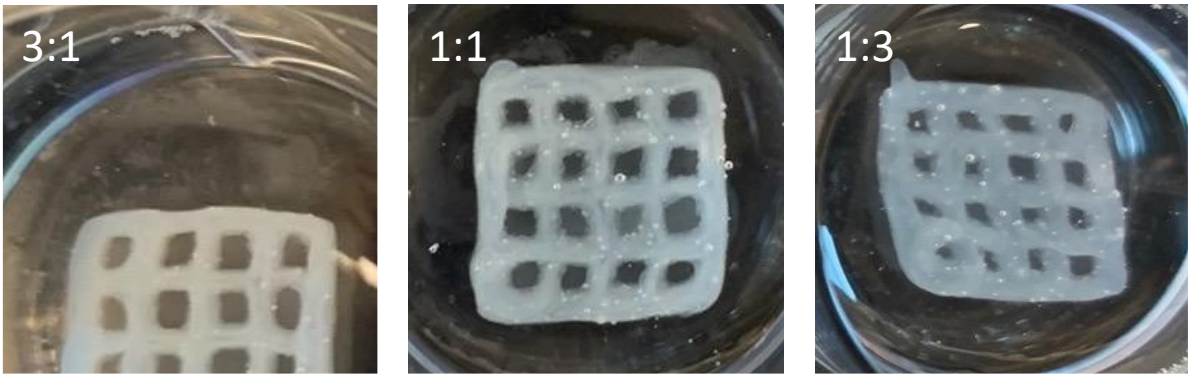

Figure S7.2: Preliminary alginate-DMAPS-OEGMA prints based on the embedded printing technique using a 3:1 (left), 1:1 (centre), or 1:3 (right) ratio of alginate-DMAPS-OEGMA-Hzd in the syringe and 3 wt%-DMAPS-OEGMA-Ald and 0.1 wt% $CaCl_2$ in the gelatin support bath.

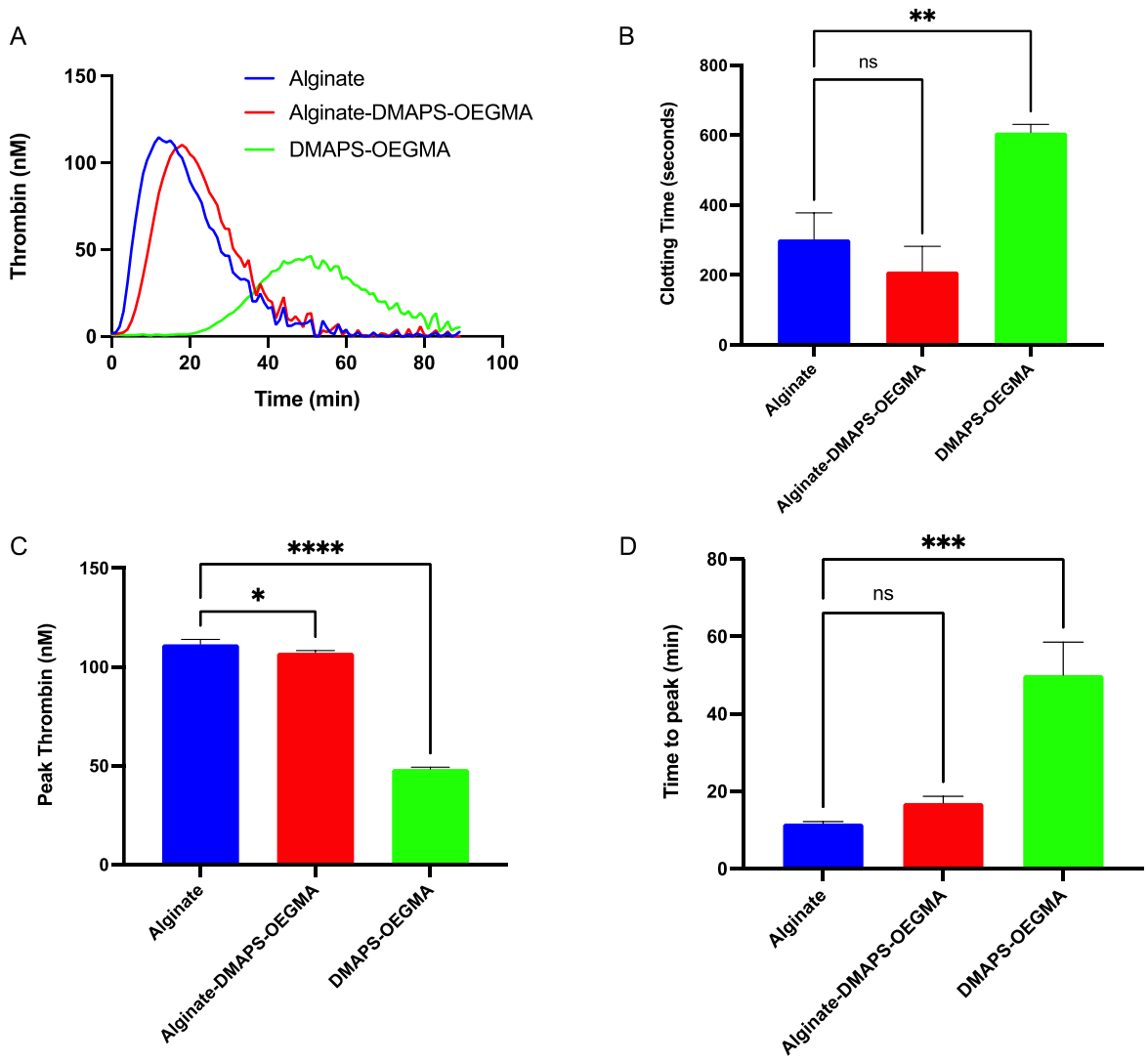

Figure S7.3: Coagulation studies on the three hydrogel inks used in the printing experiments (2 wt% alginate only, 7 wt% DMAPS-OEGMA Hzd/Ket only, and an interpenetrating network of 2 wt% alginate/7 wt% DMAPS-OEGMA Hzd/Ket): (A) thrombograms generated from the thrombin generation assay; (B) clotting times; and (C) peak thrombin and (D) time to peak thrombin quantifications based on the thrombograms. Error bars represent the standard deviation of three independent replicates. One-sided ANOVA is used at 95% confidence to assess statistical significance.

CHAPTER 8

Concluding Remarks

8.1 Scientific Contributions

The work presented in this thesis explored the translation of synthetic click chemistry hydrogel bioinks for extrusion bioprinting applications using different mixing strategies and a customized extrusion bioprinter. Overall, the main objectives for this work as outlined in **Chapter 1** were achieved and are described below along with the major contributions of this thesis to the base of knowledge within the field.

1. To demonstrate the printability of click chemistry-based hydrogel bioinks into high-resolution 3D structures. All presented chapters, except for **Chapter 6**, demonstrated the printability of synthetic hydrazone-crosslinked hydrogels bioinks without requiring the use of UV irradiation, non-physiological pH or temperature, or any other post-processing strategies to stabilize the final printed hydrogel constructs. Functional precursor polymers based on POEGMA (**Chapters 3** and **4**), DMAPS (**Chapter 5**), or a combination thereof (**Chapter 7**) were synthesized via chain transfer free radical polymerization to limit the molecular weight of the precursor polymers below the renal cut-off and were functionalized with hydrazide or aldehyde/ketone functional groups to form dynamic, yet degradable, hydrazone-crosslinked hydrogels upon mixing. The tunable gelation kinetics (from instantaneous to several minutes) allowed for distinct mixing modalities (*Objective #3*) to be evaluated in terms of the print fidelity, the homogeneity of the printed constructs (using fluorescently labelled polymers or cells), and the overall cell viability and functionality achievable using different printing approaches.

2. To fabricate hydrogel bioinks with suitable mechanical strength. Matching the mechanics of the printed hydrogel scaffolds to the native tissue is critical to achieving good cell viability and tissue-mimetic responses with the co-printed cells. **Chapters 4** and **5** demonstrate the tunability of the mechanics achievable by varying the embedded aldehyde-functionalized POEGMA polymer concentration within the gelatin support bath (**Chapter 4**),

or the precursor polymer concentrations in the pre-mixed DMAPS hydrogel formulation that can be printed into hydrazone-crosslinked small-scale liver mimics (**Chapter 5**). In addition, **Chapter 7** demonstrated the benefit of using dual-crosslinked ionic/covalent hydrogel scaffolds for preserving the mechanical properties of a printed hydrogel over time, a particular challenge with ionic-crosslinked hydrogels such as calcium-alginate that are typically used for extrusion-based 3D bioprinting.

3. To evaluate different mixing modalities for click chemistry-based hydrogel bioinks. Consideration of the combination of gelation kinetics and mixing strategy is critical to the success of using click chemistry for bioink design. Three mixing strategies were employed in this thesis: using a coaxial needle (**Chapter 3**), using an embedded strategy via the FRESH bioprinting method (**Chapters 4** and **7**), and using a pre-mixed approach by leveraging the slower-gelling ketone/hydrazide chemistry for easy incorporation of cells coupled with the favourable shear-thinning properties of the crosslinked hydrogels (**Chapter 5**). The overall objectives for using these mixing modalities were three-fold: (1) to achieve good print fidelity of the final printed structures; (2) to achieve suitable homogeneity of the functional precursor polymers for improved stability and mechanical strength; and (3) to achieve high cell viability and functionality (i.e., adhesion and release of important biomarkers) by minimizing the shear to which cells are exposed during the printing process without compromising the final mechanics of the printed structures.

4. To engineer the chemistry of the hydrogel matrix. *Chapter 6* focused on the development of a copolymer system (comprised of DMAPS and OEGMA) to overcome the immiscibility of DMAPS-only polymers with common ionic polysaccharides, such as sodium alginate. Different DMAPS:OEGMA ratios in the hydrazide-functionalized copolymers resulted in different swelling kinetics, protein uptake, and anti-coagulant properties in the resulting hydrazone-crosslinked hydrogels. Of particular interest, the incorporation of only 10 mol% of OEGMA into the polymer backbones significantly improved the miscibility of a range of carbohydrates with the zwitterionic DMAPS-based precursor polymers, a significant benefit for introducing biological cues for directing cell behavior into the anti-fouling and long-lasting DMAPS-based hydrogels.

8.2 Summary

Chapter 2 reviewed recent publications in the field of click chemistry hydrogels for tissue engineering applications and discussed the challenges inherent in translating these click chemistry hydrogels to 3D bioprinting applications. A thorough literature review was performed to understand the current examples of 3D printing covalent *in situ*-gelling hydrogels and provide a technical overview over the advantages and disadvantages of existing click chemistry hydrogel bioink development. This literature review provided the backbone of the subsequent chapters, as it described the current landscape of this emerging field and identified key challenges in the field that the subsequent experimental chapters sought to address.

Chapter 3 described the 2.5D patterning of click chemistry hydrogel bioinks using a modified coaxial needle and a customized extrusion printer. This work demonstrated the potential of a coaxial needle as a means for mixing two functional precursor polymers and forming hydrazone crosslinked hydrogels upon extrusion in precisely defined patterns (with and without cells). The diffusion profile of the polymers was successfully modeled using a computational modeling approach, allowing efficient determination of optimal process parameter ranges that were then experimentally validated using an in-house coaxial extrusion bioprinting setup. This work can be extended to other types of low-viscosity functional polymers that form a crosslinked hydrogel network upon mixing, although further development of the strategy is required to print taller 3D structures with high shape fidelity.

Chapter 4 extended the work in **Chapter 3** by providing a strategy to fabricate more 3D structures using an embedded printing technique. 3D bioprinting of synthetic click chemistry hydrogels was demonstrated using the freeform reversible embedding of suspended hydrogels (FRESH) technique coupled with a customized low-cost extrusion printer. The dynamic nature and reversibility of hydrazone crosslinking enabled reconfiguration of the initially more heterogeneous gel structure to form a more homogeneous internal gel structure, even for more highly cross-linked hydrogels, over a relatively short time (<3 days) while preserving the degradability of the scaffold over longer time frames. NIH/3T3 fibroblasts and human umbilical vein endothelial cells were co-printed with the bioinks, with high cell viability maintained (>80%) and F-actin-mediated adhesion to the scaffold supported over a 14-day *in*

vitro incubation period, demonstrating their potential use in practical tissue engineering applications.

While **Chapter 4** used a support bath for fabricating high-resolution 3D constructs, **Chapter 5** eliminated the need for the support bath by relying on the slower-gelling and highly shear-thinning ketone-hydrazide chemistry to facilitate effective free-form printing. High-resolution liver mimics could be successfully printed by pre-mixing hydrazide and ketone-functionalized zwitterionic polymers (with and without cells) and extruding the hydrogel bioink with optimized printing parameters. Co-printing with hepatocytes alone or in a co-culture with fibroblast cells resulted in high viability over a 14-day culture period, and the secretion of albumin significantly increased with the co-culture due to the presence of fibroblast cells that directly impacts the functionality of the hepatocytes. The choice of the zwitterionic polymers allowed for prolonged degradation timescales and improved anti-fouling properties, providing potential key benefits for designing implantable liver tissue mimics in which the secreted protein (i.e., albumin) can be freely released into the microenvironment over extended time periods. Moreover, the printed microporosity of the liver structures allowed for cellular reconstruction over time when co-printed with both hepatocytes and fibroblast cells while still supporting high cell retention and viability.

Chapter 6 extended the work on the functional zwitterionic polymers used in **Chapter 4** by synthesizing and characterizing a co-polymer system based on the zwitterionic monomer (DMAPS) and a PEG-analogue oligomer (OEGMA). The motivation behind this copolymer system was to ensure that the zwitterionic polymer is miscible with sodium alginate, which is often regarded as a ‘gold standard’ for current bioink development for extrusion bioprinting applications. DMAPS polymers alone were not miscible with sodium alginate while POEGMA polymer were completely miscible, motivating the development of hydrazide and aldehyde functionalized copolymers based on various ratios of DMAPS to OEGMA. The gelation time, swelling properties, single protein adsorption and coagulation in the presence of human plasma were all strong functions of the DMAPS:OEGMA ratio, with the high OEGMA ratio polymers resulting in increased gelation time to the steric hindrance in the polymer backbone and increased protein uptake when exposed to single fluorescently labelled proteins (albumin, lysozyme, fibrinogen). In particular, the 90:10 ratio of DMAPS to OEGMA performed

optimally in terms of decreasing both protein adsorption and absorption, reducing peak thrombin levels in the clotting experiment, and facilitating high miscibility with particularly anionic polysaccharides that induced phase separation when added to DMAPS-only polymers, opening new possibilities for creating 3D printable natural-synthetic polymer zwitterionic implants.

Chapter 7 leveraged the key miscibility results from **Chapter 6** to print interpenetrating network bioinks based on hydrazone-crosslinked DMAPS-OEGMA and calcium alginate-crosslinked sodium alginate using the embedded strategy described in **Chapter 4.** The dual crosslinked hydrogel ink formulations were based on both ionic crosslinking (sodium alginate crosslinked with calcium chloride) and chemical crosslinking (functional DMAPS-OEGMA polymers with hydrazide and aldehyde/ketone moieties). The different printing strategies developed in the previous chapters, including the embedded (hydrazide/aldehyde, **Chapter 4**) and pre-mixing (hydrazide/ketone, **Chapter 5**) techniques, were compared to assess differences in printability and stability over time. Printing pre-mixed DMAPS-OEGMA hydrazide/ketone polymers mixed with sodium alginate into a calcium chloride-containing support bath was identified as the method facilitating the best print fidelity and print stability, with no significant degradation or loss of mechanics observed over 14 days of incubation in calcium-supplemented cell media. While the anti-fouling benefits of including the DMAPS-OEGMA phase in the hydrogel require additional *in vivo* study to confirm, significantly reduced protein uptake was observed to the interpenetrating network printed structures, suggesting potential benefits for preventing fibrosis *in vivo.*

Collectively, this thesis described the benefits of synthetic click chemistry hydrogel bioinks for extrusion bioprinting applications. The mechanism by which the functional precursor polymers were mixed directly determined the resolution and print fidelity of the final printed constructs, and the chosen synthetic hydrogel bioinks could be successfully co-printed with different cell types and maintain high cell viability and functionality over extended culture periods.

8.3 Future Directions

Building on the results of this work, the following directions will be pursued to better understand the printability of dynamic covalent bioinks as well as optimize the bioink formulations and printing strategies for practical use.

1. The computational fluid dynamic modelling approach is currently limited to a coaxial needle design that incorporates a shorter inner needle, making the mixing of two low-viscosity functional polymers possible. To transition the work to larger constructs, two challenges have been identified: (1) (occasional) clogging of the crosslinked hydrogels within the coaxial needle design; and (2) the limitation of identical flow rates though both inner and outer needle, which is a limitation of the custom-built printer. Potential experimental solutions to these mentioned challenges include the extension of the COMSOL model to triaxial design (i.e., incorporating a sheath flow that can be removed upon depositing the crosslinked hydrogel on the chosen substrate) and introducing individualized control over core and shell flows using two separate syringe pumps.

2. **Chapters 4** and **5** demonstrate the 3D bioprinting of POEGMA and DMAPS hydrogels via embedded and free form (pre-mixed) bioprinting, respectively. Although the co-printing of one or two cell types resulted in excellent viability, cell adhesion and overall functionality, there remain two key limitations to advanced tissue printing: (1) a limited capacity to print heterogeneous structures in which cells are localized in different parts of the print to mimic the complexity of native human tissues more accurately; and (2) a lack of vascularization within the printed hydrogels constructs. The microporosity printed within the small-scale liver tissue mimics (**Chapter 5**) may provide an interesting strategy for introducing both heterogeneity and vascularization; that is, perfusing endothelial cells through the micropores in the printed structure (coupled with the demonstrated capacity of the bioink to adhere to cells within these micropores in **Chapter 5**) may facilitate blood vessel development within the printed scaffolds. Such vascularization would be highly beneficial for prolonging the functionality of the encapsulated liver cells and mimic liver tissue more accurately.

3. To extend this bioink development to more human-like tissues, co-printing human derived stem cells (or other primary cell lines) would be beneficial to ensure that the chosen bioink compositions are suitable for more sensitive cell lines. Co-printing with primary human hepatocytes to extend the work on the small-scale livers (using the bioinks developed in **Chapter 5** or **Chapter 7**) offers potential for creating implantable metabolic cell therapeutics to regenerate native liver function. In parallel to printing these more sensitive cell lines, identifying the feasibility of printing larger constructs would also be critical in this context to determine the limit of the print fidelity (if there is one) and the suitability of the mixing strategies developed to facilitating longer and more complex prints.

4. **Chapter 7** demonstrated the printability of dual-crosslinked alginate-zwitterionic hydrogels and potential improvements in terms of their anti-fouling behaviour compared to the alginate-only hydrogels. This work will be extended to include more protein uptake studies (specifically, to elucidate the differences in adsorption vs absorption) and to an *in vivo* study to ultimately determine the anti-fouling and anti-fibrotic properties of this dual-crosslinked hydrogel bioink.